Università Politecnica delle Marche

Faculty of Engineering

PhD Program

Civil, Environmental and Building Engineering and Architecture

XXXV Cycle (2019-2022)

PhD Curriculum

Civil, Environmental and Building Engineering and Architecture

Consolidation of marine dredged sediments in confined disposal facilities

by

Eng. Federica Pasqualini

A Doctoral Dissertation submitted for the degree of Doctor of Philosophy in Geotechnics (SSD ICAR/07)

Advisor

Prof. Eng. Evelina Fratalocchi

Curriculum Supervisor

Prof. Eng. Francesco Fatone

ACKNOWLEDGEMENTS

Now that my doctoral experience is almost over, the time has come to thank all the people around me who have somehow been involved in this study.

First and foremost, I want to mention my academic tutor Prof. Evelina Fratalocchi, who thoughtfully supervised my work: her guidance and expertise have been paramount for getting things into perspective. She receives all my gratitude and thanks for all the assistance, patience, and opportunities she gave me since the very first day of my PhD pathway.

I would like to thank my pre-examiners, Prof. Paola Monaco and Prof. Gianfranco Totani, for taking the time to review this dissertation with such attention and interest. Their positive feedbacks are very much appreciated, also in view of future developments of this research.

Valuable suggestions also came from Prof. Ivo Bellezza, Prof. Marta Di Sante, and Prof. Francesco Mazzieri, who provided me with explanations, insights, and literature sources which are referred to in this dissertation.

I am indebted to my friends and mates Andrea Olimpio, Mirko Felici, Jonathan Domizi, and Davide Bernardo, for the many helpful discussions and debates, support with field and lab tests, as well as for all the good times we had together in and out of the university.

I feel privileged to have worked alongside Prof. Erio Pasqualini, with whom I share the surname, although any kinship. It was a great learning experience, and I am deeply grateful to him for all the expert advice, inspiring conversations, and for his kindness.

A special thanks should be addressed to the Central Adriatic Ports Authority for having made available to our research the CDF testing site in the Ancona Harbour.

The greatest thanks should be given to my parents Carlo and Patrizia, my sister Claudia, my brother-in-law Luca, and my little wonderful grandson Tommaso, for tolerating me during the stressful times and for never let me miss their loving support and constant encouragement.

Ancona, May 2023
Federica Pasqualini

ABSTRACT

The research focused on the development of an innovative, sustainable, and cost-effective design strategy for confined disposal facilities (CDFs), which makes use of special geotubes filled with the sediments themselves to provide internal sectors to be separately consolidated while filling the adjacent ones, thus leading to optimisation of times and resources. In each sector the consolidation treatment can be performed by PVDs-assisted preloading by embankment, according the "moving embankment" concept.

The feasibility of this design strategy has been verified on the first sector of the CDF built in the Ancona Harbour, where the procedures for installation of the geotube were set up and, after filling the sector with fine-grained dredged sediments, an instrumented full-scale test field has been designed and set up to the purpose. The instrumented test field, combined with a wide set of laboratory and field investigations, allowed to study the full-scale consolidation process by the PVDs-assisted preloading with the moving embankment and to quantify the efficiency and the timing of the treatment for the future management and geotechnical design of the sectors in the Ancona CDF.

Activities of the test field have been carried out in three main phases: (1) *ante operam* characterisation of the disposed sediments; (2) PVDs installation, embankment construction and monitoring of applied loads, excess pore pressures and settlements during construction and dwell time of the embankment; (3) *post operam* characterisation, after the embankment removal.

Tests data and results from the *ante operam* phase have been analysed to define the design parameters and hydraulic conductivity constitutive relationship $k(e)$, for an accurate assessment of consolidation times. An advanced consolidation theory has been applied to model consolidation of the dredged sediments disposed into a CDF. To support engineers in drawing up this kind of filling-and-consolidation procedure, simplified design charts have been proposed, which link the main three variables (PVDs spacing, preloading magnitude and waiting time) and allow for a quick pre-design. The charts refer to the Ancona CDF, but the proposed methodology can be generalised, once known the sediments characteristics.

The results obtained from monitoring activities have been used to validate the design approach by back-analyses, which demonstrated the validity of the design assumptions. In

particular, the theory by Tang & Onitsuka (2000), which accounts for time-dependent loading, drain resistance and smear effect, both radial and vertical drainage (not negligible for small layer thickness, as in the case of concern), was found to well reproduce the consolidation process of the fine-grained dredged sediments.

From the *post operam* phase, an empirical s_u-q_t correlation has been proposed to estimate the undrained shear strength of clay-like dredged sediments after mechanical overconsolidation from CPTU results. The resulting cone factors suggest the existence of a decreasing trend with the overconsolidation ratio. Further research is necessary and will be developed in the near future in this field to corroborate the reliability of the proposed correlation, that can be useful in geotechnical design for reusing CDFs hosting clay-like sediments after their consolidation by preloading.

LIST OF CONTENTS

ACKNOWLEDGEMENTS ..... **iii**
ABSTRACT ..... **v**
LIST OF CONTENTS ..... **vii**
LIST OF FIGURES ..... **xi**
LIST OF TABLES ..... **xvii**
1 INTRODUCTION **1**
2 LITERATURE REVIEW **3**
2.1 Introduction **3**
2.2 Consolidation theories **4**
2.2.1 One-dimensional consolidation theory **4**
2.2.2 Large strain consolidation theory **9**
2.2.3 Consolidation by vertical drains **12**
2.2.3.1 Classical theories 12
2.2.3.2 Advanced theories including time-dependency 19
2.3 Interpretation of undrained shear strength of clays from CPTs **23**
2.3.1 Theoretical solutions **24**
2.3.2 Empirical solutions **27**
3 METHODS **33**
3.1 Laboratory tests **33**
3.1.1 Classification **33**
3.1.2 Water content **34**
3.1.3 X-ray diffraction analyses **34**
3.1.4 One-dimensional consolidation tests **37**
3.1.5 Triaxial tests **38**
3.2 In-situ tests **38**
3.2.1 Cone penetration test **38**
3.2.1.1 Processing of CPTU data 41
3.2.1.1.1 Correction for porewater effects *41*
3.2.1.1.2 Stress normalization *42*
3.2.1.1.3 Classification charts *43*
3.2.2 Dissipation tests **46**

4 CASE STUDY: THE ANCONA CDF 47
4.1 Introduction 47
4.2 General description of the facility 49
4.2.1 Soil profile 49
4.2.2 Construction details 50
4.3 Filling-and-consolidation: an innovative solution 53
4.4 Construction of the sector for the test field 56
4.4.1 Boundaries 56
4.4.2 Filling 58
4.4.3 Top layer 59
5 FULL SCALE TEST FIELD 61
5.1 Introduction 61
5.2 Phase 1: *ante operam* characterisation 62
5.2.1 Preliminary characterisation by laboratory testing 62
5.2.1.1 Classification tests and index properties 63
5.2.1.2 One-dimensional consolidation tests 64
5.2.2 Field investigations 68
5.2.2.1 Cone penetration tests 69
5.2.2.2 Dissipation tests 78
5.3 Phase 2: design of the test field 80
5.3.1 Drain type 81
5.3.2 Design parameters 81
5.3.3 Load analysis 82
5.3.4 Settlement analysis and target degree of consolidation 82
5.3.5 Modelling of consolidation 83
5.4 Phase 3: test field construction 88
5.4.1 PVDs installation 88
5.4.2 Monitoring instruments 89
5.4.2.1 Earth pressure cells 90
5.4.2.2 Drive-in electrical piezometers 90
5.4.2.3 Settlement gauges 91
5.4.3 Construction of the preloading embankment 92
5.5 Phase 4: *post operam* characterisation 95
5.6 Development of a general design equation 95
5.6.1 Model and hypotheses 95
5.6.2 Modelling procedure 96
5.6.3 Example of application 98
6 RESULTS AND DISCUSSION 101
6.1 Monitoring results 101
6.1.1 Back-analysis of monitoring results 105

6.2 *Post operam* characterisation 107
6.2.1 In situ tests 107
6.2.1.1 Cone penetration testing 108
6.2.1.2 In situ sampling 119
6.2.2 Laboratory tests results 122
6.2.2.1 Classification tests 124
6.2.2.2 XRD analyses 128
6.2.2.3 Overconsolidation 130
6.2.2.4 Shear strength 132
6.3 Calibration of s_u-q_t correlation for marine dredged sediments 141
6.3.1 Identification of homogeneous soil units 142
6.3.2 Smoothing of the cone penetration data 143
6.3.3 Processing of triaxial tests 144
6.3.4 Determination of cone factors and correlation 148
7 CONCLUSIONS 153
REFERENCES 157

LIST OF FIGURES

Figure 2.1. One dimensional consolidation problem (after Lancellotta, 2008). 6

Figure 2.2. Solution of one-dimensional consolidation for the case of uniform initial excess porewater pressure and doubly drained layer (after Taylor, 1948). The x-axis indicates the degree of consolidation in terms of pore pressures, U_z (Eq. (2.7)), while on the y-axis the term Z is a dimensionless depth. The curves are pore pressure isochrones representing the spatial distribution of the excess pore pressure at a fixed instant of time. 7

Figure 2.3. Average degree of consolidation for different initial isochrones (Janbu et al., 1956). 8

Figure 2.4. Schematic picture of a soil cylinder dewatered by a vertical drain: (a) idealized case; (b) real case including the effect of smear and well resistance. 15

Figure 2.5. Radius of the influence zone, R, for square and equilateral triangular spacing of the vertical drains (plan view). 15

Figure 2.6. Analysis scheme of soil cylinder with vertical drain (adapted from Tang & Onitsuka, 2000). 20

Figure 2.7. Types of time-dependent ramp loading: (a) single-ramp loading; (b) multi-ramp loading (after Tang & Onitsuka, 2000). 22

Figure 2.8. Assumed failure mechanisms for deep penetration (adapted from Durgunoglu & Mitchell, 1975). 26

Figure 2.9. Assumed relationships between cone resistance and cavity limit pressures (adapted from Yu & Mitchell, 1998). 26

Figure 3.1. Geometrical condition for X-ray diffraction according to Bragg's law (after Mitchell & Soga, 2005). Beams of X-rays having identical wavelength and phase approaching a crystal with an angle of incidence θ are scattered specularly by the atoms in lattice planes regularly spaced a distance d apart. Hence, diffracted beams deviate 2θ from incident beams. The radiation wavelength λ is comparable to the d-distance. Notice that when the extra length 2dsinθ (= BC+CD) crossed by the lower beam is equal to an integer multiple of the radiation wavelength, the diffracted beams from each atomic plane would be in phase, leading to constructive interference. When this condition is met, an XRD peak is observed. 36

Figure 3.2. Schematic of a powder X-ray diffractometer, consisting of an X-ray source, a sample mounting stage, an X-ray detector, and a goniometer to vary the incident angle θ. 36

Figure 3.3. The X-ray diffractometer Bruker D8 Advance used in this research. 37

Figure 3.4. Possible positions of the filter element in a piezocone. 39

Figure 3.5. The penetrometer Pagani TG 63-200 positioned on the test field area. 40

Figure 3.6. Pore pressure effects on cone data (after Schnaid, 2008). The net area ratio is a = A_n/A_c. 42

Figure 3.7. Normalised SBTn Q_{tn}-F_R chart after Robertson (1990). 44

Figure 3.8. Normalised SBTn Q_{tn}-F_R chart after Robertson (2016). 45

Figure 4.1. Location of the five port infrastructures involved in the dredging program. 48

Figure 4.2. The Ancona Harbour: the white circle localises the CDF (image Google Earth). 48

Figure 4.3. Stratigraphic block-diagrams of the CDF site area. 49
Figure 4.4. Stratigraphy of the seabed in the area of the CDF. 50
Figure 4.5. Sheet pile walls of the Ancona CDF. 51
Figure 4.6. Steel sheet pile sections: in the circle, the specific Larssen interlock is highlighted. 51
Figure 4.7. Installation of the sheet piles: (a) landside; (b) seaside. 52
Figure 4.8. Solutions to ensure a proper connection between sheet piles: (a) the water-swelling resin Roxan™, applied along the interlock to control seepage through the wall; (b) the declutching detector system Dixeran®, to check by short-circuit if the sheet piles are properly interlocked underground. 53
Figure 4.9. Filling and consolidation sequence at the Ancona CDF: (a) geotube installation; (b) disposal of sediments in the first sector; (c) consolidation of sediments in the first sector and simultaneous filling of the second sector; (d) consolidation of the second sector; (e) consolidation of the geotube area; (f) combined consolidation of the second sector and of the geotube are with a wider moving embankment (draws are not in scale). 56
Figure 4.10. The test field sector. 57
Figure 4.11. Installation of the geotube at the Ancona CDF: (a) placement of the geotube bag; (b) and (c) filling phases of the geotube; (d) completed installation. 58
Figure 4.12. Filling of the test field sector: (a) start-up phase; (b) filling operations from the sea-side of the CDF; (c) spreading of the disposed sediments; (d) surficial crust formed after water evaporation. 59
Figure 4.13. Construction of the top drainage layer. 60
Figure 5.1. Field test dimensions and locations. 61
Figure 5.2. Design section of the test field. 62
Figure 5.3. Compression curves obtained by IL oedometer tests on the sediments FAN. 65
Figure 5.4. Compression curves obtained by IL oedometer tests on the sediments FIN. 65
Figure 5.5. Compression curves obtained by IL oedometer tests on the sediments ISA. 65
Figure 5.6. Updated hydraulic conductivity constitutive law for sediments FAN (on the left) and FIN (on the right). 68
Figure 5.7. Planimetric layout of cone penetration tests. 69
Figure 5.8. CPTM1-ANTE. 70
Figure 5.9. CPTM2-ANTE. 70
Figure 5.10. CPTM3-ANTE. 71
Figure 5.11. CPTM4-ANTE. 71
Figure 5.12. CPTM5-ANTE. 72
Figure 5.13. CPTM6-ANTE. 72
Figure 5.14. CPTM7-ANTE. 73
Figure 5.15. CPTM8-ANTE. 73
Figure 5.16. CPTU1-ANTE. 74
Figure 5.17. CPTU2-ANTE. 74
Figure 5.18. CPTU3-ANTE. 75
Figure 5.19. CPTU4-ANTE. 75
Figure 5.20. CPTU5-ANTE. 76
Figure 5.21. CPTU6-ANTE. 76
Figure 5.22. Stratigraphic sections: CM = coarse material layer; SED = sediment layer; DS = dense sand layer; L1 and L2 are coarser lenses. 77

Figure 5.23. Dissipation curves recorded at a depth of 5.1 m during a pause of CPTU1 (on the left) and a depth of 2.1 m on CPTU6 (on the right). 79
Figure 5.24. Empirical evaluation of the rigidity index, I_R, after Keaveny & Mitchell (1986). 79
Figure 5.25. Empirical evaluation of the hydraulic conductivity, k_h, after Parez & Fauriel (1988). 80
Figure 5.26. Cross-section of the Colbonddrain® CX1000. 81
Figure 5.27. Multi-ramp loading sequence for the embankment design. 86
Figure 5.28. Excess pore pressures and average degree of consolidation for two drains spacing options. 87
Figure 5.29. Installation of the PVDs: (a) installation rig; (b) completed area. 88
Figure 5.30. Planimetric layout of monitoring instruments. 89
Figure 5.31. Earth pressure cell. 90
Figure 5.32. Drive-in piezometer: (a) instrument supply; (b) CPT rig positioning to drive piezometers. 91
Figure 5.33. Settlement gauge: (a) pressure transducer on its metal support plate, placed into a trench; (b) the reservoirs. 92
Figure 5.34. Construction of the moving embankment. 93
Figure 5.35. The finished embankment. 94
Figure 5.36. Reference scheme. 96
Figure 5.37. Preloading approach based on settlements: (a) settlements vs time; (b) load vs time. ... 96
Figure 5.38. Design chart for PVDs square grid for the Ancona CDF. 99
Figure 5.39. Design chart for PVDs triangular grid for the Ancona CDF. 99
Figure 6.1. Overlay plot of monitoring results across time. Red lines indicate the stresses detected by earth pressure cells; blue lines report excess pore pressures measured by piezometers; green lines indicate the vertical displacements measured by settlement gauges. 103
Figure 6.2. Reference geologic section for back-analysis of piezometer data. 105
Figure 6.3. Actual multi-ramp loading sequence used for the back analysis (black solid line) compared with the design loading sequence (grey dashed line) and the values of q_R recorded by the earth pressure cell C1 (red solid line). 106
Figure 6.4. Comparison of excess pore pressures modelled by Tang & Onitsuka (2000) and those measured by piezometers. 107
Figure 6.5. Planimetric layout of in situ tests performed post operam. 108
Figure 6.6. CPTM1-POST. 110
Figure 6.7. CPTM2-POST. 110
Figure 6.8. CPTM3-POST. 111
Figure 6.9. CPTM4-POST. 111
Figure 6.10. CPTM5-POST. 112
Figure 6.11. CPTM6-POST. 112
Figure 6.12. CPTM7-POST. 113
Figure 6.13. CPTM8-POST. 113
Figure 6.14. CPTU1-POST. 114
Figure 6.15. CPTU2-POST. 114
Figure 6.16. CPTU3-POST. 115
Figure 6.17. CPTU4-POST. 115
Figure 6.18. CPTU5-POST. 116
Figure 6.19. CPTU6-POST. 116

Figure 6.20. Comparison of corrected cone tip resistance between ante and post operam conditions. 117
Figure 6.21. Comparison of classification charts by Robertson (2016) for ante operam and post operam conditions for the six piezocone soundings. 118
Figure 6.22. The drilling rig S30 (by Mori s.r.l.), mounted on a crawler truck, during the geotechnical campaign after the embankment removal. 119
Figure 6.23. Core boxes from borehole S1: (a) from 0 to 5 m; (b) from 5 to 10 m. 120
Figure 6.24. Core boxes from borehole S2: (a) from 0 to 5 m; (b) from 5 to 10 m. 120
Figure 6.25. Core boxes from borehole S3: (a) from 0 to 5 m; (b) from 5 to 10 m. 120
Figure 6.26. Borehole logs and values of the undrained shear strength, s_u, derived from pocket penetrometer data for the three boreholes S1, S2, and S3. Description of the soil units: “A” = crushed stone and gravel (topsoil); “B” = silt and dark sandy silt, very plastic (dredging filling); “C” = grey silty sands (base layer). 122
Figure 6.27. Grading curves for all the samples investigated along the vertical S1. 124
Figure 6.28. Plasticity chart for the samples of vertical S1. 125
Figure 6.29. Visual representation of Atterberg Limits and grain size distribution results along the depth as associated to CPTU1. 126
Figure 6.30. Grading curves for all the samples investigated along the vertical S2. 127
Figure 6.31. Plasticity chart for the vertical S2. 127
Figure 6.32. Visual representation of Atterberg Limits and grain size distribution results along the depth as associated to CPTU3. 128
Figure 6.33. XRD pattern for the representative sample taken at 2.3 m. 129
Figure 6.34. XRD pattern for the representative sample taken at 5.3 m. 129
Figure 6.35. XRD pattern for the sample taken at 1.5 m. 129
Figure 6.36. XRD pattern for the sample taken at 4.0 m. 130
Figure 6.37. Compressibility curve for sample S1-C2. 132
Figure 6.38. Compressibility curve for sample S2-C1. 132
Figure 6.39. Results of triaxial CIUC test on reconstituted clay of sample S1-C2: (a) q-ε_z curves; (b) Δu-ε_z curves; (c) effective stress paths and critical state line in the q-p’ space; (d) effective stress circles and failure envelop in the Mohr space. 134
Figure 6.40. Results of triaxial CIUC test on undisturbed clay of sample S1-C2: (a) q-ε_z curves; (b) Δu-ε_z curves; (c) effective stress paths and critical state line in the q-p’ space; (d) effective stress circles and failure envelop in the Mohr space. 135
Figure 6.41. Results of triaxial CIUC test on undisturbed clay of sample S1-C3: (a) q-ε_z curves; (b) Δu-ε_z curves; (c) effective stress paths and critical state line in the q-p’ space; (d) effective stress circles and failure envelop in the Mohr space. 137
Figure 6.42. Results of triaxial UU test on undisturbed clay of sample S1-C3: (a) q-ε_z curves; (b) total stress circle and failure envelop in the Mohr space. 138
Figure 6.43. Results of triaxial CIUC test on undisturbed clay of sample S2-C1: (a) q-ε_z curves; (b) Δu-ε_z curves; (c) effective stress paths and critical state line in the q-p’ space; (d) effective stress circles and failure envelop in the Mohr space. 139
Figure 6.44. Results of triaxial UU test on undisturbed clay of sample S2-C1: (a) q-ε_z curves; (b) total stress circle and failure envelop in the Mohr space. 140
Figure 6.45. Results of triaxial UU test on undisturbed clay of sample S2-C2: (a) q-ε_z curves; (b) total stress circle and failure envelop in the Mohr space. 140
Figure 6.46. Identification of clay-like units in CPTU1 and CPTU3 soundings. 143
Figure 6.47. Smoothing of q_t values in the clay-like layers. 144

Figure 6.48. In-situ stress state. From the left: overconsolidation ratio (OCR); coefficient of earth pressure at rest (K_0); hydrostatic pressure (u_0) and effective vertical (σ'_{v0}), horizontal (σ'_{h0}), and mean stresses (σ'_m)..... 145

Figure 6.49. Linear regression of CIUC undisturbed samples (bold dash-dot line) and reconstituted samples (dotted line). 146

Figure 6.50. Comparison between the undrained shear strength computed from the SHANSEP model and the site-specific extrapolated law. 148

Figure 6.51. Back-calculation of cone factors for the reference verticals CPTU1 and CPTU3..... 149

Figure 6.52. Plot of back-calculated cone factors against the corresponding OCR..... 150

Figure 6.53. Comparison between the undrained shear strength determined by the SHANSEP model and the proposed empirical correlation. 152

LIST OF TABLES

Table 2.1. Constitutive models for self-weight consolidation analysis (from Hawlader et al., 2008). 11
Table 2.2. Theoretical cone factors (modified from Konrad & Law, 1987). 25
Table 2.3. Literature review of the empirical total cone factor N_k. 28
Table 2.4. Literature review of the empirical total cone factor N_{kt}. 29
Table 2.5. Literature review of the empirical effective cone factor N_{ke}. 31
Table 2.6. Literature review of the empirical effective cone factor $N_{\Delta u}$. 31
Table 3.1. Classification tests performed on the sediments. 33
Table 3.2. Technical specifications and size of the piezocone MKS Pagani used in this research. 40
Table 4.1. Dimensions and properties of the steel sheet piles profiles employed in the Ancona CDF. . 51
Table 5.1. Classification and physical characterisation of the sediments disposed into the first sector of the Ancona CDF. 64
Table 5.2. Average parameters from IL oedometer tests on the sediments FAN. 66
Table 5.3. Average parameters from IL oedometer tests on the sediments FIN. 66
Table 5.4. Average parameters from IL oedometer tests on the sediments ISA. 66
Table 5.5. Results of dissipation tests. 80
Table 5.6. PVD characteristics (from the technical sheet). 81
Table 5.7. Input data for the settlement analysis and values of computed consolidation settlements. . 83
Table 5.8. Design parameters and assumptions. 84
Table 5.9. Multi-ramp loading sequence: time schedule. 85
Table 5.10. Multi-ramp loading sequence: applied stresses and loading rates for each ramp. 85
Table 5.11. Depth of installation of the monitoring piezometers. 91
Table 6.1. Estimation of the average degree of consolidation at piezometer P4. 104
Table 6.2. Actual multi-ramp loading sequence: time schedule. 105
Table 6.3. Actual multi-ramp loading sequence: applied stresses and loading rates for each ramp. . 106
Table 6.4. Assessment of the unit volume weight of the sediments after consolidation. 109
Table 6.5. Results of pocket penetrometer tests on the drilling cores. 121
Table 6.6. Synopsis of laboratory tests performed on undisturbed and representative samples during the post-operam characterisation phase. 123
Table 6.7. Results of particle size analyses and Atterberg limits performed on the samples taken in borehole S1. 125
Table 6.8. Results of particle size analyses and Atterberg limits performed on the samples taken in borehole S2. 127
Table 6.9. Compressibility parameters from sample S1-C2 (loading stage only). 131
Table 6.10. Compressibility parameters from sample S2-C1 (loading stage only). 131

Table 6.11. Results of triaxial CIUC test on reconstituted clay of sample S1-C2. 134
Table 6.12. Results of triaxial CIUC test on undisturbed clay of sample S1-C2. 135
Table 6.13. Results of triaxial CIUC test on sample S1-C3 (undisturbed clay). 137
Table 6.14. Results of triaxial CIUC test on sample S2-C1 (undisturbed clay). 139
Table 6.15. Results of CIUC tests. 146
Table 6.16. Determination of the S parameter. 147
Table 6.17. Determination of exponent m. 147

1 INTRODUCTION

Confined disposal facilities (CDFs) are engineered diked structures designed to provide a secure permanent storage for contaminated sediments resulting from dredging activities in seabeds, riverbeds, or harbours. Typically, they are in-water structures, built near shore or within ports, bordered by impervious walls and then filled with dredged muds. As documented by Bailey et al. (2010), often CDFs represent the only alternative to disposal in waste landfills, as an environmentally and economically acceptable solution, especially if CDFs are integrated in port infrastructures as land reclamations. This is the case of the CDF in the Ancona Harbour, in Italy, which was built with the aims to collect contaminated sediments from several ports of the central Adriatic Sea and to reclaim a new area for the port commercial activities. This infrastructure is at the core of the present dissertation.

The main challenge from the geotechnical point of view of dredged sediments in CDFs relates to their slurry consistency after disposal and sedimentation. Their high compressibility would lead to large settlements after loading due to reusing of the area, as well as very long consolidation times if the fine fraction is predominant. Moreover, their poor shear strength would limit or inhibit the reuse of the area. Such initial conditions require the consolidation of sediments in CDFs, with the dual aim of anticipating post-construction settlements prior to service life and ensuring proper mechanical characteristics. If coarse material is available at the site, consolidation can be conveniently performed by a preloading embankment, coupled with prefabricated vertical drains (PVDs) to speed up the process (Shen et al., 2005).

Another issue concerning the sediments management is that, typically, sediment disposal occurs according to different time schedules and volumes, therefore the site usability is never provided until filling of the whole facility is over. Such an approach actually delays the overall time required for land reclamation. Hence, optimising filling-and-consolidation procedures is needed to make a CDF available in a short time.

The present research focused on the development of a design strategy for CDFs, which would respond to the twofold need for consolidation treatment and management optimisation. The proposed solution involves the subdivision of a CDF capacity into sectors to be separately filled and consolidated by a preloading moving embankment (i.e., using the same material in all the sectors), while simultaneously filling the adjacent sector, thus leading to the anticipated provision of the facility (whole or single areas, depending on the customer needs). The moving

embankment requires much less material than the traditional overall preloading. Sustainability of the treatment is improved if recycled material is used for the moving embankment.

The first aim of this research was to verify the feasibility of the proposed strategy, with special focus on the possible construction technologies to delimit the sectors, taking into account the requirements of an easy installation, effectiveness of containment during disposal and filling operations, and minimisation of volume consume into the CDF. The innovative use of special geotextile tubes filled with the sediments themselves has been tested.

A full-scale test field has been performed on the first filled sector of the Ancona CDF, with the following purposes:

- implement and validate the proposed solution to provide the sectorisation;
- set up the operational sequences for PVDs installation and safely building the moving embankment on soft sediments;
- get the main parameters for design of the PVD-assisted consolidation treatment;
- verify and quantify the mechanical improvement (reduced compressibility and increased undrained shear strength) gained with the consolidation treatment.

Over the three-year period, an extensive experimental program has been carried out, including both laboratory and in-situ tests, as well as geotechnical monitoring. Specifically, test field activities have been developed in three stages:

- *ante operam* geotechnical characterisation, performed prior to the PVDs installation and embankment construction, to determine the parameters required for design of the test field and modelling of consolidation, as well as the stratigraphic profiling;
- monitoring, during construction and dwell time of the embankment, to monitor the consolidation process in terms of applied stresses, excess pore pressures and settlements, to verify design assumptions;
- *post operam* geotechnical characterisation, performed soon after the embankment removal, to characterise the post-consolidation sediment.

A further goal of the research concerned the evaluation of existing theories in the literature enabling a reliable modelling of PVD-assisted consolidation for sediments in CDFs. The proper theory should allow for addressing design choices (e.g. drains spacing and preloading stress) as a function of the time required for consolidation, without foregoing a simple mathematical management.

The final part of the research has been devoted to the assessment of the undrained shear strength of the consolidated sediments from the results of cone penetration tests. A correlation linking the undrained shear strength of overconsolidated fine grained sediments and the cone penetration resistance is proposed, that can be useful for the geotechnical design of structures comprising the Ancona CDF and other CDFs in the case of sediments having a clayey-like behaviour.

2 LITERATURE REVIEW

In this chapter, the state-of-the art about the two main lines of research of this dissertation are reviewed. Large strains consolidation theories are introduced to develop consolidation constitutive laws for dredged sediments. Classical theories for drains-assisted consolidation are described, together with a more sophisticated one. Finally, theoretical and empirical solutions to interpret undrained shear strength from cone penetration test results are presented.

2.1 Introduction

Since dredged sediments typically have very high void ratios when disposed in a confined facility, their consolidation is essential to achieve suitable mechanical characteristics to reuse the area. At the same time, it is crucial to properly describe the consolidation process for design purposes. As large strains are expected, the Terzaghi's theory of one-dimensional consolidation is not suitable to study the consolidation process of dredged sediments in confined disposal facilities. Indeed, it is necessary to consider the variation of the material properties and geometry during the processes. Models that take into account constitutive relations for compressibility and hydraulic conductivity are required. Many general mathematical relations as consolidation constitutive laws for soft soils can be found in the literature; their reliable determination needs for a laboratory characterization which is particularly challenging because of the associated low effective-stress range, large strains and typically lengthy consolidation process.

The consolidation of dredged sediments in CDFs should result in proper final mechanical characteristics (e.g., low compressibility, sufficient shear resistance in drained and undrained conditions) depending on the intended reuse of the area. In particular, the assessment of the final undrained shear resistance is crucial for fine-grained sediments.

Considering the aims of this thesis, in the following the theories at the base of the present research are illustrated and discussed with reference to the consolidation of fine-grained soils, as well as to the assessment of the undrained shear strength of clayey soils from cone penetration tests.

2.2 Consolidation theories

When a saturated low permeable fine-grained soil is subjected to a surface load, its response translates to an immediate increase of total stresses and a simultaneous increase of pore water pressures throughout the soil stratum. This happens because the water phase initially holds all the pressure increase without volume variations (due to its higher volumetric stiffness compared to that of the soil skeleton), thus generating excess porewater pressures. The water is slowly expelled out over time towards draining boundaries, and excess pore pressures dissipate, while the soil skeleton compresses, since the part no longer supported by the water is gradually transferred to the effective stresses in the soil.

The transient coupled hydrodynamic phenomenon of the evolution with time of water flow and delayed deformations of the soil skeleton is called consolidation and its mathematical formulation is known, in soil mechanics, as consolidation theory.

2.2.1 One-dimensional consolidation theory

Early works on consolidation are owed to Terzaghi (1925), whose theory of one-dimensional consolidation is widely recognized, together with the principle of effective stresses, as the inception of modern soil mechanics. The Terzaghi's one-dimensional theory was originally developed under the following assumptions:

(i). the soil is homogeneous, isotropic, and water-saturated ($S_r = 1$);

(ii). both the water and the solid constituents of the soil are perfectly incompressible (ρ_w = constant, ρ_s = constant);

(iii). the water flow (drainage) and the soil displacement (compression) occur in the vertical direction only;

(iv). strains are infinitesimal (i.e., the applied load increment produces only small strains in the soil);

(v). the coefficient of compressibility, m_v, and the hydraulic conductivity, k, of the porous medium remain constant within the considered stress range;

(vi). the behaviour of the soil skeleton is expressed through a linear elastic constitutive relation of the type $\Delta\varepsilon_z = m_v \times \Delta\sigma'_z$, where ε_z are the vertical strains, σ'_z are the vertical effective stresses, and the compressibility, m_v, is the stress-strain modulus of the soil. In other terms, there is a unique relationship between the change in void ratio and the change in effective stress;

(vii). the time lag of consolidation is due entirely to the low permeability of the soil (hydrodynamic lag), no secondary compression occurs;

(viii). the Darcy's law ($v = k \times i$) governs the egress of water from the soil pores;

(ix). the principle of effective stresses applies;

(x). the consolidation stress (i.e., the surcharge responsible for consolidation) is applied instantaneously and it is kept constant over time ($\partial\sigma_z/\partial t = 0$).

Based on these assumptions, the Terzaghi's theory was developed from the continuity of the pore water through an elemental prism of soil (the volume change in the element must be the difference in flow in and out of the element in a differential time); then, by relating the volume change (i.e., change of void ratio) in the soil skeleton to the change in effective stress by means of m_v, and neglecting the self-weight of the soil, Terzaghi attained the well-known governing equation for one-dimensional consolidation:

$$\frac{\partial u_e}{\partial t} = c_v \frac{\partial^2 u_e}{\partial z^2} \tag{2.1}$$

where t is the time, z is the vertical spatial coordinate, u_e is the excess porewater pressure induced by the surcharge application, and c_v is the coefficient of vertical consolidation:

$$c_v = \frac{k}{m_v \gamma_w} \tag{2.2}$$

which condenses the relevant soil and fluid parameter governing consolidation (k is the hydraulic conductivity of the soil; m_v is the coefficient of volume change; γ_w is the unit volume weight of water).

Equation (2.1) is a homogeneous parabolic partial differential equation (PDE) with constant coefficients and, by analogy with mathematical physics, it may be viewed as a diffusion equation modelling the evolution of a given phenomenon. The solution of Equation (2.1) can be obtained considering the initial-boundary value problem (Cauchy-Dirichlet problem):

$$\begin{aligned} \frac{\partial u_e}{\partial t} &= c_v \frac{\partial^2 u_e}{\partial z^2} && 0 < z < 2H,\ t > 0 \\ u_e(z,0) &= const = u_{e,0} = \Delta\sigma_z && 0 \le z \le 2H,\ t = 0 \\ u_e(0,t) &= u_e(2H,t) = 0 && t > 0 \end{aligned} \tag{2.3}$$

The boundary conditions above refers to Figure 2.1, where a clay layer, having thickness $2H$, lies between two free draining boundaries, so that the excess porewater pressure is null therein at any time $t > 0$.

As far as the initial condition, when the surcharge Δq is applied, undrained conditions exist, owing to the low hydraulic conductivity of the clay layer; moreover, since water compressibility is negligible compared to that of the soil skeleton, no volume variations occur at the time of loading and, consequently, the initial value of the excess porewater pressure, $u_{e,0}$, equals at any depth the applied total vertical stress, $\Delta\sigma_z$. If the surcharge impressed on the surface is of

infinite extent, the increment of vertical total stress has the same value at any depth, hence also the initial excess pore pressure is uniformly distributed along the depth (constant value).

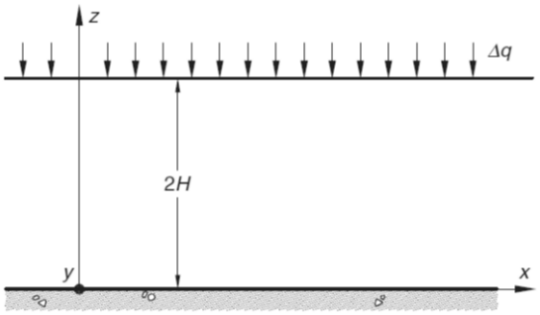

Figure 2.1. One dimensional consolidation problem (after Lancellotta, 2008).

The problem of Equation (2.3) is well posed, so a unique solution exists which depends continuously on the data. The Fourier method (i.e., separation of variables) is a good method to obtain the solution; for the sake of brevity, the mathematical derivation is omitted here[1], and the solution is directly provided:

$$u_e = \sum_{n=0}^{\infty} \frac{2u_{e,0}}{M} \sin\left(\frac{Mz}{H}\right) \exp(-M^2 T_v) \tag{2.4}$$

In the previous expression, M is a quantity depending on the summation index n through the relation:

$$M = \pi(2n + 1)/2 \tag{2.5}$$

and T_v is a dimensionless time factor for vertical consolidation, defined as:

$$T_v = \frac{c_v t}{H^2} \tag{2.6}$$

where the coefficient c_v has already been introduced (Eq. (2.2)), and the thickness H is the draining path. This latter is a characteristic length from which the excess pore pressure may dissipate by drainage towards one of the boundaries (i.e., the plane $z = H$ is a plane of symmetry). It follows that the solution of Equation (2.4) also applies to the case of a soil deposit of thickness H resting on an impervious base and with a single draining surface.

[1] The detailed development of the solution can be found in any geotechnical textbook, e.g. Lancellotta (2008).

Equation (2.4) allows to compute the value of $u_e(z,t)$ for any combination of time t and depth z, once the coefficient c_v is known. The solution is usually charted in terms of degree of pore pressure dissipation, U_z; for the analysed case of uniform initial excess pore pressure, the solution is given in Figure 2.2. By definition, U_z is the ratio, in a given point, between the excess pore pressure already dissipated and its initial value:

$$U_z = \frac{u_{e,0} - u_e}{u_{e,0}} = \frac{\Delta\sigma'_z}{\Delta\sigma_z} \tag{2.7}$$

or, in other terms, it is a local measure of how much of the imposed total stresses is transferred to the effective stresses in the soil (with 100% meaning full transfer). It is noteworthy that Figure 2.2 presents a powerful picture of how consolidation theoretically evolves in time and space, as the curves of constant T_v (the so-called "isochrones") represent U_z for subsequent instants of time throughout the compressible layer; the fastest consolidation clearly occurs at the drained faces and the slowest at the centre of the layer.

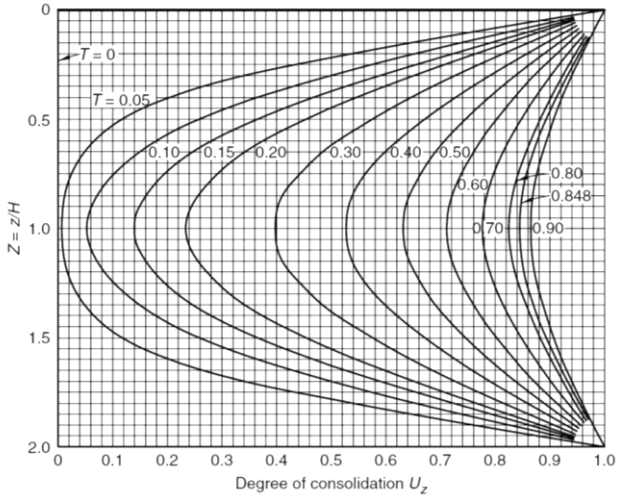

Figure 2.2. Solution of one-dimensional consolidation for the case of uniform initial excess porewater pressure and doubly drained layer (after Taylor, 1948). The x-axis indicates the degree of consolidation in terms of pore pressures, U_z (Eq. (2.7)), while on the y-axis the term Z is a dimensionless depth. The curves are pore pressure isochrones representing the spatial distribution of the excess pore pressure at a fixed instant of time.

The average degree of pore pressure dissipation for the whole layer, $\bar{U}_z$, can be computed by the following equation:

$$\overline{U}_z = \frac{\int_0^{2H} \left(u_{e,0} - u_e(t)\right) dz}{\int_0^{2H} u_{e,0} dz} \tag{2.8}$$

It can be proven that, for the one-dimensional consolidation theory, owing to the linearity of the stress-strain law, the average degree of pore pressure dissipation is equal to the average degree of consolidation in terms of settlements, $\bar{U}_s$:

$$\overline{U}_z = \overline{U}_s = \frac{\int_0^{2H} \varepsilon_z(t)dz}{\int_0^{2H} \varepsilon_\infty dz} = \frac{\delta(t)}{\delta(\infty)} \tag{2.9}$$

which is the consolidation settlement at generic time, $\delta(t)$, referred to the settlement attained at the end of consolidation, $\delta(\infty)$. The average degree of consolidation $\bar{U}_s$ reflects a global behaviour and, with a view to settlement prediction, it has major practical use in engineering applications.

The graphical representation of the average degree of consolidation versus the dimensionless time factor is depicted in Figure 2.3 for three different initial isochrones. For the case of uniform excess porewater pressure distribution at time $t = 0$ (i.e. rectangular isochrone), the theoretical consolidation curve is described by:

$$\overline{U}_s = 1 - \sum_{n=0}^{\infty} \frac{2}{M^2} \exp(-M^2 T_v) \tag{2.10}$$

Analytical solutions providing an approximated estimation of it can be found in the literature (e.g. Sivaram & Swamee, 1977; Taylor, 1948).

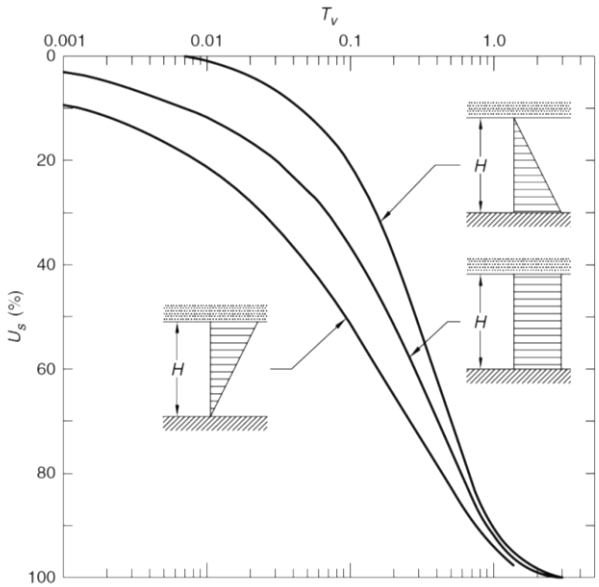

Figure 2.3. Average degree of consolidation for different initial isochrones (Janbu et al., 1956).

By observing Figure 2.3, it is apparent that the consolidation process may be deemed to be practically ended when $T_v \approx 2$, although theoretically it runs out when $t \to \infty$. This result also highlights the relative significance of the various parameters involved; in particular, when the goal is to speed up consolidation, it is much more profitable to reduce the drainage path, H (which is squared in the definition of T_v, see Equation (2.6)) rather than acting on the other variables. This concept underlies soil improvement by vertical drains, as it will be further addressed in § 2.2.3.

As a final remark, the effectiveness of the Terzaghi's theory to properly describe the consolidation of very soft soils – such as dredged sediments – should be discussed.

It is well known that the soil behaviour during consolidation is markedly non-linear, therefore a linear stress-strain law is not valid; also, the hydraulic conductivity tends to decrease during consolidation. Assuming that both compressibility m_v and permeability k remain constant during consolidation under a certain load increment – as Terzaghi does – leads to errors in the predictions which can in turn lead to systematically overestimate settlements and underestimate consolidation times. The extent of such errors is the more important, the greater is the magnitude of the load increment and of the resulting void ratio (Gibson et al., 1967).

The error on settlements would seem to be acceptable, as it is on the safe side, even though it could entail the overestimation of the disposal capacity, with undesirable problems during construction. On the other hand, it is certainly against safety to undervalue the time needed to complete the consolidation, for at least two reasons: first because this would result in an overestimation of the effective stresses developed at a certain time, with a consequent overestimation of the resistance of the soil (Gibson et al., 1981); secondly, because this may lead to unwelcome delays during construction.

A further consideration deserves the viscous component of settlement, completely neglected in the consolidation process. Indeed, it is assumed that secondary compression due to viscous phenomena occurs only once the settlements due to primary consolidation have ended. The factuality of this hypothesis is to be evaluated case by case, on the basis of the relative weight held by secondary compression on the total settlement.

2.2.2 Large strain consolidation theory

It is widely accepted that the simplifying assumptions underlying the Terzaghi's one-dimensional consolidation theory actually limit its applicability. To better simulate the actual behaviour of soils, several alternatives to Equation (2.1) were proposed in the literature since the early 1960s (e.g. Davis & Raymond, 1965; McNabb, 1960; Mikasa, 1965; Shiffman & Gibson, 1964), but none of these is suited for application to large deposits of soft dredged fills, due to their own intrinsic limitations (Cargill, 1982). For instance, some researchers sought to extend the classical theory to account for the variation of permeability and compressibility during

consolidation (Richart, 1957; Lo, 1960; Barden & Berry, 1965; Davis & Raymond, 1965; Janbu, 1965). Although this is a valuable guess, such factors have real importance only if void ratio variations and strains are appreciable, while the quoted studies were all based on the small strain hypothesis.

The first completely general theory of one-dimensional consolidation theory in soils is owed to Gibson et al. (1967), who accounted for the effect of self-weight, for the non-linear variation of k and m_v, while removing the strong restriction of small strains. The last point is the key reason why this theory is often referred to as "large strain theory" or "finite strain theory". Compared to the classical theory, the finite strain theory by Gibson et al. (1967) still assumed that the Darcy's law is obeyed, but it is written in another form relating the relative velocity of the soil skeleton and the pore fluid to the excess pore pressure gradient. Other assumptions such as non-homogeneity, time-effects intrinsic to the soil skeleton, and compressibility of the pore fluid and solids, which ensure as much generality as is likely to be required, are allowed for in this theory.

A distinction between consolidation of thick layers and thin layers is made, depending on whether the influence of self-weight of solids and pore fluid on the consolidation process are not negligible compared with those applied, or actually unimportant, respectively. In the paper by Gibson et al. (1967), the approximation of thin layers is made and the following simplifying assumptions are introduced: (i) the soil skeleton is homogeneous and free from time-dependent effects; (ii) both the pore fluid and the solids are incompressible; (iii) consolidation is monotonic (no swelling).

Under these assumptions, the soil permeability may be expected to depend only on the void ratio, so that $k = k(e)$, whereas the effective vertical stress controls the void ratio, so that $\sigma'_v = \sigma'_v(e)$. This means that the void ratio, e, is a privileged variable through which the equation governing the one-dimensional large strain consolidation process can be expressed. Indeed, the governing equation is:

$$\pm\left(\frac{\gamma_s}{\gamma_w}-1\right)\frac{d}{de}\left[\frac{k(e)}{1+e}\right]\frac{\partial e}{\partial z}+\frac{\partial}{\partial z}\left[\frac{k(e)}{\gamma_w(1+e)}\frac{d\sigma'_v}{de}\frac{\partial e}{\partial z}\right]+\frac{\partial e}{\partial t}=0 \qquad (2.11)$$

where the plus sign applies when the vertical material coordinate, z, is measured against gravity. This formulation is known to be the more general form of governing equation for one-dimensional consolidation, all of the other ones – including the conventional Terzaghi's theory – being special cases of it, as demonstrated by Shiffman (1980).

Equation (2.11) appears to be highly non-linear and its analytical solution is not possible. Nevertheless, it can be made linear, while retaining the nonlinearity of permeability and compressibility, by examining the relationship between soil properties. Indeed, once proper initial and boundary conditions are specified, it is possible to solve it numerically by continuously

updating its coefficients during the solution process, to simulate their non-linearity. The relationships $k(e)$ and $\sigma'(e)$ can be known or assumed. A number of mathematical relations can be found in the literature as consolidation constitutive laws for soft soils, as summarised in Table 2.1.

Table 2.1. Constitutive models for self-weight consolidation analysis (from Hawlader et al., 2008).

	Compressibility	Permeability	Constants	Sources and users
I	$g = -\frac{k}{\gamma_w(1+e)}\frac{d\sigma'}{de}$ = constant; $\lambda = -\frac{d}{de}\left(\frac{de}{d\sigma'}\right)$ = constant		g and λ	Gibson *et al.* (1981)
II	$g = -\frac{k}{\gamma_w(1+e)}\frac{d\sigma'}{de}$ = constant; $k = \gamma_w\bar{k}(1+e)$		g and $\bar{k}$	Been & Sills (1981)
III	$e = (e_0 - e_\infty)\exp(-\lambda\sigma') + e_\infty$	$k = k^* \exp(\kappa e)$	λ, κ and k^*	Govindaraju *et al.* (1999)
IV	$e = e^* - C_c \log\sigma'$	c_v = const.	e^*, C_c, C and D	Sills (see Bartholomeeusen *et al.* (2002))
V	$e = C_1\sigma'^{C_2} - 1$	$k = C_3(1+e)^{C_4}$	C_1–C_4 C_2 is negative	Yamaguchi *et al.* (1991)†
VI	$\sigma' = M\varepsilon^N$	$k = (1+e)(\alpha_2 + \beta_2 e)$	M, N, α_2 and β_2	Monte & Krizek (1976)
VII	$e = A\sigma'^B$	$k = Ce^D$	A, B, C & D B is negative	Somogyi (1979); McVay *et al.* (1986)
VIII	$e = A\sigma'^B$	$k = \frac{Ee^F}{1+e}$	A, B, E and F	Carrier *et al.* (1983)
IX	$e = c_1\sigma'^{c_2} + c_3$	$k = c_4(1+e)\sigma'^{c_5}$	c_1–c_5 c_2 is negative	Koppula & Morgenstern (1982)†
X	$e = A_1(\sigma' + A_2)^{A_3}$	$k = Ce^D$	A_1–A_3, C and D A_3 is negative	Liu & Znidarčić (1991)
XI	$\sigma' = K_\sigma\phi^{-n}$	$k = K_k\phi^{-n}$	K_σ, K_k and n	Winterwerp (1999); Merckelbach & Kranenburg (2004) proposed similar form using clay and sand fraction
XII	$\phi = \phi_0(1 + c_6\sigma')^{c_7}$	$k = k_0(1 + c_6\sigma')^{-c_8}$	ϕ_0, k_0, c_6–c_8	Diplas & Papanicolau (1997)†
XIII	$\sigma' = \exp(m_1 + m_2 e)$	$k = \exp(m_3 + m_4 e)$	m_1–m_4 m_2 and m_3 are negative	Van Kessel & Van Kesteren (2002)

Most empirical equations relating the vertical effective stress to the void ratio are based on power functions, as this form removes all major deficiencies of the conventional logarithmic models (i.e., the void ratio is well defined at zero effective stress and, irrespective of the stress magnitude, the void ratio never becomes negative). One of the most renowned $e(\sigma')$ relationship is owed to Liu & Znidarčić (1991):

$$e = A(\sigma' + Z)^B \tag{2.12}$$

in which A and B are constants, and Z is a soil parameter having a unit of stress.

With reference to the $k(e)$ law, the one proposed by Krizec & Somogyi (1984) expresses the hydraulic conductivity as function of the void ratio by means of two empirical constants C and D, to be determined experimentally:

$$k(e) = Ce^D \tag{2.13}$$

Both the relationships (2.12) and (2.13) have proved to give results that are extremely close to the experimentally observed behaviour; it is the reason why they have been used by Felici (2017) to develop the consolidation constitutive laws for the sediments disposed in the Ancona CDF, and updated in this research.

2.2.3 Consolidation by vertical drains

In § 2.2.1 it has been shown that the time required for consolidation is proportional to the square of the maximum drainage path, H, and inversely proportional to soil permeability, k (Eq. (2.6) and (2.2)). In fine grained soils, characterised by very low permeability values, vertical drains are used in conjunction with any preloading technique to accelerate consolidation times. Vertical drains are installed at the vertices of a regularly arranged mesh having a side lower than the maximum vertical drainage path, so that porewater is allowed to seep also in the horizontal direction towards the nearest drain. In this way, drainage paths are actually converted from upright to mainly horizontal and, taking advantage of the greater permeability of soils in the horizontal direction, a far more rapid dissipation of excess porewater pressures is achieved.

The theoretical aspects of soil improvement by vertical drains have been extensively dealt with in the literature and several analytical and numerical solutions have been proposed, with different levels of mathematical complexity (Carrillo, 1942; Kjellman, 1948b; Barron, 1948; Yoshikuni & Nakanodo, 1974; Olson, 1977; Hansbo, 1981; Onoue, 1988; Tang & Onitsuka, 2000; Leo, 2004; Zhu & Yin, 2004; Bellezza & Fentini, 2008; among others). The classical theory by Hansbo (1981) is the most common design approach still used today, by virtue of its simplicity. For the purposes of this dissertation, also an advanced theory is examined.

2.2.3.1 Classical theories

The classical analysis of consolidation in the presence of vertical drains in low-permeable soils shares some hypotheses with the conventional Terzaghi's one-dimensional consolidation theory – namely: water-saturated soil, incompressibility both of water and soil particles, vertical strains, linear stress-strain behaviour, and validity of Darcy's law[2] – while introducing some peculiar assumptions:

(i). axisymmetric conditions;

(ii). pure radial flow, that is, vertical flow is completely neglected;

[2] Some researchers (e.g. Dubin & Moulin, 1986; Hansbo, 1960; Miller & Low, 1963; Zou, 1996) questioned the validity of Darcy's law, arguing that it is sometimes invalidated at the small hydraulic gradients prevailing in field drained areas. Based on some experimental evidence, Hansbo (1960) proposed a solution accounting for non-Darcian pore water flow in drains-assisted consolidation problems. However, differences between this solution and those based on Darcian flow proved to be unimportant in most practical cases (Hansbo, 1981).

(iii). equal strains consolidation: vertical strains are uniform, as horizontal sections remain so throughout the consolidation process.

Based on the above assumptions, the problem of consolidation of soils by vertical drains has been invariably addressed by referring to a unit cell (i.e., a cylinder of soil around a single drain) under simplified boundary conditions.

A typical schematic adopted for design purposes is depicted in Figure 2.4a. A round-section vertical drain, with radius r_w and negligible stiffness, is located at the centre of a cylinder of homogeneous soil, of radius R, bounded by impervious outer boundaries (except the ends of the drain). The outer cylinder is referred to as "influence zone" and within it only radial (horizontal) flow towards the inner drain occurs, as determined by the horizontal permeability of the soil, k_h. In the drain the water flow occurs vertically towards its outlets, and it is governed by the permeability of the drain in the longitudinal direction, k_w. The length L is established by the boundary conditions, and it is equal to the soil layer thickness $2H$, or its half, H, depending on if the bottom base is impervious or not, respectively. The extent of the influence zone (i.e., its radius R) depends on the spacing, S, and on the geometric installation layout of the drains (Figure 2.5). The unit cell is stressed – and consolidation is triggered – by a constant load instantaneously applied on top, and the downward displacement of the ground level is constrained to be uniform by the hypothesis of equal strains.

Given this arrangement, the equation governing consolidation by vertical drains is:

$$\frac{\partial u_e}{\partial t} = c_h \frac{1}{r}\frac{\partial}{\partial r}\left(r\frac{\partial u_e}{\partial r}\right) \tag{2.14}$$

where r is the radial coordinate measured from the centre of the drain, and c_h is the coefficient of horizontal consolidation.

The initial-boundary value problem can be written as follows:

$$\begin{aligned} &\frac{\partial u_e}{\partial t} = c_h \frac{1}{r}\frac{\partial}{\partial r}\left(r\frac{\partial u_e}{\partial r}\right) && r_w < r < R,\ t > 0 \\ &u_e(r,0) = u_{e,0} && t = t_0 \\ &u_e(r_w,t) = 0 && t \geq 0 \\ &\partial u_e(R,t)/\partial r = 0 && t \geq 0 \end{aligned} \tag{2.15}$$

Kjellman was perhaps the first to solve the problem (Kjellman, 1948a, 1948b), but the best-known contribution came from Barron (1944, 1948). The latter, in particular, besides equal strain analysis, even solved the more rigorous case of free strains (i.e. vertical strains can develop freely), showing that the difference in terms of average degree of consolidation between the two solutions is negligible. Hence, mathematical convenience makes the approximated equal strain solution to be usually preferred, so only this will be hereinafter examined.

Incidentally, the assumption of equal vertical strains has been supported by settlement observations in the field (Holtz & Holm, 1973).

The solution of Equation (2.15) for equal strain consolidation writes:

$$u_e = \frac{u_{e,0}}{R^2 F_{id}} \left[R^2 \ln\left(\frac{r}{r_w}\right) - \frac{r^2 - r_w^2}{2} \right] \exp\left(-\frac{8T_h}{F_{id}}\right) \tag{2.16}$$

in terms of excess pore pressure, and:

$$\bar{U}_h(t) = 1 - \exp\left(-\frac{2T_h}{F_{id}}\right) \tag{2.17}$$

in terms of average degree of consolidation for radial (horizontal) flow, $\bar{U}_h$, the second formulation being at times referred to as the Kjellman-Barron solution (Fellenius, 2014). In the exponential term of the two previous equations, it is possible to recognise the dimensionless time factor for radial (horizontal) consolidation, T_h:

$$T_h = \frac{c_h t}{R^2} \tag{2.18}$$

having a formulation very similar to Equation (2.6), with the coefficient of horizontal consolidation, c_h, in lieu of the vertical one, and the radius of the influence zone, R, as the drainage length. The constant F_{id}, instead, is a factor accounting for the effect of spacing:

$$F_{id} = \frac{N^2}{N^2 - 1} \ln(N) - \frac{3N^2 - 1}{4N^2} \tag{2.19}$$

where N is the drain spacing ratio, defined as the ratio of the radius of influence to the radius of the drain:

$$N = R/r_w \tag{2.20}$$

The subscript “id” stands for ideal drain, meaning that the drain is assumed to work as an idealized well (Figure 2.4a) having infinite discharge capacity q_w (i.e. a permeability k_w infinitely high compared to that of the soil), and whose installation does not modify the soil properties.

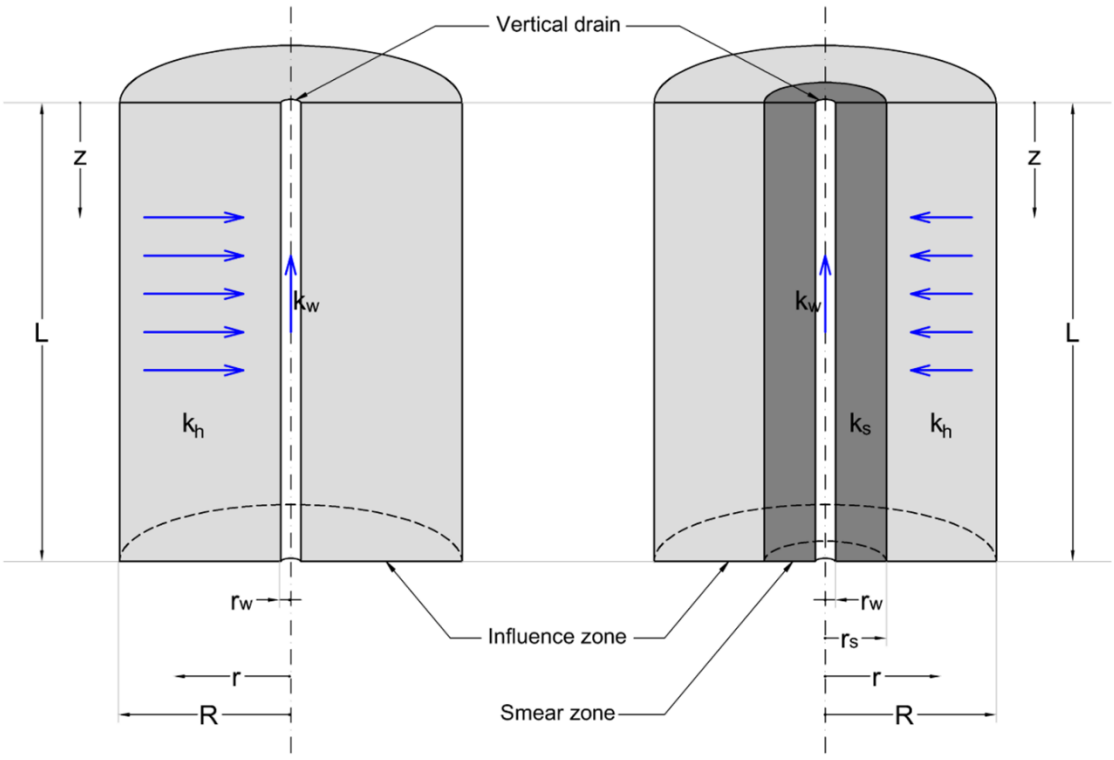

Figure 2.4. Schematic picture of a soil cylinder dewatered by a vertical drain: (a) idealized case; (b) real case including the effect of smear and well resistance.

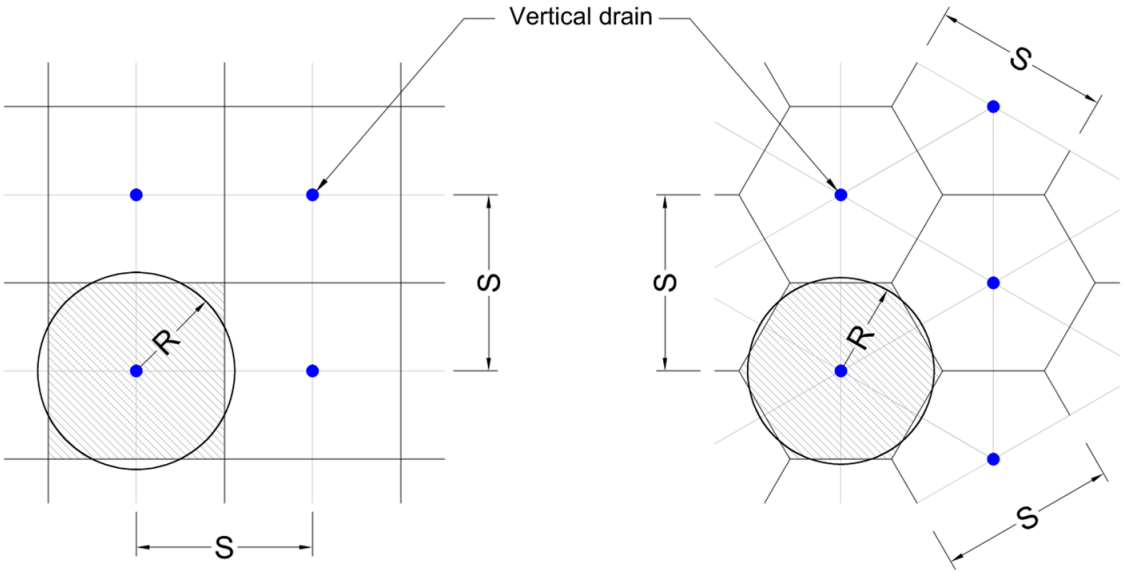

Figure 2.5. Radius of the influence zone, R, for square and equilateral triangular spacing of the vertical drains (plan view).

In reality, the discharge capacity of the drain is limited, especially in the case of long drains, which makes the well resistance to delay consolidation and the $\bar{U}_h$ computed with Equation (2.17) to be overestimated; furthermore, installation always causes remoulding of the soil close to the drain, resulting in a smear zone of radius $r_s < R$ and with a reduced permeability $k_s < k_h$ and increased compressibility (Figure 2.4b).

In the early 1980s, rigorous solutions incorporating one or both such effects had existed for some time (Barron, 1948; Yoshikuni & Nakanodo, 1974) but, albeit based on the simplifying assumption of equal strains, they were rather unwieldy and time-consuming to use in practice. Hansbo (1979, 1981) extended the classical Kjellman-Barron approach to the more general case by introducing some approximations, providing a simple closed-form solution for the analysis of consolidation by PVDs in fine-grained soils, which included both well resistance and soil disturbance. His simplifying assumptions were basically related to the size and characteristics of PVDs, as outlined below.

The first item dealt with the proper drain radius to consider in the calculations. Since band-shaped PVDs have a rectangular cross-section, an equivalent radius producing the same effect on the consolidation process should be introduced. As already suggested by Kjellman (1948b), Hansbo (1979) expressed this equivalence by matching the perimeter of the PVD with the circumference of the equivalent cylindrical drain[3]:

$$r_w = (a + b)/\pi \tag{2.21}$$

where a and b are the width and the thickness of the actual PVD, respectively. Equation (2.21) is considered appropriate when $a/b \leq 50$, otherwise a reduced radius ought to be assumed (Rixner et al., 1986).

The second approximation introduced concerned the effect of drain spacing. Since for PVDs typically $N > 12$, the following simplification of Equation (2.19) seemed justified:

$$F_{id} \approx \ln(N) - 0.75 \tag{2.22}$$

Based on these approximations, Hansbo (1979) amended Equation (2.17) as follows:

$$\bar{U}_h(t) = 1 - \exp\left(-\frac{2T_h}{F}\right) \tag{2.23}$$

[3] Kjellman (1948b) stated that «the draining effect of a drain depends to a great extent upon the circumference of its cross-section, but very little upon its cross-sectional area», and this assumption has been verified by finite element analyses (Runesson et al., 1977). However, there is no complete consensus about this, and different formulations for the equivalent radius of the drain can be found in the literature (Atkinson & Eldred, 1981; Fellenius & Castonguay, 1985; Long & Covo, 1994; Rixner et al., 1986).

$$F = F_{id} + F_r + F_s \tag{2.24}$$

where F is now a lumped parameter accounting for the effect of spacing (F_{id}), finite discharge capacity of the drain (F_r), and smear induced during installation (F_s). Although formally identical to the ideal drain solution (Eq. (2.17)), Equation (2.23) describes a consolidation delayed by the increase in the F factor due to well resistance and smear.

The well resistance factor, F_r, is determined by considering that Darcy's law applies to flow along the vertical axis of the drain. Let q_w indicate the specific discharge capacity of the drain at a unit hydraulic gradient in the vertical direction, which is given by the drain permeability multiplied per the equivalent cross-sectional area of the drain:

$$q_w = \pi r_w^2 k_w \tag{2.25}$$

hence, the well resistance factor is defined as:

$$F_r = \pi z(L - z)(k_h/q_w) \tag{2.26}$$

where z is the distance from the drainage end of the drain, L is the characteristic length. Noticed that F_r is a function of the depth z, and therefore $\bar{U}_h$ is not constant with depth. If an average value of the well resistance factor is entered in Equation (2.24), $\bar{U}_h$ can be considered the average degree of consolidation for the whole layer.

The average well resistance factor, $F_{r,m}$, can be expressed as:

$$F_{r,m} = (2\pi/3)(L^2)(k_h/q_w) \tag{2.27}$$

and typically its values are less than 5%F_{id}.

The disturbance factor, F_s, is:

$$F_s = [(k_h/k_s) - 1]\ln(r_s/r_w) \tag{2.28}$$

where k_h and k_s are the permeability of the undisturbed soil and of the zone of smear, respectively, while s is the smear ratio, defined as the ratio between the radius of the smear zone, r_s, and the equivalent radius of the drain, r_w:

$$s = r_s/r_w \tag{2.29}$$

From the definition (2.29), it is clear that two issues arise: one is to find the correct value of r_s (or, equivalently, of s); the other one is to evaluate the effect of remoulding on the smear

zone permeability, k_s. Both these unknown parameters are difficult to be determined, because of their dependency on factors such as soil structure, size and shape of the installation mandrel. The range of the smear ratio that can be found in the literature is quite wide: Hansbo (1981, 1997) estimated $s = 1.5 \div 3$; Bergado et al. (1991) proposed that the radius of the smear zone is twice the equivalent radius of the drain; Indraratna & Redana (1998) based on some investigations on a laboratory scale, indicated that s can be set equal to $4 \div 5$; Bo et al. (2000) and Xiao (2001) proposed $s = 5 \div 8$. With reference to the permeability in the smear zone, different approaches have been proposed: in the classical approach, k_s is assumed to be a constant (Barron, 1948; Hansbo, 1981; Leo, 2004); Chai et al. (1997) considered the permeability in the smear zone linearly and bi-linearly varied with radial distance and concluded that the assumption of one single average value of k_s lead to underestimation of the effect of smear; Walker & Indraratna (2006) assumed a parabolic variation. In light of the above, it is advisable to perform trials on site whenever feasible, to satisfactorily quantify these design parameters.

In spite of the approximations introduced, the analytical solution derived by Hansbo (Eq. (2.23)) gives results not so far from the aforementioned more complex solutions, while considerably simplifying the mathematical treatment. For these reasons, the Hansbo's theory has been adopted in the present study to develop a design equation, as explained in later section § 5.6.

Alongside the classical theories, more sophisticated solutions have been proposed over the years. However, the classical analytical solutions presented in this section are still very popular in practice, by virtue of their simplicity and ease of use, especially where incomplete knowledge of the soil does not justify resorting the more sophisticated methods.

As a final point, it should be emphasised that in real cases of soil improvement in presence of vertical drains, consolidation is more likely to occur by concurrent radial and vertical drainage. The relative contribution of each to the global consolidation process depends on the boundary conditions, with the radial consolidation being predominant over the vertical one the greater is the distance from the horizontal draining boundaries.

The overall average degree of consolidation due to radial and vertical flow, $\bar{U}_{hv}$, may be computed by combining the average degrees of consolidation for radial consolidation, $\bar{U}_h$, and vertical consolidation, $\bar{U}_v$, separately determined, according to well-known formula:

$$\bar{U}_{hv} = 1 - (1 - \bar{U}_h)(1 - \bar{U}_v) \tag{2.30}$$

derived by Carrillo (1942) for ideal drains in fully saturated soils and instantaneous loading. Equation (2.30) applies for a given time t, to which correspond two different values of the time factors T_h and T_v, hence two different degrees of consolidation $\bar{U}_h$ and $\bar{U}_v$.

2.2.3.2 Advanced theories including time-dependency

The aforesaid theories supposed that the surcharge load is applied instantaneously and then maintained constant throughout consolidation. Since in real cases the surcharge loading process always takes time, i.e., loading is time-dependent, this fact has theoretical and practical significance as pore pressure dissipation and settlement rate may be considerably affected by load variations over time, especially at the early stage. Hence, consolidation under time-dependent loading should be contemplated in realistic analyses.

Examples of time-dependent loading include linear loading, ramp-loading, cyclic loading. The case of ramp-loading was treated by Olson (1977) for ideal drains, and by Tang & Onitsuka (2000) and Leo (2004) for drains with smear and well resistance, under the assumption of equal strain condition. Olson (1977) directly applied Carrillo's formula to combine the effect of radial and vertical flow under time-dependent loading, without placing any evidence about the feasibility of this approach. Leo (2004) presented the development of a series of closed-form solutions which may be implemented on a spreadsheet, albeit it is not immediate. Tang & Onitsuka (2000) also presented an analytical solution for one-dimensional consolidation by vertical drains with smear and well resistance under time-dependent loading. This theory has been chosen to design the test field object of this dissertation, as described in later section § 5.3.5, and therefore its fundamental aspects are here presented.

Tang & Onitsuka (2000) noticed that, if the hypothesis of instantaneous loading fails, the basic partial differential equations (PDEs) governing consolidation by vertical drains become inhomogeneous; in this event, the impulse function method can be successfully adopted to solve such kind of PDEs, provided that initial and boundary conditions are homogenous. However, when the well resistance is taken into account, the boundary condition between the soil and vertical drain is not homogeneous, denying the direct use of the impulse function method.

Considering the scheme of Figure 2.6, with all the symbols already known, and based on the following assumptions:

(i). validity of the Barron's equation strain hypothesis. The analysis for the vertical consolidation uses the average value of the excess porewater pressure at the same depth instead of at point;

(ii). validity of Darcy's law;

(iii). the total porewater inflow through the boundary of the vertical drain equals the vertical flow within the vertical drain;

(iv). radial flow of water within the vertical drain is neglected;

(v). the horizontal coefficient of permeability of the smear zone is smaller than that of the natural soil ($k_s < k_h$), while the coefficient of volume compressibility of the smear zone and the vertical coefficient of permeability of the smear zone coincides with those of the natural soil;

the authors wrote the simultaneous basic partial differential equations for arbitrary loading for the time evolution of vertical strains in the smear zone and in the natural soil, imposed the continuity at the cylindrical surface of the vertical drain, and formulated the average excess porewater pressure at the same depth.

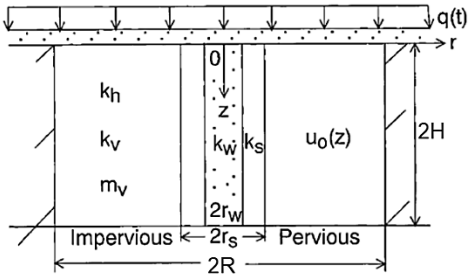

Figure 2.6. Analysis scheme of soil cylinder with vertical drain (adapted from Tang & Onitsuka, 2000).

By imposing the condition of initially zero excess porewater pressure and different boundary conditions (impermeability at $r = R$; continuity of porewater pressure at $r = r_w$ and $r = r_s$; continuity of the porewater pressure gradient at $r = r_s$; clay layer with pervious top surface and, alternatively, pervious or impervious bottom), and after some mathematical processing, the authors obtained the solution for the average excess porewater pressure at a given depth z:

$$\bar{u}_e(z,t) = \int_0^t \frac{dq}{d\tau} \sum_{m=0}^{\infty} \frac{2}{M} \sin\frac{Mz}{H} \exp[-\beta_m(t-\tau)]\, d\tau \tag{2.31}$$

and the overall average degree of consolidation for the whole layer:

$$\bar{U}(z) = 1 - \frac{1}{q_u H}\int_0^H \bar{u}_e\, dz - \int_0^t \frac{dq}{dt} \sum_{m=0}^{\infty} \frac{2}{M^2} \exp[-\beta_m(t-\tau)]\, d\tau \tag{2.32}$$

where q is the time dependent loading, q_u is the final loading (= q_R), H is half of the thickness of the compressible layer, τ is the time of application of any load. Moreover:

$$\beta_m = \beta_{zm} + \beta_{rm} \tag{2.33}$$

$$\beta_{zm} = c_v M^2 / H^2 \tag{2.34}$$

$$\beta_{rm} = 2\, c_h / [R^2 (F + D_m)] \tag{2.35}$$

$$D_m = \frac{8}{M^2}\frac{(N^2-1)}{N^2}G \tag{2.36}$$

$$G = \frac{k_h}{k_w}\left(\frac{H}{2r_w}\right)^2 \tag{2.37}$$

$$\begin{aligned} F = {} & \left(\ln\frac{N}{s} + \frac{k_h}{k_s}\ln s - 0.75\right)\frac{N^2}{(N^2-1)} \\ & + \frac{s^2}{(N^2-1)}\left(1-\frac{k_h}{k_s}\right)\left(1-\frac{s^2}{4N^2}\right) \\ & + \frac{k_h}{k_s}\frac{1}{(N^2-1)}\left(1-\frac{1}{4N^2}\right) \end{aligned} \tag{2.38}$$

$$M = \pi(2m+1)/2 \tag{2.39}$$

where m = 0,1,2,…, and, as usual, r_w is the equivalent radius of the drain, r_s is the radius of the smear zone, R is the radius of the influence zone, s is the smear ratio, N is the drain spacing ratio, k_w is the hydraulic conductivity of the drain, k_s is the horizontal hydraulic conductivity in the smear zone, k_h is the horizontal hydraulic conductivity in the undisturbed soil. The mathematics above refers to the two-way drainage; if the solution for pervious top and impervious bottom is required, the thickness H should be replaced with the whole layer thickness $2H$ into Equations from (2.31) to (2.37).

The theory was then specialised to deal with ramp loading, which is the most common type of non-instantaneous loading encountered in geotechnical engineering. Specifically, they derived the solutions for single-ramp loading (Figure 2.7a) and for multi-ramp loading (Figure 2.7b). This latter occurs whenever the surcharge final value, q_u, is achieved in more than one step, alternating gradual loading application with time frames in which the applied load is kept constant, while consolidation simultaneously develops. This is the case of a preloading embankment built in multiple lifts, each of which is left in place for a certain time before applying the next upper lift, until reaching the desired height. Since this is of interest for the design of the test pad in the Ancona CDF (section), only the multi-ramp loading solution will be presented below.

From the foregoing, the multi-ramp solution consists of two parts: loading period and non-loading period. Naming q_i the ith ramp loading, and t_i the time taken to complete it, the rate of the ith ramp loading, $\mathcal{R}_i$, can be defined as:

$$\mathcal{R}_i = q_i/(t_i - t_{i-1}) \tag{2.40}$$

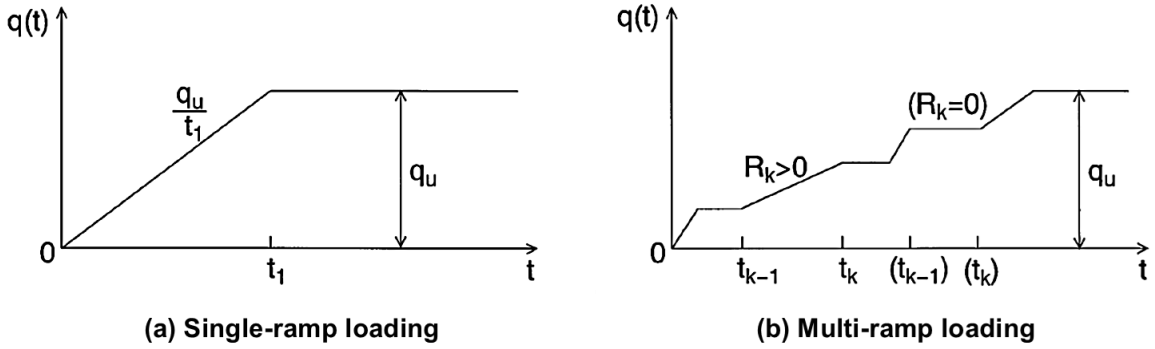

Figure 2.7. Types of time-dependent ramp loading: (a) single-ramp loading; (b) multi-ramp loading (after Tang & Onitsuka, 2000).

For loading periods (i.e. when $\mathcal{R}_k > 0$), the solutions for the average excess pore pressure at any depth, $\bar{u}(z,t)$, and the overall average degree of consolidation with time, $\bar{U}(t)$, write respectively:

$$\bar{u}(z,t) = \sum_{i=1}^{k-1} \mathcal{R}_i \sum_{m=0}^{\infty} \frac{2}{M\beta_m} \sin\frac{Mz}{H} \{\exp[\beta_m(t_i - t)] - \exp[\beta_m(t_{i-1} - t)]\} + \mathcal{R}_k \sum_{m=0}^{\infty} \frac{2}{M\beta_m} \sin\frac{Mz}{H} \{1 - \exp[\beta_m(t_{k-1} - t)]\} \tag{2.41}$$

$$\bar{U}(t) = \frac{1}{q_u} \left\{ \sum_{i=1}^{k-1} q_i + \mathcal{R}_k(t - t_{k-1}) - \sum_{i=1}^{k-1} \mathcal{R}_i \sum_{m=0}^{\infty} \frac{2}{M^2\beta_m} \{\exp[\beta_m(t_i - t)] - \exp[\beta_m(t_{i-1} - t)]\} - \mathcal{R}_k \sum_{m=0}^{\infty} \frac{2}{M^2\beta_m} \{1 - \exp[\beta_m(t_{k-1} - t)]\} \right\} \tag{2.42}$$

For non-loading period (i.e. when $\mathcal{R}_k = 0$), the following expressions apply:

$$\bar{u}(z,t) = \sum_{i=1}^{k} \mathcal{R}_i \sum_{m=0}^{\infty} \frac{2}{M\beta_m} \sin\frac{Mz}{H} \{\exp[\beta_m(t_i - t)] - \exp[\beta_m(t_{i-1} - t)]\} \tag{2.43}$$

$$\bar{U}(t) = \frac{1}{q_u}\left\{\sum_{i=1}^{k} q_i - \sum_{i=1}^{k} \mathcal{R}_i \sum_{m=0}^{\infty} \frac{2}{M^2 \beta_m}\{\exp[\beta_m(t_i - t)] - \exp[\beta_m(t_{i-1} - t)]\}\right\} \tag{2.44}$$

Again, in all the previous equations, *H* should be intended as half the thickness of the compressible layer, in order to consider double-drainage conditions (permeable top and permeable bottom).

The feasibility of Carrillo's method to consider combined vertical and radial flow under time-dependent loading was also discussed on the sidelines of their paper. They concluded that, although it was previously proved (Xie, 1987) that Equation (2.30) in such conditions is untenable for Barron's free strain condition, the influence of loading conditions gradually become smaller with time.

2.3 Interpretation of undrained shear strength of clays from CPTs

The undrained shear strength of soils is a key parameter for short-term stability analyses of engineering structures. Conceptually, according to the classical understanding on the stress-strain behaviour of soils, the undrained shear strength can be taken as the maximum shear stress for a stress path at constant volume.

As recommended by Wroth (1984), in this dissertation the symbol s_u is used for the undrained shear strength since it clearly recalls the concept of strength, instead of c_u which relates to cohesion.

The estimation of the undrained shear strength of clayey soils from cone penetration tests results is one of the main applications of CPTs and several correlations have been proposed and validated. The popularity exists despite so many tests are available to directly determine the undrained shear strength, be it in the laboratory (e.g., unconfined compression, triaxial compression, etc.) or *in situ* (e.g., field vane). However, such tests can be quite expensive and difficult to perform diffusely as part of a project. As cone penetration tests are routinely performed at early stages of a survey program, it may lead to considerable savings in time and money if a preliminary estimation of the main geotechnical properties can be made based on the CPT alone.

A large amount of work has been published on the interpretation of undrained shear strength of clays from cone penetration test results. Alongside solutions deriving from theoretical analyses, many empirical relationships based on local experiences have been proposed, the latter being usually preferred by virtue of their simplicity.

2.3.1 Theoretical solutions

Several authors attempted a theoretical approach to study the cone penetration problem and to derive the undrained shear strength of soils. The proposed solutions can be grouped in three main classes according to the theory considered: classical bearing capacity theory (Terzaghi, 1943; Meyerhof, 1951; Caquot & Kérisel, 1956; de Beer, 1977); cavity expansion theory (Meyerhof, 1951; Skempton, 1951; Gibson, 1950; Vesic, 1972), sometimes combined with conservation of energy (Baligh, 1975; Vesic, 1975); strain path theory (Baligh, 1975; Teh, 1987).

The bearing capacity theory was likely the first method employed to analyse static cone penetration. Originally developed for shallow foundations, this classical theory relied on a plasticity approach as formulated by Prandtl (1920) and Terzaghi (1943), under the hypotheses of continuity, homogeneity, isotropy, and rigid-plastic behaviour of the soil. It was later extended to deep foundations, and then to static penetration problems, assimilating the cone resistance, q_c, to the ultimate load capacity, q_{ult}, of a deep circular foundation, as expressed by the well-known bearing capacity equation for undrained analyses:

$$q_c = q_{ult} = N_c s_u + \sigma_{v0} \tag{2.45}$$

where N_c is a bearing factor and σ_{v0} the total overburden stress. To determine the collapse load, limit equilibrium or slip-line analyses can be carried out (Yu & Mitchell, 1998); in any case, a failure mechanism should be assumed. A few of the mechanisms proposed in the literature for plain strain analyses are shown in Figure 2.8, but also axisymmetric solutions should be mentioned (e.g. Koumoto & Kaku, 1982). Some of the N_c factors obtained by applying the bearing capacity theory to cone penetration are listed in Table 2.2, ranging between 7.0 and 9.9. Actually, solutions strongly depend on the shape assumed for the plastic zone (Konrad & Law, 1987). The major weaknesses of the bearing capacity theory applied to cone penetration lie in neglecting soil deformations and the influence of the penetration process on the initial stress regime around the cone shaft (Yu & Mitchell, 1998), as well as in the inconsistency of failure mechanisms with boundary conditions, which make this approach – and the resulting N_c factors – adequate only for analysing shallow penetration.

Some of the drawbacks above were overcome by the solutions based on the cavity expansion analogy, according to which the pressure required to produce a deep hole in an infinite elastic-plastic medium is proportional to that needed to expand a cavity of the same volume under the same conditions (Yu & Mitchell, 1998; Yu, 2000). Saying p_{ult} the ultimate internal pressure in the cavity, the general relationship between q_c and s_u is:

$$q_c = p_{ult} = N_c s_u + \sigma_i \tag{2.46}$$

which has actually the same form of Equation (2.45). Several authors worked on cavity expansion theory (Vesic, 1972; Carter et al., 1986) presenting as many expressions for the N_c factor, with different level of sophistication, as reported in Table 2.2. The term σ_i in Equation (2.46) denotes the initial *in situ* total stress, which can be vertical, σ_{v0}, horizontal, σ_{h0}, or mean stress, σ_m, depending on the stress-strain model adopted for the soil. As far as the cavity shape, the traditionally accepted suitability of spherical cavity to describe the soil behaviour around the cone tip was questioned by some experimental evidence (e.g. Tavenas et al., 1982), suggesting that cylindrical cavity should be preferred. However, cavity expansion theory does not properly model the actual shape of the penetrometer and the resulting N_c factors are generally underpredicted (Teh, 1987).

The third theoretical approach is represented by the strain path method, in which the penetration of a cone into an isotropic homogeneous soil is treated as a steady state problem. The basic concept is that, for an observer moving with the penetrometer, the deformation pattern in the soil remains unchanged over time; hence, by shifting the reference coordinate system, the penetration process can be viewed as a steady state flow of soil passing a stationary cone and a set of strain paths can be determined. The solution procedures based on this method can be found in Teh (1987); some examples for cohesive soils are given in Table 2.2. However, the application did not meet full success.

Table 2.2. Theoretical cone factors (modified from Konrad & Law, 1987).

Authors	**Solution group**	**Initial *in situ* total stress, σ_i**	**Theoretical cone factor, N_c**	**Notes**
Terzaghi (1943)	BC	σ_{v0}	7.41	-
Meyerhof (1951)	SCE	σ_{v0}	$^4/_3\left[1+\ln\left(E_{u,t}/3s_u\right)\right]+1$	-
Skempton (1951)	SCE	σ_{v0}	$^4/_3\left[1+\ln\left(E_{u,s}/s_u\right)\right]+1$	-
Caquot & Kérisel (1956)	BC	σ_{v0}	7.0	-
Meyerhof (1961)	BC	σ_{v0}	9.3	-
Begemann (1965)	BC	σ_{v0}	14.0	-
Vesic (1972)	SCE	σ_{v0}	$^4/_3[1+\ln(G/s_u)]$	-
Ladanyi & Johnston (1974)	SCE	σ_m	$3.16+1.33\ln(G/s_u)$	-
Vesic (1975)	SCE	σ_{v0}	$3.90+1.33\ln(G/s_u)$	-
Baligh (1975)	CCE	σ_{h0}	$12.0+1.33\ln(G/s_u)$	-
de Beer (1977)	BC	σ_{v0}	9.94	-
Koumoto & Kaku (1982)	BC		9.8	-
Teh (1987)	SP	σ_{v0}	$0.19+2.64\ln(G/s_u)-\sigma'_{v0}(1-K_0)/s_u+2\alpha$	-
Yu (1993)	CCE		$4.18+1.155\ln\left(\sqrt{3}G/2s_u\right)$	smooth cone
Yu (1993)	CCE		$9.4+1.155\ln\left(\sqrt{3}G/2s_u\right)$	rough cone

Note: BC = bearing capacity; SCE = spherical cavity expansion; CCE = cylindrical expansion; SP = strain path; $E_{u,t}$ = initial tangent modulus; $E_{u,s}$ = secant modulus at 50% failure; G = shear modulus; α = roughness coefficient.

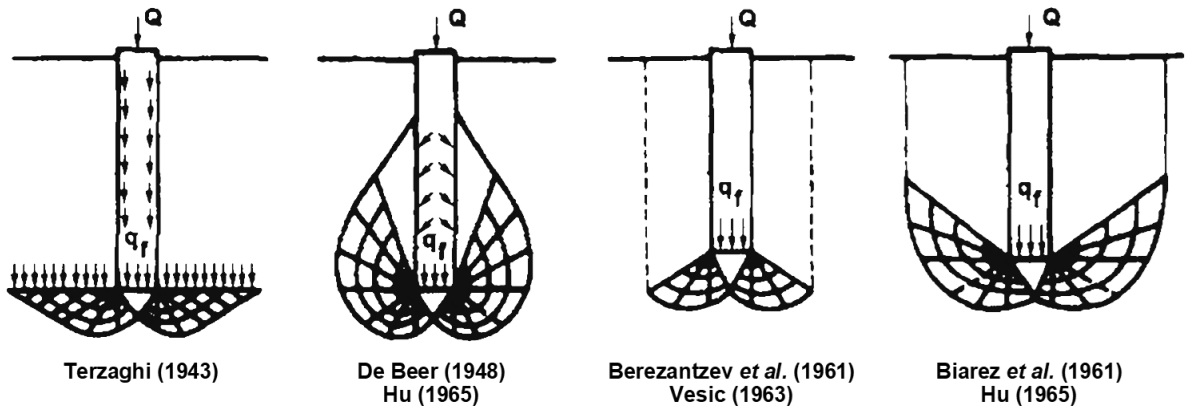

Figure 2.8. Assumed failure mechanisms for deep penetration (adapted from Durgunoglu & Mitchell, 1975).

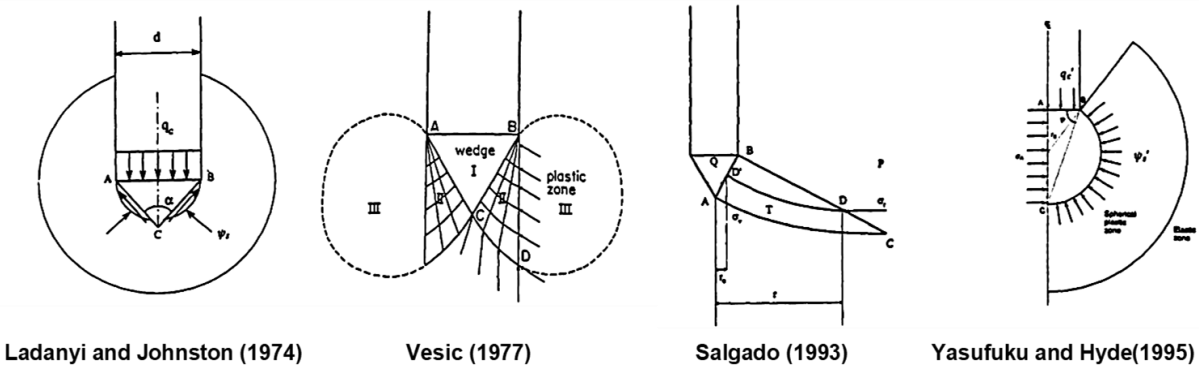

Figure 2.9. Assumed relationships between cone resistance and cavity limit pressures (adapted from Yu & Mitchell, 1998).

This brief review of theoretical proposals does not claim to be exhaustive; a detailed summary is documented in Konrad & Law (1987), Lunne et al. (1997), Yu & Mitchell (1998). However, it is worth noting that, regardless of the theory adopted, all the theoretical solutions so far quoted result in a relationship of the form:

$$s_u = \frac{q_c - \sigma_i}{N_c} \tag{2.47}$$

which is in essence the original Terzaghi's formula of ultimate resistance of footings under undrained conditions, rewritten to bring out the shear resistance.

The main credit for the theoretical solutions has been to demonstrate that a reliable relationship between undrained shear strength and cone tip resistance can be established (provided that the *in situ* stress state is accounted for), thus setting the theoretical basis for later empirical correlations. However, their application is based on some simplifying hypotheses concerning

soil behaviour, boundary conditions and failure mechanisms which limit modelling of the real soil response under conditions of varying stress history, anisotropy, sensitivity, ageing and microfabric. Theoretical solutions may also require inputting some parameters (like cone roughness, α, lateral stress state, K_0, rigidity index, $I_R = G/s_u$, etc.) to be assessed beforehand. Theoretical solutions need validation by actual field and/or laboratory tests, as well. Hence, the use of site-specific empirical correlations still seems to be the best procedure for the interpretation of s_u from CPTs.

2.3.2 Empirical solutions

Empirical correlations to predict the undrained shear strength from CPTs are commonly defined by the same equation form of Equation (2.47), that is:

$$s_u = \frac{q_c - \sigma_{v0}}{N_k} \tag{2.48}$$

where the empirical cone factor is now denoted by N_k to distinguish it from the theoretical cone factor, N_c. Experience and theorical studies suggested that the N_k factor is larger than N_c (Janbu & Senneset, 1974).

Because of the complex effects of stress history, mode of failure, strain rate, and soil anisotropy, no single undrained shear strength value exists. Hence, it is of paramount importance that any interpretation of CPT in terms of undrained shear strength should clearly state which undrained shear strength refers to.

Over the last five decades, several analyses were carried out to back calculate N_k factors by Equation (2.48) for different soil types and reference tests, as reported in Table 2.3.

Lunne et al. (1976) attempted to correlate cone resistance to field vane shear strength for Scandinavian soft to medium stiff marine clays. The values of s_u measured with vane tests were adjusted by applying the Bjerrum's correction factor, μ (Bjerrum, 1973) – which depends upon the plasticity index – in order to get the "true" undrained field strength. In this way, the authors obtained a cone factor varying between 15 and 19, with an average value of 17. Always considering the field vane as reference test, results from an extensive review by Lunne & Kleven (1981) indicated $N_k = 11 \div 19$, with an average value of 15, for normally consolidated marine clays.

Kjekstad et al. (1978) compared electric cone results and strength measurements by laboratory compression tests (CIU, UU, and UC tests) for stiff overconsolidated clays of glacial origin in the North Sea. They obtained $N_k = 15 \div 20$, with an average value of 17, and no correlation with neither the water content nor the liquid limit. They also ascribed the wide scatter in the N_k values mainly to the scatter in the laboratory strength determinations (because of non-

perfect sampling and testing of the clayey specimens) and to small variations in soil structure and composition.

Stark & Delashaw (1990) developed a correlation between q_c and s_u from UU triaxial tests on specimens of normally to lightly overconsolidated clays, obtaining N_k = 8.5÷16.5, with an average value of about 12. Terzaghi et al. (1996) indicated N_k = 11÷30 for s_u obtained from UU compression triaxial tests on specimens of stiff fissured clays, with values depending on the soil plasticity and on fissure spacing.

Eid & Stark (1998) proposed a cone factor relating the unconfined compression strength to q_c; for soft to stiff saturated clays with I_P = 15÷50%, they obtained N_k = 8÷25, with an average value of about 16.

Table 2.3. Literature review of the empirical total cone factor N_k.

Authors	**Reference test**	**Soil**	**Empirical cone factor, N_k**	**Remarks**
Lunne et al. (1976)	FV	Marine soft clays	13÷24 (15÷19)	$N_{k,corr}$ decreases with I_P
Kjekstad et al. (1978)	CIU, UU, UC	Preconsolidated low plasticity clays	15÷20 (17)	-
Lunne & Kleven (1981)	FV	NC marine clays	11÷19 (15)	-
Stark & Delashaw (1990)	UU	Soft to medium alluvial clay	8.5÷16.5 (12)	-
Terzaghi et al. (1996)	UU	Clays	11÷30	-
Eid & Stark (1998)	UC	Soft to stiff saturated clays	8÷25 (16)	I_P = 15÷50%
Chen (2001)	-	Malaysia clay	5÷12	-
Gebreselassie (2003)	-	Different soil types	7.6÷28.4	-
Anagnostopoulos et al. (2003)	UU	Different soil types in Greece	18.3	-
Rémai (2013)	CU, UC	Soft Holocene clays	10.5÷27.6 (18.6)	no correlation with B_q
Cheshomi (2018)	UC	Quaternary fine-grained alluvium soil	18÷29 (22)	no correlation with I_P

Note: FV = field vane; CIU = triaxial consolidated undrained; UU = triaxial unconsolidated-undrained; UC = unconfined compression; the value in parentheses is the mean value or the best value for the specific data set; $N_{k,corr} = N_k/\mu$, with μ the Bjerrum's (1973) correction factor.

As the piezocone became more popular worldwide, Equation (2.48) was rephrased using q_t, instead of q_c, to account for the pore pressure effects (§ 3.2.1.1.1):

$$s_u = \frac{q_t - \sigma_{v0}}{N_{kt}} \tag{2.49}$$

with the empirical cone factor, N_{kt}, including the subscript "t" to denote the expression using the corrected total cone resistance. The correction for pore pressure effects is particularly important for soft clays, where the magnitude of measured pore pressures can be comparable to that of the measured tip resistance. This approach was followed by many authors, yielding to a very wide set of cone factors, as reported in Table 2.4.

Table 2.4. Literature review of the empirical total cone factor N_{kt}.

Authors	**Reference test**	**Soil**	**Empirical cone factor, N_{kt}**	**Remarks**
Aas et al. (1986)	Tx compression, Tx extension, Direct shear	Clays	8÷16	for I_P = 3÷50%, N_{kt} increases with I_P
La Rochelle et al. (1988)	-	Clays	11÷18	no correlation with I_P
Rad & Lunne (1988)	Tx compression	Clays	8÷29	varies with *OCR*
Powell & Quarterman (1988)	Tx compression	Clays	10÷20	varies with I_P
Karlsrud et al. (1996)	Tx compression	Clays	6÷15	decreases with B_q, decreases if *OCR* increases
Karlsrud et al. (2005)	TxCK$_0$U	Clays	5.7÷15.3	increases with *OCR*
Hong et al. (2010)	Tx compression	Busan clay, Korea	7÷20	I_P = 25÷40%
Low et al. (2010)	Tx compression	Lightly OC clays	10÷14	-
de Almeida et al. (2010)	FV	High plasticity soft clays	4÷16	I_P = 42÷400%
Shin & Kim (2011)	CIU	Clayey soils in Indiana	8.0÷13.4	increases with I_P
Rémai (2013)	CU, UC	Soft Holocene clays	11.9÷32.1 (23.3)	no correlation N_{kt} - B_q
Cheshomi (2018)	UC	Quaternary fine-grained alluvium soil	18÷31 (23)	no correlation with I_P

Note: FV = field vane; CK$_0$U = triaxial anisotropically consolidated undrained; CIU = triaxial isotropically consolidated undrained; CU = triaxial consolidated undrained; UU = triaxial unconsolidated-undrained; UC = unconfined compression.

Aas et al. (1986) developed a correlation between the cone factor N_{kt} and the plasticity index, I_P, of the soil. As the reference undrained shear strength they used an average value from laboratory tests, $s_{u,lab}$ = ⅓ (s_{uc} + s_{ud} + s_{ue}), being s_{uc}, s_{ud}, s_{ue} the undrained shear strengths from triaxial compression, direct simple shear and triaxial extension tests, respectively. Their results showed that N_{kt} is a direct function of I_P and that N_{kt} varies between 8 and 16 when I_P = 3÷50%

and only triaxial compression tests are considered. Conversely, La Rochelle et al. (1988) did not confirm the correlation between N_{kt} and I_P; they found N_{kt} = 11÷18.

A broader range of N_{kt} values was presented by Rad & Lunne (1988), who used triaxial compression as reference test to determine s_u; namely, they found N_{kt} = 8÷29, with OCR being the main variable. Powell & Quarterman (1988) also working from triaxial compression tests, found that N_{kt} varied from 10 to 20 depending on plasticity index (similarly to Aas et al., 1986) and rate effects. They also showed that scale effects (significant in fissured clays) could raise the upper bound of N_{kt} range up to 30.

Two alternative methods to estimate s_u from piezocone data consisted in using the effective cone resistance, q_e, or the excess pore pressure, Δu, in the numerator, as expressed by the equations:

$$s_u = \frac{q_e}{N_{ke}} = \frac{q_t - u_2}{N_{ke}} \tag{2.50}$$

$$s_u = \frac{\Delta u}{N_{\Delta u}} = \frac{u_2 - u_0}{N_{\Delta u}} \tag{2.51}$$

where N_{ke} and $N_{\Delta u}$ are the empirical cone factors for the expressions using q_e or Δu, respectively.

The effective cone resistance is of interest in other fields of geotechnical engineering, such as soil classification and prediction of pile bearing capacity, so it seemed natural to find a correlation between this value and the undrained shear strength. However, in very soft clays it is generally not recommended to estimate s_u using an effective cone resistance, the latter being a small quantity, sensitive to small errors in the measurement of tip resistance and/or porewater pressure. In such cases, the use of Equation (2.51) is deemed to be a better approach to find a reliable correlation. Table 2.5 and Table 2.6 list some of the values of N_{ke} and $N_{\Delta u}$ proposed in the literature.

Several authors worked on all the cone factors N_k, N_{kt}, N_{ke}, $N_{\Delta u}$. Based on anisotropically consolidated undrained compression (CAUC) triaxial tests, Lunne et al. (1985) showed that the pore pressure parameter, B_q, correlates to some extent with the total cone factor N_{kt}, but a better correlation could be established if the effective cone factor, N_{ke}, or the excess pore pressure cone factor, $N_{\Delta u}$, are considered. However, as pointed out by Karlsrud et al. (2005), this manner of plotting can be misleading, since B_q is equal to the ratio $N_{\Delta u}/N_{kt}$, therefore the cone factors actually appear on both axes.

Karlsrud et al. (1996) assessed s_u of low-plasticity soft clays by CAUC tests on high-quality block samples and found a good correlation of the cone factors with B_q, with N_{ke} = 2÷10, N_{kt} = 6÷15, increasing with decreasing OCR. On the contrary, no clear dependency was found between $N_{\Delta u}$ and B_q ($N_{\Delta u}$ = 6÷8). Also working on block samples, Karlsrud et al. (2005)

proposed new correlations where the cone factors N_{kt} and $N_{\Delta u}$ depend on the stress history, plasticity and sensitivity.

Table 2.5. Literature review of the empirical effective cone factor N_{ke}.

Authors	Reference test	Soil	Empirical cone factor, N_{ke}	Remarks
Senneset et al. (1982)	-	Clays	6÷12	I_P = 3÷50%
Lunne et al. (1985)	CAU	Clays	1÷13	varies with B_q
Karlsrud et al. (1996)	Tx compression	Clays	2÷10	decreases with B_q
Hong et al. (2010)	Tx compression	Busan clay, Korea	3÷18	I_P = 25÷40%
Rémai (2013)	CU, UC	Soft Holocene clays	10.9÷28.6 (18.3)	no correlation with B_q
Cheshomi (2018)	UC	Quaternary fine-grained alluvium soil	17÷31 (22)	no correlation with I_P

Note: CAU = triaxial anisotropically consolidated undrained; CU = triaxial consolidated undrained; UC = unconfined compression.

Table 2.6. Literature review of the empirical effective cone factor $N_{\Delta u}$.

Authors	Reference test	Soil	Empirical cone factor, $N_{\Delta u}$	Remarks
Lunne et al. (1985)	CAU	Clays	4÷10	varies with B_q
La Rochelle et al. (1988)	-	Clays	7÷9	-
Karlsrud et al. (1996)	Tx compression	Clays	6÷8	no clear dependency on B_q
Hong et al. (2010)	Tx compression	Busan clay, Korea	4÷9	I_P = 25÷40%
Rémai (2013)	CU, UC	Soft Holocene clays	1.8÷13.1 (6.3)	correlation with B_q
Cheshomi (2018)	UC	Quaternary fine-grained alluvium soil	2.8÷5.9 (3.8)	no correlation with I_P
Duan et al. (2019)	FV	Marine clay	8.03	-

Note: FV = field vane; CAU = triaxial anisotropically consolidated undrained; CU = triaxial consolidated undrained; UC = unconfined compression.

More recently, Rémai (2013) determined all the four empirical cone factors for some surface deposits of soft silts and clays of varying plasticity, where the measured cone tip resistance was always less than 2 MPa. Consolidated-undrained triaxial compression tests and unconfined compression tests were performed to determine s_u. Cheshomi (2018) determined the cone factors for quaternary fine-grained alluvium soils, with UC as reference test.

At the close of this review, it is important to note the wide scatter in the empirical cone factors and that no single cone factor value exists that will cover all types of clays, penetrometers and laboratory testing conditions. Therefore, notwithstanding the increased database, it is generally recommended to calibrate the cone factors locally and not to use the cone factors uncritically for other areas, as suggested by Schmertmann (1975) and Andresen et al. (1979).

3 METHODS

This chapter summarises the test methods used to investigate the sediments of the test field in the Ancona CDF, performed during the ante operam and post operam phases described in Chapter 4. The chapter is divided in two main sections: laboratory tests and field tests. The standards by the American Society for Testing and Materials (ASTM) were the reference standards for most of testing.

3.1 Laboratory tests

3.1.1 Classification

Several classification tests (Table 3.1) have been performed on each of the 3 different batches of the dredged sediments before and after their disposal in the first sector of the Ancona CDF where the test field has been constructed.
The different sediments were classified according to the unified soil classification systems (USCS) on the basis of their grain size distribution and consistency limits by means of the plasticity chart. For a deeper characterisation, sedimentation analyses were also performed to assess the clay fraction (grain size < 2 μm).

The same classification tests have been also repeated on samples taken from the sediment layers after their consolidation in the test field area.

Table 3.1. Classification tests performed on the sediments.

Grain size distribution	Sieving	ASTM D6913/D6913M-17 (2017)
	Sedimentation (Hydrometer) analysis	ASTM D7928-21 (2021)
Atterberg limits	Liquid limit, plastic limit	ASTM D4318-17 (2017)
Classification system	USCS	ASTM D2487-17 (2017)

3.1.2 Water content

The standard test method used for the laboratory determination of the water content of soils is the oven-drying method covered by ASTM D2216-19 (2019). For each sample at least two separate moisture content determinations were always performed and the water content was assumed as the average value.

If the porewater is saline, as in the case of concern, the dissolved salts will remain in the soil after drying and an incorrect moisture content can result. A more appropriate value is the fluid content, i.e., the mass of fluid (water plus salts) per unit dry mass of soil. Knowing that the seawater contains about 40 g per litre of dissolved salts, the water content was always calculated as the fluid content, taking into account the mass of dissolved salts, i.e.:

$$w = M_{sw}/M_{ds} \tag{3.1}$$

where M_{sw} is the mass of the sea water and M_{ds} is the mass of the dry sediment, according to ASTM D4542-15 (2015).

3.1.3 X-ray diffraction analyses

X-ray diffraction (XRD) is the most widely used technique for identification of clay minerals and the study of their crystal structure (e.g., Mitchell & Soga, 2005). This method works with X-radiation, which is the part of the electromagnetic spectrum ranging in wavelength from approximately 10^{-11} m to 10^{-8} m. In principle, X-radiation can be generated by electron displacement or by rapid deceleration of fast-moving electrons as they impinge on matter, depending on whether they collide or not with other electrons[4].

X-ray diffraction occurs when incident X-rays are scattered by atoms arranged in an orderly array in crystals. The atoms act as scattering centres, re-emitting X-rays at the same wavelength as the incident radiation. Given the periodicity of atoms in a crystal lattice, the scattered X-rays can be in phase in certain specific directions (dictated by symmetry and atomic spacing) or out of phase in all other directions. X-rays that are in phase constructively interfere and emerge as intense beams (diffracted X-rays) from the crystal, while those that are out of phase result in a destructive interference and have minimal emergence (Harris & Norman White,

[4] In the first case, the high-speed electron strikes and dislodges an electron from an inner shell of one of the atoms of the target material; to lower the energy state of the atom, an electron from one of the outer shells falls into the vacancy, causing the emission of an X-ray photon of wavelength and intensity characteristic of the target atom and of the particular electronic position. In the second case, no collisions occur but the high-speed electron slows down in the intense electric fields near atomic nuclei; the decrease in energy is converted to heat and X-ray photons. These two effects act together and result in a composite relationship for X-ray intensity as a function of wavelength (Mitchell & Soga, 2005).

2015). Constructive interference, which forms the basis for X-ray diffraction analyses, occurs when geometrical conditions satisfy the Bragg's law:

$$n\lambda = 2d \sin\theta \tag{3.2}$$

relating the radiation wavelength, λ, to the diffraction angle, θ, and to the spacing of interatomic planes in the crystal, d (Figure 3.1). If the diffraction order, n, is a positive integer, the Bragg's condition is met and a peak in X-ray intensity can be detected.

Since no two minerals have the same spacings of lattice planes in three dimensions, the angle at which diffraction occurs is unique and can be used to univocally identify them. Specifically, once the wavelength λ is fixed, by XRD analyses it is possible to compute the d-spacing from the measured angle 2θ.

Such measurements can be conducted on individual crystals, but in soil mineralogy the use of powders (of single minerals or mixtures) is preeminent, given the small size of most clay minerals. This method is known as powder X-ray diffraction (PXRD), and it relies on the assumption that, when grinded into a fine powder, the soil sample contains such a large number of particles that random orientation can be assumed, so that all possible diffraction directions of the lattice are represented.

A PXRD analysis is commonly performed via an X-ray diffractometer, whose typical arrangement is sketched in Figure 3.2. In a diffractometer, the generation of X-rays is accomplished by using an evacuated tube consisting of a tungsten filament cathode and a metal target anode; a voltage drop makes electrons stream from the filament (electron source) to the target, where X-rays are emitted according to the two mechanisms of electron displacement or deceleration already introduced. Target materials commonly used produce monochromatic radiation (i.e. single wavelength) with wavelengths of the same order of the spacing between interatomic planes[5]. X-rays thus generated exit the tube through a window, where they are collimated and focused at some angle θ on the soil powder housed on a sample stage, to enable diffraction. At the opposite side, an X-ray detector receives the diffracted X-rays and records their intensity as the soil sample is scanned over an angular range of 2θ angles over time. Modern detectors consist of a transducer producing an electrical signal when exposed to X-radiation; they are often used as photon counters, so the radiation intensity is determined by the number of counts in a certain amount of time. The output of the test is a chart (diffractogram) showing the intensity of diffracted X-rays as a function of 2θ.

[5] The spacing between interatomic planes in crystalline materials is of about 1 A° (=1×10^{-10} m), hence X-ray wavelengths of the same order are suited for the analysis of crystal structures. A number of target materials are available that produce radiation of various wavelength (from 0.71 A° of molybdenum to 2.29 A° of chromium), but the copper target (λ = 1.54 A°) is commonly used for mineral identification.

Figure 3.3 shows the X-ray diffractometer used in this research (Bruker D8 Advance) supplied to the Physics Laboratory of the SIMAU Department of the Università Politecnica delle Marche. The software Diffrac.eva v.4.3 was used for mineral identification. This software searches in its extensive library of spectra the peaks sequence that better fits the measured diffractogram, starting from the highest peaks and gradually excluding what has already been identified.

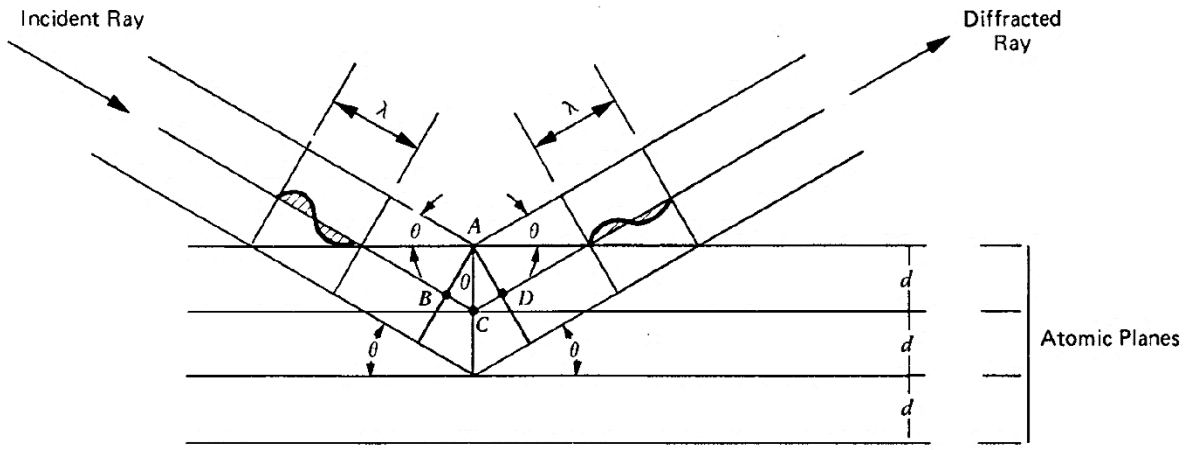

Figure 3.1. Geometrical condition for X-ray diffraction according to Bragg's law (after Mitchell & Soga, 2005). Beams of X-rays having identical wavelength and phase approaching a crystal with an angle of incidence θ are scattered specularly by the atoms in lattice planes regularly spaced a distance d apart. Hence, diffracted beams deviate 2θ from incident beams. The radiation wavelength λ is comparable to the d-distance. Notice that when the extra length 2dsinθ (= BC+CD) crossed by the lower beam is equal to an integer multiple of the radiation wavelength, the diffracted beams from each atomic plane would be in phase, leading to constructive interference. When this condition is met, an XRD peak is observed.

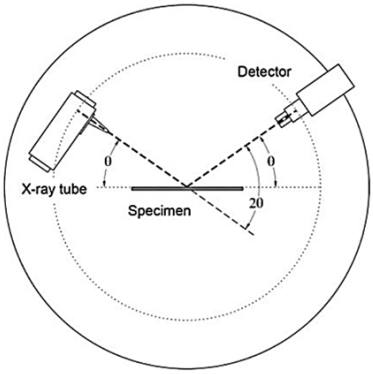

Figure 3.2. Schematic of a powder X-ray diffractometer, consisting of an X-ray source, a sample mounting stage, an X-ray detector, and a goniometer to vary the incident angle θ.

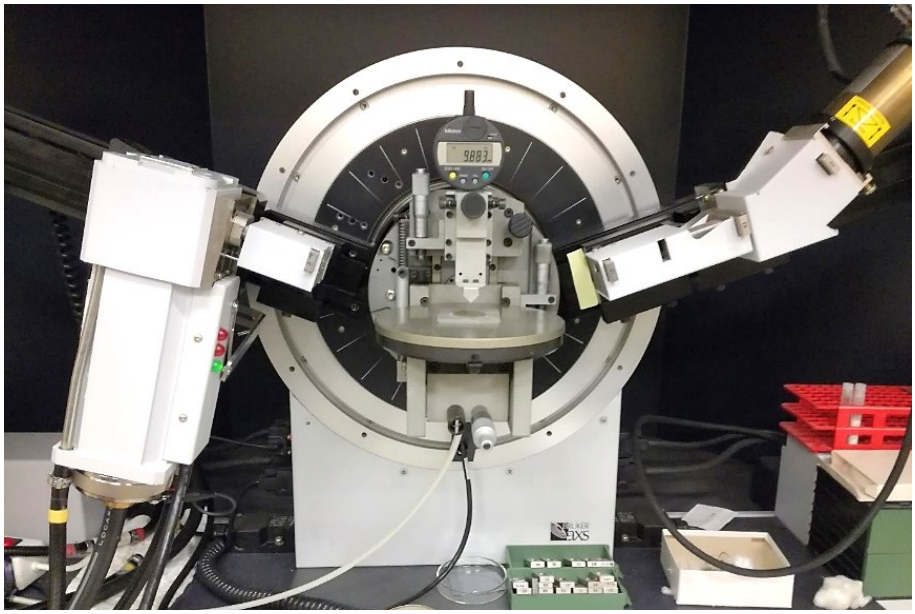

Figure 3.3. The X-ray diffractometer Bruker D8 Advance used in this research.

PXRD analyses provide qualitative or, at best, semiquantitative information about the mineralogical composition of the soil. Quantitative determination of the amounts of various minerals in the soil based on the simple comparison of the diffraction peaks heights or areas under is uncertain because of several factors (e.g., differences in mass absorption coefficients of different minerals, particle orientations, sample weights, surface texture of the sample, mineral crystallinity, hydration, etc.).

3.1.4 One-dimensional consolidation tests

The one-dimensional consolidation test by incremental loading (also referred to as oedometer test) was performed both on reconstituted and undisturbed samples of the sediments of the first sector of the CDF, according to the standard ASTM D2435/D2435M-11 (2020). Sea water was used as the pore liquid for the reconstituted samples and as submerging liquid in all the tests. The reconstituted samples were prepared by thorough mixing of sediments and sea water to obtain the desired water content (always corresponding to the fluid state) and poured into the mould.

The coefficient of vertical consolidation, c_v, was always determined with the procedure by Casagrande (1936), from the plots of the measured settlements versus the logarithm of time for each load increment, according to the following equation:

$$c_v = \frac{T_v H_{d,50}^2}{t} \tag{3.3}$$

where $H_{d,50}$ is the length of the maximum drainage path and T_v is the dimensionless time factor, both at 50% consolidation ($T_v = T_{v,50} = 0.197$).

The preconsolidation pressure, σ'_p, was always determined on the compressibility curve by the tangent method (Holtz & Kovacs, 1981).

3.1.5 Triaxial tests

Isotropically consolidated-undrained triaxial tests (Tx-CIU) and unconsolidated-undrained triaxial tests (Tx-UU) were performed on specimens reconstituted according to the procedure by Burland (1990), as well as on specimens taken from undisturbed samples from the sediment layers after the field test consolidation (*post operam* phase). The Tx-CIU tests allowed to determine both the shear strength parameters and the undrained shear strength at different effective confining pressure levels. The Tx-UU tests were used to assess the undrained shear strength of the sediments at the depth of sample collection.

The confining pressures applied in the Tx-CIU tests on the undisturbed samples were selected considering the geostatic effective mean stress, $\sigma'_{m0} = (\sigma'_{v0} + 2\sigma'_{h0})/3$, at the depth at which the sample was taken. The three specimens (diameter = 38 mm; height = 76 mm) were consolidated under isotropic effective stresses, σ'_c, of about 0.5, 1 and 1.5 times the geostatic effective mean stress.

The consolidated undrained triaxial compression tests were performed according to the standard ASTM D4767-11 (2020) at a constant rate of axial deformation of 0.01%/min. The standard method for the unconsolidated undrained triaxial compression test was ASTM D2850-15 (2015).

3.2 In-situ tests

3.2.1 Cone penetration test

The Cone Penetration Test (CPT) is undoubtedly the most widely used and versatile test for soil exploration. CPT produces fast and near-continuous soil profiling, provides repeatable and reliable data (independent of operator) and is cost-effective and productive. In addition, CPT can now look back on a sound theoretical basis and a significant number of case histories for interpretation.

Applications of CPT in the site investigation process sweep from the determination of sub-surface stratigraphy and soil identification to the estimation of geotechnical parameters. For such reasons CPTs have been carried out on the test field area both before the moving embankment construction and after its removal. In particular, mechanical cone penetration tests (CPTM) and piezocone tests (CPTU) have been performed.

CPTM tests have been performed by the Begemann (1953) friction-cone, which is perhaps the most common mechanical-type penetrometer world-wide. It is a telescoping penetrometer endowed with a cylindrical adhesion jacket behind the conical point, to also measure the friction component of penetration resistance. The point features a 60° apex angle and a base diameter of 35.7 mm, resulting in a projected area of 10 cm^2. The friction sleeve has a surface area of 150 cm^2. All the tests with the Begemann friction-cone penetrometer were performed according to the standard ASTM D3441-16 (2016). Basically, once the thrust machine is positioned over the sounding location and fixed, and the hydraulic ram feed rate set to drive the penetrometer downward at 2.0±0.5 cm/s, the procedure consists of a three-step cycle of measurements repeated at intervals of about 20 cm. It is inherent in this procedure that the cone tip resistance, q_c, and the frictional resistance, f_s, are not determined at exactly the same depth, and that only discontinuous measurements can be recorded. Despite these aspects and a lower accuracy compared to enhanced cones (such as the piezocone), the Begemann penetrometer has been used because of its low cost and robustness.

CPTU tests have been performed by the reference standard piezocone having a 60° apex angle, a 10 cm^2 base area and a 150 cm^2 friction sleeve placed above the cone. The porous filter element is positioned just behind the cone, in the so-called u_2 location (Figure 3.4), which is usually preferable because it is much less prone to damage, measurements are less affected by the element compressibility and can be used directly to correct cone resistance (§ 3.2.1.1.1). The standard test method followed for CPTUs is ASTM D5778-20 (2020). In particular, saturation of the piezocone has been provided for all the piezo elements (filter element, transducer housing cavity, and tubing between them) by assembling them in a glycerine or silicon oil bath; next the assembled system has been protected from evaporation by enclosing the porous element inside a fluid-filled latex membrane, then tore as penetration started. The penetrometer was advanced in the sediments at a constant rate of 2.0±0.5 cm/s. Readings of cone resistance, q_c, friction sleeve resistance, f_s, and porewater pressure, u_2, have been recorded simultaneously at depth intervals of 1 cm.

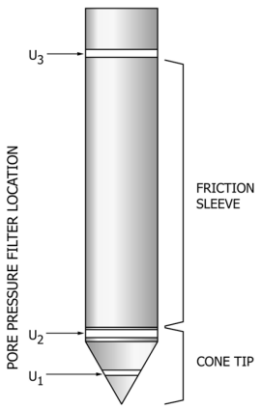

Figure 3.4. Possible positions of the filter element in a piezocone.

All cone penetration tests have been performed by means of the tracked vehicle penetrometer Pagani TG 63-200 shown in Figure 3.5. In the case of the mechanical cone the load cell was installed inside a removable unit (manual selector), which presses alternately on the inner and outer rods, while readings are displayed on an electronic acquisition board; the piezocone instead allows the continuous acquisition of data. The main technical features of the piezocone used in this study are reported in Table 3.2.

Figure 3.5. The penetrometer Pagani TG 63-200 positioned on the test field area.

Table 3.2. Technical specifications and size of the piezocone MKS Pagani used in this research.

q_c sensor full scale (MPa)	50÷100	Weight (kg)	1.66
f_s sensor full scale (MPa)	1.6	Length (mm)	290
u_2 sensor full scale (MPa)	2.5	Diameter (mm)	36
Tilt sensor full scale (°)	0÷20	Cone apex angle (°)	60
Tip area factor, a (-)	0.80	Cone base area (cm^2)	10
Sleeve area factor, b (-)	0	Side sleeve surface (cm^2)	150

3.2.1.1 Processing of CPTU data

3.2.1.1.1 Correction for porewater effects

The porewater pressure measured by the piezocone is a total parameter including equilibrium pore pressure, u_0, and the excess porewater pressure generated during penetration, Δu. The equilibrium porewater pressure is nearly always the hydrostatic pressure established from the position of the groundwater table, while the excess porewater pressure reflects a transient state associated with changes in octahedral normal and shear-induced stresses in the clay (Mayne et al., 1990).

Since the total porewater pressure around a penetrating cone affects the measured values of cone resistance and the measured porewater pressure is in turn influenced by the location of the filter, Campanella et al. (1982) proposed the following correction to account for what they called "unequal-end area effect":

$$q_t = q_c + (1 - a)u_2 \tag{3.4}$$

where, besides the symbols already introduced, q_t is the corrected cone-tip resistance, and a is the net area ratio of the tip (Figure 3.6). Typical values of a range from 0.9 to 0.55 (Lunne et al., 1997); for the piezocone used in this research, a = 0.8 (cfr. Table 3.2).

The correction for porewater effects[6] is of paramount importance in soft fine-grained saturated soils, where q_c is typically low relative to the high water pressures acting behind the cone due to the undrained penetration process. In this research, Equation (3.4) has been systematically applied to correct the q_c readings.

An analogous correction should be applied to the measured values of f_s, since the sleeve also has end-areas exposed to porewater pressure. During testing, the induced porewater pressures are not constant along the penetrometer shaft, so that the values measured at the lower (u_2) and upper (u_3) ends of the sleeve normally differ. The corrected sleeve friction, f_t, can be given by:

$$f_t = f_s - \frac{(u_2 A_{sb} - u_3 A_{st})}{A_s} \tag{3.5}$$

where A_s is the mantel area of the sleeve, A_{sb} and A_{st} are the cross-section areas of base and bottom of the sleeve, respectively. The magnitude of this correction can be negligible by having

[6] Equation (3.4) is valid for u_2 location; whenever the filter is in the u_1 location, Lunne et al. (1997) provided a formula to switch from u_1 location to the u_2 location: $(u_2\text{-}u_0) = K(u_1\text{-}u_0)$, where K is an adjustment constant with values ranging from 0.2 to 0.8 depending on the soil, with the higher values pertaining to clays.

equal end areas and making them as small as possible, as in the case of the tests of this research. Since u_3 was not measured, as typically occurs, no corrections has been done to the measured sleeve friction as suggested by Lunne et al. (1997).

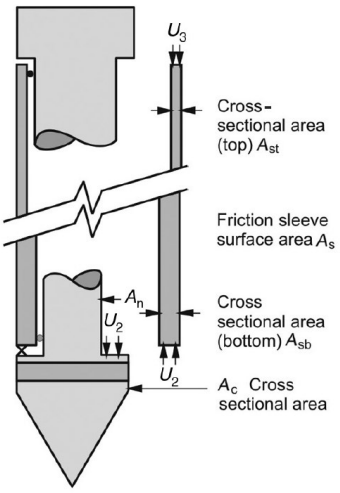

Figure 3.6. Pore pressure effects on cone data (after Schnaid, 2008). The net area ratio is a = A_n/A_c.

3.2.1.1.2 Stress normalization

Based on the theoretical work of Wroth (1984, 1988) and Houlsby (1988), a rational interpretation of cone test results requires the use of normalised (and dimensionless) parameters:

- Normalised cone resistance:

$$Q_t = \frac{(q_t - \sigma_{v0})}{\sigma'_{v0}} = \frac{q_{net}}{\sigma'_{v0}} \tag{3.6}$$

- Normalised friction ratio:

$$F_r = \frac{f_s}{(q_t - \sigma_{v0})} 100\% \tag{3.7}$$

- Pore pressure ratio:

$$B_q = \frac{(u_2 - u_0)}{(q_t - \sigma_{v0})} = \frac{\Delta u}{q_{net}} \tag{3.8}$$

where σ_{v0}, σ'_{v0}, and u_0 are the *in situ* total vertical stress, effective stress and equilibrium water pressure, respectively. The difference q_t - σ_{v0} is sometimes referred to as net cone resistance, q_{net}; the difference u_2 - u_0 quantifies the excess porewater pressure generated during penetration, Δu.

It is worth to note that the normalised parameters above consider only vertical stresses. Jamiolkowski & Robertson (1988) remarked that penetration resistance is strongly affected by horizontal effective stresses, hence any normalisation to account for increasing stress should also consider their influence; however, in lack of a prior knowledge of *in situ* horizontal stresses, this concept has still little practical benefit (Robertson, 2012).

Robertson & Wride (1998), as part of soil liquefaction studies, and the update by Zhang et al. (2002), suggested to modify the normalised cone resistance as follows:

$$Q_{tn} = \frac{(q_t - \sigma_{v0})}{p_{atm}} \left(\frac{p_{atm}}{\sigma'_{v0}}\right)^n \tag{3.9}$$

where p_{atm} is the atmospheric pressure and n is a stress exponent varying with the soil behaviour type, with values around 0.5 for sands and close to 1.0 for clays, as formerly suggested by Olsen & Malone (1988); when $n = 1$, $Q_{tn} = Q_t$. An iterative procedure to establish the proper value of n was also proposed.

The appropriate stress normalisation has been later debated by many researchers (e.g. Idriss & Boulanger, 2004; Moss et al., 2006; Cetin & Isik, 2007). Robertson (2009) concluded that it is preferable to use a stress exponent varying with both soil type and stress level:

$$n = 0.381(I_c) + 0.05(\sigma'_{v0}/p_a) - 0.15 \tag{3.10}$$

where $n \leq 1$, and I_c is the soil behaviour type index:

$$I_c = [(3.47 - \log Q_{tn})^2 + (1.22 + \log F_r)^2]^{0.5} \tag{3.11}$$

whose significance is explained in the next section. Of course, an iterative procedure is needed to determine the proper value of n. The normalised parameters above are commonly used to interpret cone penetration test results for classification purposes (§ 3.2.1.1.3).

Normalisation came in for criticism because of the dependency of effective stresses on the soil unit weight and, to a greater extent, to the pore pressure distribution. In the case of concern, soil unit weights and water levels are known with a certain accuracy, hence it was considered to use normalised parameters in post-processing of CPT data.

3.2.1.1.3 Classification charts

Soil profiling and classification is one of the major applications of CPTs. Mayne (2014) identified the approach to do this by soil behaviour charts. Early soil profiling charts appeared in literature were evidently based on mechanical cone penetrometer data (Begemann, 1965;

Sanglerat et al., 1974; Schmertmann, 1978; Searle, 1979) and, later, on electric CPT data (Douglas & Olsen, 1981; Vos, 1982). All these classification systems basically relied on the link between cone resistance, q_c, and friction ratio, $R_f = (f_s/q_c)$. Nevertheless, the measurement of sleeve friction is deemed to be less accurate and more susceptible to variations in the penetrometer design. The advent of the piezocone enhanced soil profiling from cone penetration tests, by introducing the recorded porewater pressure as classification parameter (e.g. Jones & Rust, 1982; Robertson & Campanella, 1983), and the use of q_t data instead of q_c (Robertson et al., 1986).

Robertson et al. (1986) used the basic raw q_t and R_f measurements to provide a chart with twelve numbered areas to group soil types, allowing for a real-time classification. The term "soil behaviour type" (SBT) was introduced to indicate that CPT-based charts are predictive of soil behaviour: in fact, the cone responds to the in situ mechanical behaviour of the soil (e.g. strength, stiffness and compressibility) and not directly to classification criteria based on grain-size distribution and soil plasticity (e.g. USCS). However, there is often good agreement between CPT-based soil behaviour types and USCS (e.g. Molle, 2005).

Robertson (1990) introduced the use of normalised parameters Q_t, F_R, and B_q to draw a normalised (SBTn) classification chart, arguing that normalisation delivers more reliable identification of soil behaviour types. The Q_t-F_R chart, shown in Figure 3.7, separates soils in nine SBTn zones, and it has seen extensive use in engineering practice.

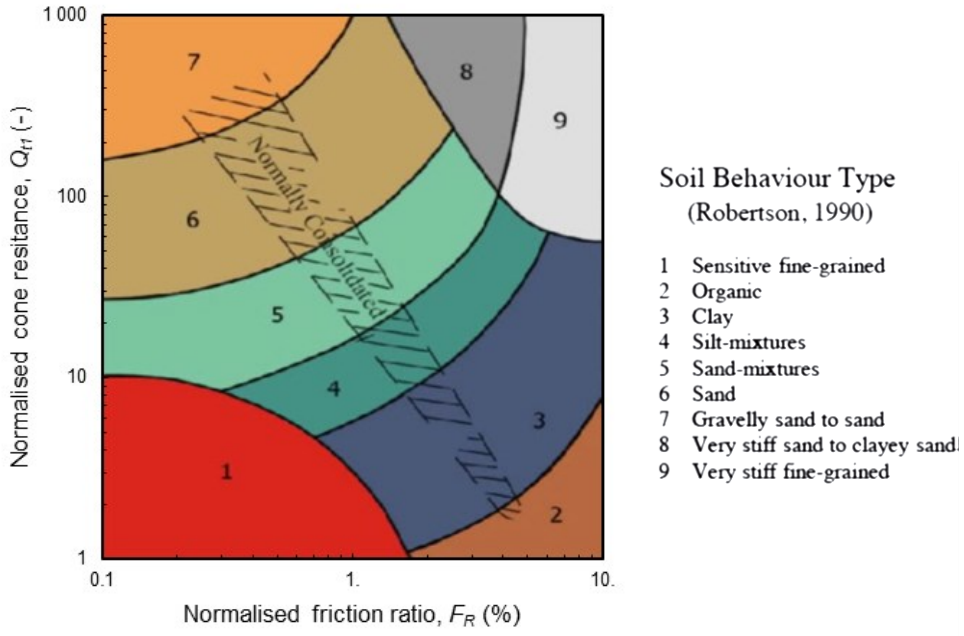

Figure 3.7. Normalised SBTn Q_{tn}-F_R chart after Robertson (1990).

Jefferies & Davies, 1993 realised that, if vertical and horizontal scales are suitably distorted, the boundaries between soil behaviour types can be approximated as concentric circles, whose radius is called soil behaviour type index, I_c. Robertson & Wride (1998) modified the definition of I_c to apply to the Robertson (1990) chart, providing Equation (3.11), later updated by Robertson (2009) with the introduction of the variable stress exponent (3.10) in the term Q_{tn}; the authors also suggested that $I_c = 2.6$ could be seen as an approximated boundary to classify soils as either sand-like ($I_c < 2.6$) or clay-like ($I_c > 2.6$) in their behaviour.

The latest refinement to the SBTn chart was presented by Robertson (2016), who proposed to replace the misinterpreting textural nomenclature of soil groups with more consistent behaviour-based descriptions (Figure 3.8). A contractive-dilative boundary is added to the chart, as represented by the following equation:

$$CD = 70 = (Q_{tn} - 11)(1 + 0.06F_R)^{17} \tag{3.12}$$

When CD > 70, the soil is likely dilative at large shear strains. The two hyperbolic lines $I_B = 32$ and $I_B = 22$ identify the boundaries of a transitional region between sand-like and clay-like behaviour, where I_B is a modified soil behaviour type index:

$$I_B = 100(Q_{tn} + 10)/(Q_{tn}F_R + 70) \tag{3.13}$$

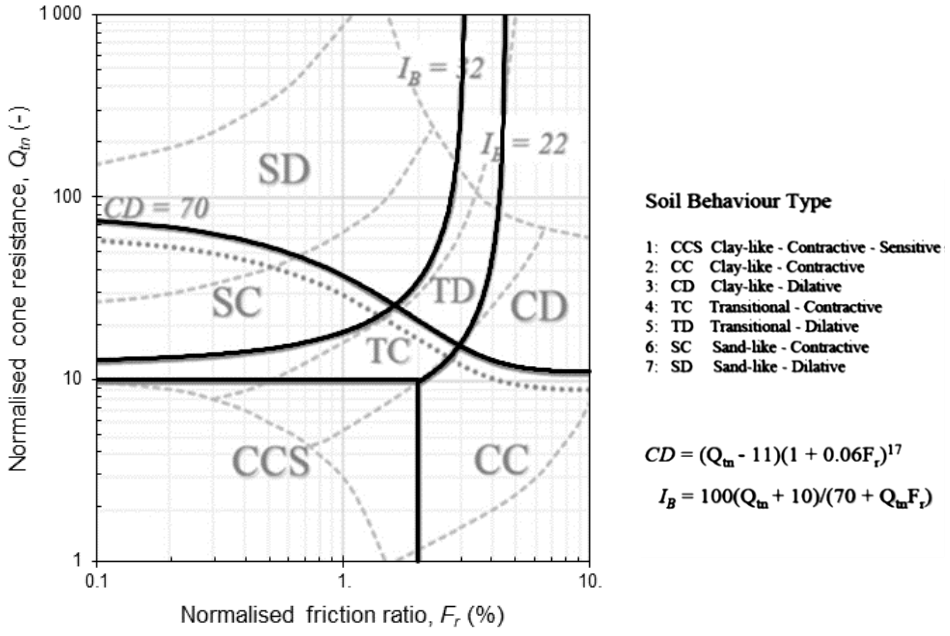

Figure 3.8. Normalised SBTn Q_{tn}-F_R chart after Robertson (2016).

In this research, the SBTn index has been computed along the depth to provide stratigraphic profiling, as well as to assess the applicability of this classification system to dredged sediments.

The weak point of Q_{tn}-F_R charts, as pointed out by Eslami & Fellenius (1997, 2004), is the violation of plotting principles, as the axis are not independent (cone resistance data are plotted against their own inverse self). The authors proposed their own non-normalised chart using effective cone resistance, $q_E = q_t - u_2$ and f_s. However, the effective cone resistance suffers from lack of accuracy in soft-grained soils, where q_t and u_2 are potentially comparable in magnitude (Robertson, 2012).

3.2.2 Dissipation tests

A dissipation test consists of temporarily stopping the piezocone penetration at a given depth and monitoring the decay of porewater pressure with time[7].

Since dissipation occurs faster at the beginning, it is generally recommended to collect data more frequently in the initial part of the test; a logarithmic time scale would be more appropriate to plot earlier data. In this way, a dissipation curve can be drawn, where the transient porewater pressure, $u(t)$, is expressed by the sum of the equilibrium porewater pressure, u_0, and the transient excess porewater pressure, $\Delta u(t)$. The collection of data shall be continued until the equilibrium porewater pressure, u_0, at that testing depth is attained (i.e. no further dissipation is observed) or, as oftentimes with low-permeable fine-grained soils, until at least 50% of the initial excess pore pressure, $\Delta u(t=0)$, has dissipated, to enable the coefficient of consolidation to be predicted via one of the theoretical solutions or semi-empirical procedures proposed in the literature (Torstensson, 1975, 1977; Randolph & Wroth, 1979; Battaglio et al., 1981; Senneset et al., 1982; Levadoux & Baligh, 1986; Houlsby & Teh, 1988; Jamiolkowski, 1995; Danziger et al., 1997; Sully et al., 1999; Burns & Mayne, 1998). In the present research, the strain path solution proposed by Houlsby & Teh, 1988 has been considered to evaluate the coefficient of consolidation (Mayne, 2007).

[7] When piezocone penetration is paused, any excess porewater pressure generated around the cone starts to dissipate, predominantly in the horizontal direction (Baligh & Levadoux, 1986), with a rate depending upon the coefficient of consolidation, which means upon soil compressibility and permeability. It is well understood that the dissipation test is especially relevant for silts and clays, where the generation of excess porewater pressures is a consequence of undrained penetration of the cone. In sands, where full dissipation occurs almost instantly, the test can be useful to retrace the groundwater position from the recorded equilibrium porewater pressure value.

4 CASE STUDY: THE ANCONA CDF

In this chapter, the case study of the confined disposal facility (CDF) built in the Ancona Harbour is introduced. After a brief insight into its construction features, an innovative and sustainable design strategy to overcome the typical and site-specific geotechnical issues concerning filling and consolidation of CDFs is presented. A sector was created in the Ancona CDF and filled with dredged sediments to apply and validate the proposed strategy through a full scale test field.

4.1 Introduction

The natural silting of the seabed is a long-standing problem affecting the operativity of several port infrastructures serving the local economy in the Marche region, in particular the harbours of Fano, Senigallia, Numana, Civitanova Marche and Ancona, which play a strategic function in the whole Adriatic region. In the last few decades, environmental concerns about sediments contamination also emerged in these port areas as a result of industrial activities therein, thus revealing the twofold need of dredging seabeds both as maintenance and remediation activity.

In the late 2000s a program agreement was signed by local governments (region and municipalities), the Central Adriatic Port Authority and the national environmental agency, to start a multi-year dredging program involving all the aforesaid port infrastructures (Figure 4.1) and to reuse the resulting material in a sustainable way. Specifically, the uncontaminated sediments were destined for littoral nourishment and other beneficial uses, whereas it was established to convey the poor-quality[8] materials into a CDF to be constructed in the Ancona Harbour, thus

[8] According to the applicable regulation in Italy (D.M. 173/2016), the excavation materials are assigned a quality class based on a combined chemical and ecotoxicological classification obtained through the application of weighted integration criteria. The resulting nomenclature consists of five classes lettered A to E (in order of growing hazard), which also set forth the compatible management options. The sediments for which placement in a waterproofed confined environment (e.g. CDFs) is compulsory belong to class D, while for the classes of better quality it is optional. Class E sediments are the most contaminated, therefore they require particular environmental precautions and specific removal procedures.

seizing the opportunity for a land reclamation project as a virtuous alternative to landfilling. Upon completion, the reclaimed land of the CDF will be used as container storage yard.

The designed CDF was situated in the commercial dock of the Ancona Harbour (Figure 4.2), it had an overall volume capacity of about 300,000 m^3 and insisted on a surface of about 95,000 m^2 mostly submerged. This aspect considerably complicated construction and filling operations, since they occur underwater.

Figure 4.1. Location of the five port infrastructures involved in the dredging program.

Figure 4.2. The Ancona Harbour: the white circle localises the CDF (image Google Earth).

The construction of the Ancona CDF was completed in 2014; to date its filling is in progress. Only one sector has been completed, while minor widespread disposals of sediments have been sporadically undertaken in the remainder part of the CDF.

On the first filled sector, a full-scale test field was designed and built to verify the feasibility of the sectors and to set up the operational procedures related to the installation of the geotubes, vertical drains and preloading moving embankment. Based on the results of the instrumented test field, the management of the residual capacity (about 180,000 m^3) has been designed. All this is dealt with in the following chapters.

4.2 General description of the facility

4.2.1 Soil profile

The geological and geotechnical investigations performed to design the CDF walls revealed that the site is a deposit dating back to Early Pliocene, Late Pleistocene, and Holocene. The uppermost formation of the stratigraphic succession is basically a loose silty sand resting on a dense stratum of fine sands, which in turn overlies a clayey complex of low to medium consistency; below this the older formation, consisting of an overconsolidated silty clay with marly levels, was found to be rarely topped by a very thin heterometric layer. The spatial distribution of these lithostratigraphic units, although conform to the indicated sequence, is somewhat heterogeneous in terms of thicknesses and depths variability, as it can be seen in the stratigraphic block-diagrams in Figure 4.3. The reference stratigraphy at the CDF site is shown in Figure 4.4.

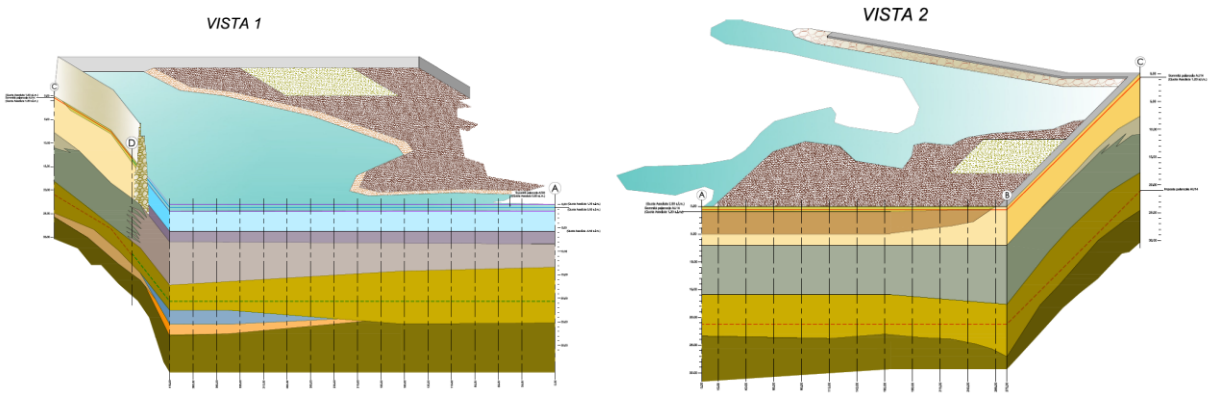

Figure 4.3. Stratigraphic block-diagrams of the CDF site area.

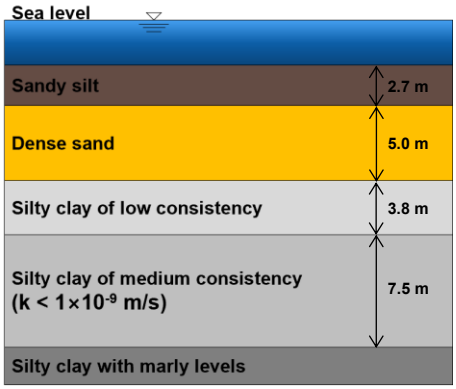

Figure 4.4. Stratigraphy of the seabed in the area of the CDF.

4.2.2 Construction details

As required by the national law, the management option compliant with contaminated (class D) sediments is the disposal in a sealed basin (e.g., CDF) capable of retaining all liquids and solid particles size fractions of sediments, paralleled by environmental monitoring. Hence, similarly to waste landfills, impermeable boundaries should be provided.

In the case of concern, the impervious bottom base was provided by the natural impervious cohesive layer (silty clay with medium consistency, Figure 4.4), whose presence, extent, and hydraulic suitability (i.e., hydraulic conductivity, $k \leq 1\times10^{-9}$ m/s) was detected during the investigation campaign preliminary to the CDF construction. The presence of the natural impervious layer avoided the need of an artificial bottom layer, with undoubted advantages in terms of cost savings and ease of execution.

The lateral confinement was provided by a continuous steel sheet piling embedded into the impervious natural bottom base for at least 1 m. On the side facing the sea, a breakwater was externally built to counteract the filling sediment pressure and preserve the structure from boats collisions. Different technologies of the piling walls were used for the ground and the seawater sides, as shown in Figure 4.5. The landside sheet piling serves only as a hydraulic barrier, as it is fixed for almost the entire length in the soil; hence, earth and water pressures on either side of the piling actually cancel. Conversely, the seaside sheet piling has also a structural function, since it works in imbalance conditions, both during construction and in operating phase. In light of the above, the sturdier "Z" profile (Figure 4.6a) was preferred for the seaside installation, while the "U" profile (Figure 4.6b) was selected for the landside. Table 4.1 shows the dimensions and properties of the different sheet piles. A total of no. 972 AU14 section sheet piles 20.5 m long were installed landside, for an overall development of 730 m, whereas the seaside piling consisted of no. 448 AZ26 section sheet piles 20.0 m long, for an overall development of 565 m. The perimeter totals 1,295 m.

Figure 4.5. Sheet pile walls of the Ancona CDF.

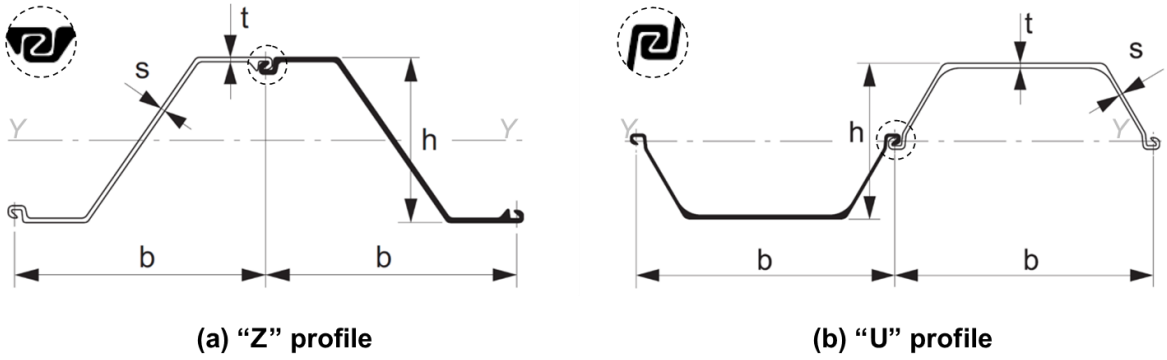

Figure 4.6. Steel sheet pile sections: in the circle, the specific Larssen interlock is highlighted.

Table 4.1. Dimensions and properties of the steel sheet piles profiles employed in the Ancona CDF.

Section	Width, b	Height, h	Flange thickness, t	Web thickness, s	Sectional area, A	Mass, M	Moment of inertia, I_Y	Static moment, S_Y
(-)	(mm)	(mm)	(mm)	(mm)	(cm^2/m)	(kg/m^2)	(cm^4/m)	(cm^3/m)
AZ26 (Figure 4.6a)	630	427	13.0	12.2	198	155	55,510	1,530
AU14 (Figure 4.6b)	750	408	10.0	8.3	132	104	28,680	820

Note: Y-Y is the neutral axis.

Driving operations were carried out by a vibratory hammer in different ways for landside and seaside, because of the uneven pile profiles (the "U" piles were singly driven, the "Z" ones were paired) and of the different boundary conditions: for the in-water installation a pontoon and a suspended walkway for workers were required (Figure 4.7). It is worth mentioning that, given the exposure to tidal fluctuations and splashing of the waves, before installation all the seaside sheet piles were coated with an epoxy resin in their upper half, as a protection against dry-wet cycles.

To ensure the watertightness of the sheet pile connections, that is, to get a performance equivalent to 1 m-thick layer with $k \leq 1 \cdot 10^{-9}$ m/s, the piles interlocks were sealed for the whole length with a polyurethane hydro-expansive waterproofing product (Roxan™, Figure 4.8a), while joint continuity and integrity along the depth was ascertained by means of an electric device (Dixeran®, Figure 4.8b). Special hydraulic tests were carried out to assess the reliability of the sealing system (Cianca, 2015).

At the end of the CDF construction, a web-based station was installed to collect weather-marine parameters and to check water levels inside and outside the CDF in real-time[9]. The continuous monitoring demonstrated that the CDF and the sea are independent hydraulic systems, thus confirming the watertightness of the perimetral cut-off (Felici, 2017). The station also allows remote controls of the two sluice gates installed along the seaside of the CDF (Figure 4.5), to manage levels and discharge water from the CDF when the maximum allowable inner level is reached.

Figure 4.7. Installation of the sheet piles: (a) landside; (b) seaside.

[9] Meteorological and water levels data recorded by the monitoring station installed in the Ancona CDF are freely accessible at https://www.irbim.cnr.it/sitoss-dettagli/stazione-meteo-marina-vasca-di-colmata-ancona/.

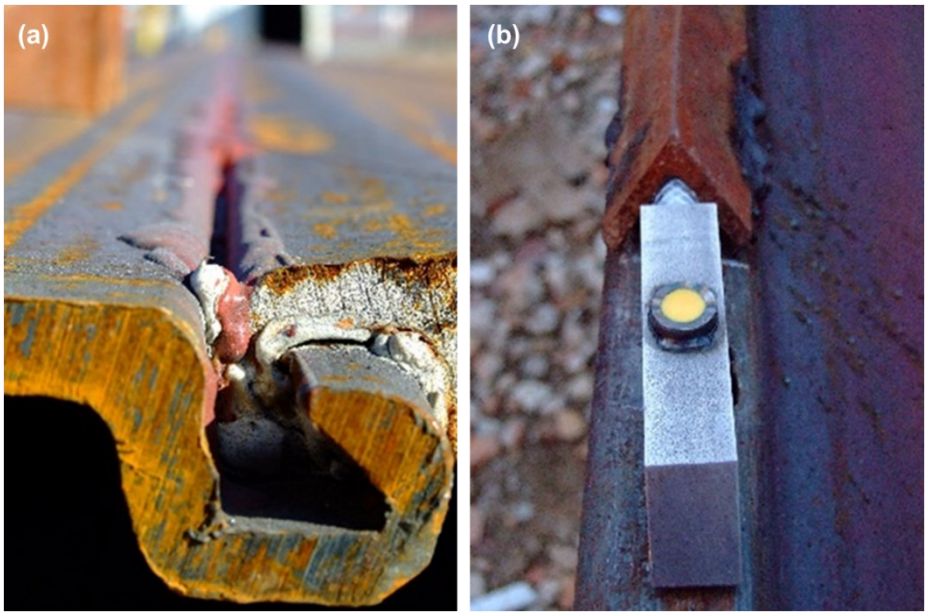

Figure 4.8. Solutions to ensure a proper connection between sheet piles: (a) the water-swelling resin Roxan™, applied along the interlock to control seepage through the wall; (b) the declutching detector system Dixeran®, to check by short-circuit if the sheet piles are properly interlocked underground.

4.3 Filling-and-consolidation: an innovative solution

Given the fine-grained nature of the sediments to be disposed into the Ancona CDF and the presence of water inside the facility, high void ratios and water contents were expected after their disposal. By way of example, de Lillis et al. (2020) documented water-to-solid volumetric ratios in the range of 6÷12 for fine-grained sediments hydraulically dredged and disposed in containment facilities.

The typical slurry consistency of fine-grained sediments clearly entails high compressibility and very poor mechanical properties of the sediments. Therefore, the improvement of their geotechnical properties is necessary to make a CDF a sustainable solution for dredged sediments, i.e., in the case of the Ancona CDF, its future use as reclaimed area.

The improvement technology and procedure for the sediments of concern were selected and designed considering sustainability, costs and time to complete.

Since a significant amount of coarse material was available at the Ancona CDF site from demolition waste of port structures, boulders, etc., preloading by embankment was selected as the improvement technique, coupled with prefabricated vertical drains (PVDs) to accelerate the consolidation process.

The different time schedules and volumes of dredged sediments to be disposed in the Ancona CDF would result in a long time before starting the consolidation treatment, hence a long time for land reclamation.

To maximise the CDF capacity and to make it available for its intended use in a shorter time, a method to optimise the filling and consolidation procedures was conceived for the first time with an idea by Prof. Erio Pasqualini. The proposed solution consisted in splitting the capacity of the CDF into sectors so that each can be filled and consolidated while the filling is in progress in the adjacent sector; the consolidation can be performed in each sector by a pre-loading "moving embankment", i.e. an embankment of limited size that can be sequentially built, dismantled, and re-built in other sectors, reusing the same material. This design strategy has several advantages:

- optimisation of resources and costs, since the moving embankment consists of waste materials;
- flexibility in the sediments management, considering the disposal schedules;
- reduction of the overall time required for the improvement, thus leading to the anticipated provision of the area for its intended use.

To provide such a "sectorisation", internal walls are needed. As a prime requirement, internal walls should ensure an effective containment during sediments disposal and consolidation procedures, to prevent collapses. Moreover, the sectorisation is best applied if internal walls minimise volume consume into the CDF and are easy and quick to install. Geotextile tubes (geotubes) filled with the sediments themselves have proven to meet all the requirements above, as detailed in § 4.4.1.

Referring to the Ancona CDF, Figure 4.9 illustrates the ideal sequence to be applied when filling and consolidation are to be performed by sectors with the moving embankment concept. After having positioned and filled the geotube (a), sediments are disposed in the first sector (b), until the sector is completely filled; then, after PVDs installation, the sediments are consolidated by the moving embankment, while in the meantime filling in the adjacent sector can start (c); once also this second sector is completed and PVDs installed, the mobile embankment is "moved" above it to begin consolidation (d), leaving for last the band zone between the two sectors (e); as an alternative, the area around the geotube can be consolidated together with the adjacent sector (f), depending on the sector size. In any case, particular care should be paid to the consolidation of the sediments close to the geotube, considering also its mechanical behaviour and properties; to this regard, stability analyses must be performed to assess the minimum distance between the geotube and the moving embankment.

The application of this innovative solution to the Ancona CDF allowed to complete the filling of a first sector and then to apply the selected consolidation treatment in a full-scale test field, as described in the following.

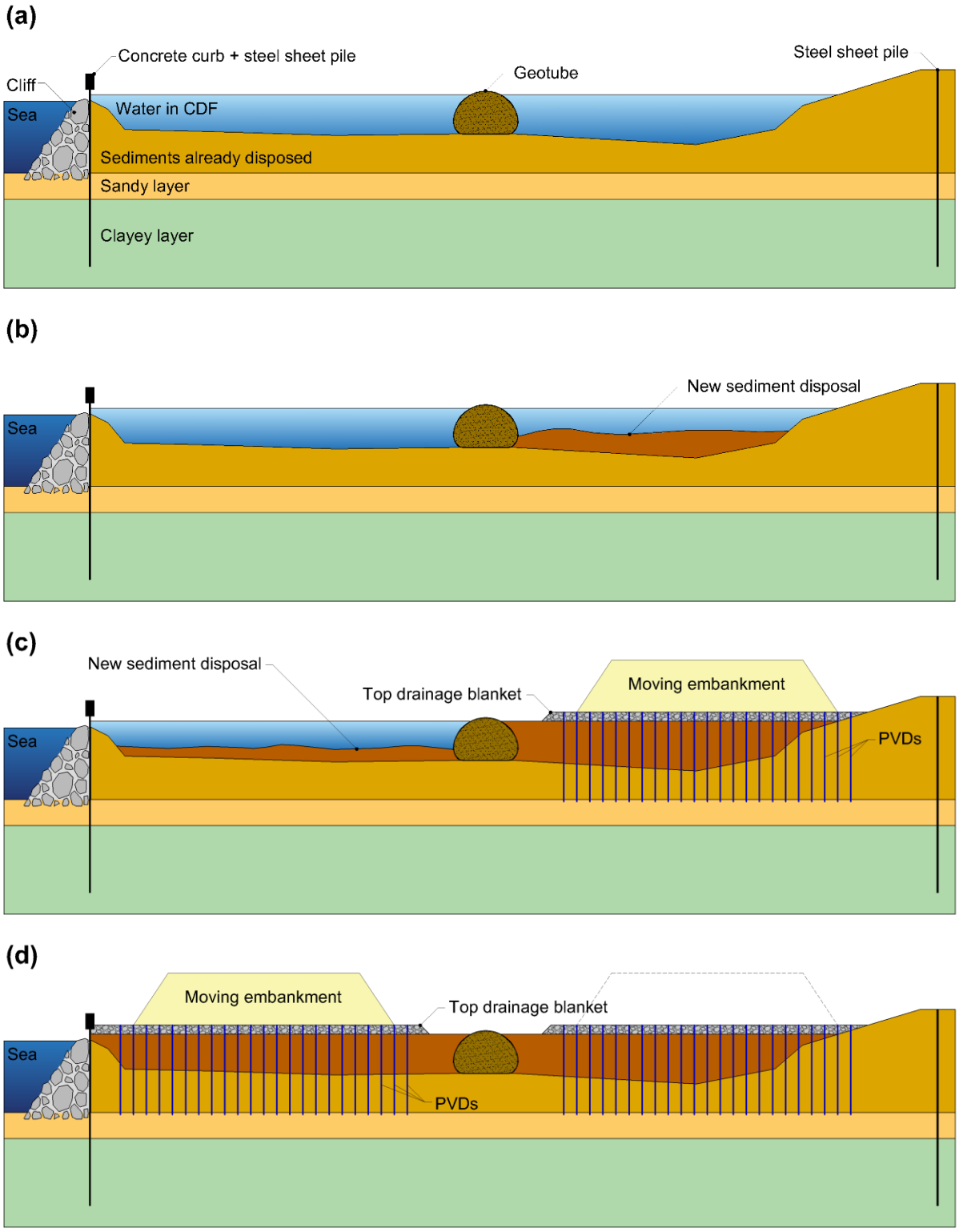
(a)
Concrete curb + steel sheet pile
Steel sheet pile
Cliff
Geotube
Sea
Water in CDF
Sediments already disposed
Sandy layer
Clayey layer
(b)
New sediment disposal
Sea
(c)
New sediment disposal
Top drainage blanket
Moving embankment
Sea
PVDs
(d)
Moving embankment
Top drainage blanket
Sea
PVDs

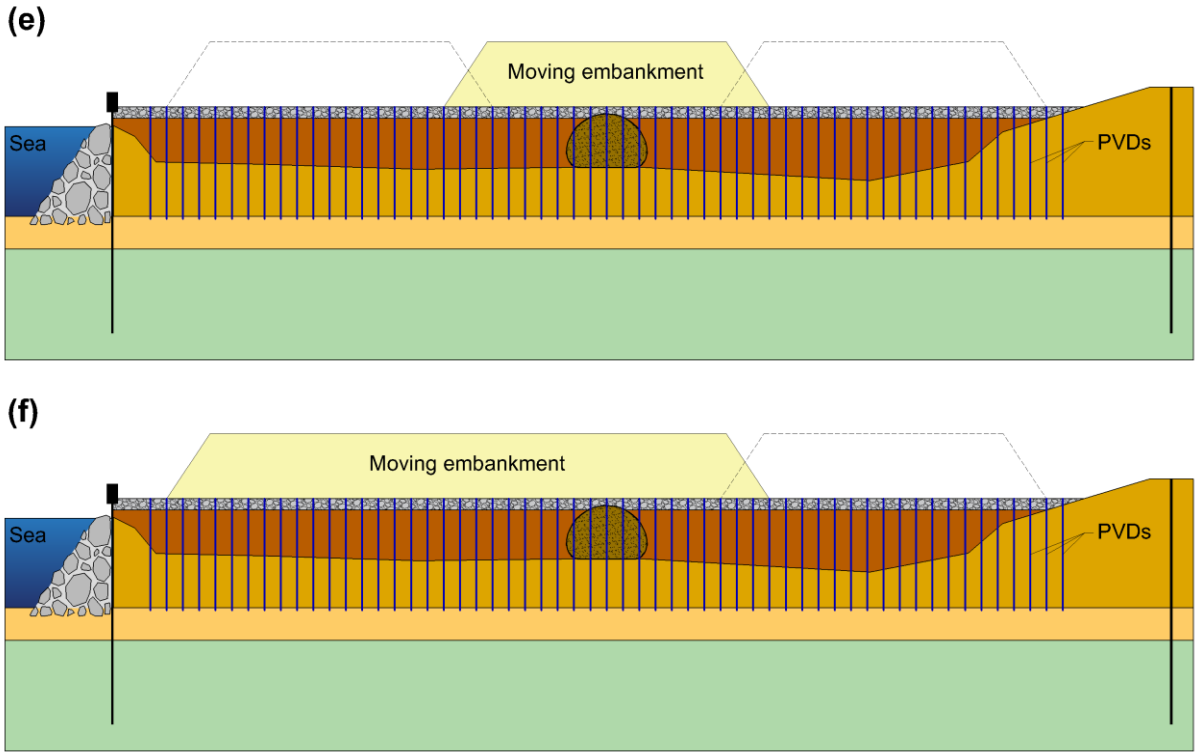

Figure 4.9. Filling and consolidation sequence at the Ancona CDF: (a) geotube installation; (b) disposal of sediments in the first sector; (c) consolidation of sediments in the first sector and simultaneous filling of the second sector; (d) consolidation of the second sector; (e) consolidation of the geotube area; (f) combined consolidation of the second sector and of the geotube are with a wider moving embankment (draws are not in scale).

4.4 Construction of the sector for the test field

A first lot of dredged material had early been deposited just immediately after the CDF construction: for this reason, a layer of soft sediments – which need to be consolidated – already covers the bottom. Above it, a water head of about 3 m is inside the facility. The test field were created on the first sector that had been completely filled with sediments of heterogeneous origin, by superimposing new sediment lots to the previous widespread sediments.

4.4.1 Boundaries

The sector identified for the test field construction (“Sector 0”) was situated on the southern corner of the CDF (Figure 4.10). This position was ideal both for filling by the sea and for providing a short-distance land access to the various equipment needed for building, testing, and installing monitoring tools.

Figure 4.10. The test field sector.

This sector covered a roughly rectangular area of 50 m × 80 m. On two sides it was bordered by the steel sheet piling, while a third side was provided by the sediment heap already present inside the facility, which emerged of about 1 m out of the water. A special 50 m long geotextile tube (MacTube®) filled with the sediments themselves was adopted to close the sector.

The installation of the geotube resulted quite easy and fast. To provide an adequate support surface to the geotube, a layer of gravel was preliminarily spread and hand-compacted on its footprint by specialized scuba divers. Next the geotextile bag was floated over the water surface on the design position, taking care to fix its ends to stabilise it against wind (Figure 4.11a). Then the dredged slurry was pumped inside through each of the top filling ports (Figure 4.11b), giving the geotube an oval shape (Figure 4.11c). Frequent switching of the pumping inlet along the geotube assured its quite uniform filling and sinking. During pumping, sediments were retained inside the tube and water drained out through the geotextile wall.

In general, the filling time for this kind of geotubes is variable, depending on factors such as the type and quantity of available equipment, weather conditions, etc. For the delimitation of the test field sector in the Ancona CDF, all the installation, including preliminary operations, lasted only one week.

The filled geotextile tube had a final height[10] of about 3 m and rested above the 3 m thick layer of sediments already present inside the facility – as a result of previous widespread

[10] The tube diameter can be customized according to the filling depth, but it should exceed the water head inside the CDF. If necessary, more than one geotubes can be overlapped to form a stack structure.

disposals – which were still very compressible. At the end of installation, the top of the geotube resulted partially emerged (Figure 4.11d).

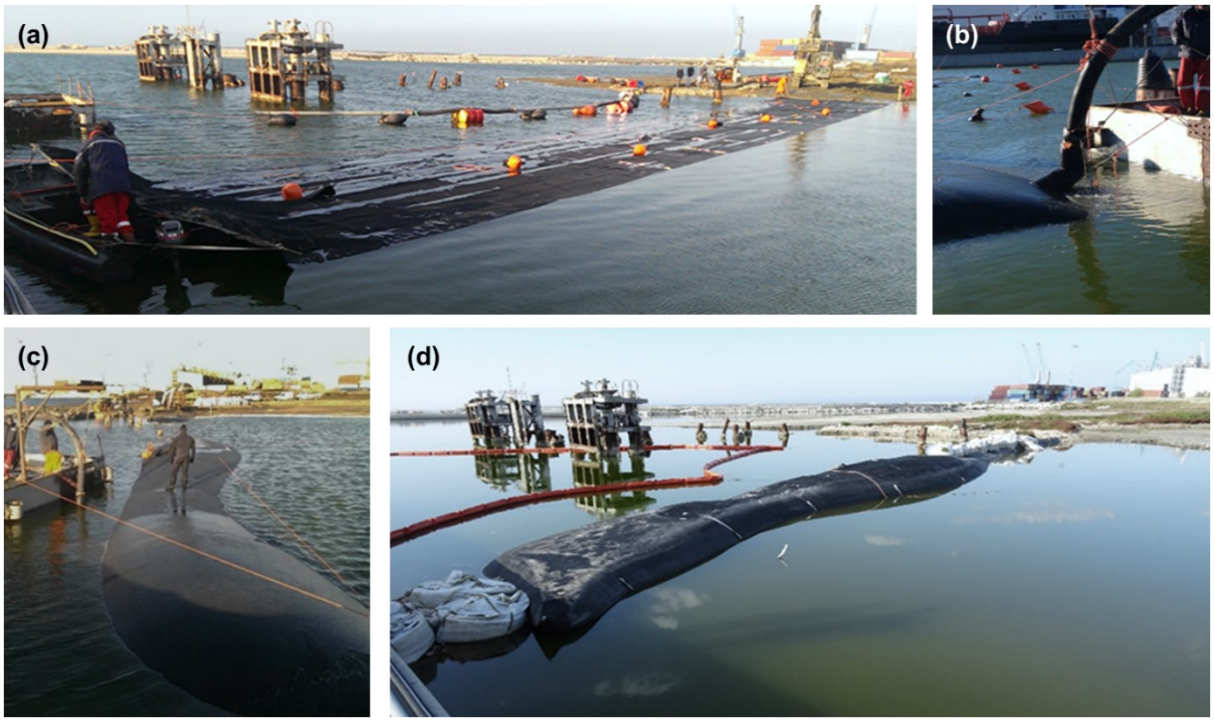

Figure 4.11. Installation of the geotube at the Ancona CDF: (a) placement of the geotube bag; (b) and (c) filling phases of the geotube; (d) completed installation.

4.4.2 Filling

The filling material for this sector came from dredging activities in the Fano Harbour and in two different areas of the Ancona Harbour ("Isa Palumbo" and "Fincantieri"). Disposal of all the sediments were carried out by sea, by means of a mechanic grab operating from a crane equipped pontoon (Figure 4.12b). The maximum crane boom extension was not sufficient to cover the whole area, but an all-terrain crawler machine proved helpful for handling and distributing the sediments inside the sector (Figure 4.12c). At the end of these operations, sediments emerged of about 1 m from the water level inside the CDF.

Right after disposal sediments exhibited a slurry consistency, which precluded transit of vehicles and workers. Therefore, a waiting period was required for self-weight sedimentation and desiccation of the sediment layer above water. Taking advantage of favourable weather conditions (summer period), after a few weeks a surficial crust formed by evaporation, of a thickness of about 30 cm (Figure 4.12d), which had sufficient bearing capacity to allow light vehicles to operate safely.

Figure 4.12. Filling of the test field sector: (a) start-up phase; (b) filling operations from the sea-side of the CDF; (c) spreading of the disposed sediments; (d) surficial crust formed after water evaporation.

4.4.3 Top layer

A layer of coarse material was spread above the dried sediments, with a dual purpose: it served as base layer to allow the transit of vehicles to install PVDs, equipment for the test field and the moving embankment; moreover, it acted as the top drainage blanket for the vertical drains. It consisted of heterogeneous material, with grain size in the range 1÷120 mm, and average thickness of about 70 cm. Only in the test field area this layer consisted of finer grains (1÷30 mm) to ensure, alongside the draining function, also an easier installation of the monitoring instruments (§ 5.4.2), as shown in Figure 4.13.

Prior to laying the top layer (i.e. the base layer for the embankment), all organic residues (mainly lumber) were removed, as their deterioration could have caused differential settlements.

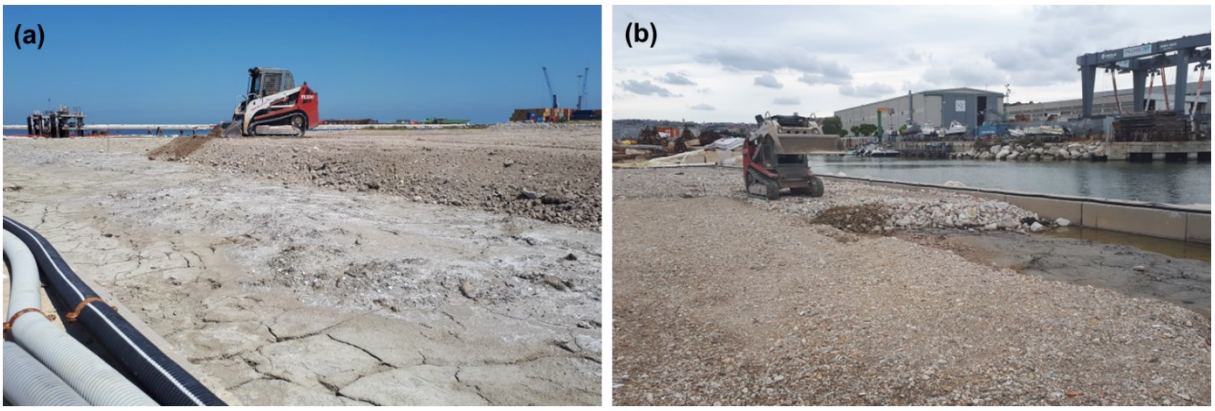

Figure 4.13. Construction of the top drainage layer.

5 FULL SCALE TEST FIELD

This chapter presents the phases in which the test field was articulated, with special focus on the experimental activities preceding and following the moving embankment construction, whose results provided the basis for design. An advanced consolidation theory was applied to model PVDs-assisted consolidation. Simplified charts are proposed to expedite the design decision-making process.

5.1 Introduction

The test field was set over a squared area of 30 m × 30 m in the first filled sector of the CDF, at a safe distance from the borders and from the concrete perimeter curb (Figure 5.1). Such dimensions were chosen to obtain virtually oedometer boundary conditions in the compressible layer under the central part of the area, thus enabling the use of one-dimensional consolidation theories for design and modelling. The reference design section is depicted in Figure 5.2.

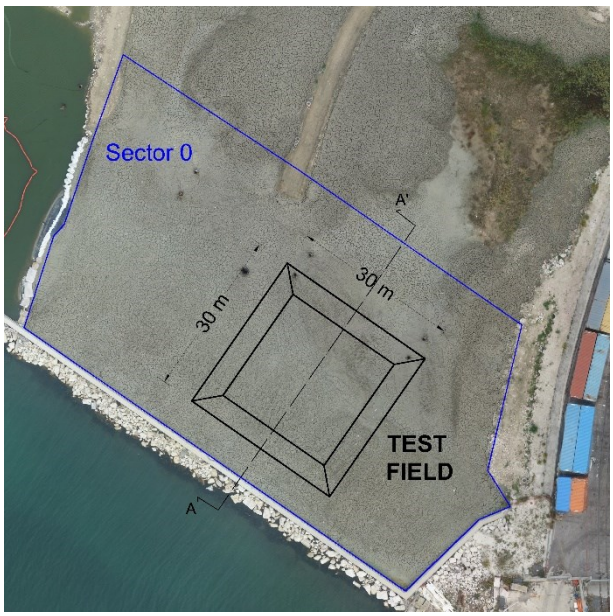

Figure 5.1. Field test dimensions and locations.

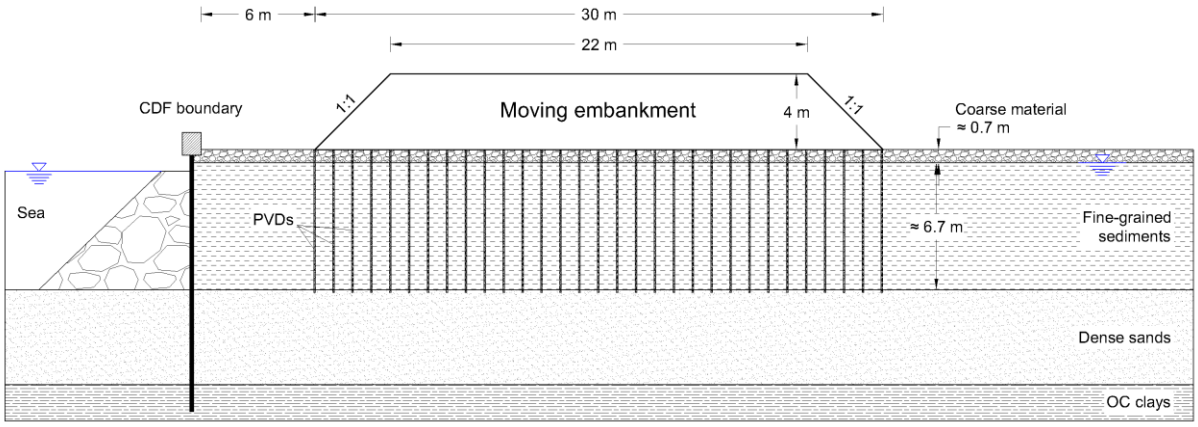

Figure 5.2. Design section of the test field.

Activities related to the test field were divided into four phases. In the early phase, an intensive laboratory testing program and subsurface investigations were carried out, to provide detailed information on drainage conditions and engineering properties of the compressible sediment layer. Since such activities concerned the deposit state prior to the consolidation treatment, it is here referred to as "*ante operam characterisation*".

Based on the findings of the first phase, the design of the test field was finalised, comprising the prediction of total anticipated settlements and rate of primary consolidation with and without drains at several spacings, to be compared with tolerable amount of post-construction settlement and project time requirements. In this phase, a rough evaluation on stability was also performed, to establish safe heights of the moving embankment and the possible need for staged construction.

The third phase consisted in the test field set up, i.e., installation of PVDs and monitoring tools and construction of the embankment.

In the last phase the embankment was removed and in situ tests were performed to verify and quantify the efficiency of the consolidation treatment. Undisturbed samples were also collected to complement the characterisation by laboratory tests. This last testing phase is referred to as "*post operam characterisation*".

5.2 Phase 1: *ante operam* characterisation

5.2.1 Preliminary characterisation by laboratory testing

As previously detailed (§ 4.4.2), three different lots of dredged sediments (named Fano, Isa Palumbo and Fincantieri) were used to fill the sector of the test field. For convenience' sake, hereinafter sediments will be named with an acronym according to their provenance (FAN = Fano sediments; FIN = Fincantieri sediments; ISA = Isa Palumbo sediments).

The slurry consistency of the sediments soon after dredging or disposal made impractical the recovery of undisturbed samples. Therefore, laboratory testing could only occur on samples taken directly from the dredger hold or collected inside the sector right after disposal and re-constituted in the laboratory.

Remoulded samples of the sediments were taken from each lot, both before and after disposal for laboratory testing. Before testing, sediments belonging to the same source were thoroughly mixed in the laboratory by a grout mixer drill, in order to get homogeneous samples, then they were stored in sealed barrels in a cold room at 5°C to prevent water evaporation. Since the samples were taken from a marine environment, the presence of salts in the pore fluid could not be ignored. The presence of salts may affect the physical characteristics and index properties of the sediments, therefore seawater collected into the CDF was used in the tests to avoid variation in soluble salts concentration. The salt concentration, determined by measuring the weight of the salt crystals by drying the unit volume of seawater, was 40 g/L. All the parameters determined by oven-drying procedures were corrected for the presence of salt crystals.

Classification tests were performed, and their main physical characteristics were determined. The compressibility and hydraulic conductivity of the sediments as function of the stress level and initial void ratio were then investigated for modelling consolidation process by one-dimensional compression tests and hydraulic conductivity tests on remoulded specimens. Most of the results are outlined in the doctoral thesis by Felici (2017); they are summarised and briefly discussed in the following together with those obtained in the present research.

5.2.1.1 Classification tests and index properties

Grain-size distributions of the three homogenised sediment batches were determined by combining wet sieving and hydrometer analyses. For hydrometer tests, the amount of particles with diameter greater than 2 mm (retained on the No. 10 sieve) was very little and consisted almost entirely of shell fragments, removed by hand.

Atterberg's limits were determined on the sediments as such (not oven-dried before testing), to avoid degradation of organic matter which could significantly affect the consistency limits.

Table 5.1 summarises classification and the main physical properties of the three batches of sediments disposed in the first sector of the CDF. For each property, the results are provided in terms of range of values (minimum and maximum values obtained from at least four determinations).

Sediments FAN and FIN resulted very similar with regard to the grain size distribution; both consisted of fine fraction (<75 μm) for at least 90%, with silt being the major component and clay (<2 μm) about one third of the total, with a minimal percentage of organic matter. At sampling, both sediments exhibited a consistency from fluid to very fluid, as attested by the

values of consistency index, because of the high water contents (w = 90÷140%). According to the Unified Soil Classification System (USCS) they were identified as silts and silty clays of medium plasticity.

In contrast, sediments ISA mainly consists of coarse fraction (more than 60%), with a low clay content and devoid of organic fraction; according to the USCS, it resulted a silty sand. The water content of the homogenised sample resulted equal to 45%. ISA sediments represent less than 15% of the total volume disposed into the first sector of the CDF.

Table 5.1. Classification and physical characterisation of the sediments disposed into the first sector of the Ancona CDF.

	FAN	**FIN**	**ISA**
Gravel (%)	0÷1	1÷2	8÷15
Sand (%)	0÷3	6÷7	51÷59
Silt (%)	60÷66	55÷57	15÷20
Clay (%)	30÷35	36÷38	5÷11
Liquid limit, w_L (%)	53÷58	44÷50	20÷26
Plasticity index, I_P (%)	25÷28	18÷22	NP
Liquidity index, I_L (%)	2.3	3.3	-
Activity, A (-)	0.82	0.54	-
Organic content, O (%)	6	4	0
USCS	MH	ML-CL	SM
Specific gravity, G_s* (-)	2.72	2.67	2.61

5.2.1.2 One-dimensional consolidation tests

The compressibility of the marine dredged sediments disposed in the first sector was studied through a series of oedometer tests for each sediment batch. For the reasons already stated, remoulded specimens were tested, and seawater was used as test fluid. The vertical pressure applied during the tests ranged from 6.25 kPa to 400 kPa, the ratio between increments being constant. The samples were reconstituted at initial void ratios in the range of those of the sediments in the sector (assuming the relevant value of the specific gravity, § 5.2.1.1).

Three oedometer tests were carried out on the sediments FAN. The resulting compressibility curves are shown in Figure 5.3. For the sediments FIN, six oedometer tests were performed starting from samples prepared in a wide range of initial void ratios (initial water contents up to 145%). The resulting compressibility curves are illustrated in Figure 5.4. The compressibility of the sediments ISA (Figure 5.5) was investigated by three reconstituted specimens, whose initial values of void ratio and water content were lower.

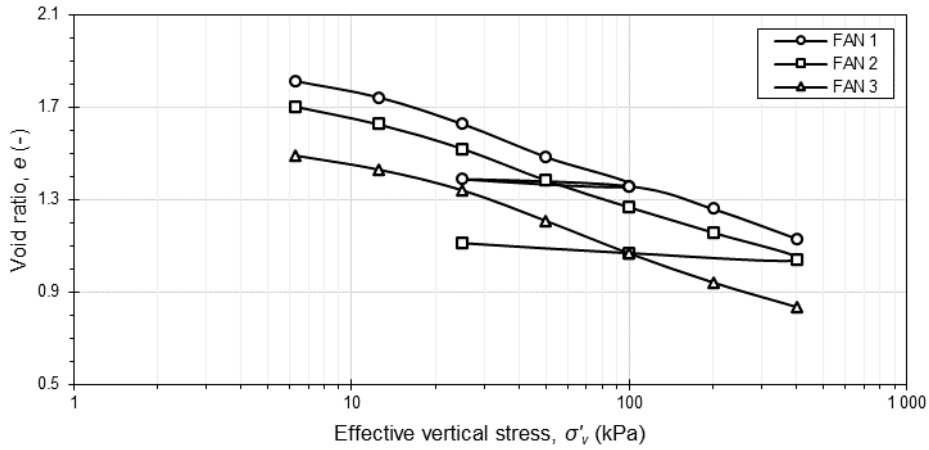

Figure 5.3. Compression curves obtained by IL oedometer tests on the sediments FAN.

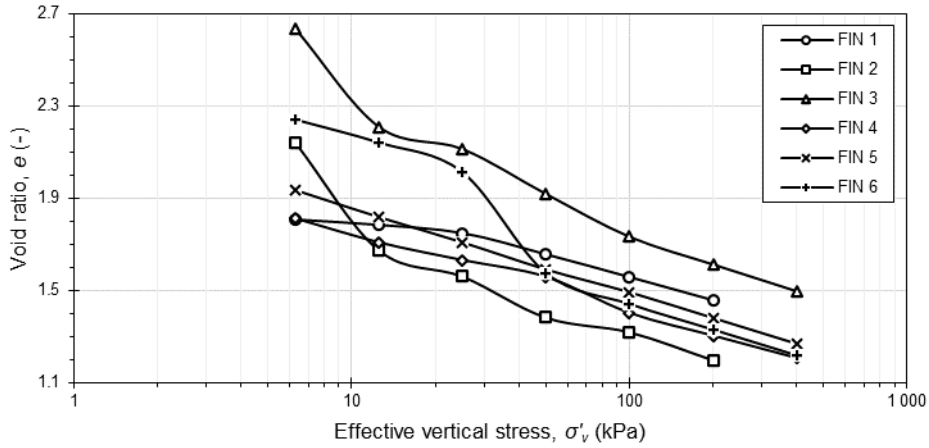

Figure 5.4. Compression curves obtained by IL oedometer tests on the sediments FIN.

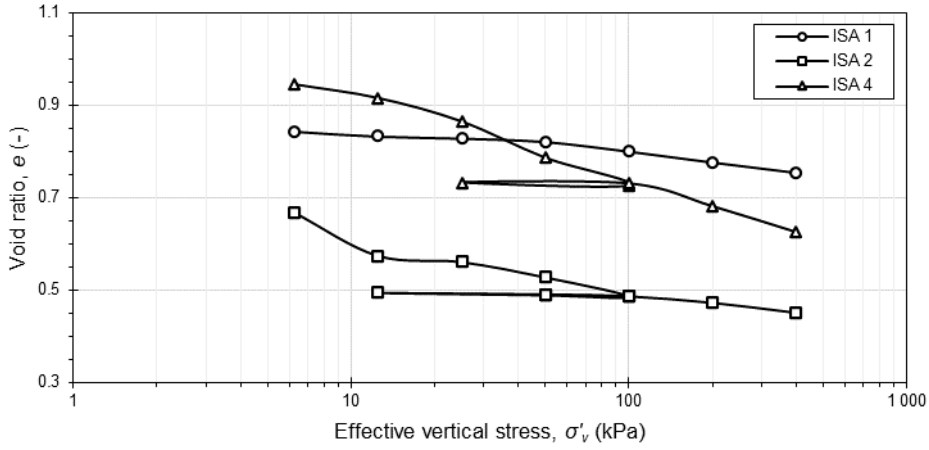

Figure 5.5. Compression curves obtained by IL oedometer tests on the sediments ISA.

Table 5.2, Table 5.3 and Table 5.4 show the compressibility parameters for sediments FAN, FIN and ISA, respectively, obtained by averaging the results of all the tests for each loading step.

Table 5.2. Average parameters from IL oedometer tests on the sediments FAN.

Effective vertical stress, σ'_v	Constrained modulus, M	Void ratio, e	Compression index, c_c	Coefficient of vertical consolidation, c_v	Vertical hydraulic conductivity, k_v
(kPa)	(MPa)	(-)	(-)	(cm^2/s)	(m/s)
6.25	0.06	1.67	0.48	1.2×10^{-4}	3.2×10^{-9}
12.5	0.20	1.60	0.23	1.7×10^{-4}	1.0×10^{-9}
25	0.26	1.50	0.34	1.6×10^{-4}	6.9×10^{-10}
50	0.40	1.36	0.46	1.8×10^{-4}	5.5×10^{-10}
100	0.87	1.23	0.43	2.3×10^{-4}	3.2×10^{-10}
200	2.07	1.12	0.37	2.4×10^{-4}	1.4×10^{-10}
400	3.64	1.00	0.39	2.2×10^{-4}	6.8×10^{-11}

Table 5.3. Average parameters from IL oedometer tests on the sediments FIN.

Effective vertical stress, σ'_v	Constrained modulus, M	Void ratio, e	Compression index, c_c	Coefficient of vertical consolidation, c_v	Vertical hydraulic conductivity, k_v
(kPa)	(MPa)	(-)	(-)	(cm^2/s)	(m/s)
6.25	0.08	2.08	0.73	3.2×10^{-4}	5.3×10^{-9}
12.5	0.22	1.89	0.68	2.4×10^{-4}	3.1×10^{-9}
25	0.58	1.81	0.29	4.4×10^{-4}	1.0×10^{-9}
50	0.68	1.64	0.57	3.1×10^{-4}	5.1×10^{-10}
100	1.62	1.52	0.44	3.9×10^{-4}	2.9×10^{-10}
200	3.13	1.40	0.37	3.9×10^{-4}	1.3×10^{-10}
400	6.73	1.32	0.37	4.2×10^{-4}	6.7×10^{-11}

Table 5.4. Average parameters from IL oedometer tests on the sediments ISA.

Effective vertical stress, σ'_v	Constrained modulus, M	Void ratio, e	Compression index, c_c	Coefficient of vertical consolidation, c_v	Vertical hydraulic conductivity, k_v
(kPa)	(MPa)	(-)	(-)	(cm^2/s)	(m/s)
6.25	0.07	0.82	0.24	3.1×10^{-4}	4.4×10^{-9}
12.5	0.59	0.77	0.15	2.1×10^{-4}	4.8×10^{-10}
25	1.11	0.71	0.11	1.8×10^{-3}	5.8×10^{-10}
50	3.06	0.71	0.13	9.6×10^{-4}	3.3×10^{-10}
100	2.99	0.67	0.14	1.4×10^{-3}	3.8×10^{-10}
200	8.80	0.64	0.10	1.5×10^{-3}	2.0×10^{-10}
400	14.35	0.61	0.11	1.8×10^{-3}	1.3×10^{-10}

From the tabulated values it can be observed that compression indexes for the sediments FAN and FIN resulted averagely high, especially for stress levels up to 50 kPa. In particular, in the case of sediments FIN, the values of c_c are greater than 0.5, on average, which entails the development of large settlements due to primary consolidation. In contrast, the values of c_c obtained for the sediments ISA resulted significantly lower (in the range 0.11÷0.24), and this is hardly surprising, given their prominent coarse-grained nature. The larger compressibility of the silty and clayey sediments is also evidenced by the very low values of the constrained modulus, M, especially for low stress levels.

With reference to the coefficient of vertical consolidation, c_v, the average values obtained for the sediments FAN and FIN are always on the order of 10^{-4} cm^2/s, as it is typical for fine-grained soils, to which correspond quite long consolidation times. In particular, for effective stresses lower than 100 kPa (i.e. in the range comprising the service load and the preloading stress level of the test field embankment, see next § 5.3), the coefficient of vertical consolidation resulted in the range $1\div3\times10^{-4}$ cm^2/s and $2\div5\times10^{-4}$ cm^2/s for FAN and FIN, respectively. In the same stress range, the sediment ISA presented a higher average c_v value and a larger variability.

Starting from the definition of c_v based on the one-dimensional consolidation theory (Eq. (2.2)), the values of the vertical hydraulic conductivity, k_v, were also calculated for each loading step. For stress levels up to 100 kPa, the k_v values obtained are always quite low, of the order of $10^{-7}\div10^{-8}$ cm/s, decreasing with increasing effective vertical stress, that is with decreasing void ratio, as shown in Figure 5.6. From the graph it can be observed that the trends of k_v as a function of e for the fine-grained sediments are very similar, whereas for the coarser sediments ISA the values of k_v for the same void ratios are on one order of magnitude higher, but still in the range of values for low-permeable soils, to reflect the fact that the fine fraction, although in percentage between 20% and 30%, significantly affects the hydraulic behaviour of the sediments.

While the inference of vertical hydraulic conductivity from the results of oedometer tests is fairly common in the literature, it is widely recognised that this indirect approach can lead to values very different with respect to the actual ones, mainly because of the hypothesis of linear elastic behaviour of the soil. Hence, it is usually recommended to directly measure the values of the hydraulic conductivity. However, from the comparison of the hydraulic domain determined from oedometer test results on the dredged sediments in the Ancona CDF and the $k(e)$ constitutive law obtained on the same sediments from direct measurements in consolidometer, Felici et al. (2019) showed that when the void ratio is no greater than 1.8 (as in the case of concern), oedometer test results agree well, or at most underestimates, the hydraulic conductivity, leading to a cautionary overestimation of consolidation times.

By virtue of these findings, in the present research new oedometer test data from sediments FAN and FIN have been integrated, in order to update and further investigate the

hydraulic conductivity constitutive laws originally presented by Felici (2017). Results of the fitting procedure are shown in Figure 5.6. These relationships are ready-for-use in more sophisticated consolidation models. Further research will be devoted to implement these relationships in the analysis of consolidation by vertical drains, to account for the potential effect of large strains (e.g. Fox & Berles, 1997).

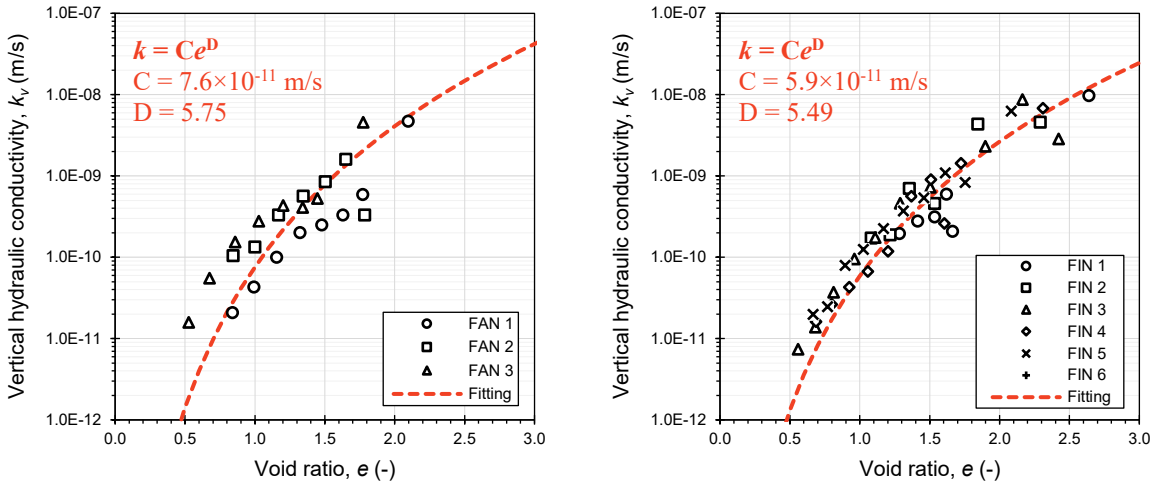

Figure 5.6. Updated hydraulic conductivity constitutive law for sediments FAN (on the left) and FIN (on the right).

5.2.2 Field investigations

The in situ characterisation was aimed at stratigraphic profiling, as well as defining the hydraulic and mechanical properties of the sediment layer. The stratigraphic profile was essential to establish the thickness of the compressible layer and to ascertain its homogeneity (e.g., presence of lenses of sediments with different geotechnical characteristics). Geotechnical parameters such as hydraulic conductivity, consolidation parameters, stiffness and undrained shear strength were essential to design the test field, to interpret the monitoring results and to quantify the efficiency of the soil improvement.

Field investigations before consolidation of the sediments were done by cone penetration tests (CPTs). In particular, 8 mechanical CPTMs and 6 piezocone CPTUs were performed within the embankment footprint area, according to the planimetric layout of Figure 5.7. The more accurate piezocone tests were located in the central portion of the test field, to estimate geotechnical parameters where the consolidation process will not be much affected by boundary effects. Since the stratigraphy of the seabed was known from previous investigations (§ 4.2.1), all cone penetration tests stopped once reached the dense sandy layer underneath, clearly identified by a sharp increase in the cone tip resistance and a fast drop of the pore pressure. Pre-

holes of about 70 cm, filled with sand, were necessary to go across the coarse top layer. Two of the piezocone tests also served as dissipation tests, to assess the horizontal consolidation coefficient of the sediments.

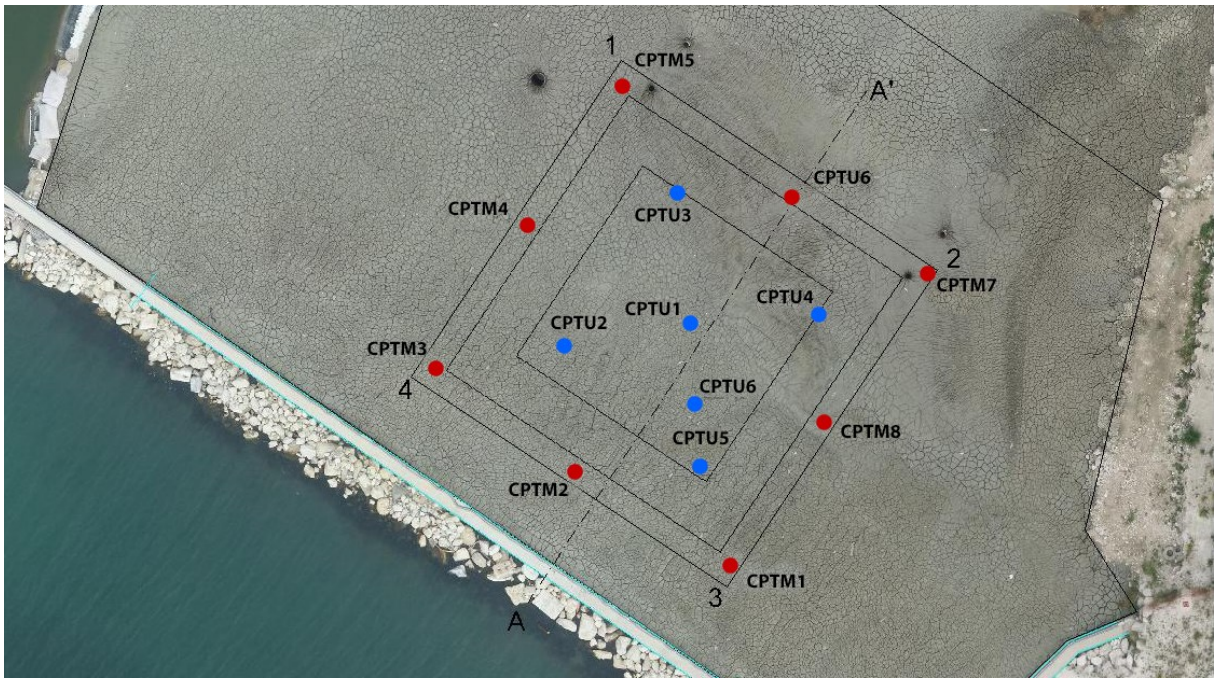

Figure 5.7. Planimetric layout of cone penetration tests.

5.2.2.1 Cone penetration tests

Figure 5.8 to Figure 5.15 show the profiles of cone tip resistance, q_c, sleeve friction, f_s, and friction ratio, R_f, measured by the mechanical cone. These data pointed out the very poor consistency of the sediments, as evidenced by the low values of the cone tip resistance, always below 2 MPa. The dense sandy layer was found at a depth varying between 5.8 and 8.4 m from the ground surface. This meant that the thickness of the sediment layer (i.e. the compressible layer) varied between 5.1 and 7.7 m, considering that the top layer had an average thickness of 70 cm.

Figure 5.16 to Figure 5.21 show the profiles of cone resistance, sleeve friction and pore pressure measured by the piezocone. The same stratigraphy detected by the mechanical cone tests was confirmed by the piezocone tests. In particular, the depth of the sandy layer varied between a minimum of 5.8 m to a maximum of 7.8 m from the ground level, which entailed a thickness of the sediment layer varying between 5.3 and 7.1 m. The u_2 profiles indicated that at certain depths the measured porewater pressure deviates from the hydrostatic trend, usually increasing; the generation of excess pore pressures confirmed the low hydraulic conductivity of those sediments.

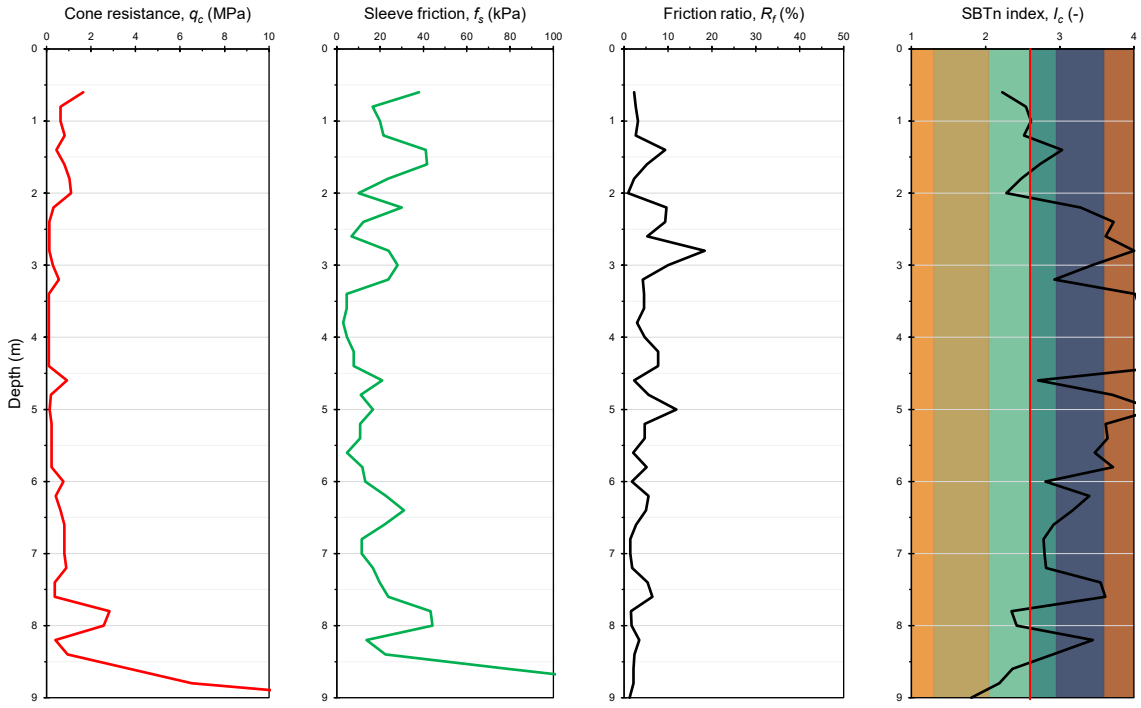

Figure 5.8. CPTM1-ANTE.

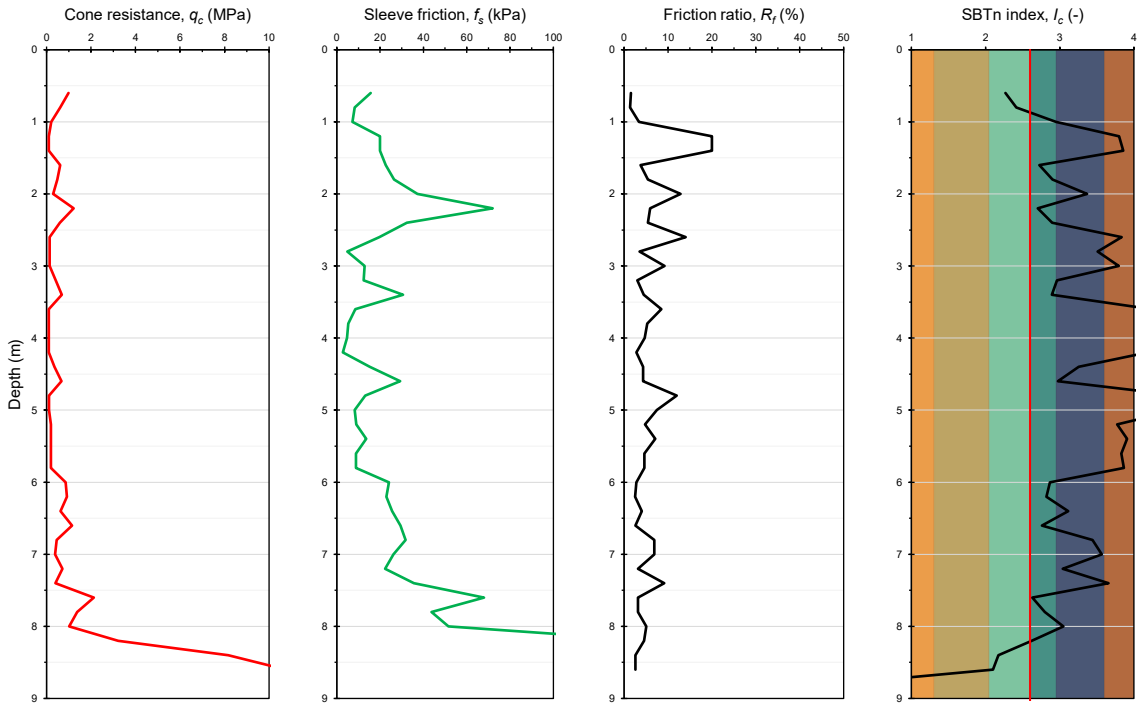

Figure 5.9. CPTM2-ANTE.

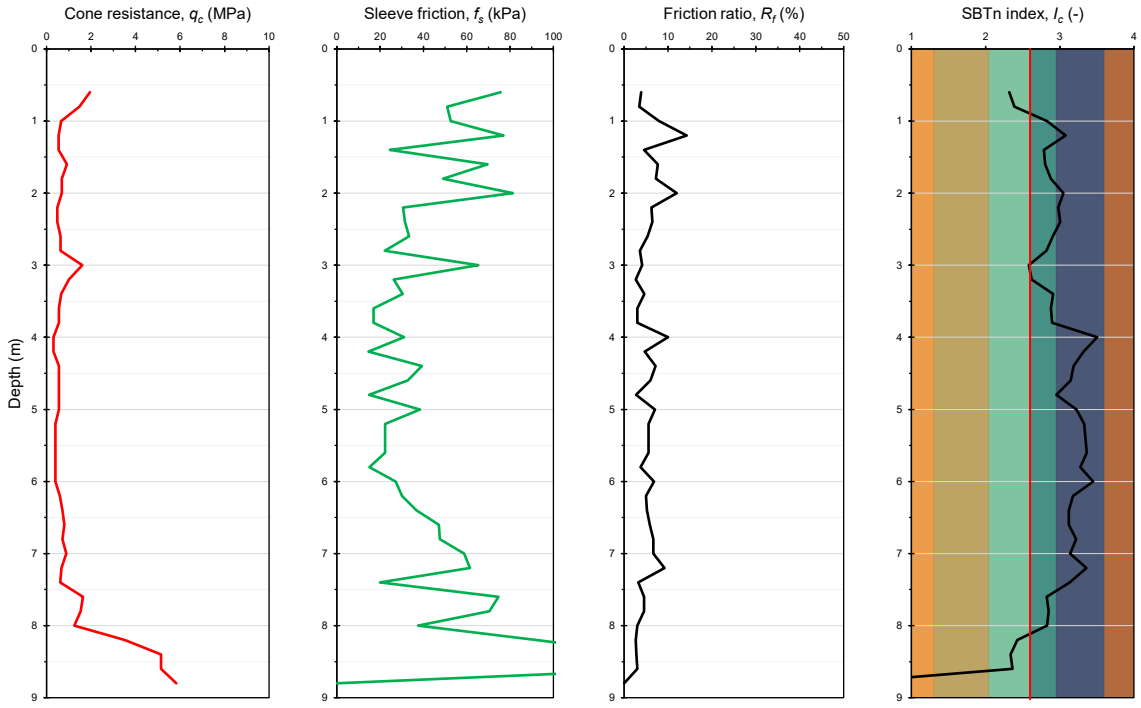

Figure 5.10. CPTM3-ANTE.

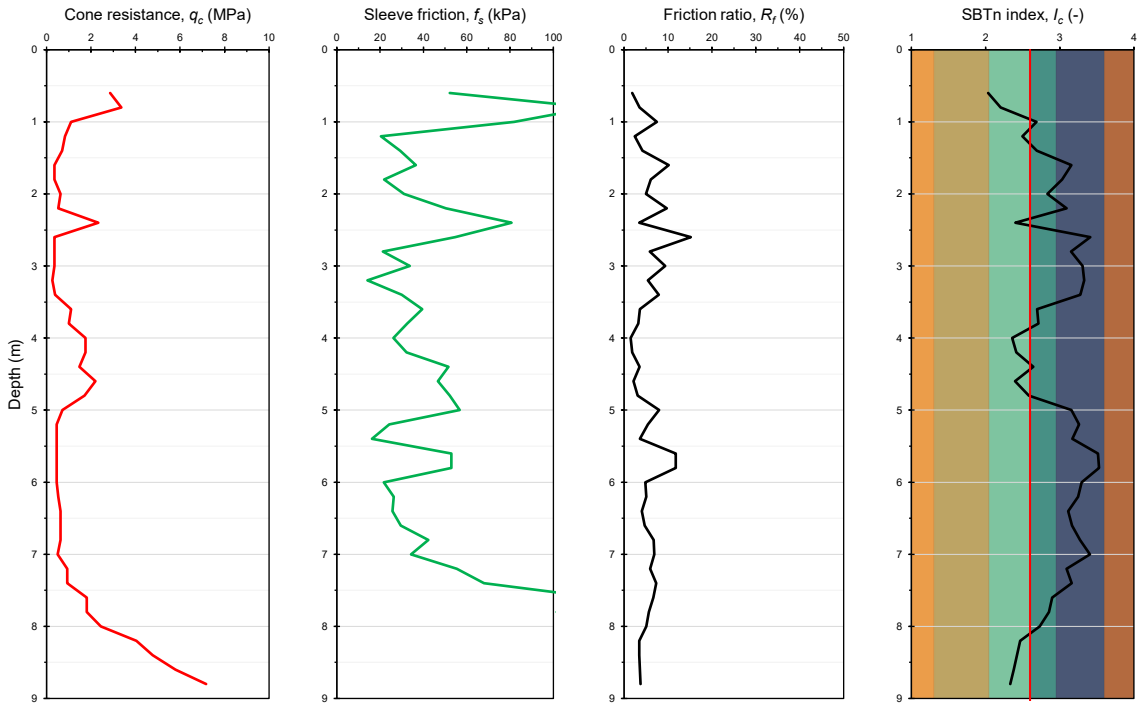

Figure 5.11. CPTM4-ANTE.

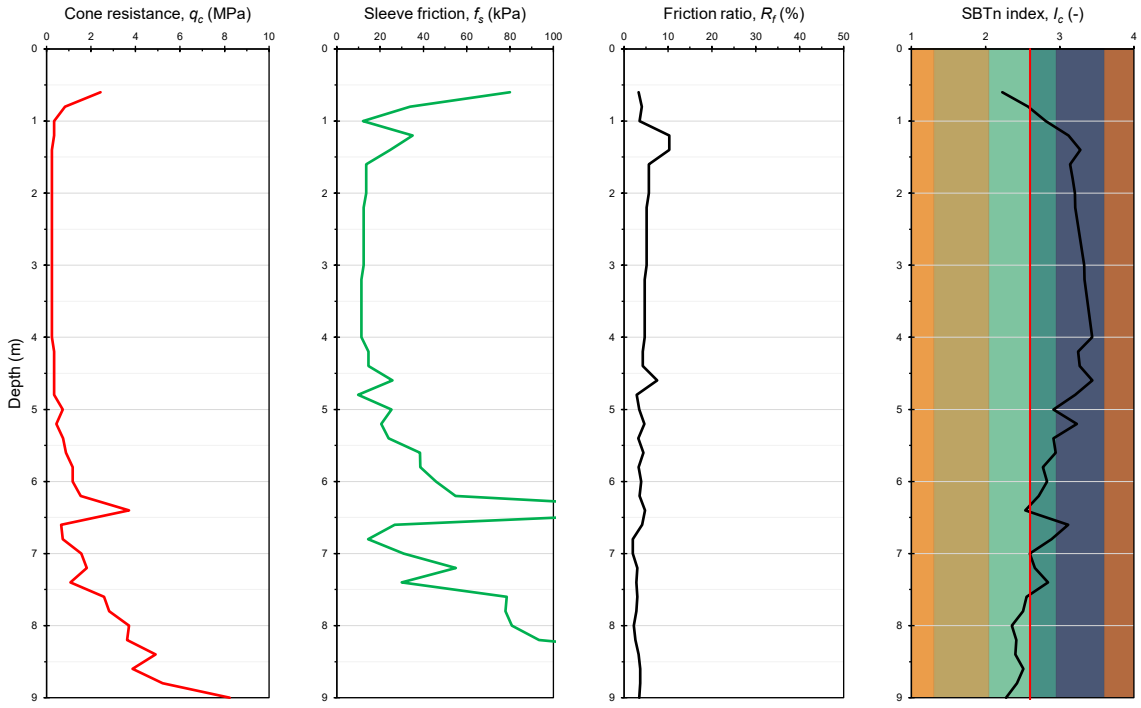

Figure 5.12. CPTM5-ANTE.

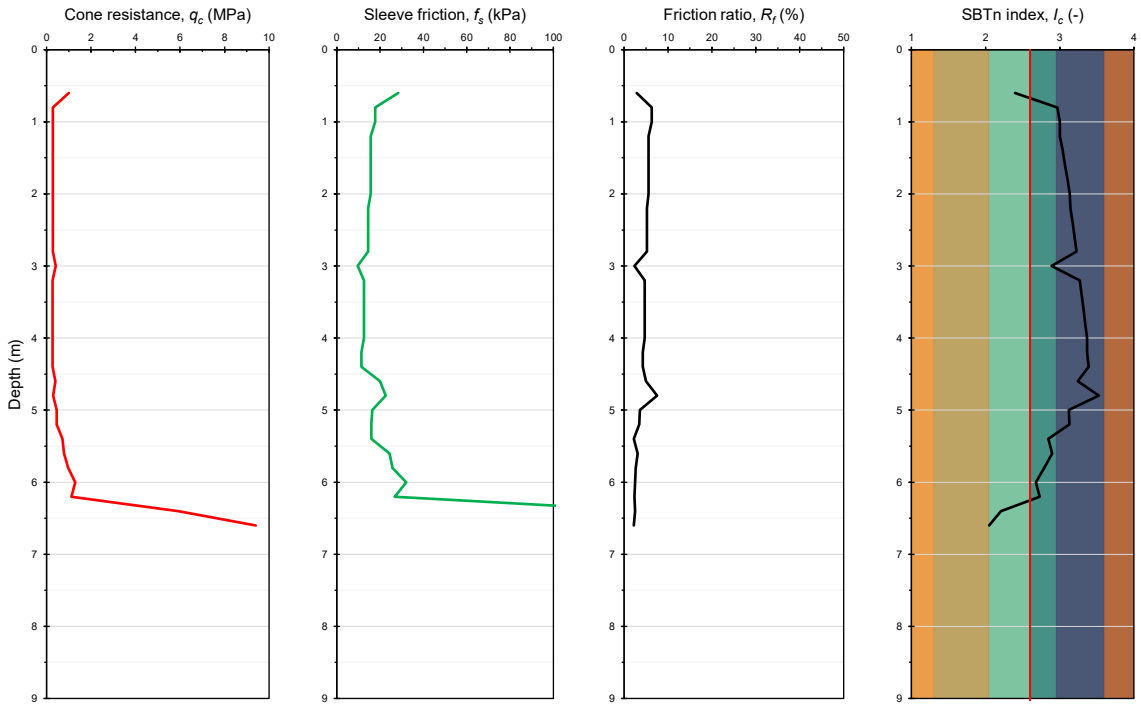

Figure 5.13. CPTM6-ANTE.

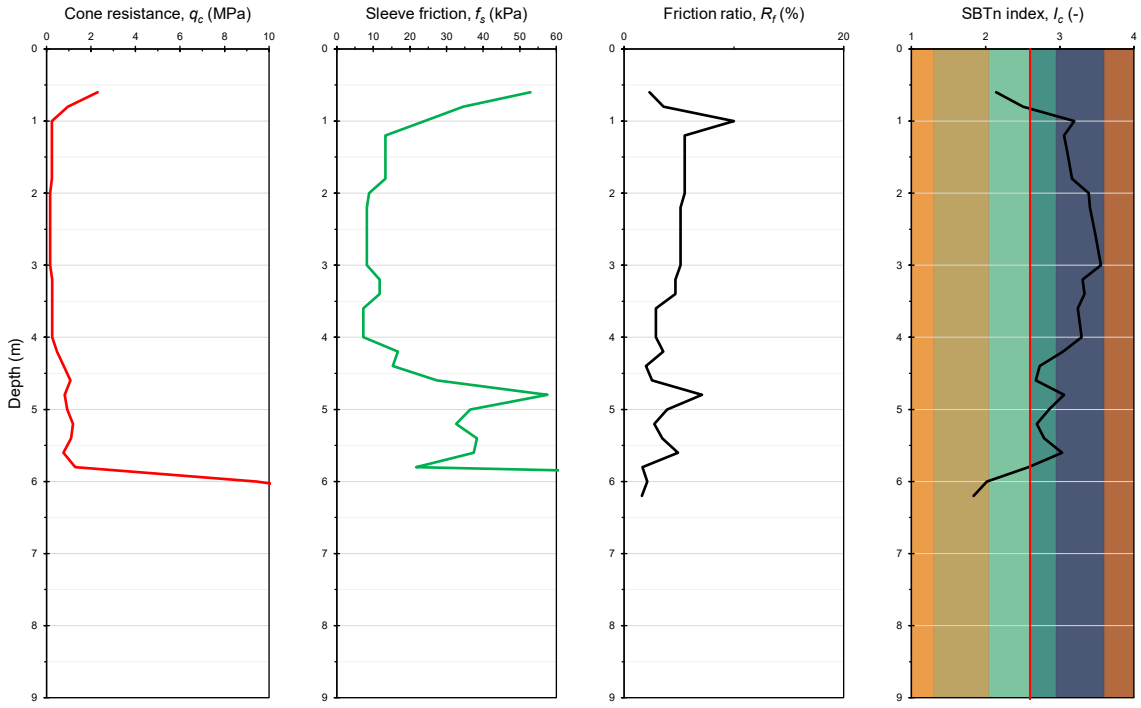

Figure 5.14. CPTM7-ANTE.

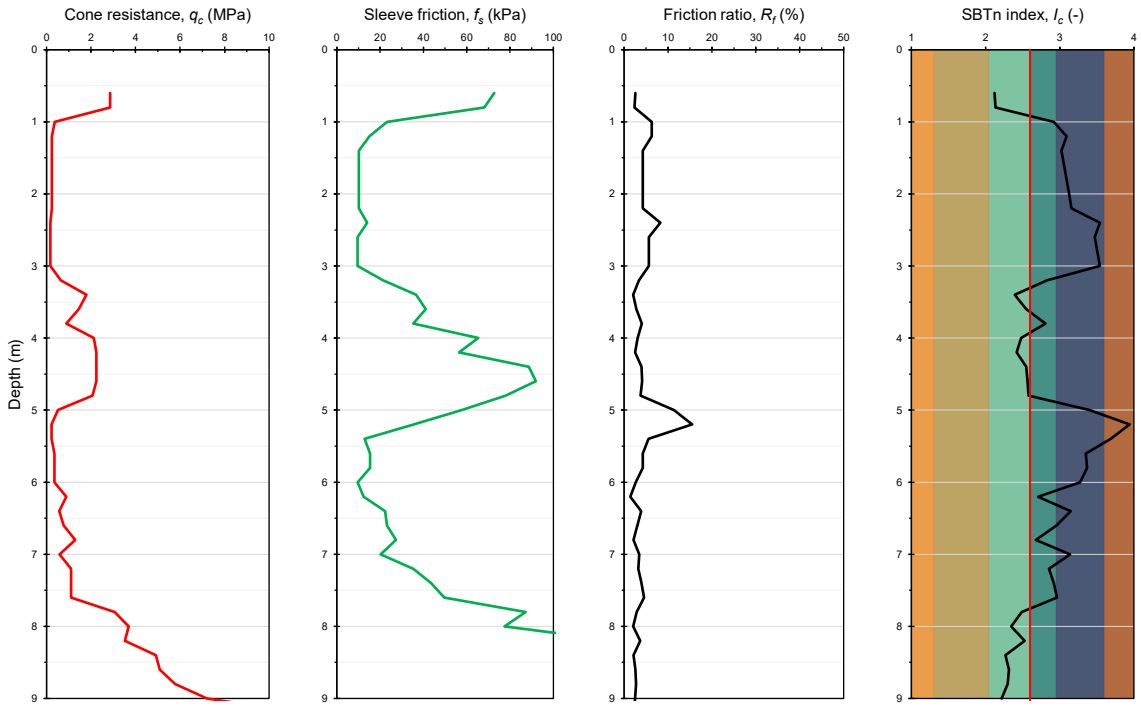

Figure 5.15. CPTM8-ANTE.

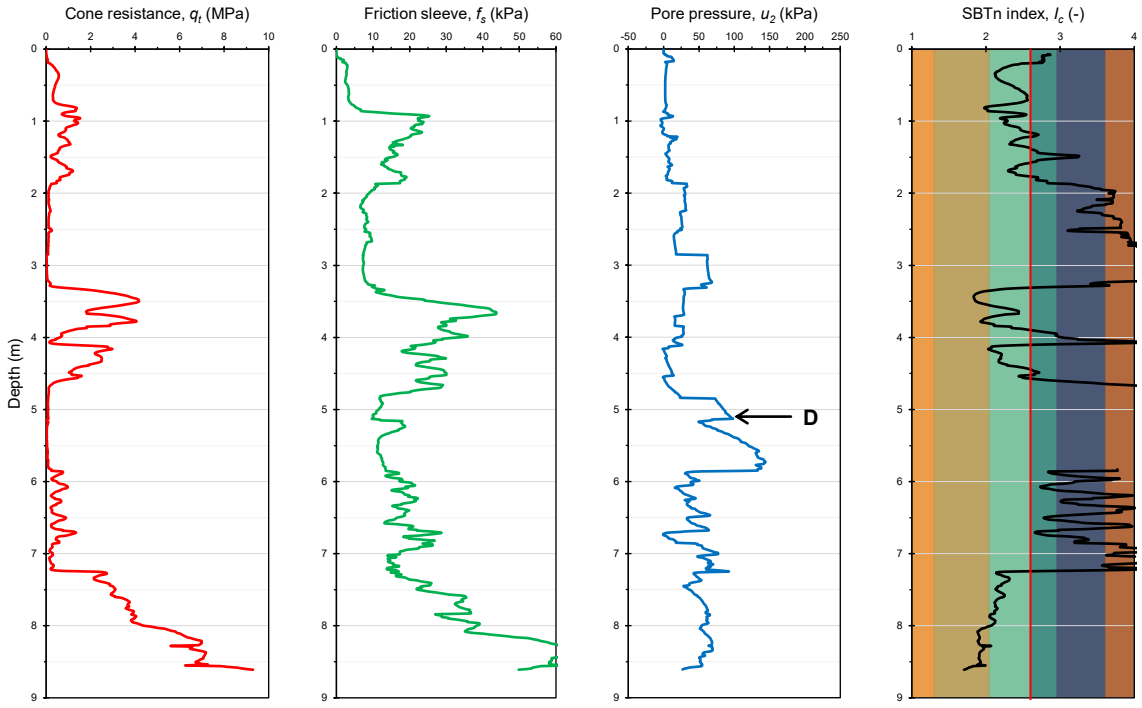

Figure 5.16. CPTU1-ANTE.

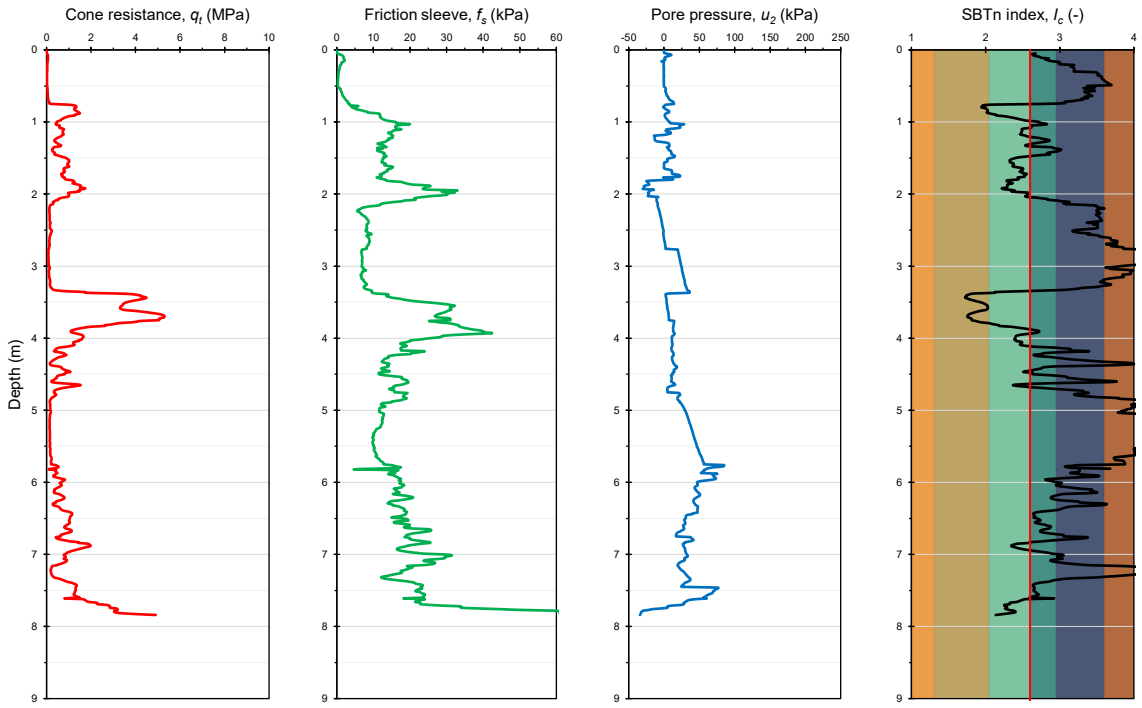

Figure 5.17. CPTU2-ANTE.

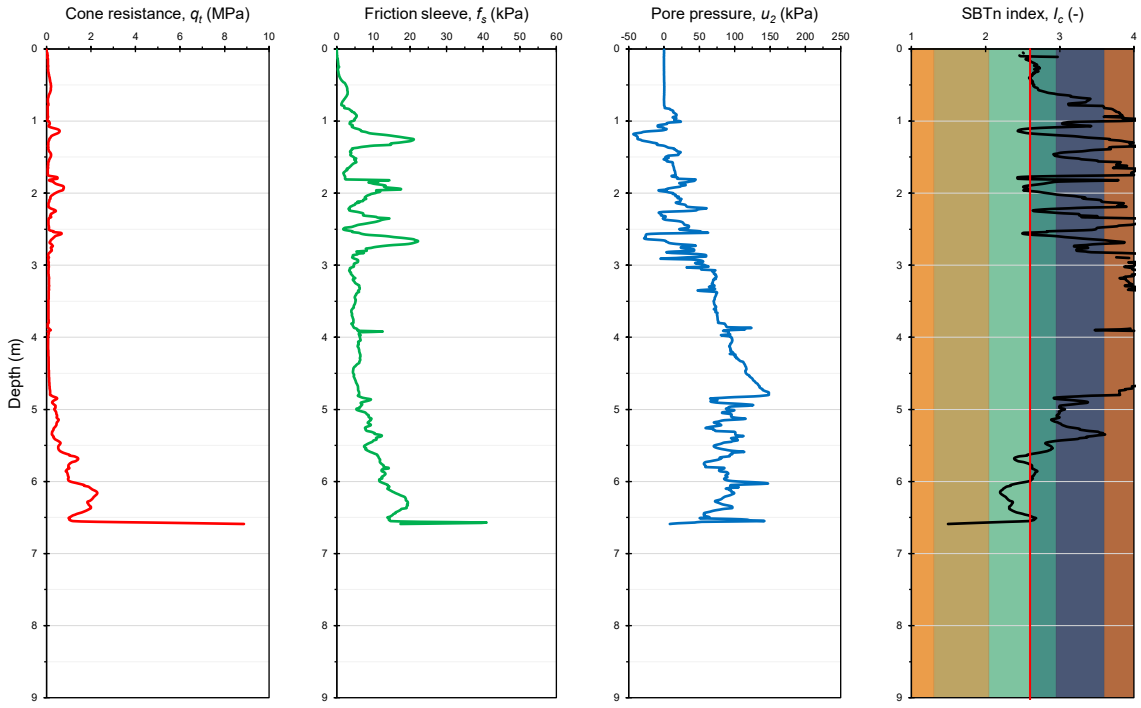

Figure 5.18. CPTU3-ANTE.

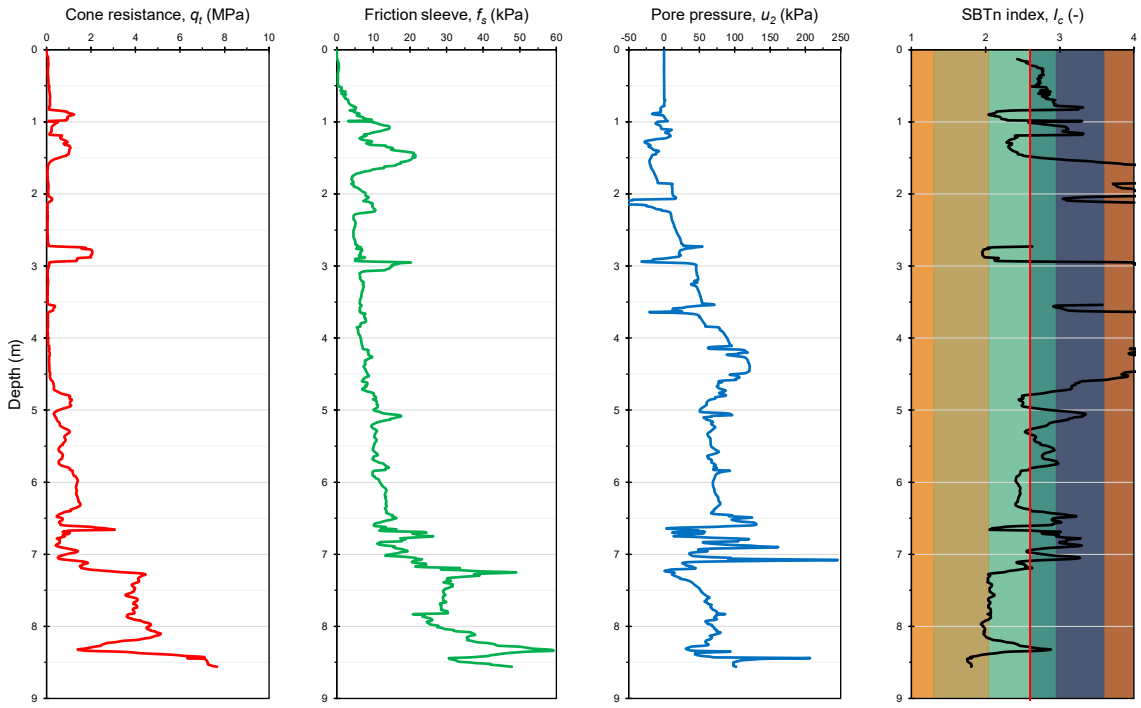

Figure 5.19. CPTU4-ANTE.

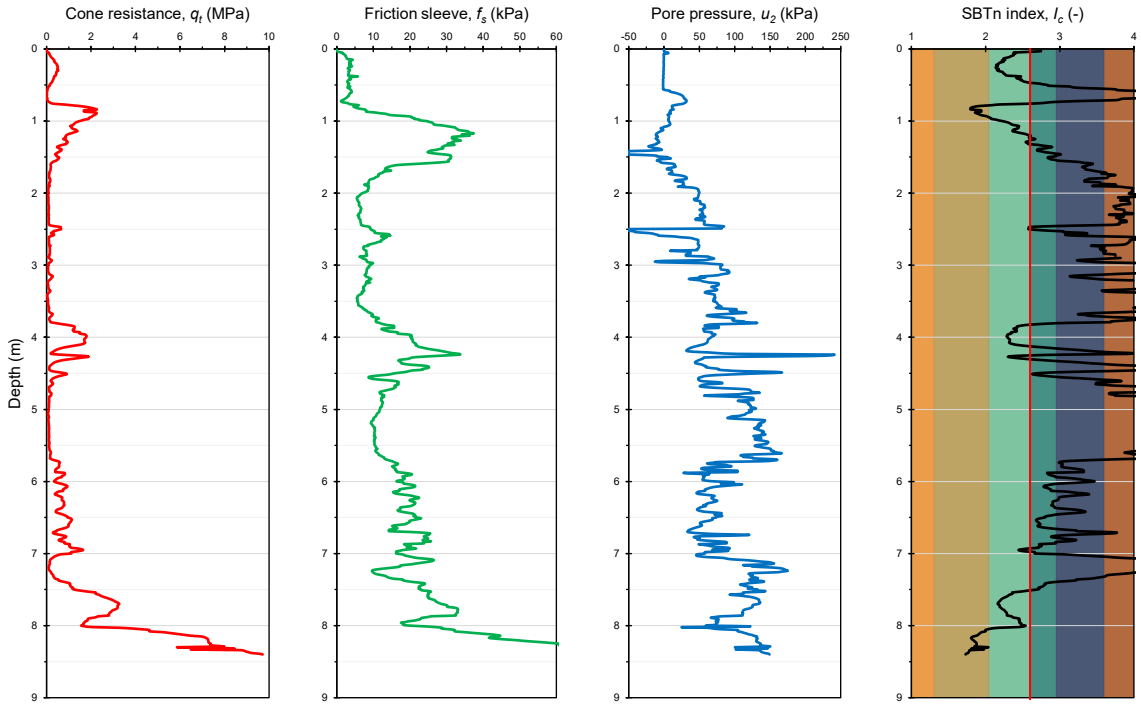

Figure 5.20. CPTU5-ANTE.

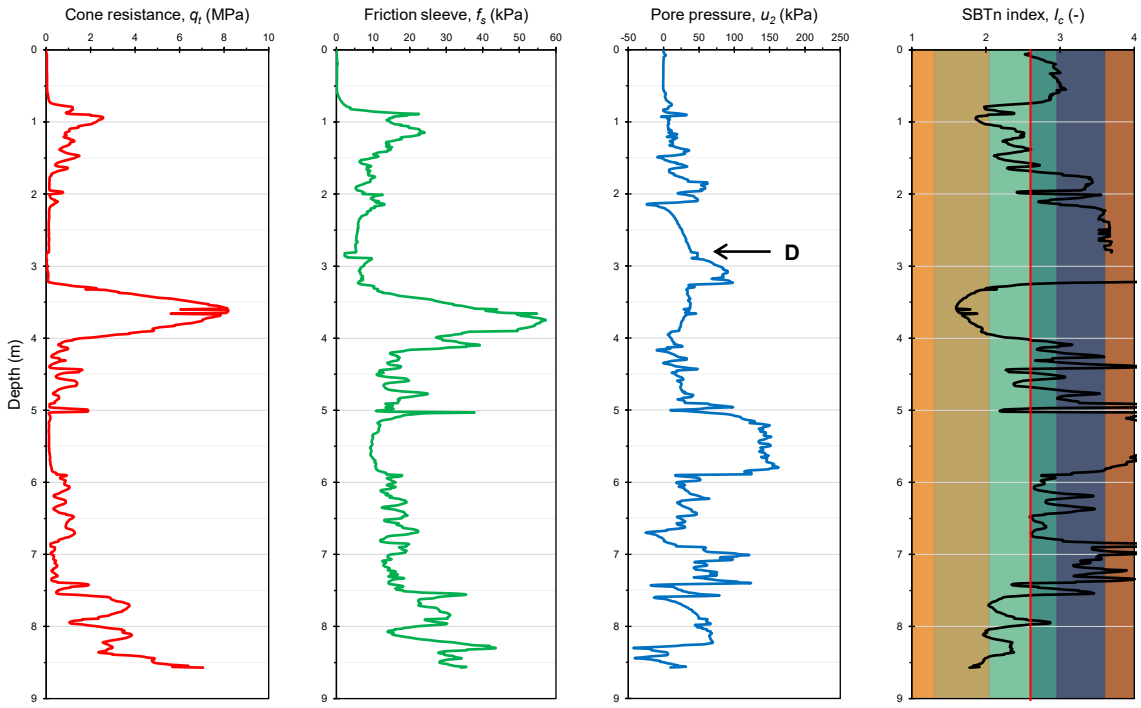

Figure 5.21. CPTU6-ANTE.

Stratigraphic profiling was performed by the unified interpretation approach proposed by Robertson (2009), which is based on a normalised soil behaviour type index (SBTn), as detailed in § 3.2.1.1.2. To apply normalisation of data, it was necessary to input some parameters about soil unit weights and groundwater conditions. The sediments layer was assigned a unit volume weight, γ_{sed}, equal to 16.9 kN/m^3, based on the average results of laboratory tests. For the granular loose mixture forming the top drainage layer, a slightly higher unit volume weight, γ_{top} = 17.0 kN/m^3, was assumed, for a thickness of 70 cm over the whole area of the test field. The water table was set at the interface between the top layer and the sediments, like the water level observed inside the CDF. Salt water was assumed to saturate pores in the sediments, with a unit volume weight, γ_w, equal to 10.1 kN/m^3. The resulting profiles of I_c are shown next to measured profiles in Figure 5.8 to Figure 5.21.

Stratigraphic profiling brought to light the presence of clay-like soils ($I_c > 2.6$, mainly silty mixtures and clays) for almost the entire depth, except for some depths where sand mixtures (silty sands to sandy silts) were identified. The presence of such coarser lenses is clearly due to the non-homogeneity of sediments disposed in the sector. Two of the reconstructed stratigraphic sections are reported in Figure 5.22.

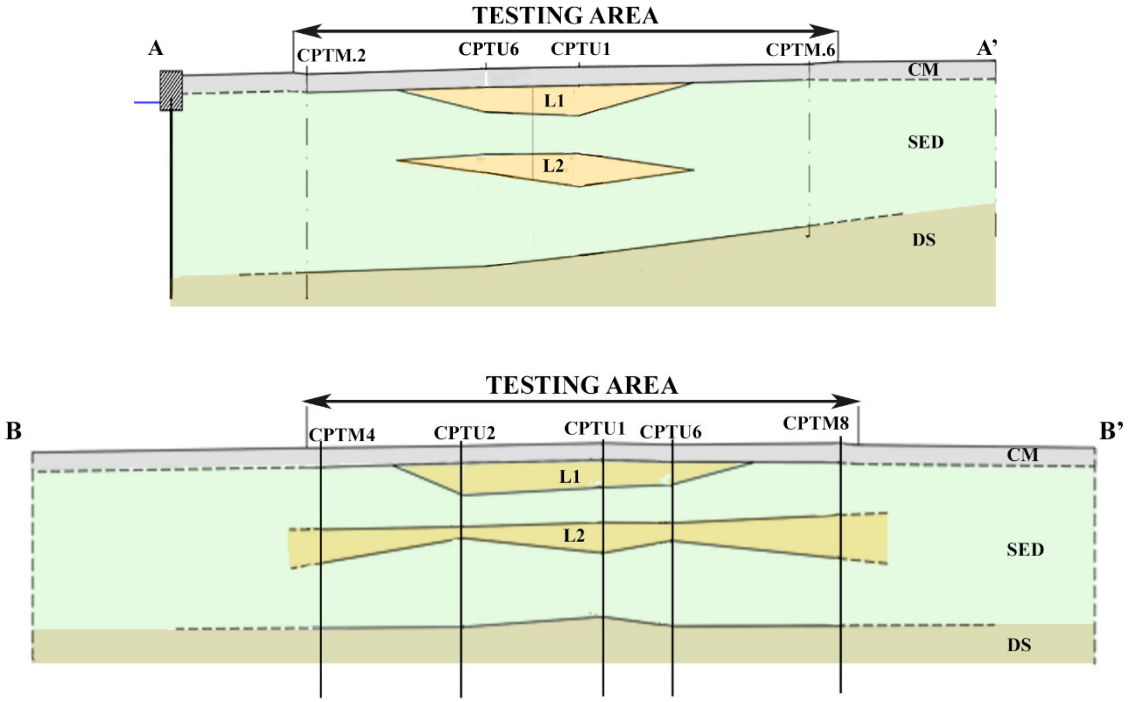

Figure 5.22. Stratigraphic sections: CM = coarse material layer; SED = sediment layer; DS = dense sand layer; L1 and L2 are coarser lenses.

5.2.2.2 Dissipation tests

To estimate the coefficient of consolidation and the hydraulic conductivity of sediments directly *in situ*, two (partial) dissipation tests were performed: one on CPTU1, at a depth of 5.1 m, and the other one on CPTU6, at a depth of 2.8 m, as indicated in Figure 5.16 and Figure 5.21, respectively. Both tests were stopped once at least half dissipation was reached.

The recorded dissipation curves, shown in Figure 5.23, were interpreted by the strain path solution by Houlsby & Teh (1988), Teh & Houlsby (1988, 1991), according to which the coefficient of horizontal consolidation, c_h, can be written as:

$$c_h = \frac{T_h^* r_c^2 \sqrt{I_r}}{t_{50}} \tag{5.1}$$

where T_h^* is a modified dimensionless time factor, r_c is the cone radius, I_R is the undrained rigidity index (i.e. the ratio between the shear modulus and the undrained shear strength of the soil, $I_r = G/s_u$), and t_{50} is the measured time to reach 50% dissipation.

The time t_{50} was inferred directly from the dissipation curves, by identifying the point corresponding to half dissipation, u_{50}:

$$u_{50} = u_0 + 0.5\Delta u \tag{5.2}$$

where the excess pore pressure, Δu, is given by the difference between the pore pressure value recorded when stopping piezocone penetration, $u_{2,in}$, and the hydrostatic pore pressure, u_0, computed by assuming the water level at a depth of 0.7 m from the ground level. For both tests the time t_{50} resulted to be approximately 70÷80 minutes.

The terms r_c and T_h^* in Equation (5.1) depend on the kind of piezocone used: for the standard 10-cm^2 piezocone, r_c = 1.785 cm, and for the u_2 location, T_h^* = 0.245 (at the reference 50% dissipation). The rigidity index was assessed by the empirical correlation of Keaveny & Mitchell (1986), relating I_R to overconsolidation ratio, *OCR*, and plasticity index, I_P, as shown in Figure 5.24. For the sediments *OCR* = 1 and I_P = 20÷30 (cfr. Table 5.1), therefore I_R = 105÷160.

Lastly, the coefficient of horizontal hydraulic conductivity, k_h, was determined from the empirical method provided by Parez & Fauriel (1988), based on the measured t_{50} value:

$$k_h \approx \left(\frac{1}{250 t_{50}}\right)^{1.25} \tag{5.3}$$

where t_{50} is expressed in seconds, and k_h in cm/s, as shown in Figure 5.25.

Table 5.5 lists the resulting c_h and k_h values. As it can be observed, c_h varies in a narrow range ($c_h = 1.4 \div 2.4 \times 10^{-7}$ m^2/s), with values one order of magnitude larger than the c_v values determined in the laboratory for similar stress levels on sediments FIN and FAN ($c_v \approx 1.0 \div 4.0 \times 10^{-8}$ m^2/s, see Table 5.2 and Table 5.3). The coefficient k_h also resulted in a narrow range ($k_h = 2.0 \div 3.0 \times 10^{-10}$ m/s), with values corresponding to, or slightly lower than, those measured in the laboratory on FIN sediments for void ratios lower than 2.5. These results confirmed the low hydraulic conductivity of sediments.

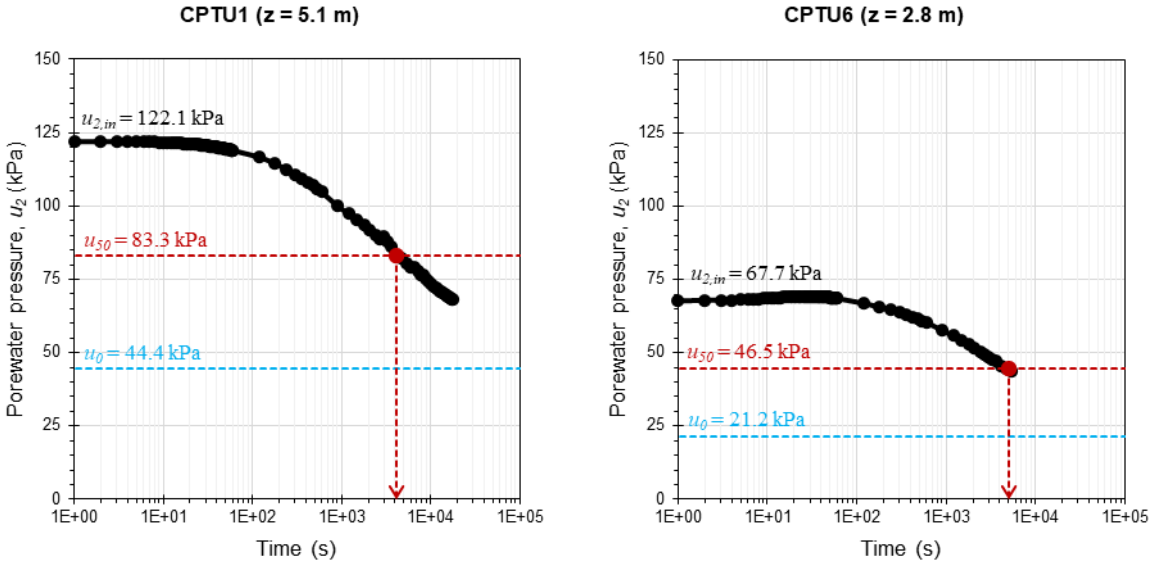

Figure 5.23. Dissipation curves recorded at a depth of 5.1 m during a pause of CPTU1 (on the left) and a depth of 2.1 m on CPTU6 (on the right).

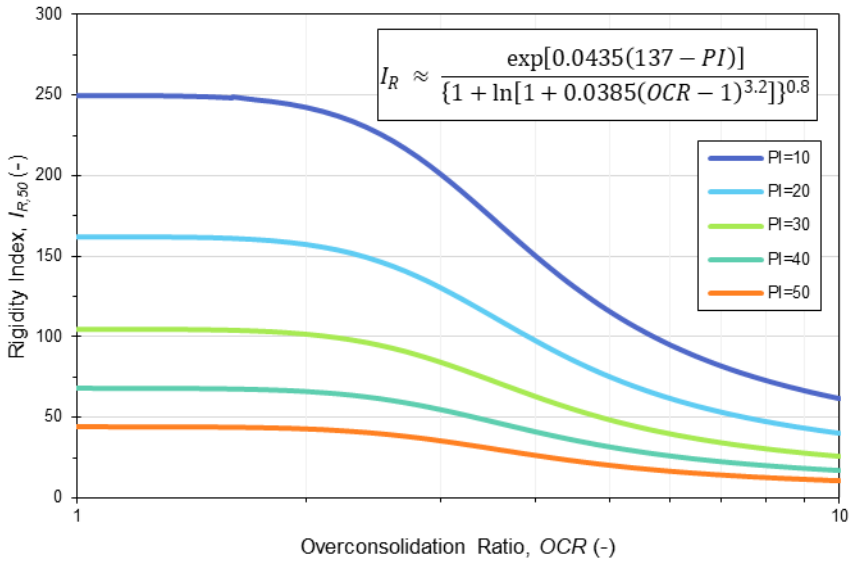

Figure 5.24. Empirical evaluation of the rigidity index, I_R, after Keaveny & Mitchell (1986).

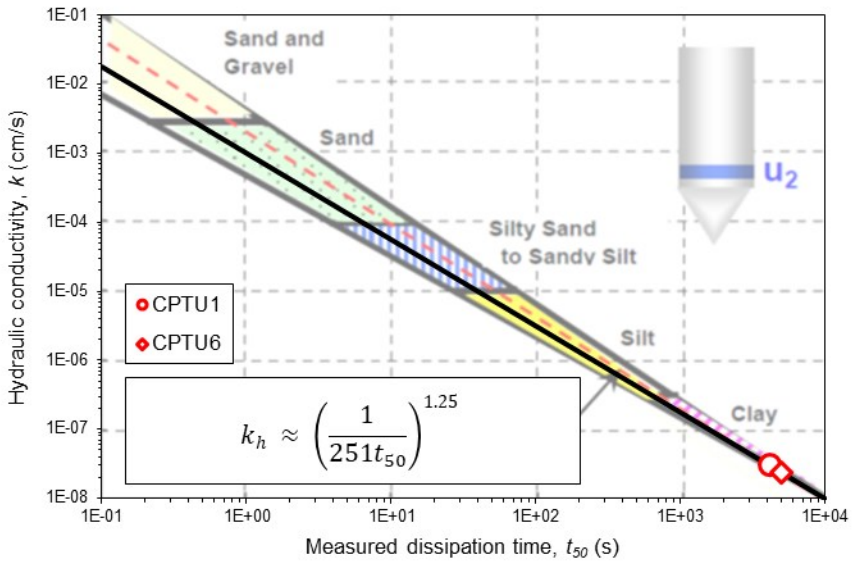

Figure 5.25. Empirical evaluation of the hydraulic conductivity, k_h, after Parez & Fauriel (1988).

Table 5.5. Results of dissipation tests.

	CPTU1		CPTU6	
Plasticity index, I_P (%)	20	30	20	30
Rigidity index, I_R (-)	160	105	160	105
Coefficient of horizontal consolidation, c_h (m^2/s)	2.4×10^{-7}	1.9×10^{-7}	1.7×10^{-7}	1.4×10^{-7}
Hydraulic conductivity, k_h (m/s)	3.0×10^{-10}	3.0×10^{-10}	2.0×10^{-10}	2.0×10^{-10}

5.3 Phase 2: design of the test field

Coupling preloading to vertical drains was necessary to promote the required consolidation within an acceptable timeframe, i.e. a few months, as required by the Ancona Port Authority.

When soil improvement is applied by PVDs-assisted preloading, three are the main design parameters governing the consolidation process:

- the vertical stress to be applied by the embankment, q_R;
- the waiting time of the embankment, t_R;
- the spacing of the drains, S.

The design procedure started from the choice of the drains type, then the surcharge load was defined, and its waiting time assessed by varying the drain spacing. The consolidation process was modelled considering a time-dependent loading theory, using results from the *ante operam* characterisation, as far as compressibility and hydraulic conductivity of the sediments are concerned.

5.3.1 Drain type

The choice of the drain type was mainly dictated by two key reasons: on the one hand, difficulties associated with working above a deposit of very soft sediments, imposing the use of light vehicles for drains installation; on the other hand, the need to opt for a cost-effective product. Prefabricated vertical drains (PVDs) address both these requirements while also providing the advantage of a high installation productivity. Therefore, they were picked to the purpose.

The high performance Colbonddrain® CX1000 was chosen. It is a band-shaped vertical drain featuring a patented corrugated cross section (Figure 5.26) which offers a high resistance to damage during installation and a maximum water flow capacity even when buckled. Its main features are listed in Table 5.6. The solid drainage core is made of post-consumer recycled polyethylene, covered on both sides with a strong and permeable fabric filter jacket, to form a homogeneous geocomposite product; thermal bonding on the whole surface of the core structure ensures that the filter is kept taut across the flow channels.

Table 5.6. PVD characteristics (from the technical sheet).

Width, a	10 cm
Thickness, b	0.5 cm
Discharge capacity, q_w	140 mL/s (=140×10^{-6} m^3/s)
Opening of the filter, O_{90}	75 µm

Figure 5.26. Cross-section of the Colbonddrain® CX1000.

In the long term, the marine environment and sediments contamination might impair the hydraulic performance of such kind of drains, as a result of textile fibres degradation and filter structure modifications (Rollin & Lombard, 1988). In the case of concern, the PVD durability is compatible with the time expected for sediment consolidation, in the order of few months.

5.3.2 Design parameters

The design parameters for the sediments were obtained from the *ante operam* characterisation. Only laboratory parameters related to the sediments FAN and FIN were considered, as they

represent more than 85% of the volume of the sector, whereas the small amount of ISA sediments was reasonably assumed to not significantly affect the consolidation process when the whole sediment layer is considered (Felici et al., 2021).

In particular, the average values from oedometer tests in the stress range including the initial and final vertical stress level in the middle of the sediment layer (i.e. 25÷100 kPa) were considered. To account for the scale effect (laboratory versus site), the coefficient of vertical consolidation, c_v, was amplified by a factor of 5, as suggested in the literature (Burghignoli & Calabresi, 1975; Robertson et al., 1992; de Lillis & Miliziano, 2016). The coefficient of horizontal consolidation, c_h, was instead determined as the average value from the results of in situ dissipation tests. The relevant design parameters are listed in Table 5.8.

5.3.3 Load analysis

Based on the indications of the Ancona Port Authority, the service load, q_E, associated to the intended use of the CDF (i.e. containers storage yard) was computed considering the assembly of five overlapping 30-tons-container as a vertical tower with a base of 2.5 m × 12.5 m. Hence, q_E = 47 kPa.

The preload embankment designed for the test field was essentially a truncated square-based pyramid with a side equal to 30 m and a height of 4 m, with slopes of 1:1 leading to an upper square surface of side 22 m (Figure 5.2). Such dimensions enabled to assume that the overall sediment layer below the embankment – with an average thickness of 6.7 m – is largely in oedometric conditions. Because of the inability to use a heavy compactor, a unit volume weight, γ_R = 16.5 kN/m^3 was set for the coarse material composing the embankment. Based on these data, the vertical stress applied by the embankment, q_R, resulted equal to 66 kPa, i.e. about 1.4 times q_E.

5.3.4 Settlement analysis and target degree of consolidation

Due to the large extent of the embankment compared to the overall thickness of the sediment layer, and to the greater stiffness of the underlying dense sandy layer, the vertical stress increment induced by the preloading can be assumed constant along the depth. All this enables to compute the final consolidation settlement ΔH_R due to q_R by assuming a one-dimensional deformation, according to the following equation:

$$\Delta H_R = \frac{H_0}{1 + e_0} c_c \log\left(\frac{\sigma'_{v0} + q_R}{\sigma'_{v0}}\right) \tag{5.4}$$

where H_0 is the thickness of the consolidating layer, c_c is the compression index, e_0 is the initial void ratio at the middle of the layer and σ'_{v0} is the geostatic effective vertical stress at the same point.

Similarly, the expected consolidation settlement ΔH_E associated to the service load was estimated simply by replacing q_R with q_E in Equation (5.4).

In the specific case, the average thickness of the sediment layer, H_0, was equal to 6.7 m, whereas the value of σ'_{v0} at the midpoint of the compressible layer (z = 4.05 m from the ground level) was computed considering the water table at an average depth of 0.7 m from the ground level, as inferred from monitoring of water levels inside the CDF. As far as the sediment parameters e_0 and c_c, the average values inferred from the results of laboratory testing (§ 5.2.1.2) were entered in Equation (5.4). The expected consolidation settlements ΔH_R and ΔH_E are given in Table 5.7.

The ratio between these two settlements returned the target overall degree of consolidation, $\bar{U}_{ref}$, to be obtained by preloading:

$$\bar{U}_{ref} = \Delta H_E / \Delta H_R \tag{5.5}$$

Table 5.7. Input data for the settlement analysis and values of computed consolidation settlements.

Parameter	Value
Sediment layer thickness, H_0 (m)	6.7
Mean geostatic vertical effective stress, σ'_{v0} (kPa)	34.7
Initial void ratio, e_0 (-)	1.5
Compression index, c_c (-)	0.42
Service load, q_E (kPa)	47
Total stress applied by the embankment, q_R (kPa)	66
Settlement due to service load, ΔH_E (m)	0.42
Settlement due to preloading embankment, ΔH_R (m)	0.52
Target degree of consolidation, $\bar{U}_{ref}$ (-)	0.80

5.3.5 Modelling of consolidation

Modelling of consolidation process requires the definition of a proper soil model (parameters and boundary conditions) and the adoption of an adequate theory.

As usual for consolidation in presence of vertical drains, the soil was modelled considering the unit cell concept, having a height equal to the drainage path, and comprising three concentric cylindrical domains (i.e., drain, smear zone and influence zone, from the centre outwards, see Figure 2.4b). Each domain requires data about geometry and permeability characteristics, which are collected in Table 5.8 and briefly discussed below.

The selected band-shaped PVD (§ 5.3.1) was converted into a cylinder-shaped drain having the same periphery (the a/b ratio did not exceed 50), hence Equation (2.21) was used to compute the equivalent radius, $r_w = 3.3$ cm. The drain length was set equal to the thickness of the compressible layer. The drain discharge capacity, q_w, was set equal to 8.4 L/min, as stated in the technical sheet by the manufacturer. These data allowed to determine the axial hydraulic conductivity of the equivalent drain, k_w.

To define the smear zone, a smear ratio $s = 6$ was assumed, based on the significant remoulding observed in the field during installation trials. This value is in the range proposed in the literature ($s = 1 \div 8$; Hansbo et al., 1981; Bergado et al., 1991; Indraratna & Redana, 1998; Bo et al., 2000) and entails a smear zone radius $r_s = 20$ cm. The hydraulic conductivity value of the sediments in the smear zone, k_s, was assumed to be constant and equal to half of the horizontal hydraulic conductivity of the sediments, k_h, as suggested by Terzaghi et al. (1996). The value of k_h was estimated from dissipation tests.

As far as the influence zone is concerned, two different square spacing options were considered: S1 = 1.0 m and S2 = 1.5 m; hence, the radius R varied accordingly (56 cm and 85 cm, respectively), as well as the spacing ratio, N.

Given the presence of the top blanket and the bottom sandy layer, the double-drainage condition was assumed.

Table 5.8. Design parameters and assumptions.

Parameter	**Value**	
Drain spacing, S (m)	1.0	1.5
Zone of influence		
Radius of the zone of influence, R (m)	0.564	0.846
Spacing ratio, N (-)	16.881	25.321
Horizontal hydraulic conductivity, k_h (m/day)	2.2×10^{-5}	
Coefficient of horizontal consolidation, c_h (m^2/day)	1.6×10^{-2}	
Coefficient of vertical consolidation, c_v (m^2/day)	2.4×10^{-3}	
Amplified c_v (m^2/day)	1.2×10^{-2}	
Smear zone		
Smear ratio, $s = r_s/r_w$ (-)	6	
Radius of the smear zone, r_s (m)	0.201	
Hydraulic conductivity in the smear zone, $k_s = k_h/2$ (m/day)	1.1×10^{-5}	
Cylindrical drain equivalent to the PVD		
Cross-sectional area, $A_w = a\times b$ (m^2)	5×10^{-4}	
Equivalent radius, r_w (m)	0.033	
Discharge capacity, q_w (m^3/day)	12.1	
Axial permeability, $k_w = q_w/A_w$ (m/day)	2.4×10^{4}	

Once defined the design parameters and boundary conditions, the consolidation process was modelled by the advanced theory for vertical drains by Tang & Onitsuka (2000), since it enables to combine radial and vertical flow under time-dependent loading, in equal strains conditions, considering both smear and well resistance. The main theoretical aspects of this theory are given in § 2.2.3.2 of this dissertation.

The first step consisted in the definition of the multi-ramp loading sequence. The embankment was planned to be built in three equal lifts, each of them to be constructed in two days, waiting a week before construction of the subsequent one, according to the following piecewise function:

$$q_R(t) = \begin{cases} \mathcal{R}_1 t, & 0 < t \leq t_1 \\ q_{R,1}, & t_1 < t \leq t_2 \\ q_{R,1} + \mathcal{R}_2(t - t_2), & t_2 < t \leq t_3 \\ q_{R,2}, & t_3 < t \leq t_4 \\ q_{R,2} + \mathcal{R}_3(t - t_4), & t_4 < t \leq t_5 \\ q_{R,3}, & t_5 < t \leq t_{fin} \end{cases} \tag{5.6}$$

The timeline is detailed in Table 5.9 and the values of applied stress and ramp loading rate given in Table 5.10. The loading function q_R(t) is shown in Figure 5.27.

Table 5.9. Multi-ramp loading sequence: time schedule.

t_1 (days)	t_2 (days)	t_3 (days)	t_4 (days)	t_5 (days)	t_{fin} (days)
2	9	11	18	20	180

Note: days are counted from the start of consolidation (time zero).

Table 5.10. Multi-ramp loading sequence: applied stresses and loading rates for each ramp.

Ramp	$i = 1$	$i = 2$	$i = 3$
Total applied stress, $q_{R,i}$ (kPa)	22	44	66
Ramp loading rate, $\mathcal{R}_i$ (kPa/day)	11	11	11

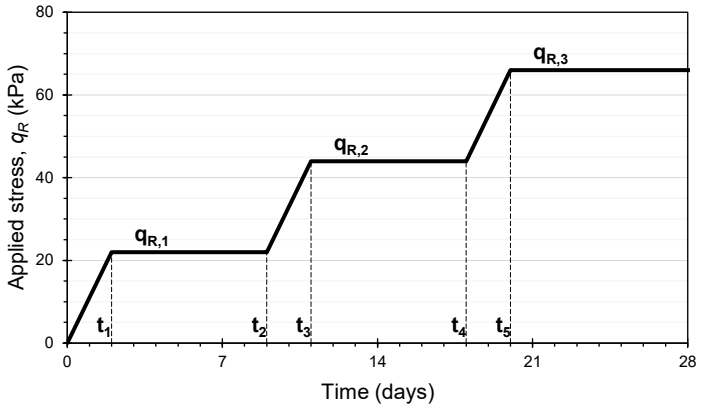

Figure 5.27. Multi-ramp loading sequence for the embankment design.

Based on the data of Table 5.7 and Table 5.8, the coefficients *βm, F, G, D* (Equations from (2.33) to (2.39)) accounting for disturbing effect were computed. Notice that the effect of drain spacing and smear are included in the coefficient *F*, whereas the well resistance is included in the coefficient *G*. To allow for the numerical development, the upper bound of summation was fixed equal to 100.

According to Equations (2.41) and (2.43), the average excess pore water pressure, $\bar{u}(z,t)$, was defined as follows:

$$\bar{u}(z,t) = \begin{cases} \mathcal{R}_1 \sum_{m=0}^{100} \not{f}\{1-\exp[-\beta_m t]\}, & 0 < t \le t_1 \\ \mathcal{R}_1 \sum_{m=0}^{100} \not{f}\{\exp[\beta_m(t_1-t)]-\exp[-\beta_m t]\}, & t_1 < t \le t_2 \\ \mathcal{R}_1 \sum_{m=0}^{100} \not{f}\{\exp[\beta_m(t_1-t)]-\exp[-\beta_m t]\} + \mathcal{R}_2 \sum_{m=0}^{100} \not{f}\{1-\exp[\beta_m(t_2-t)]\}, & t_2 < t \le t_3 \\ \mathcal{R}_1 \sum_{m=0}^{100} \not{f}\{\exp[\beta_m(t_1-t)]-\exp[-\beta_m t]\} + \mathcal{R}_2 \sum_{m=0}^{100} \not{f}\{\exp[\beta_m(t_3-t)]-\exp[\beta_m(t_2-t)]\}, & t_3 < t \le t_4 \\ \mathcal{R}_1 \sum_{m=0}^{100} \not{f}\{\exp[\beta_m(t_1-t)]-\exp[-\beta_m t]\} + \mathcal{R}_2 \sum_{m=0}^{100} \not{f}\{\exp[\beta_m(t_3-t)]-\exp[\beta_m(t_2-t)]\} + \mathcal{R}_3 \sum_{m=0}^{100} \not{f}\{1-\exp[\beta_m(t_4-t)]\}, & t_4 < t \le t_5 \\ \mathcal{R}_1 \sum_{m=0}^{100} \not{f}\{\exp[\beta_m(t_1-t)]-\exp[-\beta_m t]\} + \mathcal{R}_2 \sum_{m=0}^{100} \not{f}\{\exp[\beta_m(t_3-t)]-\exp[\beta_m(t_2-t)]\} + \mathcal{R}_3 \sum_{m=0}^{100} \not{f}\{\exp[\beta_m(t_5-t)]-\exp[\beta_m(t_4-t)]\}, & t_5 < t \le t_{fin} \end{cases} \tag{5.7}$$

where loading and non-loading periods are alternated, and the symbol $\not{f}$ is used here to sum up the term $(2/\beta_m M)\sin(Mz/H)$, due to lack of space.

Likewise, according to Equations (2.42) and (2.44), the overall average degree of consolidation, $\bar{U}(t)$, was written as follows:

$$\bar{U}(t) = \begin{cases} \frac{1}{q_{R,3}}\left\{\mathcal{R}_1 t - \mathcal{R}_1 \sum_{m=0}^{100} \mathcal{F}\{1-\exp[-\beta_m t]\}\right\}, & 0 < t \le t_1 \\ \frac{1}{q_{R,3}}\left\{q_{R,1} - \mathcal{R}_1 \sum_{m=0}^{100} \mathcal{F}\{\exp[\beta_m(t_1-t)] - \exp[-\beta_m t]\}\right\}, & t_1 < t \le t_2 \\ \frac{1}{q_{R,3}}\left\{q_{R,1} + \mathcal{R}_2(t-t_2) - \mathcal{R}_1 \sum_{m=0}^{100} \mathcal{F}\{\exp[\beta_m(t_1-t)] - \exp[-\beta_m t]\} - \mathcal{R}_2 \sum_{m=0}^{100} \mathcal{F}\{1-\exp[\beta_m(t_2-t)]\}\right\}, & t_2 < t \le t_3 \\ \frac{1}{q_{R,3}}\left\{q_{R,2} - \mathcal{R}_1 \sum_{m=0}^{100} \mathcal{F}\{\exp[\beta_m(t_1-t)] - \exp[-\beta_m t]\} - \mathcal{R}_2 \sum_{m=0}^{100} \mathcal{F}\{\exp[\beta_m(t_3-t)] - \exp[\beta_m(t_2-t)]\}\right\}, & t_3 < t \le t_4 \\ \frac{1}{q_{R,3}}\left\{q_{R,2} + \mathcal{R}_3(t-t_4) - R_1 \sum_{m=0}^{100} \mathcal{F}\{\exp[\beta_m(t_1-t)] - \exp[-\beta_m t]\} - \mathcal{R}_2 \sum_{m=0}^{100} \mathcal{F}\{\exp[\beta_m(t_3-t)] - \exp[\beta_m(t_2-t)]\} - \mathcal{R}_3 \sum_{m=0}^{100} \mathcal{F}\{1-\exp[\beta_m(t_4-t)]\}\right\}, & t_4 < t \le t_5 \\ \frac{1}{q_{R,3}}\left\{q_{R,3} - \mathcal{R}_1 \sum_{m=0}^{100} \mathcal{F}\{\exp[\beta_m(t_1-t)] - \exp[-\beta_m t]\} - \mathcal{R}_2 \sum_{m=0}^{100} \mathcal{F}\{\exp[\beta_m(t_3-t)] - \exp[\beta_m(t_2-t)]\} - \mathcal{R}_3 \sum_{m=0}^{100} \mathcal{F}\{\exp[\beta_m(t_5-t)] - \exp[\beta_m(t_4-t)]\}\right\}, & t_5 < t \le t_{fin} \end{cases} \quad (5.8)$$

where again loading and non-loading periods are alternated, and the symbol $\mathcal{F}$ denotes the ratio $2/\beta_m M^2$.

Calculations were performed by the math software Mathcad. Results of the computation in terms of excess pore pressures at the middle of the sediment layer, and degree of consolidation, both as a function of time, resulting from the supposed loading sequence, are shown in Figure 5.28 for the two different drain spacings. It can be observed that, with the square spacing S1 = 1.0 m, the reference average degree of consolidation is reached in about two months, whereas with the square spacing S2 = 1.5 m, almost four months are required. Based on the time needs of the Port Authority, the drain spacing S1 has been chosen for the test field.

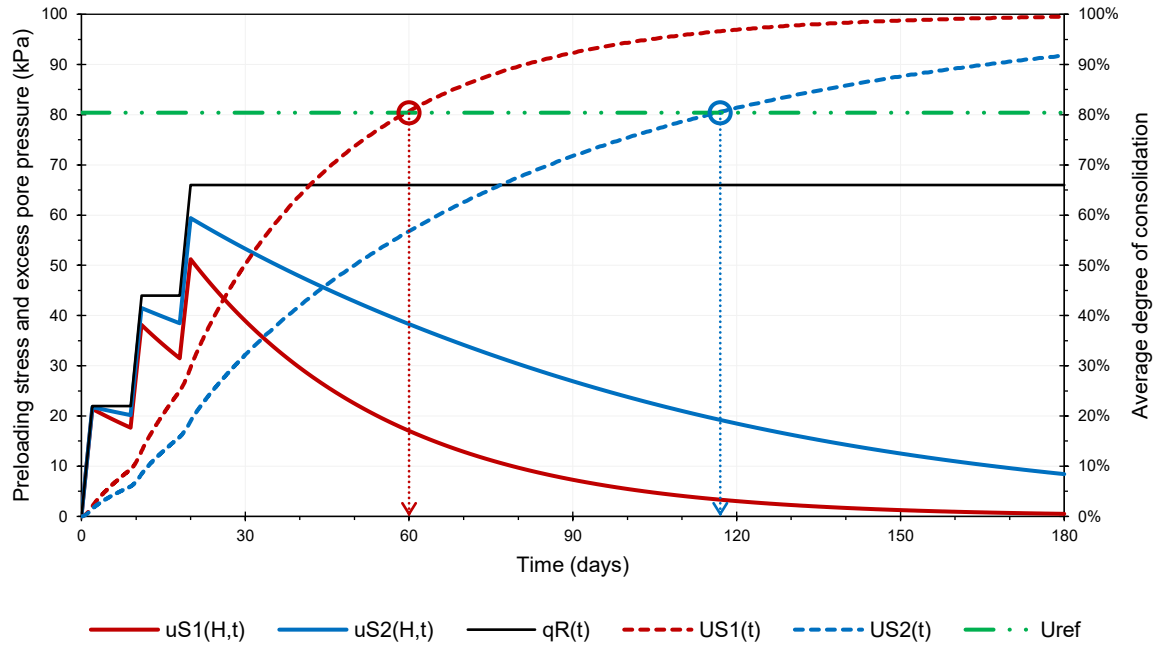

Figure 5.28. Excess pore pressures and average degree of consolidation for two drains spacing options.

5.4 Phase 3: test field construction

5.4.1 PVDs installation

After the creation of the base layer (§ 4.4.3), the working surface for the test field was levelled. A topographic survey was carried out of the ground level to fix target points and datum elevations for monitoring instruments. Stakes were used to materialise the vertices of the test field area and the position of monitoring instruments, while fluo-spray paint was used to draw the nodes of the drain mesh directly on the ground.

A purpose-built installation rig mounted on a lightweight excavator was used to push the PVDs (supplied in rolls) on the test field area (Figure 5.29a). It consisted of an 8-m-tall tower supporting a vibrating thrust system connected to a rectangular mandrel fitted with a steel plate at the bottom. The lower strip of the drain was wrapped and attached to the plate and then pushed into the soil by the mandrel, which acted as a guide; once reached the specified depth, the mandrel was retrieved and the excess tape on the surface cut out. The installation depth was about 7-7.5 m from ground level by the need to operate with light equipment. This meant that, given the average thickness of the sediment layer (6.7 m), the PVDs reached or were very close to the underlying sandy layer (see Figure 5.2).

PVDs were installed with a square mesh 1-m-sided over the whole footprint area of the embankment (Figure 5.29b), except for the perimeter areas below the slopes; hence, they covered an area of 26 m × 26 m, for a total of 729 draining verticals. Considering an average length of 7.3 m for each drain (the strip poking out of the ground is not counted), an overall length of PVDs of about 5,300 m was installed.

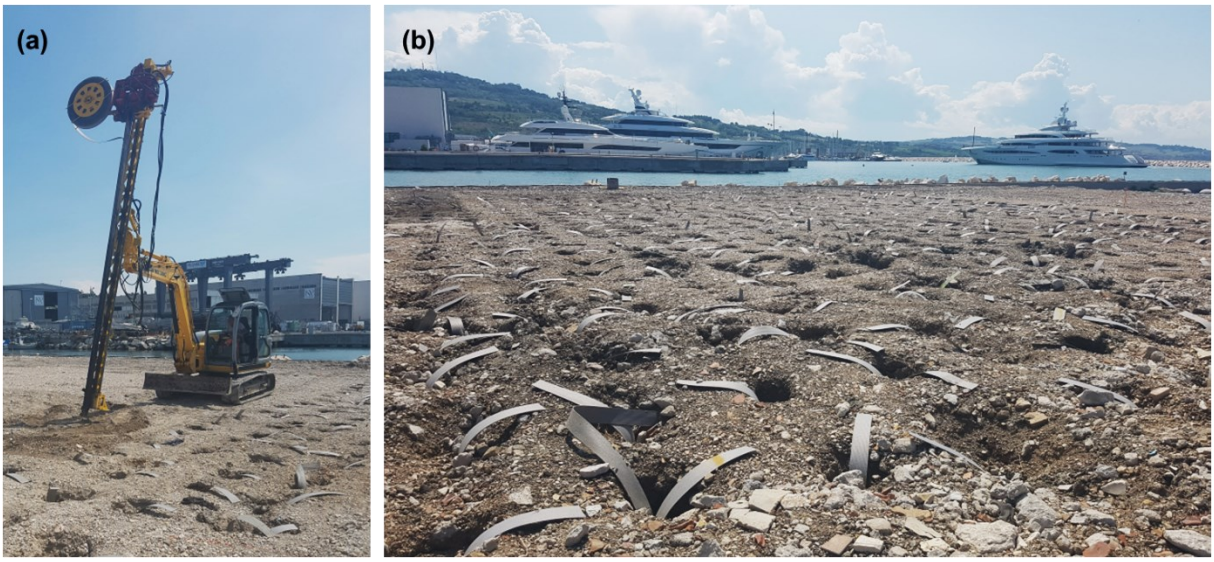

Figure 5.29. Installation of the PVDs: (a) installation rig; (b) completed area.

To minimise manoeuvring, the PVDs installation followed a linear path; to cover the whole area of the test field, it took nine working days (i.e. ~80 verticals/day), but the productivity is reasonably likely to increase in wider areas (up to 100÷120 verticals/day).

Lastly, some trials were performed outside the testing area, to check the enforceability of PVDs installation in tougher conditions (through a coarser base layer).

5.4.2 Monitoring instruments

A monitoring system was installed beneath the embankment prior to its construction, to continuously control and record applied stresses, pore pressure variations and settlements over time. The monitoring equipment consisted of 2 total pressure cells, 5 drive-in electrical piezometers and 10 settlement gauges, placed as depicted in Figure 5.30. Number and position of the instruments have been selected to fully monitor the consolidation process in the sediment layer, also in the event of malfunction. A brief description of the monitoring instruments is given in the following.

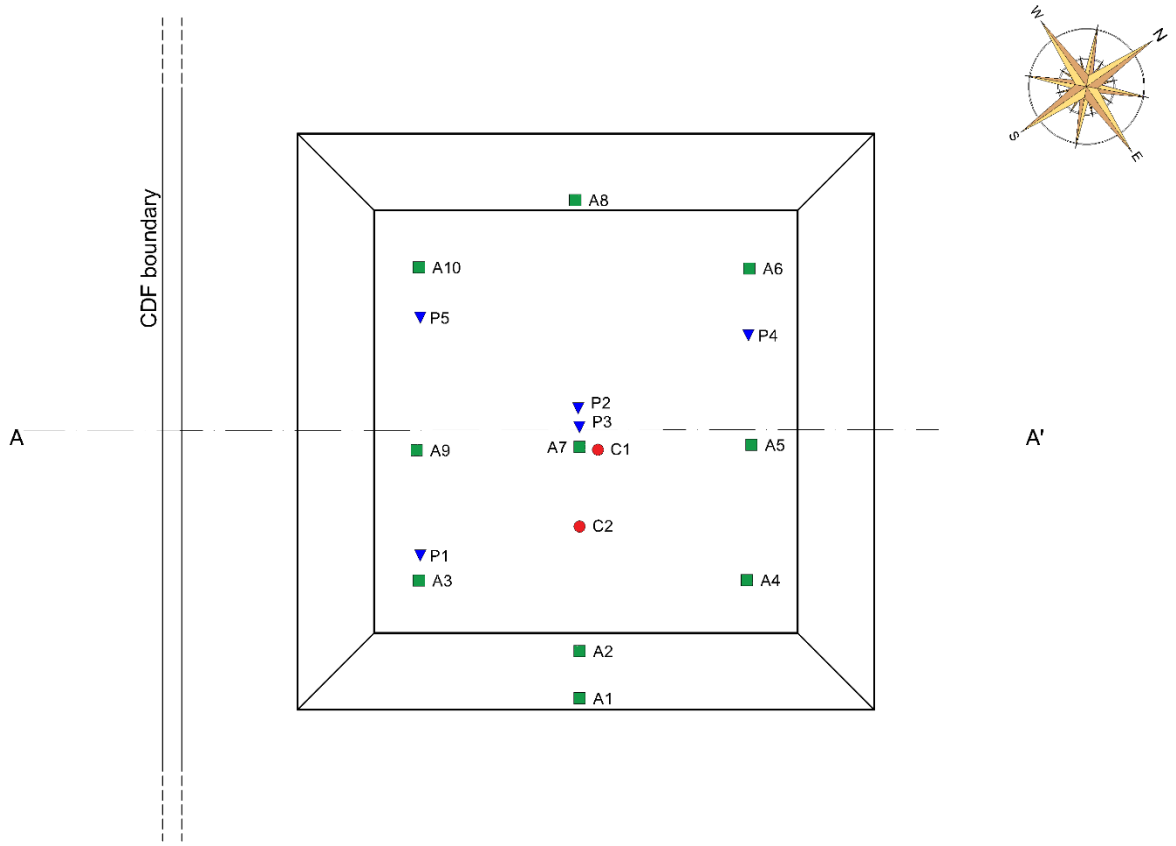

Figure 5.30. Planimetric layout of monitoring instruments.

5.4.2.1 Earth pressure cells

Earth pressure cells have been employed to monitor changes in total stresses resulting from the embankment construction and to check design assumptions. They consist of a couple of 20-cm-diameter steel plates (Figure 5.31) welded together around their periphery and separated by a narrow gap saturated under vacuum with a fluid (deaired oil). A stainless-steel tube, which is also saturated, provides the connection of the cell to a pressure transducer, forming a closed hydraulic system. Any earth stress acting on the cell plates is thus balanced by an equal pressure induced in the internal fluid; the pressure transducer then converts it to an electric signal remotely readable on a data logger.

Each of the two pressure cells has been embedded inside an excavated trench about 50-60 cm deep, where a compacted sand bed has been prepared beforehand to level the bottom; then the trench has been filled with the sand.

Figure 5.31. Earth pressure cell.

5.4.2.2 Drive-in electrical piezometers

Monitoring of excess pore water pressures induced by preloading has been accomplished by means of electrical piezometers, as they provide fast response times (of the order of a few minutes even for very low permeable soils) and continuous measurements. The drive-in version has been preferred mainly because it does not require to drill a borehole for its installation; it is pushed directly into the soil using conventional equipment. This feature makes drive-in piezometers particularly suited for saturated soft soils and shallow depths, as in the case if concern.

Figure 5.32a shows a piezometer used in the test field. It consists of a cylinder-shaped metal body housing the electronic components (including a piezoelectric sensor) and a hydraulic chamber connected to the environment by means of a porous filter. In front of the filter, the cylinder is fitted with a stainless-steel conical tip, whose larger diameter (40 mm) facilitates its insertion into the soil, whilst at the opposite end an electric cable makes the connection to a readout unit. The operating principle is based on the ability of the piezoelectric sensor to sense

pressure variations across deflections of its flexible steel membrane, producing proportional variations of the electrical output signal; the electrical measurements are then converted into engineering units.

A CPT rig (Figure 5.32b) has been used to push the five piezometers down at the depths listed in Table 5.11. The different depths have been selected considering the presence of the coarser sediment lenses detected during the in-situ investigation, in order to monitor the sediment consolidation process as their composition varies.

Table 5.11. Depth of installation of the monitoring piezometers.

Piezometer	P1	P2	P3	P4	P5
Depth from g.l. (m)	2.20	3.40	5.10	3.20	2.50

Figure 5.32. Drive-in piezometer: (a) instrument supply; (b) CPT rig positioning to drive piezometers.

5.4.2.3 Settlement gauges

A multipoint liquid level system has been used to monitor settlements over the footprint area of the embankment. This system is based on the concept that a column of liquid exerts a pressure

as a function of its height, so any pressure variation over time (that is, any shift in the height of the liquid) corresponds to the vertical displacement of the monitored point.

The system here installed consisted of two small reservoirs (Figure 5.33b) and ten measuring spots connected via polyethylene tubing, to form a hydraulic circuit, and electrical wires, to plug in the data acquisition device. Tubing is filled with a chemically inert mixture of water and glycerine, as it ensures better low-temperature performance. Reservoirs are secured at a higher elevation – so as to put the system under pressure – and at fixed location outside the settlement area, as they serve as a datum level to measure relative settlements. Each measurement spot is composed by a zinc-coated steel support plate above which a settlement gauge (pressure transducer) is mounted (Figure 5.33a). Pressure transducers send out a signal which corresponds to the pressure variation resulting from the vertical displacement of the point relative to the datum level inside the tanks, which is fixed and known. In particular, the gauge reports higher pressure if settlement occurs.

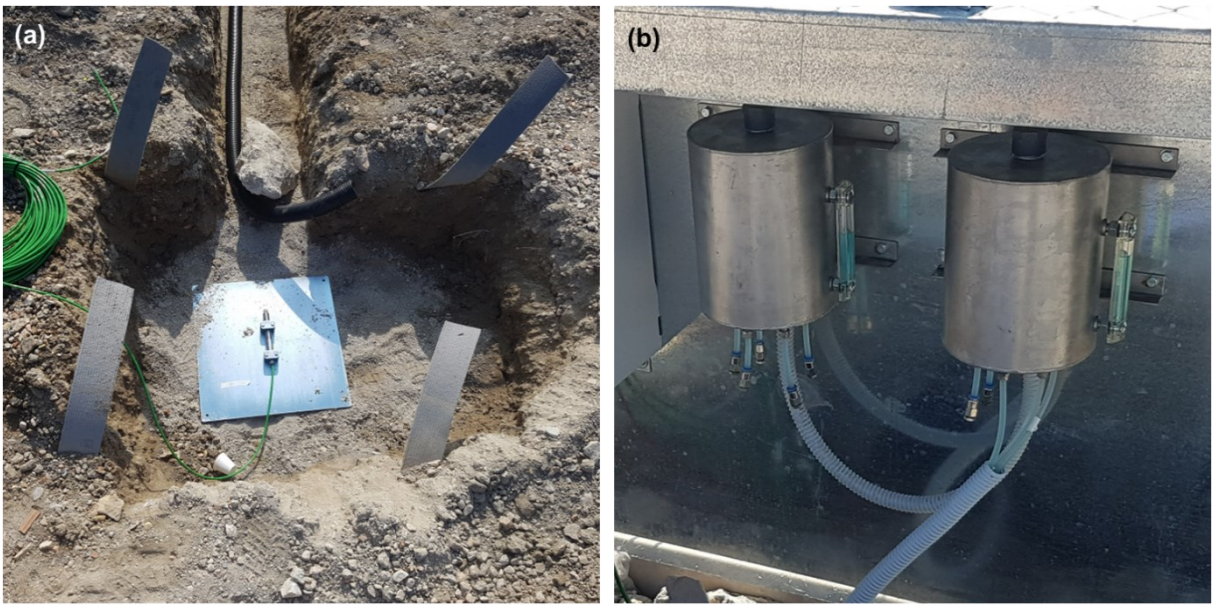

Figure 5.33. Settlement gauge: (a) pressure transducer on its metal support plate, placed into a trench; (b) the reservoirs.

5.4.3 Construction of the preloading embankment

To build the preloading embankment, coarse grained material available at the site was used, from debris from demolition of reefs and port structures. The size ranges from a minimum of some millimetres to more than 20 cm.

The embankment was built by excavators soon after the installation of PVDs and monitoring instruments. Staged construction was implemented to prevent local and global instability, and to ensure safety conditions during work. To reach the final height of 4 m, three loading

steps were applied – according to the design – to allow for a partial consolidation of sediments after each step, thus gaining an increment of the shear resistance before the elevation of the next lift. Figure 5.34 reports some construction phases; Figure 5.35 shows the finished embankment.

Figure 5.34. Construction of the moving embankment.

The first lift had a thickness of about 1 m, and it was constructed within a day, by distributing the coarse material over the whole area and advancing. The lift was built by overlapping thin layers without compaction. Particular care was taken to not damage the monitoring instruments installed just below the ground level, which were already working during construction. At the end of this phase, the earth pressure cell C1 recorded a total vertical stress of about

15 kPa. After one week, the second lift was built, with a thickness of about 1 m; the earth pressure cell C1 registered a stress of about 32 kPa. After 10 days, the third lift was built, reaching the theorical final heigh of 4 m foreseen in the design. At the end of construction, the cell C1 recorded a stress of 66 kPa, corresponding to the desired value.

By means of topographic levelling of the embankment and considering the settlements already measured in the meanwhile, the final heigh was determined as about 3.5 m. From this value the effective unit volume weight of the material used for the embankment construction was backfigured, and it resulted equal to 17.5 kN/m^3. Since the same material and construction procedure will be reused for the consolidation treatment of the other sectors of the CDF, the field test allowed to know the unit weight of the embankment, that is, its height to obtain the desired loading level.

After about two months, a fourth lift was built to further investigate the consolidation process and verify the efficiency of the PVDs which could be affected by physical and/or microbiological clogging. The final applied pressure resulted of 85 kPa.

Figure 5.35. The finished embankment.

The embankment was left in place for seven months during which monitoring of applied stresses, porewater pressures and settlements was carried out. The embankment was then dismantled and the material set aside on the site, to be reused for further sectors. After removal, topographic levelling of the area was performed to check the settlements and perform field investigations.

5.5 Phase 4: *post operam* characterisation

Just after the embankment removal, the same series of cone penetration tests described in § 5.2.2.1 was replicated, approximately at the same positions of the previous ones, to compare recorded profiles and quantify the achieved improvement with respect to the *ante operam* condition. Results are reported in § 6.2.1.1.

Three continuous coring boreholes performed next to CPTUs allowed to get a more detailed stratigraphic profile and to collect undisturbed samples for laboratory testing. In particular, several classification tests and mineralogical analyses were performed along the investigated verticals, as illustrated in § 6.2.2. Undisturbed samples were essential to study sediment compressibility and undrained shear strength after the consolidation.

5.6 Development of a general design equation

As already introduced, when soil improvement is applied by PVDs-assisted preloading, three are the main design parameters governing the consolidation process: the vertical stress to be applied by the embankment, q_R, its waiting time, t_R, and the drains spacing, S. These three variables can be mathematically linked and collected in a single chart to aid engineers in designing the filling and consolidation procedures (Pasqualini F. et al., 2021; Felici et al., 2022).

5.6.1 Model and hypotheses

The problem can be drawn out as in Figure 5.36. Vertical drains are installed at a given spacing S into a homogeneous compressible layer of thickness H_0 lying between one or two draining boundaries (whichever is applicable). A preloading embankment on the surface impresses a total stress q_R to the compressible layer. Since the embankment width, B, is set larger than the double of the thickness of the compressible layer ($B > 2H_0$), the simplified hypothesis of one-dimensional deformation holds, and Equation (5.4) can be used to evaluate the settlements ΔH_R and ΔH_E produced by the embankment and the service load, respectively, once the compression index, c_c, the initial void ratio, e_0, and the in-situ effective vertical stress, σ'_{v0}, at the midpoint of the consolidating layer are known.

The magnitude of the service load, q_E, is established by the intended use of the sector area. The magnitude of the total vertical stress applied by the moving embankment, q_R, shall exceed the service load ($q_R > q_E$) to gain a real benefit from the improvement technique, but it is bounded by the embankment-foundation system stability.

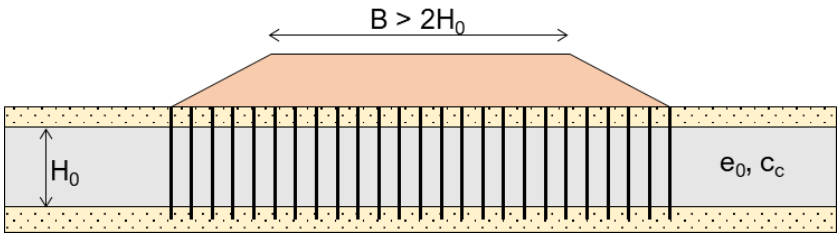

Figure 5.36. Reference scheme.

The preloading stress q_R must be maintained for a time t_R such that the settlement ΔH_R for $t = t_R$ equals the final settlement $\Delta H_{E,\infty}$ (at the end of consolidation) associated to the service load, as illustrated schematically in Figure 5.37a. To take into account of the time required for the embankment construction, it can be assumed that the effect induced by a linearly applied stress in a given time t_c (ramp-loading) is equivalent to the effect produced by same stress applied instantaneously at a fraction of this time. In other terms, the waiting time, t_R, is given by the sum:

$$t_R = f\,t_c + t_{cons} \tag{5.9}$$

where t_{cons} is the consolidation time, t_c is the construction time, and f is a fraction. In the present model, f = ½ (Figure 5.37b).

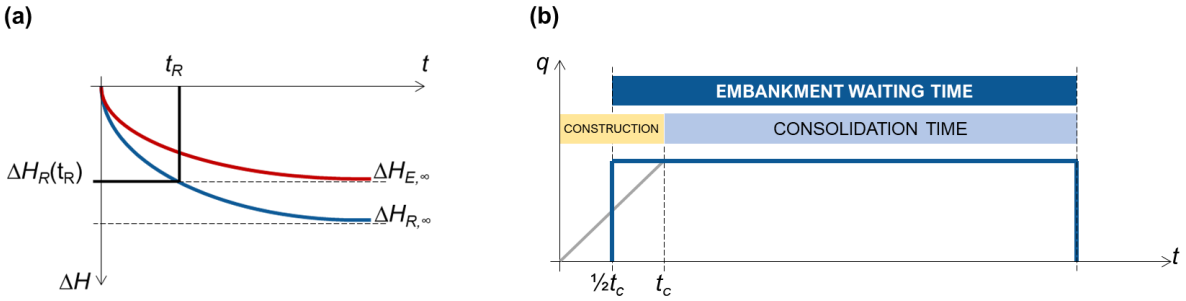

Figure 5.37. Preloading approach based on settlements: (a) settlements vs time; (b) load vs time.

5.6.2 Modelling procedure

In contrast to the actual design of the test field in the Ancona CDF, where an advanced time-dependent theory was applied for modelling consolidation (see § 5.3.5), in this case a theoretical model less complex from the mathematical standpoint was opted for, as explained in the following. It is worth repeating that the goal is to produce an easy-to-apply solution for a strategic planning and optimisation of sectors in a CDF and for the preliminary design of the proposed consolidation technique and procedures.

Therefore, similarly to other studies (e.g. Chai et al., 2001), radial and vertical drainage were studied separately and then combined by the theoretical solution of Carrillo, 1942, which expresses the average global degree of consolidation by Equation (2.30). Carrillo's solution is valid only for ideal drains and instantaneous load; nevertheless, the error involved in using this solution is generally quite small even in case of ramp loading (Tang & Onitsuka, 2000). Therefore, the use of Carrillo's solution can be considered a reasonable approximation if compared with the uncertainties associated with the determination of soil parameters, smear, well resistance and equivalent drain radius.

With reference to the contribution of pure radial consolidation, the Hansbo's theory (§ 2.2.3.1) was adopted because, despite some simplifying assumptions, it gives results in good agreement with more rigorous solutions (Onoue, 1988). In particular, the average degree of consolidation at time t for pure radial flow, $\bar{U}_h$, was computed by Equation (2.23):

$$\bar{U}_h(t) = 1 - \exp\left(-\frac{2T_h}{F}\right) \tag{2.23}$$

where the numerical coefficient F is here approximated as:

$$F = \ln\frac{R}{r_s} - 0.75 + \left(\frac{k_h}{k_s}\right)\ln\frac{r_s}{r_w} + \frac{2}{3}\frac{\pi k_h L^2}{q_w} \tag{5.10}$$

For the average degree of consolidation for vertical flow only, $\bar{U}_v$, reference can be made to the classical Terzaghi's theory (§ 2.2.1), on the basis of the coefficient of vertical consolidation, c_v, and the maximum vertical drainage path. In this case, the following approximated solution was adopted:

$$\bar{U}_v = \begin{cases} 2\sqrt{T_v/\pi}, & T_v < 0.196 \\ 1 - 0.8106(0.08476)^{T_v}, & T_v \geq 0.196 \end{cases} \tag{5.11}$$

Finally, by imposing that the overall degree of consolidation $\bar{U}_{hv}$ at time $t = t_R$ is equal to the ratio of settlements $\Delta H_E/\Delta H_R$ (i.e., to the target degree of consolidation $\bar{U}_{ref}$ to be reached by the improvement technique), which means combining Equations (2.30) and (5.5), the following general equation was obtained:

$$q_R = \sigma'_{v0}\left\{10^{\left[\frac{\delta_E(1+e_0)}{H_0 c_c\{1-(1-U_h)(1-U_v)\}}\right]} - 1\right\} \tag{5.12}$$

Equation (5.12) can be used for a quick evaluation of the influence of drain spacing, waiting time and surcharge load in the design of a PVD-assisted preloading treatment.

It is noted that the equation assumes implicitly a step loading. Actually, the construction of the moving embankment requires a finite time which can be reasonably considered proportional to q_R. This aspect must be taken into account in using Equation (5.12) for design purposes. In the absence of more detailed data about the rate of loading to reach q_R, a simple ramp loading scheme can be assumed, and the actual time required for the preloading treatment can be roughly obtained as the sum of t_R given by (5.12) and a fraction (0.5-1) of the construction time.

In the following an application of the aforesaid procedure is shown with reference to the Ancona CDF.

5.6.3 Example of application

The application of the proposed general design Equation (5.12) requires a preliminary evaluation of the soil properties and drain characteristics.

For the first filled sector of the Ancona CDF (area of about 4,000 m^2), both laboratory and in situ tests (CPTM and CPTU with dissipation) have been performed to achieve a comprehensive characterisation of the soil prior to the consolidation process. The input data for the sediment layer and PVDs characteristics and parameters are the same used in the test field design (§ 5.3).

By the data of Table 5.8, the design charts in Figure 5.38 and Figure 5.39 have been obtained by Equation (5.12). The effect of the construction time, t_c, is included in the charts, always considering a gradual construction of the embankment of 1.5 m/week, i.e. 3.5 kPa/day and assuming that the effect of a ramp loading is equivalent to a step loading starting at $t_c/2$.

As expected, the required drain spacing S increases as waiting time t_R and preloading pressure q_R increase; conversely, for an assigned drain spacing, the required preloading pressure decreases for increasing waiting time.

To build the charts, the following assumptions were made on the main variables:

- the drain spacing, S, is assumed to be discrete variable varying from a minimum value of 0.8 m (which is approximately the double of the smear zone diameter) and a maximum of 2.4 m (which is lower than the vertical drainage path);
- the preloading stress, q_R, is considered in the range 47÷100 kPa, the upper value being established from stability analyses.

As an example, considering a maximum waiting time t_R = 6 months (depending on the time necessary to fill the adjacent sector) the curves of Figure 5.38 and Figure 5.39 allow to obtain different combinations of spacing and preloading pressure to be used in the design. For a triangular mesh two bound solutions are obtained (Figure 5.39): the first solution involves a drain spacing of S = 1.4 m and preloading pressure q_R = 50 kPa, which implies about 18,900 m

of PVDs (of length 8 m) and about 11,000 m^3 of material for the embankment (considering a 45° slope of the embankment); the second solution requires a drain spacing of 2.4 m combined with preloading load equal to q_R = 74 kPa, which implies about 6,400 m of PVDs and about 16,000 m^3 for the embankment. The optimal solution can be chosen considering costs of both PVDs and the material for the embankment, this latter mainly depending on the availability of the material in or close to the site.

The results of monitoring the consolidation process in the test field (§ 6.1) were found in good agreement with the predicted ones as shown in Figure 5.38. It must be pointed out that the design charts of Figure 5.38 and Figure 5.39 are related to the first sector of the Ancona CDF. For the future sectors the same procedure can be applied, provided that a new preliminary characterisation of sediments is performed.

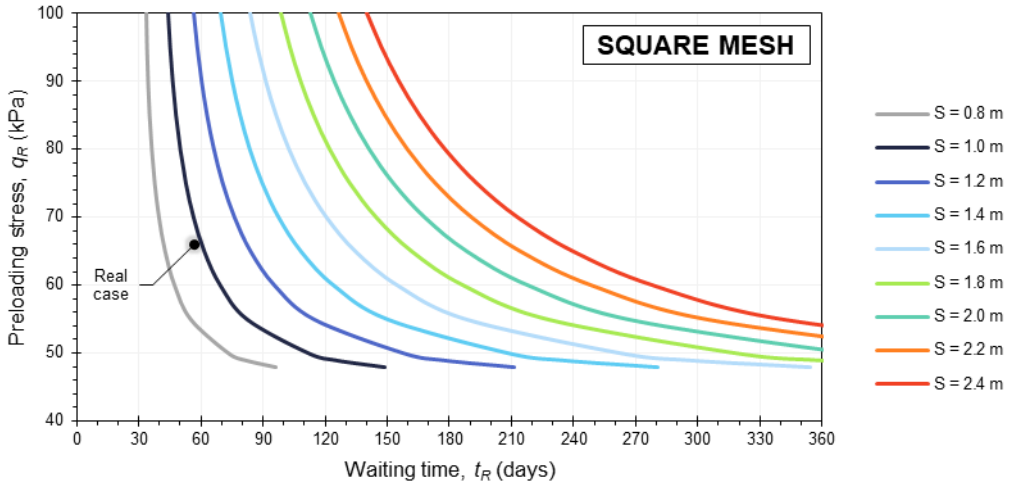

Figure 5.38. Design chart for PVDs square grid for the Ancona CDF.

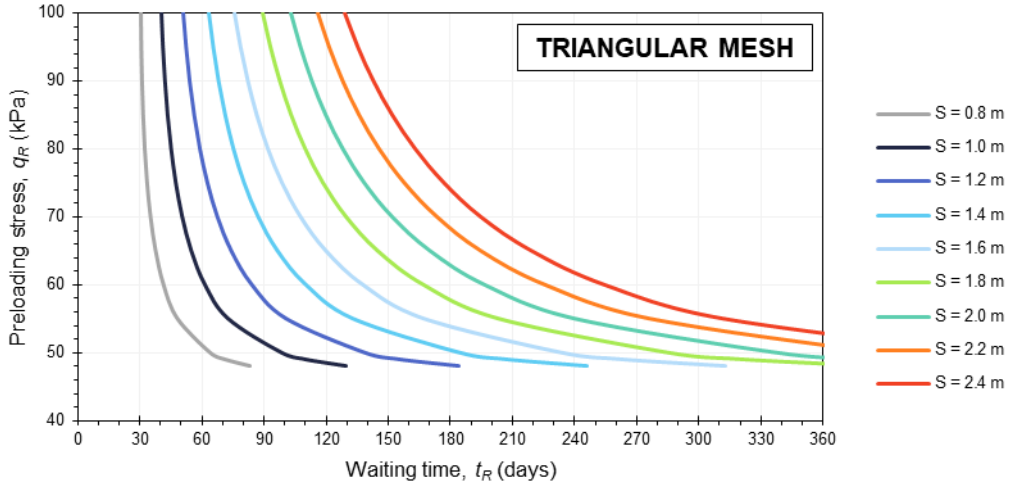

Figure 5.39. Design chart for PVDs triangular grid for the Ancona CDF.

6 RESULTS AND DISCUSSION

In this chapter the results of monitoring and post-operam characterisation are presented and discussed. Monitoring data were back-analysed to check and validate the design assumptions. Field and laboratory testing after the embankment removal allowed to ascertain the effectiveness of the improvement technique, as well as to propose a site-specific empirical correlation derive the undrained shear strength of sediments indirectly from CPTU tests.

6.1 Monitoring results

In this section, results of the monitoring activity are presented and analysed. Before going through the main findings, a few comments are given with regard to the assumptions made and special circumstances which may affect the interpretation of monitoring data.

A first premise concerns the consolidation settlements induced by the top layer alone. As anticipated in § 4.4.3, the need to ensure the safe transit of vehicles and workers imposed the construction of the top layer before installing the monitoring instruments, but this implied that the associated settlements could not be detected by the system. Therefore, topographic levelling of the test field area was carried out right before the construction of the top layer, and repeated three months after its completion. This time was deemed to be sufficient for developing of most of the consolidation settlements due to the top layer because PVDs were installed within one month, during which consolidation occurred because of the presence of the draining blanket itself on the top and the sandy layer below, while in the following two months PVDs fully contributed. Settlements between 7 and 10 cm were measured after 3 months, corresponding to a vertical deformation of 1-1.5%. The average amount equal to 8 cm, however negligible, has been subtracted from the initial thickness of the sediment layer for the consolidation analysis due to preloading.

With reference to the excess pore pressure induced by the preloading embankment over time, it was calculated by subtracting the hydrostatic pressure, daily monitored inside the CDF, from the porewater pressure measured by the piezometer. This calculation posits that sediments respond immediately to fluctuations of the hydrostatic porewater pressures, not in compliance with the hydraulic behaviour of the sediments. However, the water level inside the CDF varied

so slowly over time that errors associated to the above assumption can be considered negligible. The only exception occurred after about ten weeks of monitoring, when the water level inside the CDF rapidly increased due to storm surges; in that circumstance, the assumption of immediate response of hydrostatic pressure entailed the underestimation of excess porewater pressure in all piezometers, as shown in Figure 6.1. The increased overburden pressure due to the construction of the fourth lift of the embankment, already scheduled, did not allow a reliable estimation of the response time.

About three weeks elapsed between the installation of piezometers and the beginning of the embankment construction; throughout this period, piezometers P1, P2 and P5 sensed an almost constant value of the pore pressure corresponding to the actual groundwater table depth (0.8-1.1 m from the ground level), which meant virtually zero excess pore pressure before the embankment construction, as expected. In contrast, piezometer P4 initially recorded a seemingly weird value of $\Delta u \approx 14$ kPa, reasonably due to different loads during installation of monitoring instruments (i.e., access tracks, stored materials and equipment). Dissipation almost halved this amount throughout the following three weeks; the residual had to be dissipated together with the Δu induced by the embankment construction.

Finally, it must be pointed out that a few monitoring data could not be used, as specified in the following.

- The earth pressure cell C2 always registered a stress value significantly lower than that actually applied which, by contrast, was duly sensed by cell C1. This gap has been ascribed to arching effect, since the trench of installation resulted too narrow.
- The piezometer P3, placed in the center of the testing area at a depth of 5.1 m from the ground level, never provided reliable porewater pressure values, probably because of an incorrect installation or a factory defect.
- The settlement gauge A8, located along one of the sides of the embankment, suffered an abrupt breakdown after the first three weeks of proper operation, giving rise to suspicious on reliability of the subsequent data, which have been therefore discarded.

Nevertheless, the large number of instruments installed over the test field area permitted to fully monitor the consolidation process of the sediment layer.

Figure 6.1 shows the overlay plot of porewater pressures (measured by piezometers), the applied total pressure (measured by the earth pressure cells) and settlements (measured by settlement gauges) with time.

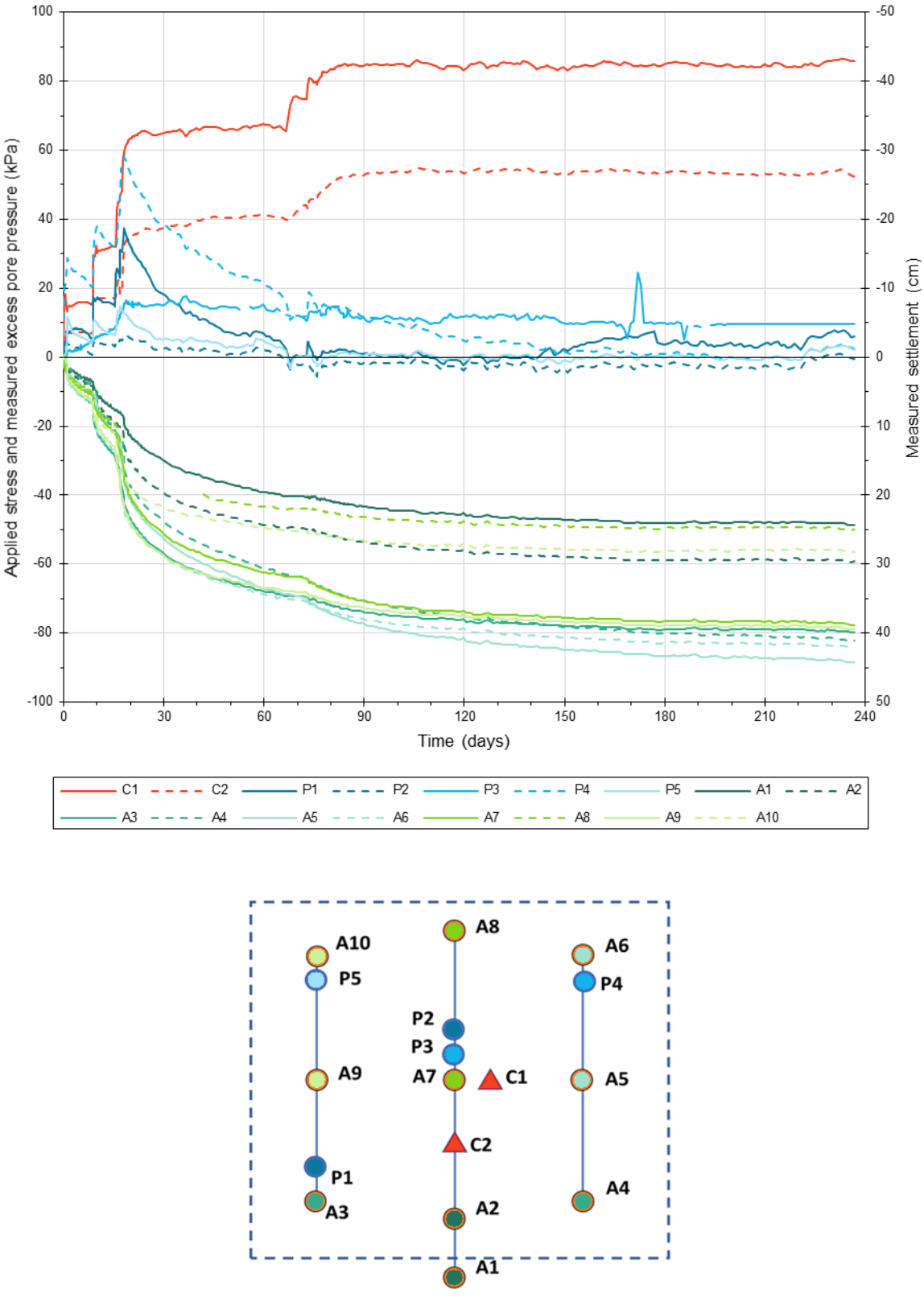

Figure 6.1. Overlay plot of monitoring results across time. Red lines indicate the stresses detected by earth pressure cells; blue lines report excess pore pressures measured by piezometers; green lines indicate the vertical displacements measured by settlement gauges.

It may be noted that each load step is matched by an abrupt increase in the measured pore pressure, followed by a slower dissipation, confirming the overall low permeability of the sediments disposed in this sector. Both piezometers P1 and P4, installed in fine-grained sediments, recorded high values of excess pore pressure and a slow dissipation, whereas P2 and P5, placed within and close to coarser lens respectively, recorded smaller increases of the pore pressure. In particular, for the piezometer P2, for which it would be reasonably assumed that the initial excess pore pressure was equal to the applied vertical stress (given its central position), a local degree of consolidation of about 99% can be seen after one month.

For piezometer P1, installed below the slopes of the embankment, where the vertical stress applied by the embankment is lower than 66 kPa, after one month of consolidation the local degree of consolidation can be estimated to be of about 60%, and about 80% after two months. This result is confirmed by settlements measured by the adjacent settlement gauge A3, which are practically constant with time after two months.

Piezometer P4 was installed where there are no coarser lenses. It recorded the higher values of Δu, as it is installed in the midpoint of the compressible layer, at the maximum distance from draining boundaries. At the end of the third loading step, the peak excess pore pressure was about 58 kPa and, after two months, the recorded Δu had dropped to 18 kPa. The average degree of consolidation can be estimated referring to the settlement measured by the adjacent settlement gauges A5 and A6 just before the fourth loading step and the final settlement at the end of consolidation induced by the fourth step, as summarized in Table 6.1. After about two months from the embankment construction, the average degree of consolidation is at least equal to 80%.

In light of the above, it might be concluded that it is possible to obtain an average degree of consolidation of at least 80% in a waiting period of two months; this period is lower if lenses of coarser material are present in the stratigraphy.

From Figure 6.1 it is possible to observe that the magnitude of settlements registered with the design load (66 kPa) after two months from the beginning of the embankment construction, is in the range 25÷35 cm, corresponding to vertical strains $\leq$ 5%. This result allows to model consolidation due to PVDs assisted preloading with the assumption of small strains.

Table 6.1. Estimation of the average degree of consolidation at piezometer P4.

Settlement gauge	Settlement measured before 4th step, ΔH_{66}	Final settlement due to 4th step, $\Delta H_{f,85}$	Average degree of consolidation, $\Delta H_{66}/\Delta H_{f,85}$
	(cm)	(cm)	
A5	34.3	43.5	79%
A6	35.0	41.5	84%

The excess pore pressure trends over time in Figure 6.1 (in particular, piezometers P1 and P4) show that the installed PVDs did not exhibit significant biological or physical clogging for at least 4-5 months after their installation since the excess pore pressure was effectively dissipated.

6.1.1 Back-analysis of monitoring results

The results obtained from monitoring activities allowed to validate the approach used to design the test field and to estimate the time to reach the reference degree of consolidation. For the purpose, the reference geological section is the one in Figure 6.2. Data from the earth pressure cell C1 and from the piezometers P1, P2, P4, and P5 were considered.

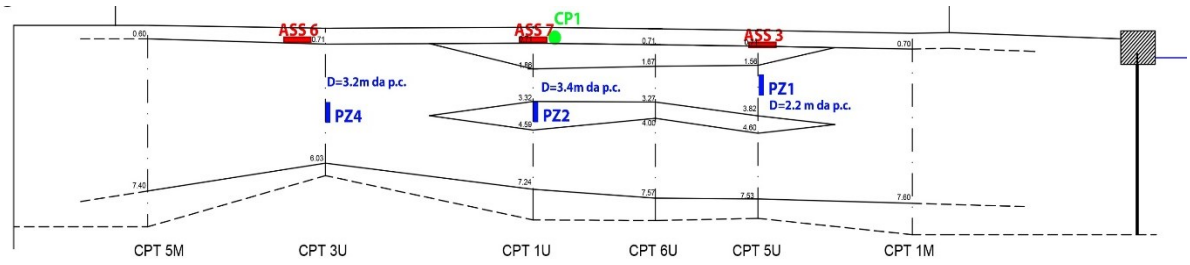

Figure 6.2. Reference geologic section for back-analysis of piezometer data.

The multi-ramp loading sequence assumed in the design has been updated to make it consistent with the loading sequence actually applied in the test field. Specifically, the real timeline followed during the embankment construction (Table 6.2) and the stresses actually recorded by the cell C1 (Table 6.3) have been implemented in the piecewise function (5.6). The actual loading sequence is depicted in Figure 6.3. It is noteworthy that the stress recorded by the cell C1 during the first two steps was about 27% lower than the stress hypothesised in the design sequence (Figure 5.27), but either way, the final value $q_{R,3} = 66$ kPa was reached after about 20 days, as originally supposed (Felici et al., 2021).

The excess pore pressure $\Delta u(z,t)$ and degree of consolidation $U(t)$ for loading and non-loading periods have been recomputed by the same Equations (5.7) and (5.8) used in the design phase. In addition, the lens L1 has been considered as a drainage contour, as inferred by CPTUs.

Table 6.2. Actual multi-ramp loading sequence: time schedule.

t_1 (days)	t_2 (days)	t_3 (days)	t_4 (days)	t_5 (days)	t_{fin} (days)
1	9	10	16	19	180

Note: days are counted from the start of consolidation (time zero).

Table 6.3. Actual multi-ramp loading sequence: applied stresses and loading rates for each ramp.

Ramp	$i = 1$	$i = 2$	$i = 3$
Total applied stress, $q_{R,i}$ (kPa)	16	32	66
Ramp loading rate, $\mathcal{R}_i$ (kPa/day)	16	16	11.3

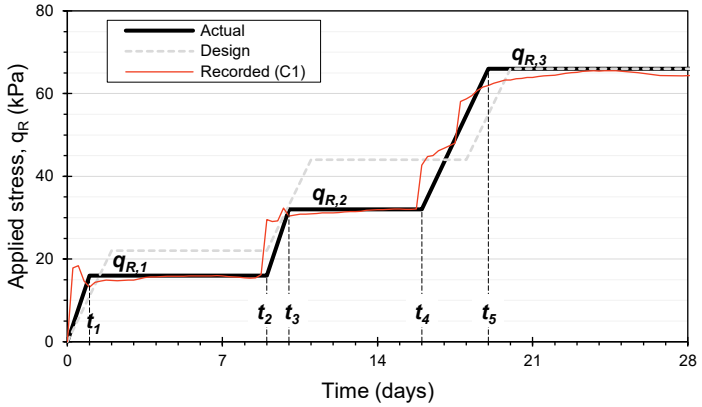

Figure 6.3. Actual multi-ramp loading sequence used for the back analysis (black solid line) compared with the design loading sequence (grey dashed line) and the values of q_R recorded by the earth pressure cell C1 (red solid line).

Calculations have been performed for three relevant depths:

- $z = 0.1$ m from the top draining boundary, as this location is representative of the excess pore pressure dissipation very close to the top draining boundary;
- $z = 0.5$ m from the top draining boundary;
- $z = H$, i.e., at the midpoint of the sediment layer, where the larger excess porewater pressure is expected.

Figure 6.4a shows the trends of the excess pore pressure measured by piezometers P1 and P5, both located at z < 0.5 m. The peaks of Δu correspond to the stress increment resulting from the three preloading steps. The measured values fall in the range of Δu computed for the depth 0.1 and 0.5 m from the draining boundary, confirming that the theory by Tang & Onitsuka (2000) well describes the consolidation behaviour of the sediments. In the same picture, the piezometer P2, located into a lens, measured very low increments of pore pressure at the beginning of construction of each lift, as evidence of the sandy nature of the lenses.

Figure 6.4b shows the comparison between the excess pore pressure computed in the midpoint of the compressible layer and that measured by piezometer P4, placed in the middle of the sediment layer. It can be observed that the computed values overestimate the measured data during the first twenty days from the beginning of preloading, but the modelled trend traces over the measured data after the end of the embankment construction. The difference can be explained by the operating procedure during embankment construction. The coarse-grained

material used to build the embankment was supplied by trucks and temporary stored close to the test area to be distributed across the embankment print by means of excavators. Since the piezometer P4 is located close to this area, the initial high values of Δu are reasonably caused by the temporary presence of the material necessary for the entire layer in this small area, resulting in a pressure temporary higher than that due to the embankment layer. This explanation is confirmed by the subsequent trend, which is conversely well described by the model. The final established load is reached, and the discrepancy is no more effective.

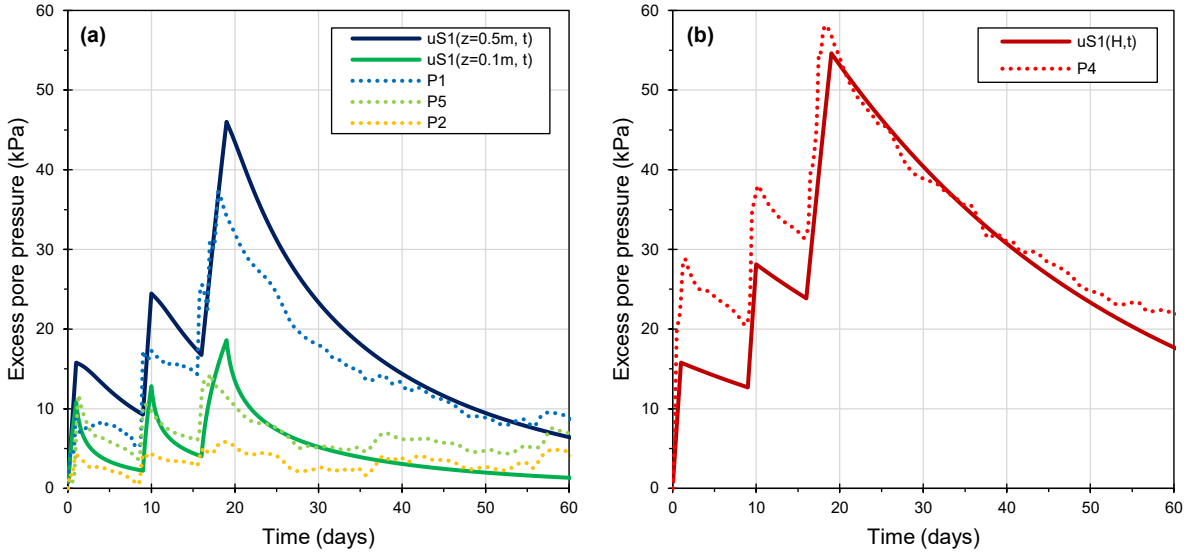

Figure 6.4. Comparison of excess pore pressures modelled by Tang & Onitsuka (2000) and those measured by piezometers.

The results above confirm that, starting from a geotechnical model based on the availability of laboratory and field tests, the time-dependent loading theory by Tang & Onitsuka, 2000 can be effectively applied to model consolidation of dredged sediments by PVDs for design purposes.

6.2 *Post operam* characterisation

6.2.1 In situ tests

After the embankment removal, the same series of CPTMs and CPTUs performed for the *ante operam* characterisation, described in § 5.2.2, was replicated, approximately at the same positions of the previous ones (Figure 6.5) to compare the recorded profiles and quantify the achieved improvement on the *ante operam* condition. Three continuous coring boreholes

performed next to as many CPTUs (Figure 6.5) allowed to get a more detailed stratigraphic profile and to collect undisturbed samples for laboratory testing (§ 6.2.2).

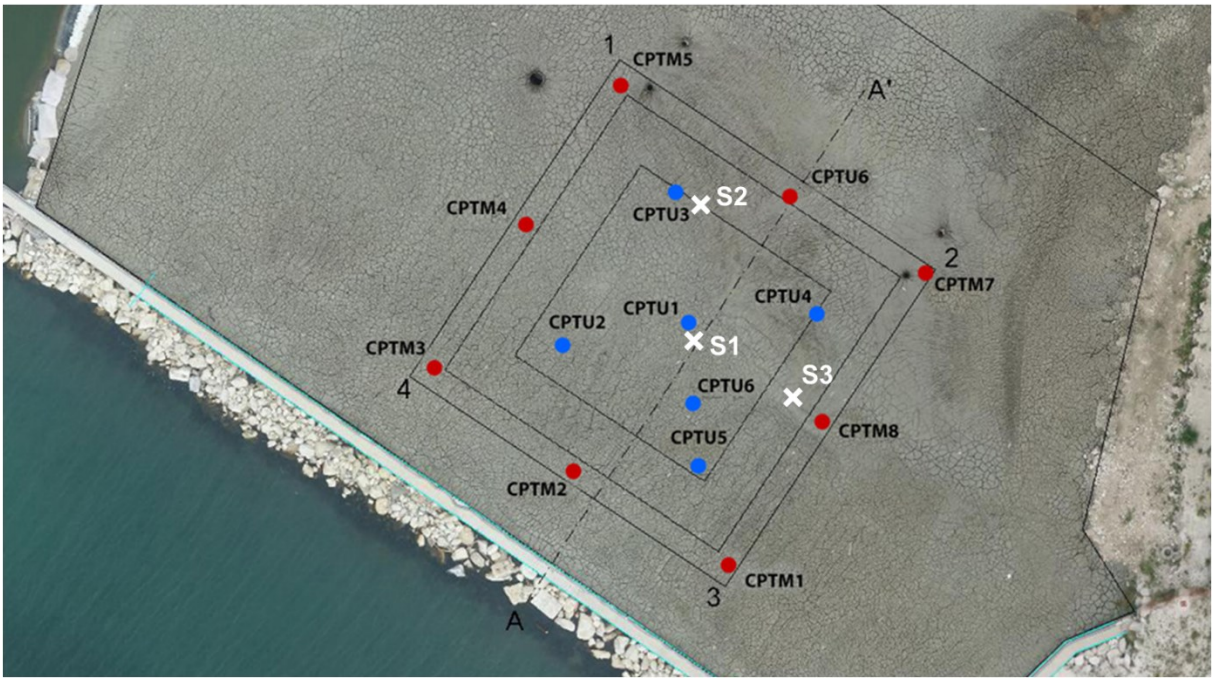

Figure 6.5. Planimetric layout of in situ tests performed post operam.

6.2.1.1 Cone penetration testing

Figure 6.6 to Figure 6.13 show the recorded profiles of the cone penetration resistance, q_c, sleeve friction, f_s, and friction ratio, R_f, obtained from the CPTMs performed after the embankment removal.

Figure 6.14 to Figure 6.19 show the recorded profiles of the corrected cone penetration resistance, q_t, sleeve friction, f_s and of the measured porewater pressure, u_2, obtained from the six CPTUs; the normalised soil behaviour type index, I_c, is also shown.

As already discussed (§ 3.2.1.1.2), normalisation of CPTU data required information about the unit weight of the sediment and depth of the water table, in order to assess the effective geostatic stresses. Similarly to the cone penetration tests performed before the embankment construction (§ 5.2.2.1), the depth of the water table was assumed with reference to the level of water inside the CDF. Thanks to the CNR monitoring, it was possible to trace the inner water level back to the dates of in situ testing, which resulted at about 70÷80 cm from the ground level. Salt water was assumed to saturate sediment porosity, with a unit volume weight, γ_w, equal to 10.1 kN/m^3.

As far as the unit volume weight of the sediments, γ_{sed}, in this case it was considered to be increased compared to the value *ante*, as a result of consolidation. Given the spatial

heterogeneity of the deposit, an average value of γ_{sed} was assigned to all the consolidated sediment layer, based on the experienced reduction of porosity. Starting from the results of CPTUs *ante*, for each vertical sounding the initial (i.e., before consolidation) thickness of the layer, H_0, and the total settlement, ΔH, recorded by the adjacent settlement gauge were considered to calculate the vertical strain, ε_z, induced by the preloading embankment, as reported in Table 6.4. The corresponding variation of the void ratio, Δe, was computed assuming an average value of the initial void ratio, $e_0 = 1.5$ (as inferred from *ante operam* data), leading to the final (i.e., after consolidation) void ratio, e_f, or, equivalently, the final porosity, n_f. Provided that the sediments are fully saturated, their unit volume weight after consolidation, $\gamma_{sed,f}$, was computed by:

$$\gamma_{sed,f} = \gamma_w G_s(1 - n_f) + \gamma_w n_f \tag{6.1}$$

with G_s = specific gravity of the sediments. The overall average value of the sediment unit weight after consolidation resulted equal to 17.3 kN/m^3.

Table 6.4. Assessment of the unit volume weight of the sediments after consolidation.

	CPTU1	**CPTU2**	**CPTU3**	**CPTU4**	**CPTU5**	**CPTU6**
	A7	A10	A6	A4	A3	A7-A3
Initial void ratio, e_0 (-)	1.50	1.50	1.50	1.50	1.50	1.50
Initial porosity, n_0 (-)	0.60	0.60	0.60	0.60	0.60	0.60
Initial thickness of the layer, H_0 (m)	7.20	7.60	6.00	7.10	7.50	7.60
Total settlement, ΔH (m)	0.46	0.36	0.50	0.49	0.47	0.47
Vertical strain, ε_z (-)	0.06	0.05	0.08	0.07	0.06	0.06
Void ratio variation, Δe (-)	0.16	0.12	0.21	0.17	0.16	0.15
Final void ratio, e_f (-)	1.34	1.38	1.29	1.33	1.34	1.35
Final porosity, n_f (-)	0.57	0.58	0.56	0.57	0.57	0.57
Unit volume weight of sea water, γ_w (kN/m^3)	10.10	10.10	10.10	10.10	10.10	10.10
Specific gravity, G_s (-)	2.67	2.67	2.67	2.67	2.67	2.67
Initial unit volume weight of sediments, $\gamma_{sed,0}$ (kN/m^3)	16.90	16.90	16.90	16.90	16.90	16.90
Final unit volume weight of sediments, $\gamma_{sed,f}$ (kN/m^3)	17.32	17.19	17.47	17.36	17.32	17.30

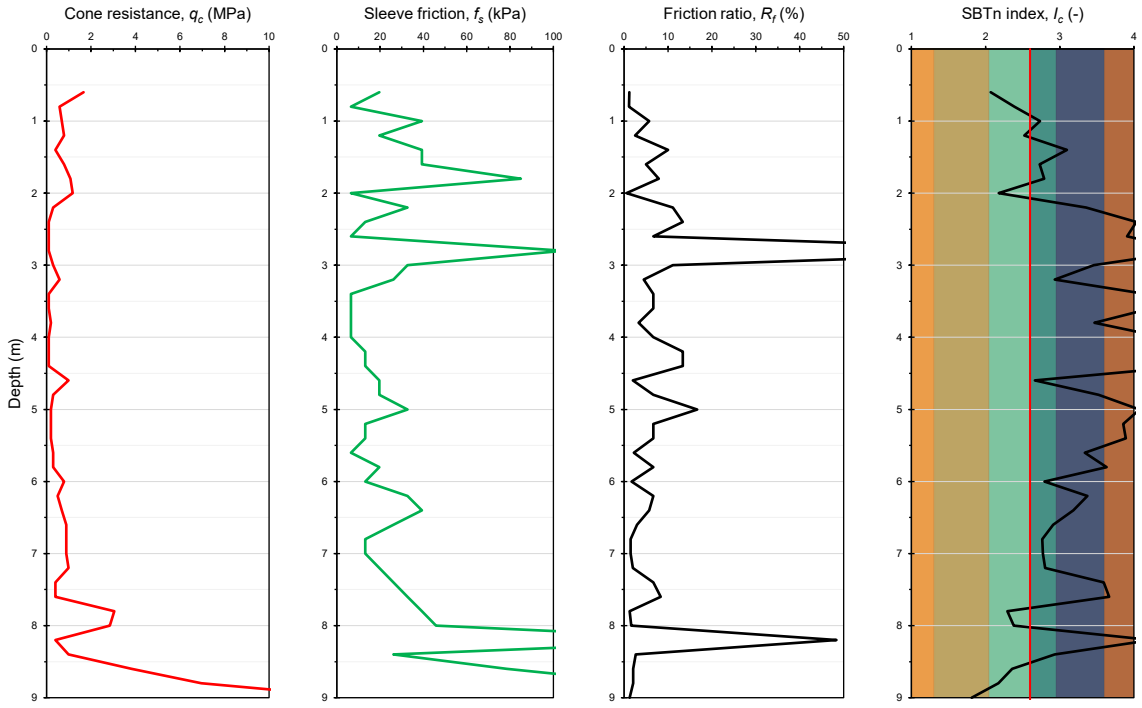

Figure 6.6. CPTM1-POST.

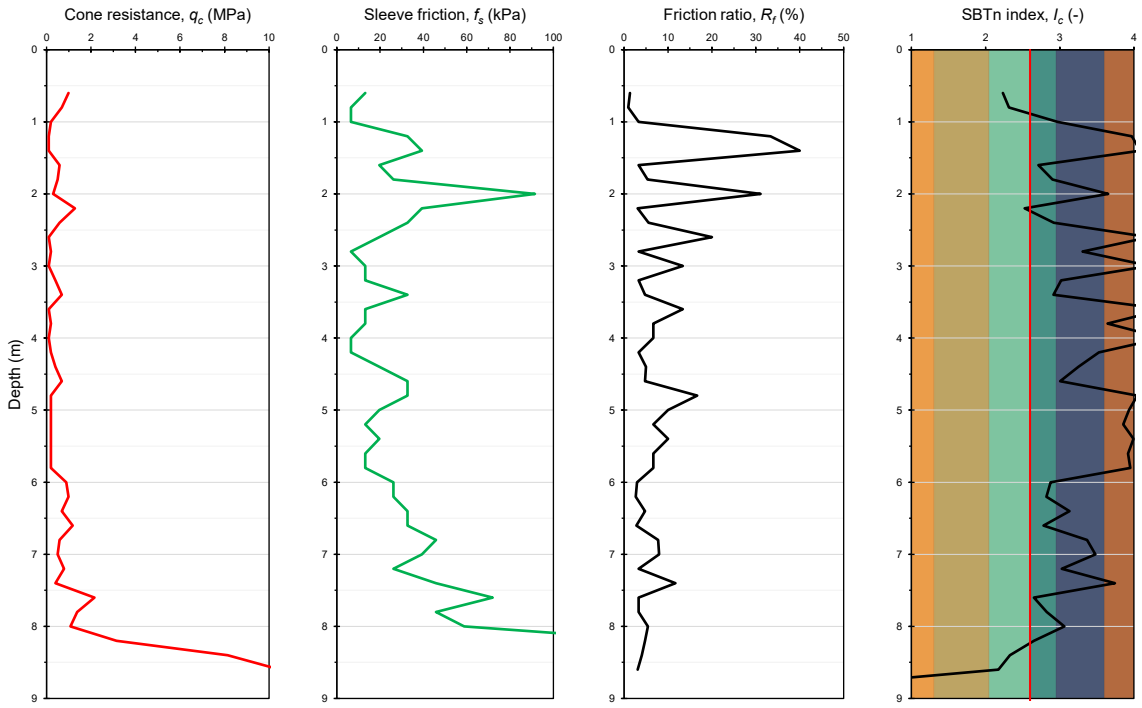

Figure 6.7. CPTM2-POST.

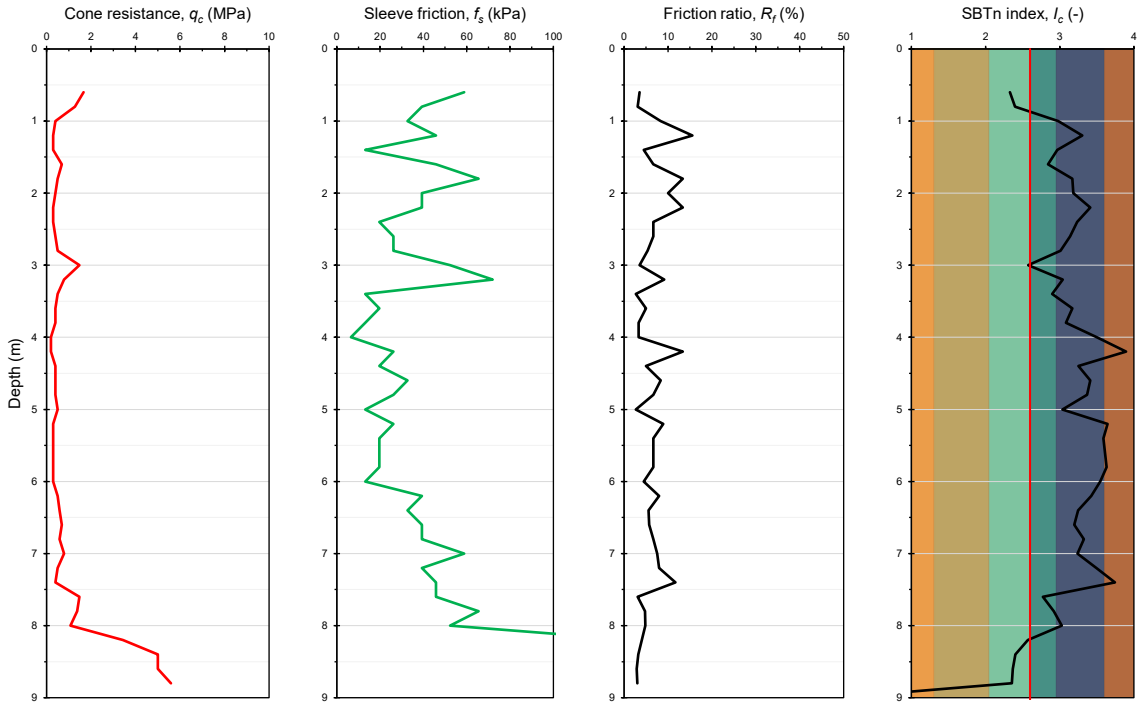

Figure 6.8. CPTM3-POST.

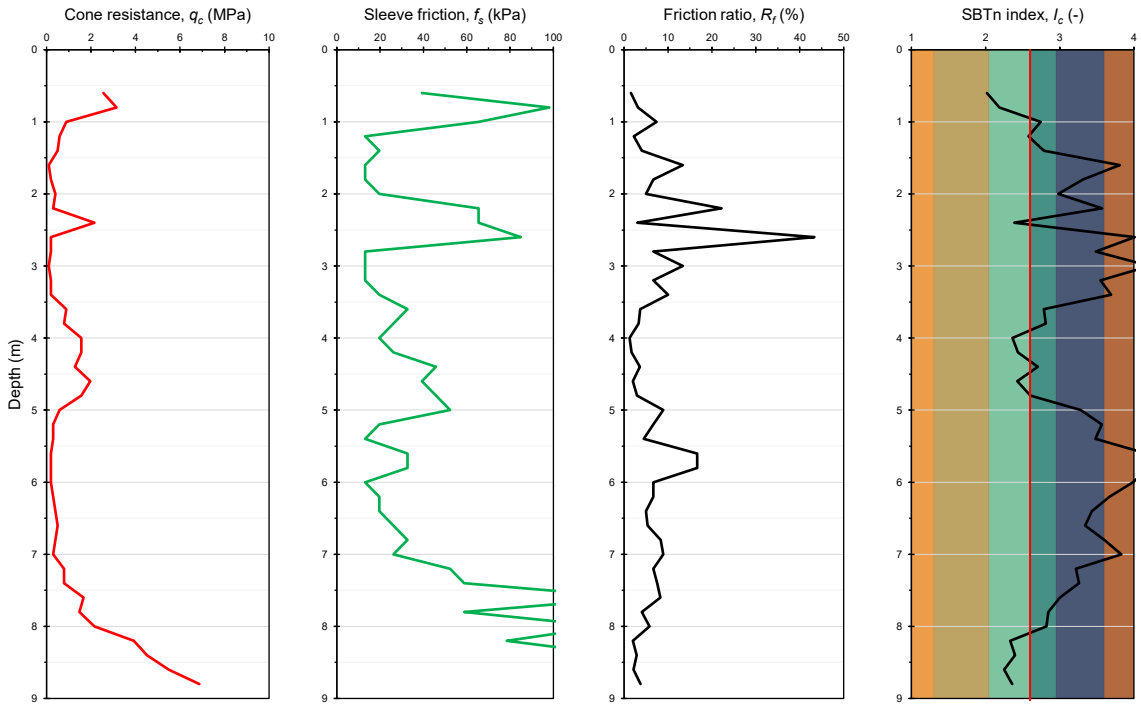

Figure 6.9. CPTM4-POST.

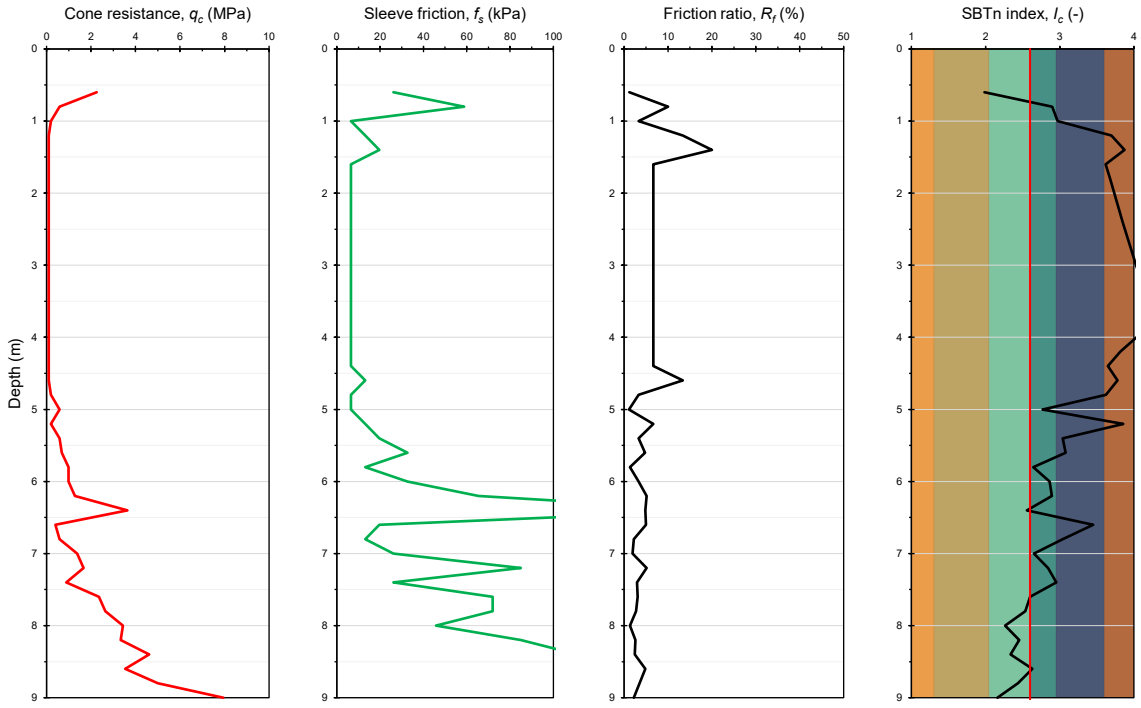

Figure 6.10. CPTM5-POST.

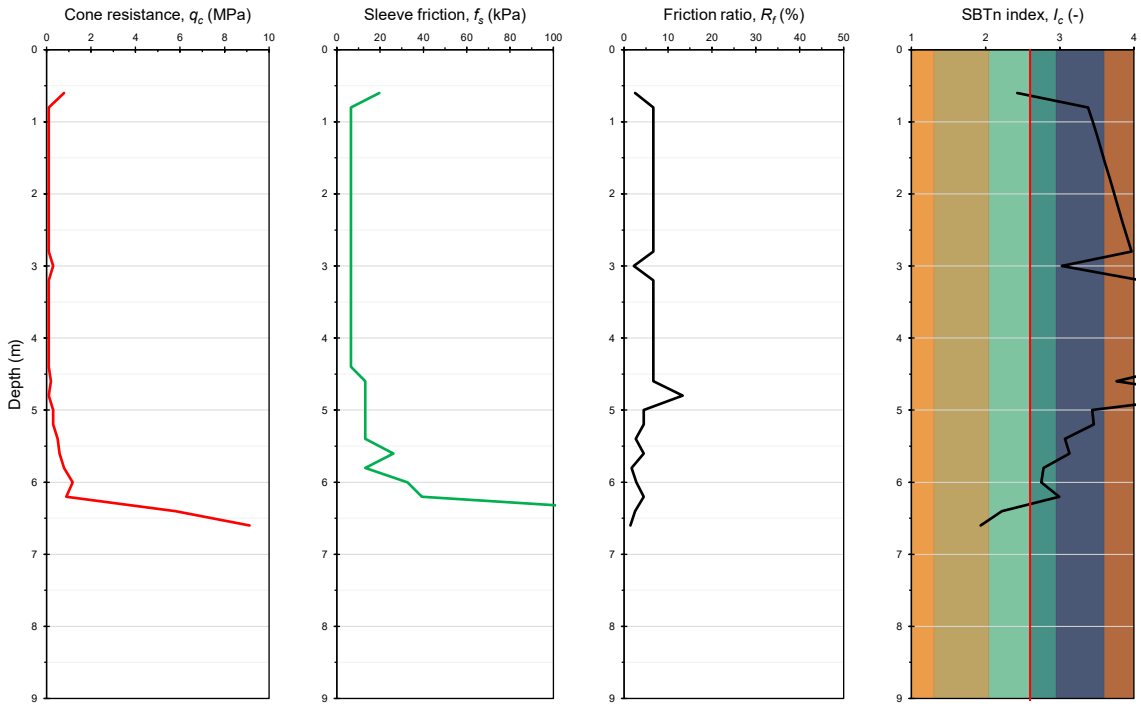

Figure 6.11. CPTM6-POST.

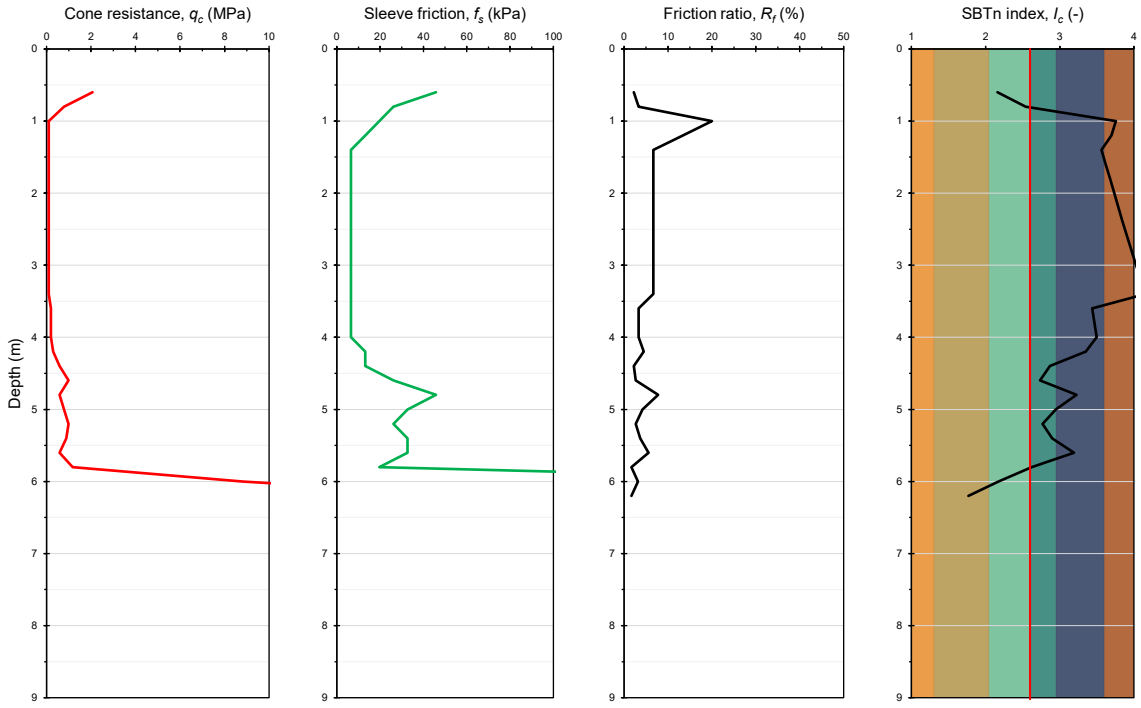

Figure 6.12. CPTM7-POST.

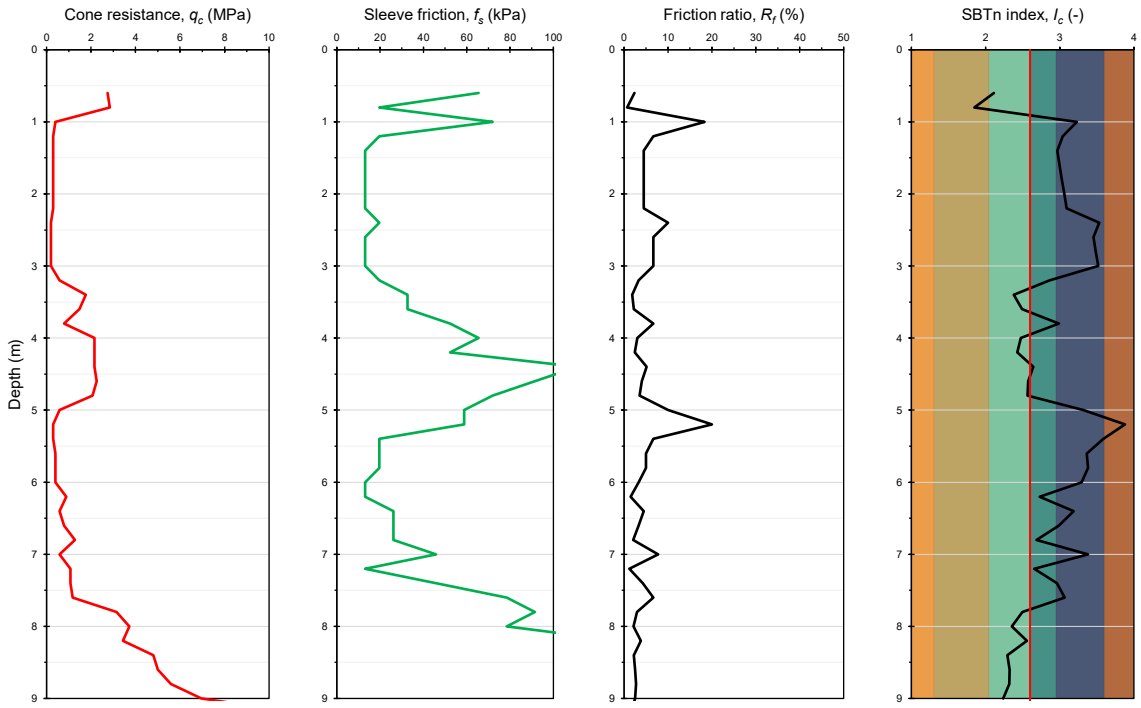

Figure 6.13. CPTM8-POST.

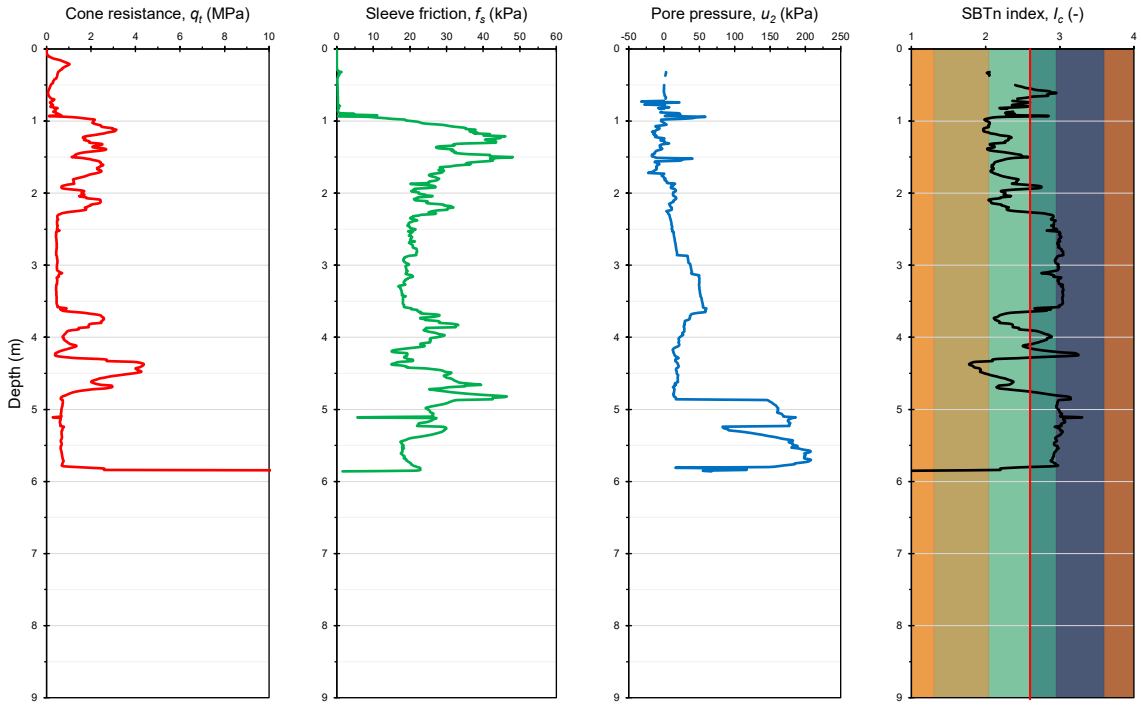

Figure 6.14. CPTU1-POST.

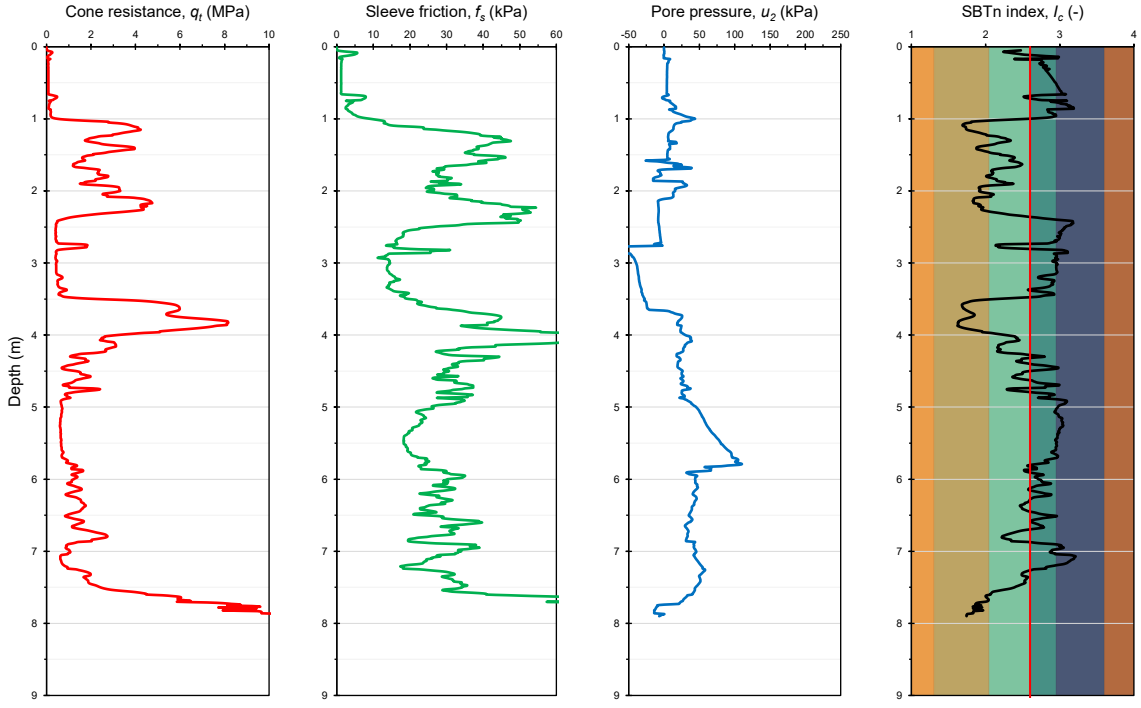

Figure 6.15. CPTU2-POST.

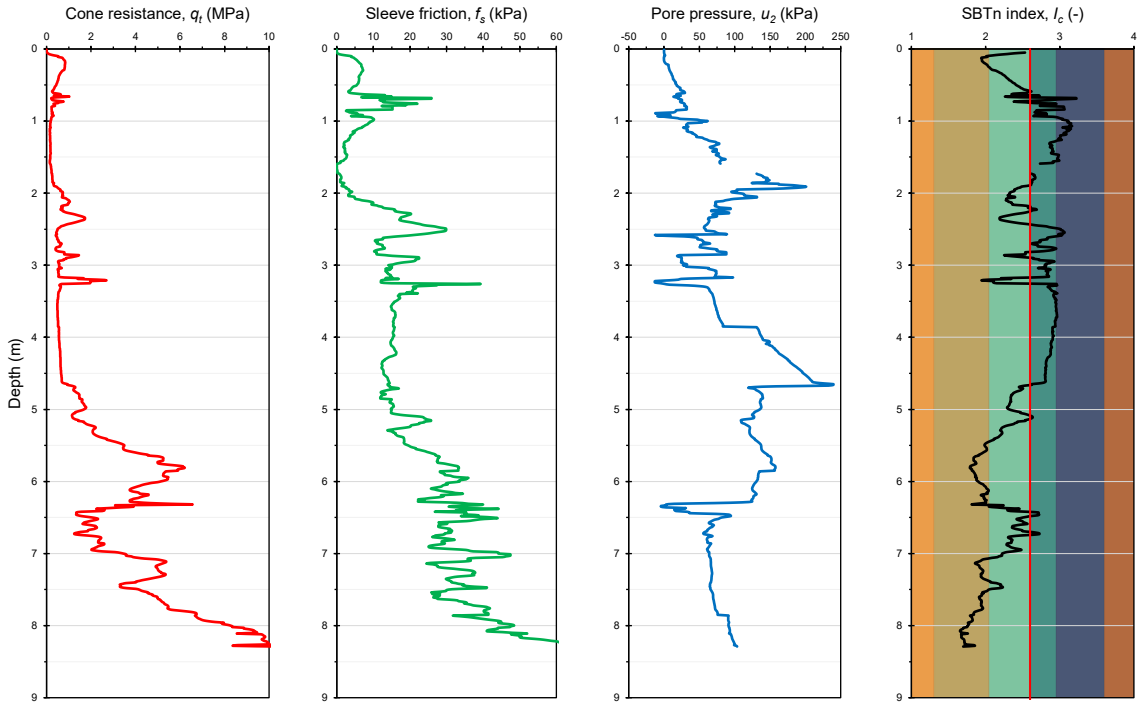

Figure 6.16. CPTU3-POST.

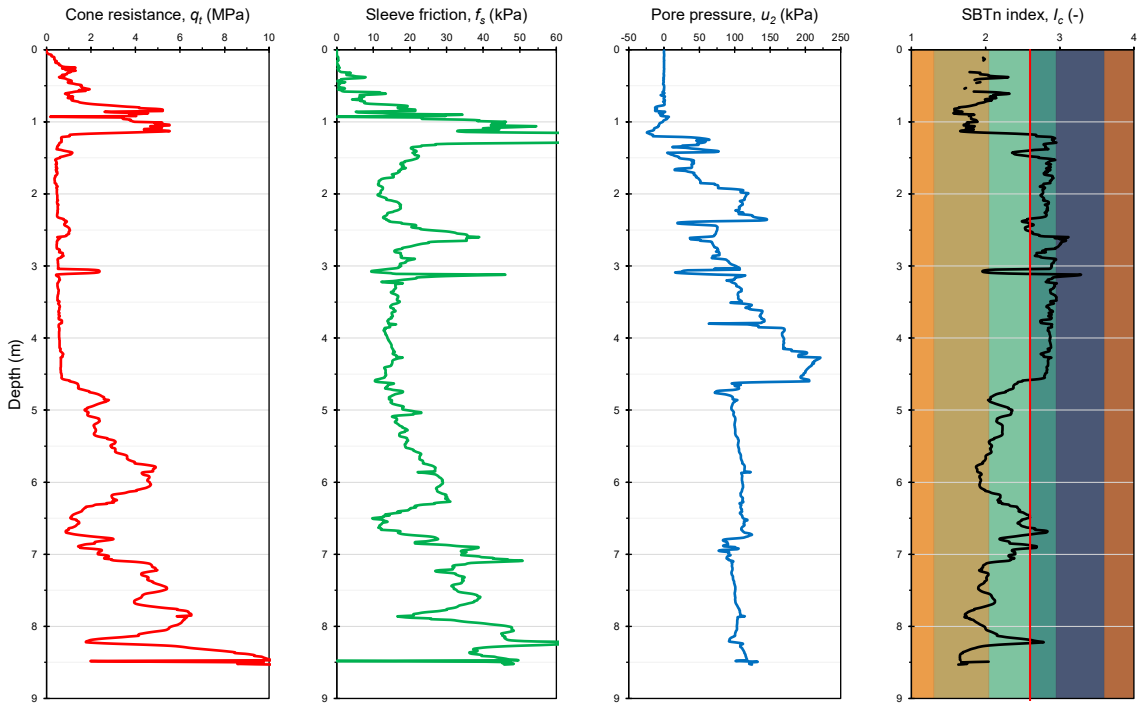

Figure 6.17. CPTU4-POST.

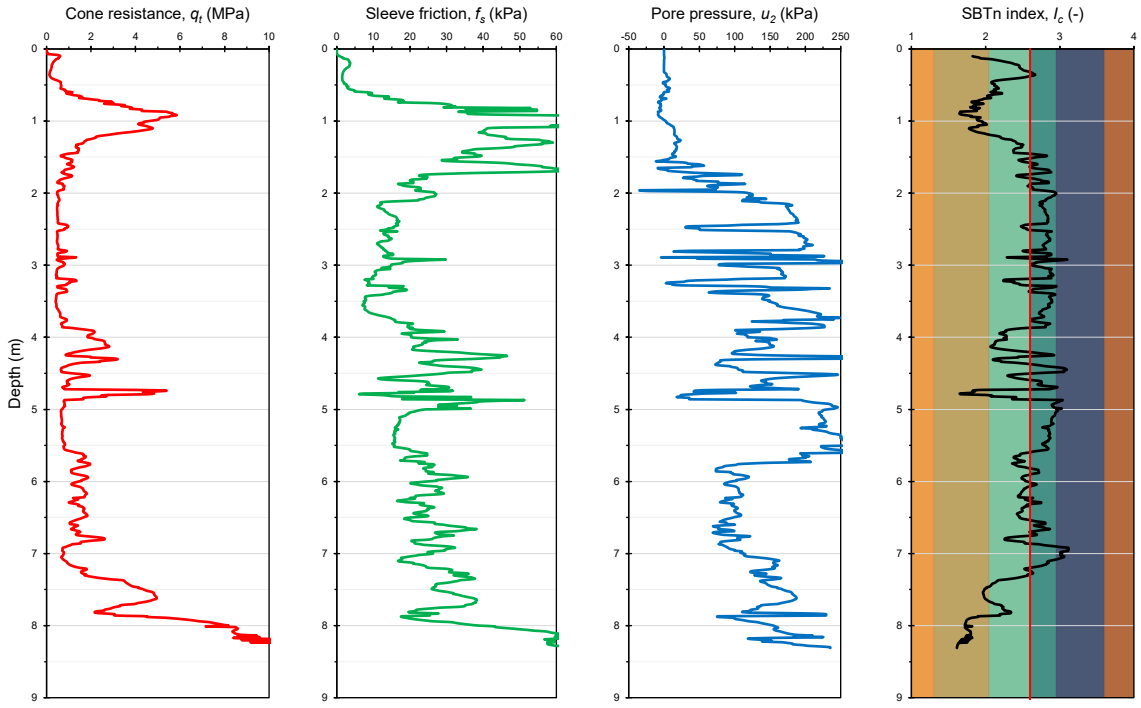

Figure 6.18. CPTU5-POST.

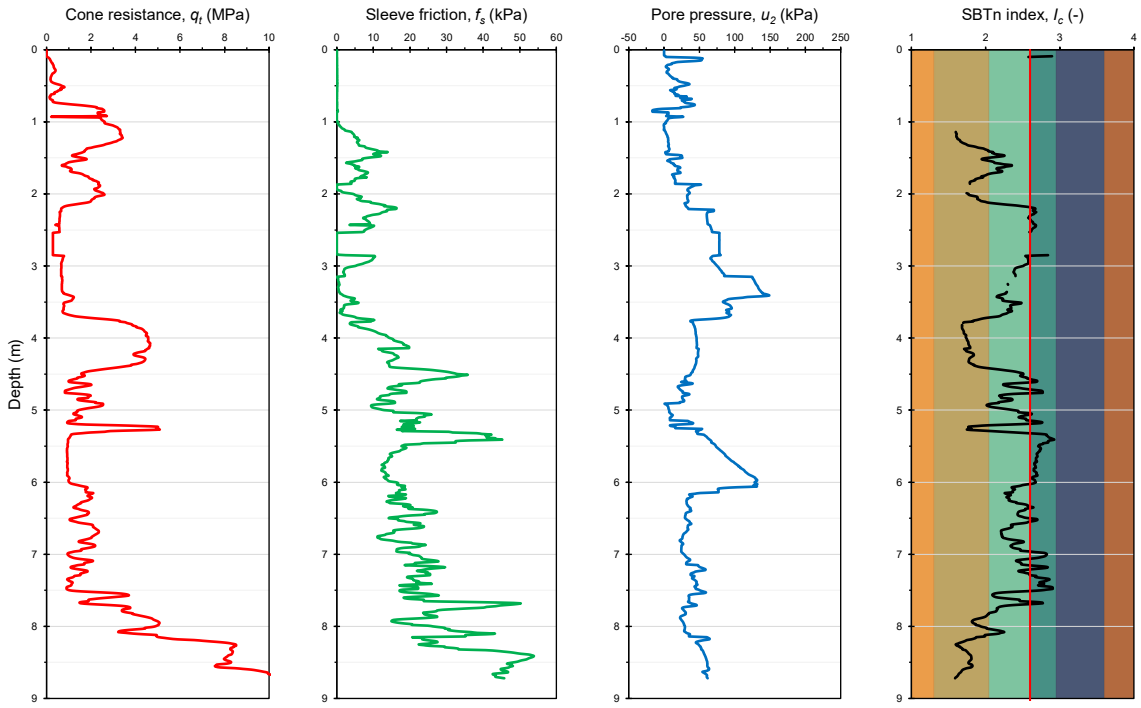

Figure 6.19. CPTU6-POST.

Figure 6.20 shows the q_t profiles for *ante* and *post* conditions for each CPTU location. For convenience, the q_t profiles *ante* and *post* have been reported at the same zero, disregarding the consolidation settlements of the ground level[11]; unless the depth offset, the picture offers a good view of the improvement achieved by consolidation. With particular reference to the clay-like layers, the corrected cone tip resistance almost quintupled, from about 100 kPa before the embankment construction to at least 500 kPa after its removal.

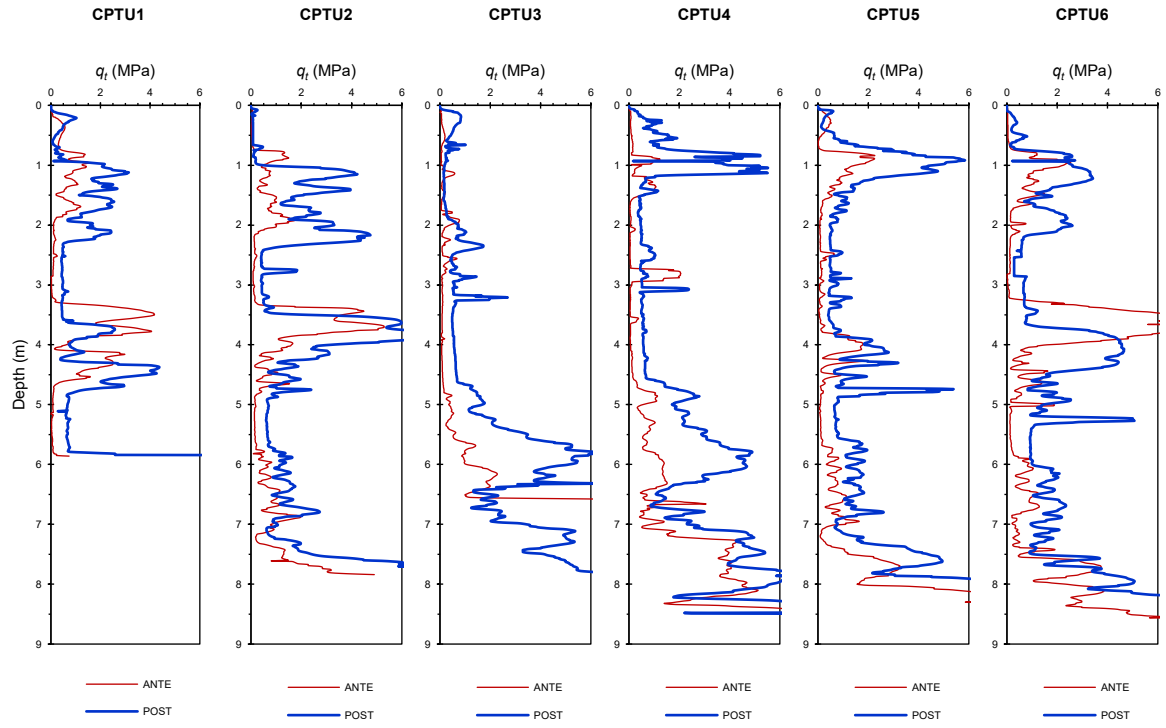

Figure 6.20. Comparison of corrected cone tip resistance between ante and post operam conditions.

The impact of the applied mechanical overconsolidation can be also appreciated by comparing the soil classification resulting from CPTU tests for the *ante* and *post* conditions. From the Robertson (2016) charts reported in Figure 6.21, a migration of *post* data towards the upper left corner is plainly visible, as evidence of a more sand-like response to penetration (increased strength and stiffness), and transition from contractive to dilative behaviour.

[11] A perfect matching is virtually impossible, because not all sediment layers contribute equally to deformation (fine-grained sediments have compressed more than stiffer sandy lenses), and because of unavoidable spatial variability between CPTU soundings *ante* and *post*.

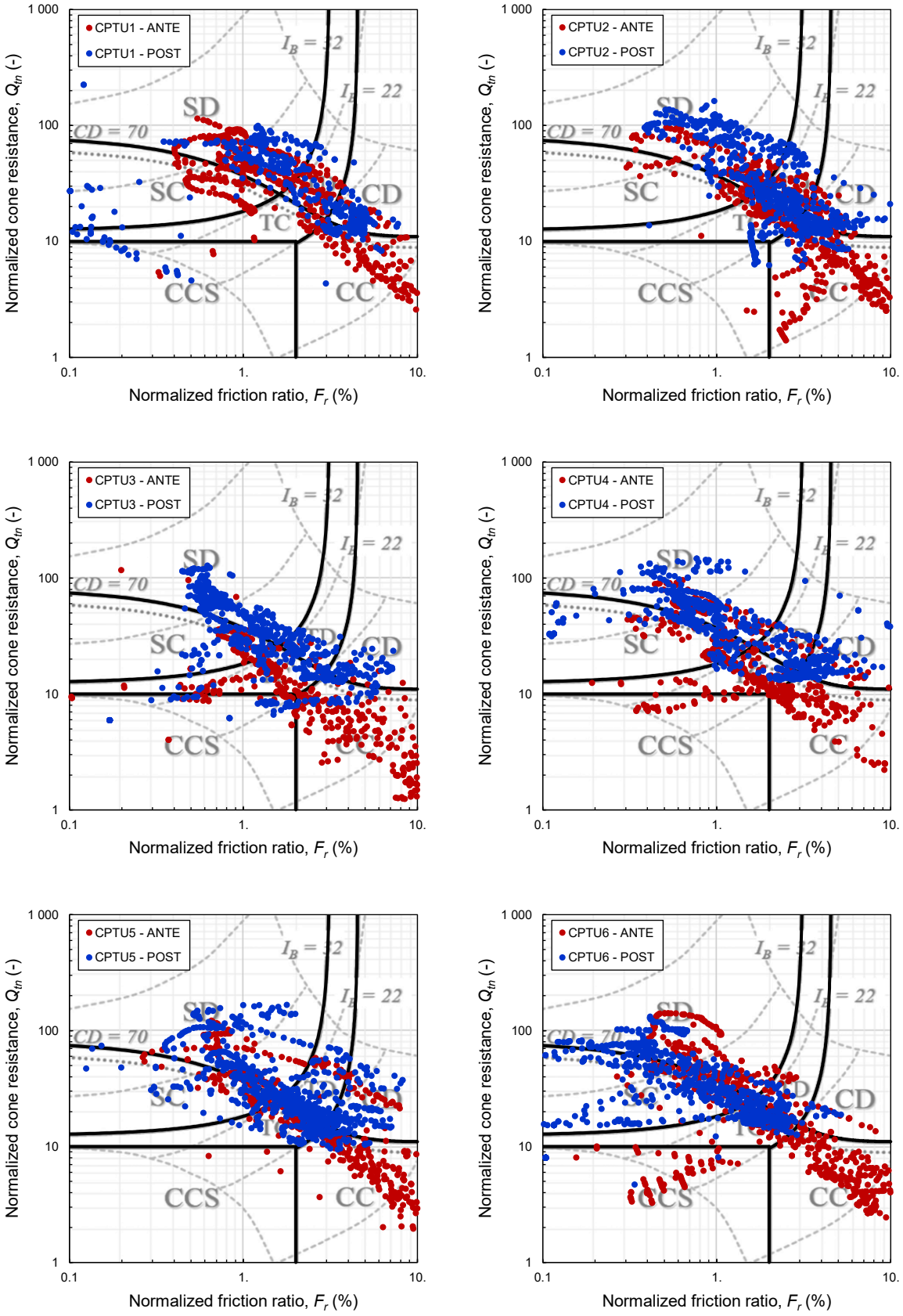

Figure 6.21. Comparison of classification charts by Robertson (2016) for ante operam and post operam conditions for the six piezocone soundings.

6.2.1.2 In situ sampling

After about 2 months from the embankment removal, three borings were drilled in the test field area, with the twofold aim of recovering undisturbed samples and proving confirmation of the desk study about stratigraphy. Depths larger than 7 m below the ground level were explored, in order to reach the dense sandy layer of the original seabed. Specifically, the verticals S1, S2, and S3 were drilled up to depths of 7.5, 7.7 and 9.0 m below the ground level, respectively, by means of the rotary drilling apparatus shown in Figure 6.22.

Figure 6.22. The drilling rig S30 (by Mori s.r.l.), mounted on a crawler truck, during the geotechnical campaign after the embankment removal.

As reported in the plan view of Figure 6.5, the three boreholes were drilled in proximity (about 1 m away) of cone penetration test logs, in order to associate cone penetration results to the actual stratigraphic profile and to the physical and mechanical properties measured on the samples. In particular, 8 undisturbed samples were collected (cfr. Table 6.6) using a thin-wall sampler tube with a diameter of 101 mm. Drill cores were then placed in the cataloguing PVC boxes, to use them for classification tests. Figure 6.23, Figure 6.24, and Figure 6.25 show the core boxes for the three boreholes.

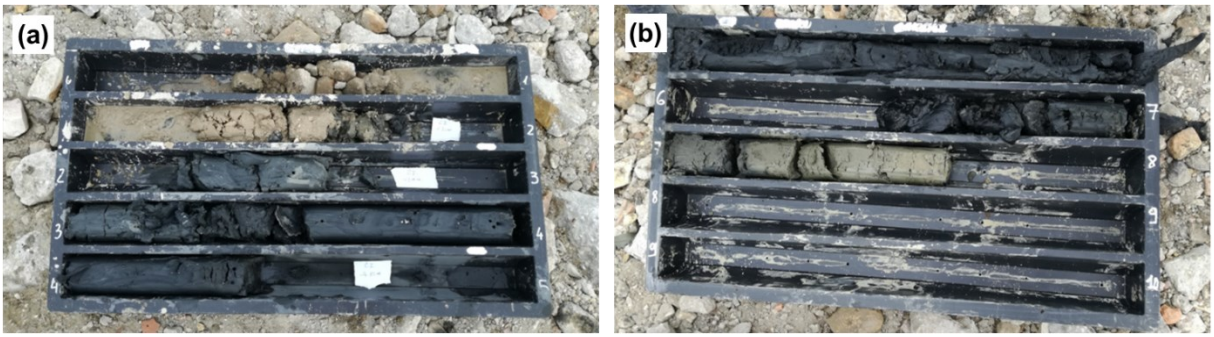

Figure 6.23. Core boxes from borehole S1: (a) from 0 to 5 m; (b) from 5 to 10 m.

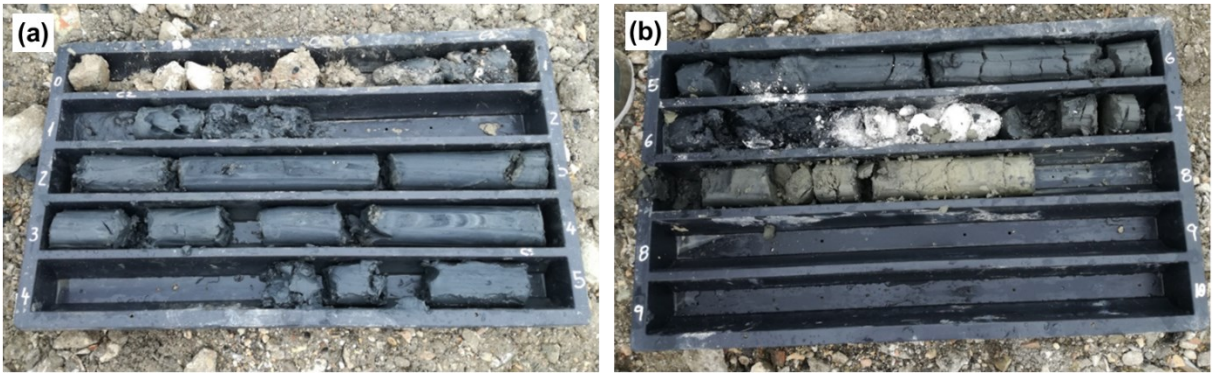

Figure 6.24. Core boxes from borehole S2: (a) from 0 to 5 m; (b) from 5 to 10 m.

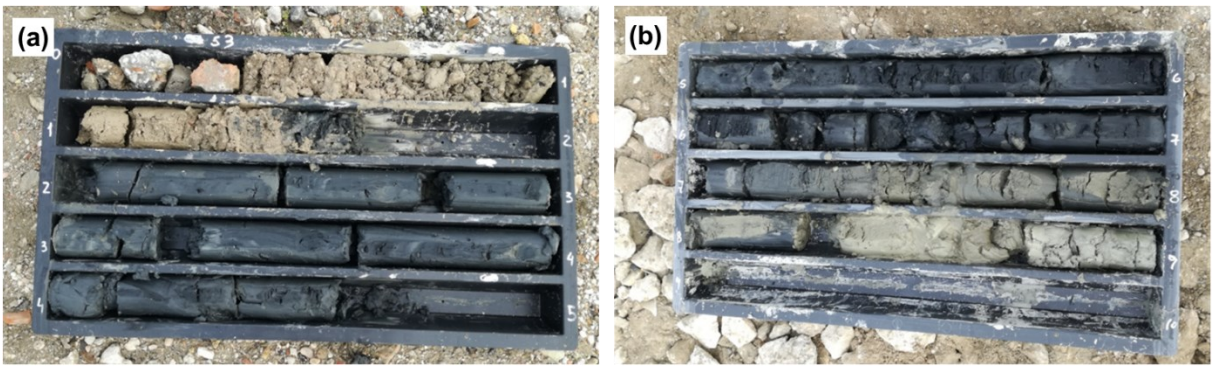

Figure 6.25. Core boxes from borehole S3: (a) from 0 to 5 m; (b) from 5 to 10 m.

In all the boreholes, three main soil units were detected. From the top downwards:

- Unit A: consisting of crushed stones and gravels, it forms basically the coarser layer appositely laid out to serve as paving and top drainage boundary.
- Unit B: described as silts and sandy silts, it is characterised by a very dark colour and high plasticity. This is the dredged sediment.
- Unit C: it consists of dense silty sands identifying the original seabed (base layer).

The borehole S1 was drilled near the CPTU1, at the centre of embankment footprint. In this borehole the thickness of Unit A was detected to be of about 1.7 m. The dredged sediment thickness was about 5.5 m, with a decrease in the amount of sand from the depth of 4.50 m (Figure 6.26a). The borehole S2 was drilled next to CPTU3. Here the thickness of the topsoil was 1.0 m, and the sediment layer had a thickness of 6.0 m (Figure 6.26b). The borehole S3 was performed next to CPTM8. Here the thickness of the topsoil was 1.5 m, the sediment layer 6.0 m; from the depth of 5.2 m, the sand fraction was found to increase (Figure 6.26c).

On the intact cohesive drilling cores packed in the boxes, fast measurements of the unconfined compressive strength, q_u, were made in the field by means of a pocket penetrometer. This allowed for a rough estimate of the undrained shear strength, s_u, since for saturated clays the following relation applies:

$$s_u = q_u/2 \tag{6.2}$$

Measured data of q_u and the derived values of s_u are reported in Table 6.5 for the three borehole logs. The distribution of the s_u values along the depth is also illustrated in Figure 6.26. Noticed that values of s_u are mostly included in the range 20÷40 kPa typically indicated for soft clays.

Table 6.5. Results of pocket penetrometer tests on the drilling cores.

	S1		S2		S3	
Depth, z	Unconfined compressive strength, q_u	Undrained shear strength, s_u	Unconfined compressive strength, q_u	Undrained shear strength, s_u	Unconfined compressive strength, q_u	Undrained shear strength, s_u
(m)	(kg/cm^2)	(kPa)	(kg/cm^2)	(kPa)	(kg/cm^2)	(kPa)
2.0	-	-	-	-	0.5	24.5
2.5	0.8	39.2	0.8	39.2	0.7	34.3
3.0	-	-	0.8	39.2	0.6	29.4
3.5	0.6	29.4	0.8	39.2	0.6	29.4
4.0	0.8	39.2	0.8	39.2	0.7	34.3
4.5	0.5	24.5	-	-	0.8	40.7
5.0	-	-	0.6	29.4	0.4	19.6
5.5	0.7	34.3	0.6	29.4	0.8	39.2
6.0	1.0	49.0	0.6	29.4	0.5	24.5
6.5	-	-	-	-	0.6	29.4
7.0	-	-	1.1	53.9	0.6	29.4
7.5	-	-	1.3	63.7	0.8	39.2

Note: values of q_u are measured, values of s_u are computed.

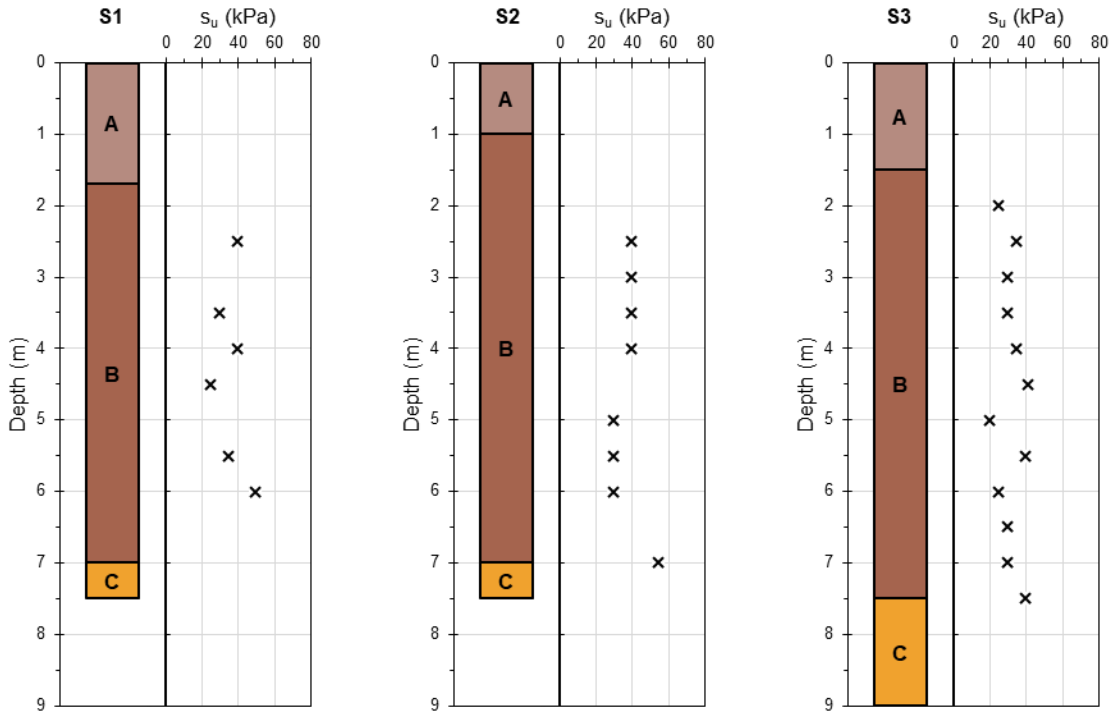

Figure 6.26. Borehole logs and values of the undrained shear strength, s_u, derived from pocket penetrometer data for the three boreholes S1, S2, and S3. Description of the soil units: "A" = crushed stone and gravel (topsoil); "B" = silt and dark sandy silt, very plastic (dredging filling); "C" = grey silty sands (base layer).

6.2.2 Laboratory tests results

After the consolidation treatment, the sediment deposit reached such a consistency to allow for collecting also undisturbed samples, together with representative samples to perform classification tests and mineralogical analyses along the investigated verticals. Undisturbed samples were essential to study sediment compressibility and undrained shear strength after the consolidation treatment; specifically, oedometer tests and triaxial tests were carried out to the purpose.

Table 6.6 presents a synopsis of all the laboratory tests performed in the *post operam* phase; for each sample, the borehole of origin and the sampling depth are indicated, together with the designation: undisturbed sample are denoted by the letter "C" and a serial number; representative samples, taken from the drilling cores, are marked by "R" and the sampling depth.

Table 6.6. Synopsis of laboratory tests performed on undisturbed and representative samples during the post-operam characterisation phase.

Borehole	Sample	Depth	Performed laboratory tests
S1	R-1.3m	1.3 m	Hydrometer test
			Sieve analysis
			Atterberg limits
	C1	1.7÷2.0 m	---
	R-2.3m	2.3 m	Hydrometer test
			Sieve analysis
			Atterberg limits
			XRD analysis
	C2	2.5÷3.0 m	Oedometer test by incremental loading
			Atterberg limits
			CIU on undisturbed clay
			CIU on reconstituted clay
	R-3.1m	3.1 m	Atterberg limits
	R-3.4m	3.4 m	Hydrometer test
			Atterberg limits
	R-3.8m	3.8 m	Hydrometer test
			Atterberg limits
	R-4.0m	4.0m	Hydrometer test
	C3	4.5-5.0 m	Hydrometer test
			Atterberg limits
			CIU on undisturbed clay
			UU on undisturbed clay
	R-5.3m	5.3 m	Hydrometer test
			Sieve analysis
			Atterberg limits
			XRD analysis
	R-5.5m	5.5 m	Atterberg limits
	C4	6.0÷6.5 m	Determination of amount material finer than 75 μm
			Sieve analysis on the material retained on No. 200 ASTM sieve
S2	C1	1.5 m	Hydrometer test
			Atterberg limits
			XRD analysis
			Oedometer test by incremental loading
			CIU on undisturbed clay
			UU on undisturbed clay
	C2	4.0 m	Hydrometer test
			Atterberg limits
			XRD analysis
			UU on undisturbed clay
S3	C1	1.5 m	---
	C2	4.5 m	---

Note: C = undisturbed sample; R = representative sample.

6.2.2.1 Classification tests

Several classification tests were performed both on undisturbed and representative samples taken in the borehole S1, in order to assess if there exist any consistency between the physical description of the sediments and the behaviour-based description in the adjacent CPTU1 sounding. The few shells found in the samples were removed by hand before each test and, in most cases, all the material passed the no. 10 sieve, with only few exceptions; hence, the hydrometer test was carried out systematically.

Figure 6.27 shows all the grading curves. A certain similarity between the samples taken at depths of 2.3, 3.8, 4.0, 5.0, and 5.3 m from the ground level can be noticed, all being fine-grained (fine fraction, $FF > 90\%$), with a clay fraction between 35% and 40%, whereas the grading curves at 3.4 m and 6.0 m are indicative of a transition towards more coarser sediments ($FF \approx 50\%$). The sediment at 1.3 m is completely different from the others, with a predominant sandy fraction and a low fine content ($FF \approx 15\%$).

Figure 6.28 shows the plasticity chart for all the samples tested along the vertical S1. Results of both grain-size distribution and Atterberg limits have been combined in Table 6.7, to provide the USCS classification. In particular, the fine-grained sediments were identified as fat clays (CH) or elastic silts (MH), while the coarser lenses were essentially silty sands (SM).

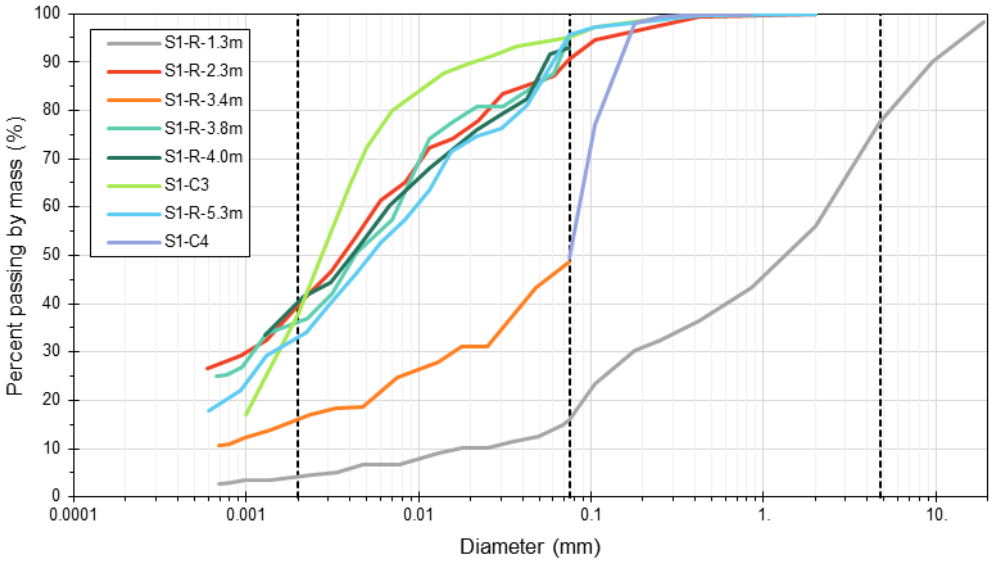

Figure 6.27. Grading curves for all the samples investigated along the vertical S1.

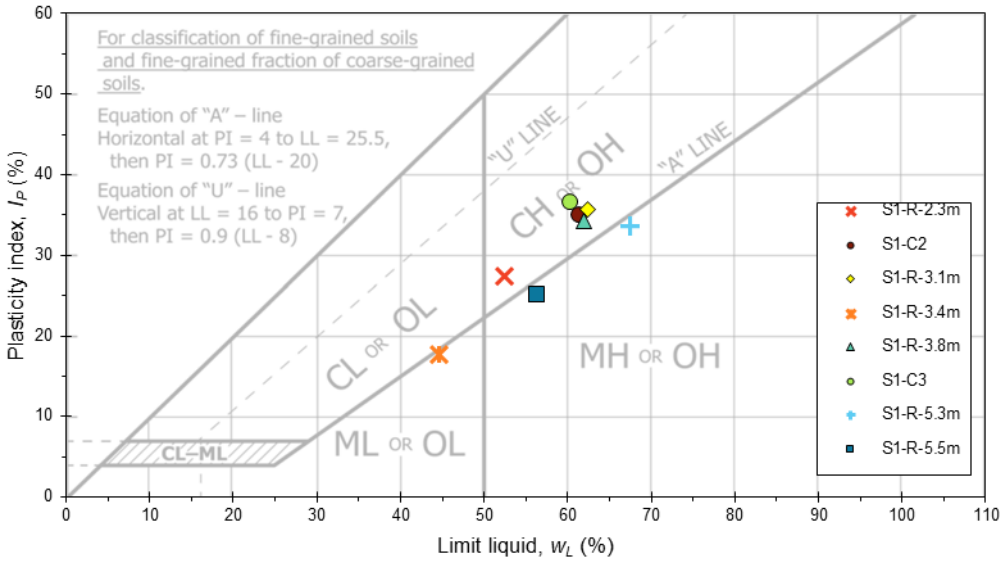

Figure 6.28. Plasticity chart for the samples of vertical S1.

Table 6.7. Results of particle size analyses and Atterberg limits performed on the samples taken in borehole S1.

Sample	Clay	Silt	Sand	Gravel	LL	PL	PI	USCS
	(%)	(%)	(%)	(%)	(%)	(%)	(%)	(-)
S1-R-1.3m	4.2	11.9	61.5	22.4	-	-	NP	SM
S1-R-2.3m	39.6	51.1	9.3	0.0	52.4	25.0	27.4	CH
S1-C2 (2.5m)	-	-	-	-	61.4	26.3	35.1	CH
S1-R-3.1m	-	-	-	-	62.4	26.7	35.7	CH
S1-R-3.4m	16.1	32.5	51.4	0.0	44.7	26.9	17.7	SM
S1-R-3.8m	36.4	59.0	4.6	0.0	62.0	27.7	34.3	CH
S1-R-4.0m	40.2	52.7	7.0	0.0	-	-	-	CH
S1-C3 (5.0m)	38.1	57.1	4.8	0.0	60.3	23.6	36.7	CH
S1-R-5.3m	33.0	62.6	4.4	0.0	67.4	33.9	33.6	MH
S1-R-5.5m	-	-	-	-	56.3	31.2	25.1	MH
S1-C4 (6.0m)	-	-	50.1	0.0				SM

In Figure 6.29 particle size fractions and Atterberg limits have been associated to the profile of the cone penetration resistance recorded in CPTU1, to get a visual representation of the results along the depth. It can be observed that those layers identified as clay-like soils by the CPT-based classification chart, exhibit the same plasticity and grain size characteristics. In particular, wherever fine fraction is the main component of the sediment ($FF > 90\%$), the plasticity index is systematically around 35%. Where the fine content is significantly lower, the

plasticity is also reduced (mainly by the decrease in the liquid limit), up to the non-plastic sandy sediments.

It may be concluded that a reasonably good correspondence exists between the cone sounding CPTU1 and the boring S1 drilled within a few meters from it, unless minor unavoidable differences which can be attributed to the not perfectly level disposal of the sediments inside the CDF.

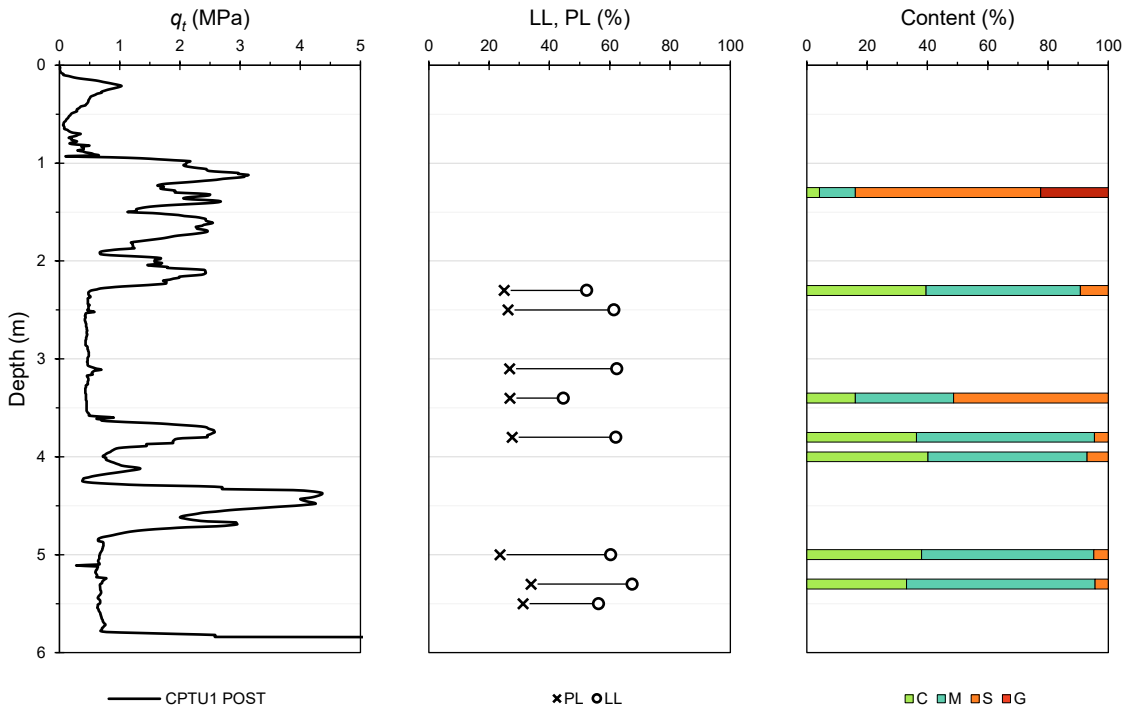

Figure 6.29. Visual representation of Atterberg Limits and grain size distribution results along the depth as associated to CPTU1.

The same classification tests were also performed on the two undisturbed samples collected from boring S2. Grading curves and plasticity chart are shown in Figure 6.30 and Figure 6.31, respectively. As indicated in Table 6.8, the shallower sample was classified as a sandy lean clay (CL) having about 30% of sand, while the deeper sample resulted to be a fat clay (CH), very similar to that of vertical S1 (fine fraction, $FF \approx 95\%$; clay fraction, $CF \approx 40\%$).

As already done for vertical S1, Figure 6.32 depicts physical descriptors next to the cone penetration resistance profile measured in the adjacent CPTU3 sounding. Although in this case only two points were investigated, a quite good correspondence with soil-behaviour type description can be established.

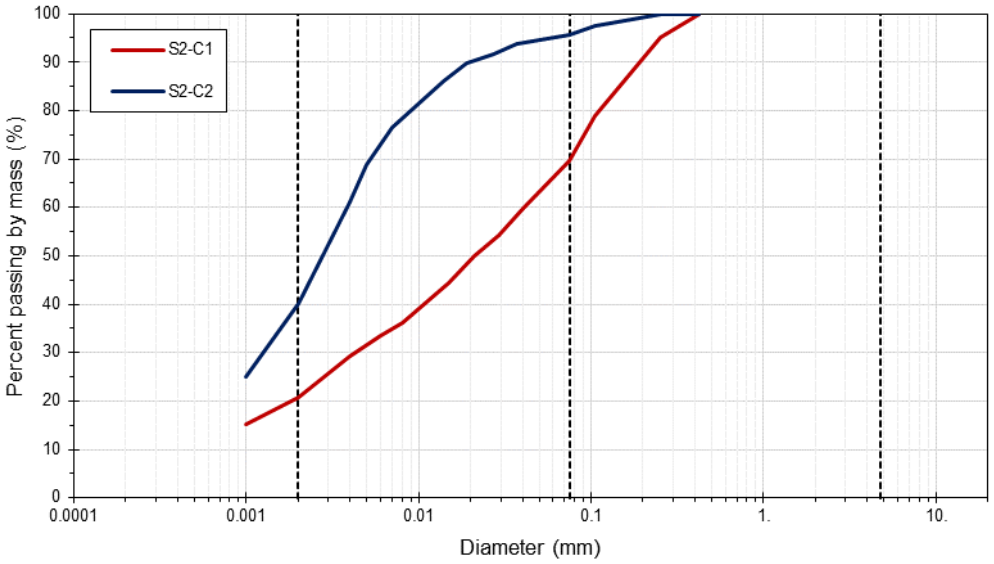

Figure 6.30. Grading curves for all the samples investigated along the vertical S2.

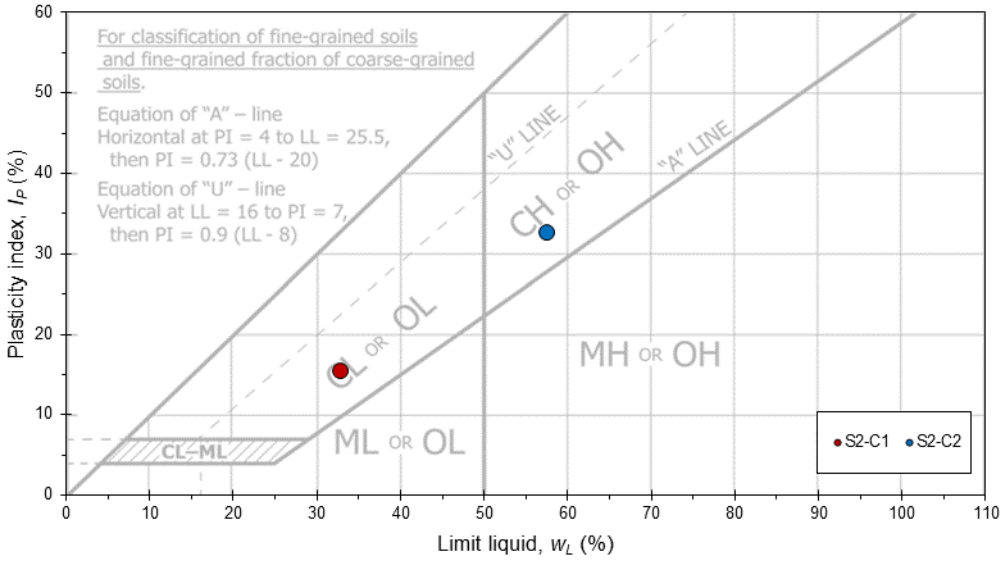

Figure 6.31. Plasticity chart for the vertical S2.

Table 6.8. Results of particle size analyses and Atterberg limits performed on the samples taken in borehole S2.

Sample	Clay	Silt	Sand	Gravel	LL	PL	PI	USCS
	(%)	(%)	(%)	(%)	(%)	(%)	(%)	(-)
S2-C1 (1.5m)	20.9	48.7	30.4	0.0	32.8	17.4	15.4	CL
S2-C2 (4.0m)	40.2	55.4	4.4	0.0	57.5	24.9	32.6	CH

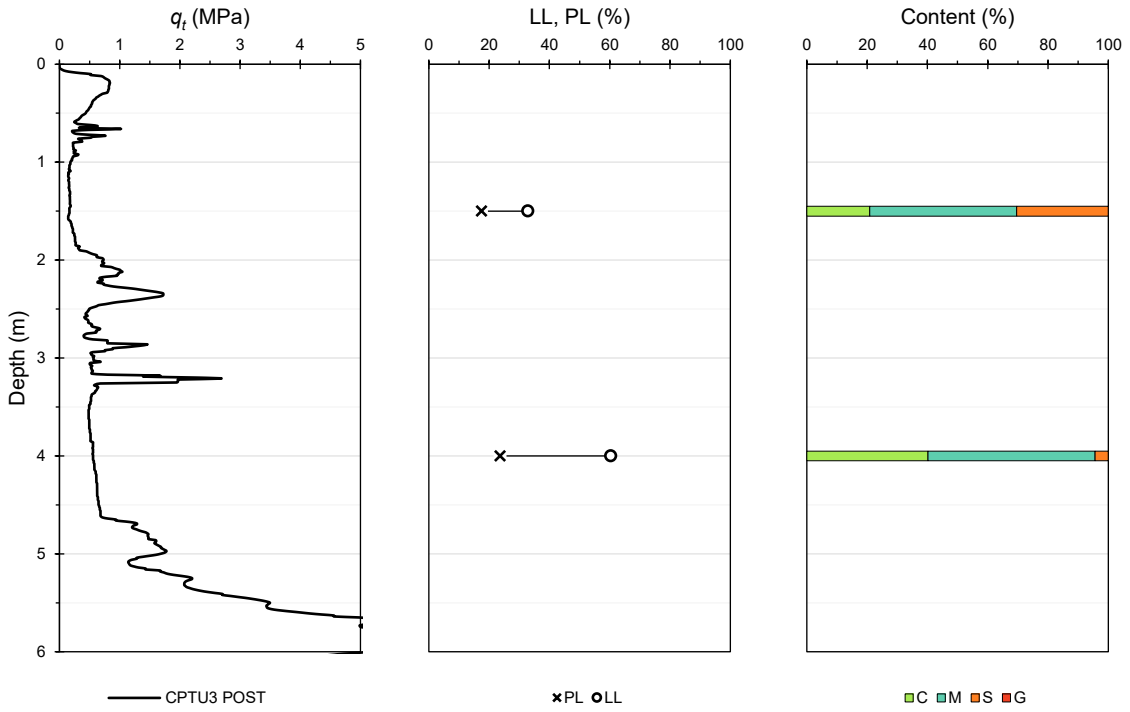

Figure 6.32. Visual representation of Atterberg Limits and grain size distribution results along the depth as associated to CPTU3.

The results of X-ray diffractometry performed on four samples further convince about the similarity of layers, as shown in the next § 6.2.2.2.

6.2.2.2 XRD analyses

In order to assess the mineralogical composition of the dredged sediments, two XRD analyses were performed on two representative samples taken in those layers resulted as clay-like from the soil profiling.

Figure 6.33 shows the XRD pattern relative to the representative sample taken along the vertical S1 at a depth of 2.3 m from the ground level. The main mineral phases detected in the dredged sediments are calcite ($CaCO_3$) and quartz (SiO_2), with minor contents of muscovite ($KAl_2(Si_3Al)O_{10}(OH,F)_2$), clinochlore ($(Mg,Fe)_6(Si,Al)_4O_{10}(OH)_8$), dolomite ($CaMg(CO_3)_2$). The same crystals have been found in the representative sample collected in the same vertical at a depth of 5.3 m (Figure 6.34), and on two samples taken along the vertical S2 at depths of 1.5 m (Figure 6.35) and 4.0 m (Figure 6.36).

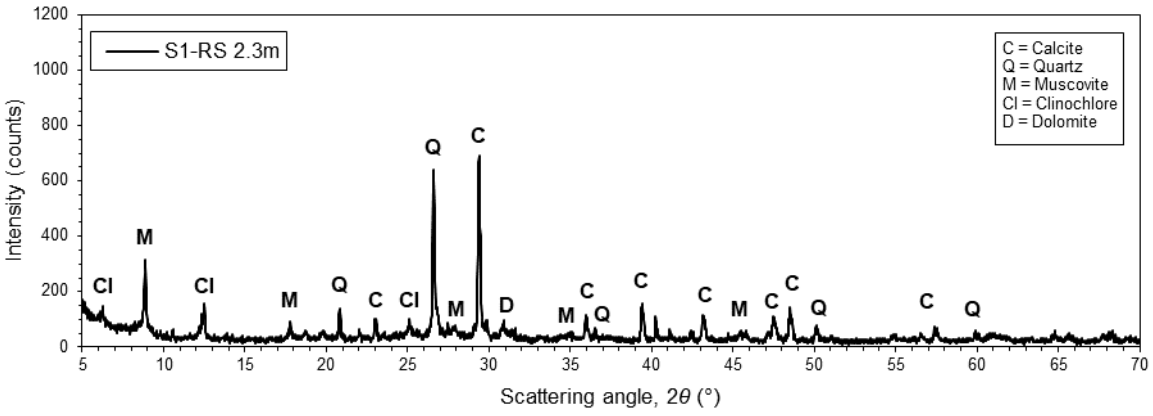

Figure 6.33. XRD pattern for the representative sample taken at 2.3 m.

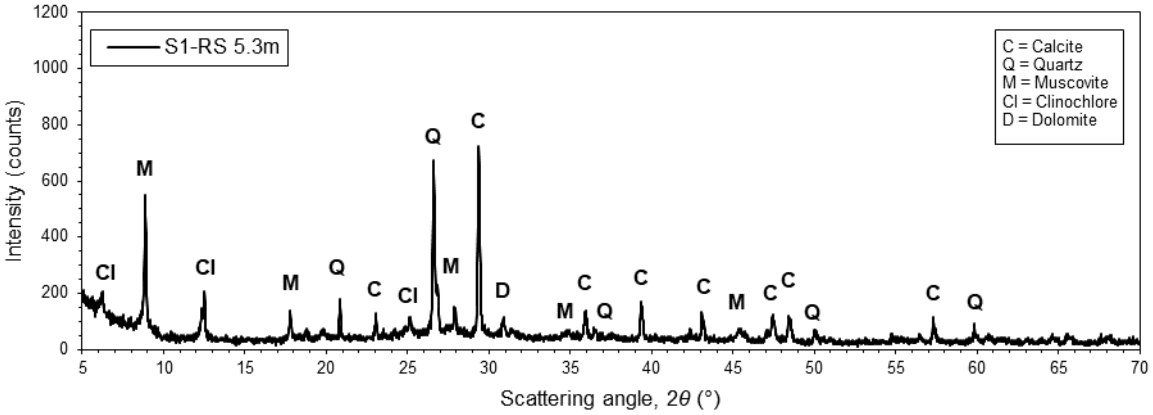

Figure 6.34. XRD pattern for the representative sample taken at 5.3 m.

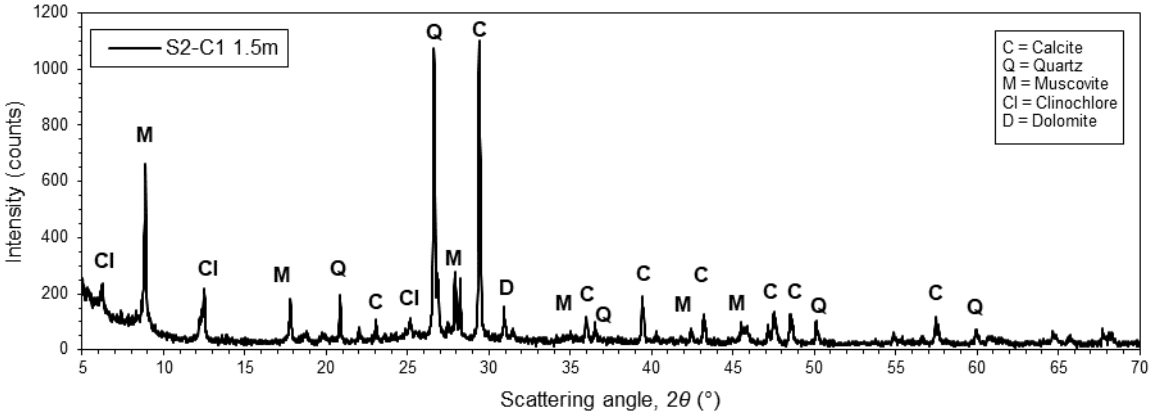

Figure 6.35. XRD pattern for the sample taken at 1.5 m.

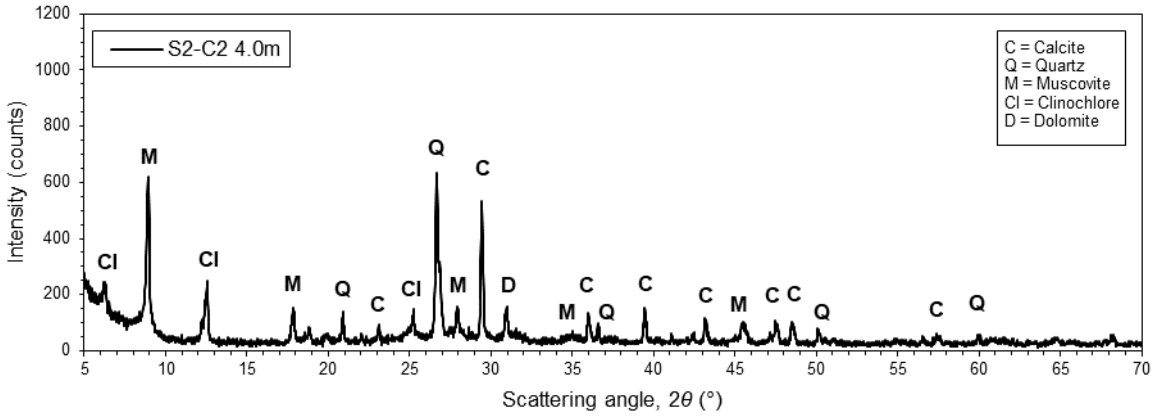

Figure 6.36. XRD pattern for the sample taken at 4.0 m.

It is rather notable that the four patterns are practically overwhelming, unless very slight differences in the intensity of some peaks (e.g. the higher peaks of muscovite detected on the last three samples). On sample S2-C1, the appreciably higher peaks of the two main components (quartz and calcite) are indicative of a better crystallisation and, at least from a qualitative standpoint, they can be associated to the greater abundance of sand observed in the grain-size distribution.

From the above it can be concluded that the four layers of concern can be assumed to be the same from a mineralogical point of view. This result corroborates the hypothesis of sediment homogeneity for the development of a correlation between the values of penetration resistance and undrained shear strength discussed in § 6.3.

6.2.2.3 Overconsolidation

Because of dredging and recent disposal into the CDF, besides sedimentation and self-weight consolidation soon after disposal, the only event was the application of the preloading embankment (~85 kPa considering the fourth lift, see § 5.4.3) and its subsequent removal, which actually determined the mechanical overconsolidation of the sediment deposit. Given the very small thickness of the deposit with reference to the load base, oedometric conditions can be assumed under most of the loading area and the total stress increment can be considered constant along the depth.

As far as the sample S1-C2 is concerned, at the sampling depth the preconsolidation stress would be $\sigma'_p \approx 110$ kPa, based on the imposed stress history. From the experimental compressibility curve shown in Figure 6.37, the "most probable preconsolidation stress" as defined by Holtz & Kovacs, 1981 (tangent method) is identified by the intersection of the compression line (red dotted line) and recompression line (the blue dotted line); in this case, σ'_p resulted to be 109 kPa, which is practically the value expected from stress history.

The experimental compressibility curve for sample S2-C1 is shown in Figure 6.38. In this case, the graphical construction of tangent method returned a most probable preconsolidation stress $\sigma'_p \approx 104$ kPa, which again is very close to the value expected at the sampling depth from stress history (i.e. $\sigma'_p \approx 105$ kPa).

With reference to the compressibility parameters, the improvement with respect to the *ante operam* condition (§ 5.2.1.2) is clear and self-evident. For effective stress levels less than 100 kPa, the constrained modulus, M, increased of about one order of magnitude.

The coefficient of vertical consolidation, c_v, determined according to the log-time method by Casagrande (1936), resulted in the order of 10^{-4} cm^2/s for both samples, and the indirectly determined vertical hydraulic conductivity, k_v, resulted of the order of 10^{-8} cm/s for the effective stress level of interest (Table 6.9 and Table 6.10).

Table 6.9. Compressibility parameters from sample S1-C2 (loading stage only).

Effective vertical stress, σ'_v	Constrained modulus, M	Void ratio, e	Re- and Compression index, c_r and c_c	Coefficient of vertical consolidation, c_v	Vertical hydraulic conductivity, k_v
(kPa)	(MPa)	(-)	(-)	(cm^2/s)	(m/s)
12.5	3.2	0.995	0.01	3.8×10^{-4}	1.2×10^{-10}
25	2.5	0.985	0.03	3.6×10^{-4}	1.4×10^{-10}
50	2.9	0.968	0.06	5.2×10^{-4}	1.8×10^{-10}
100	2.8	0.932	0.12	5.2×10^{-4}	1.9×10^{-10}
200	4.0	0.882	0.17	5.4×10^{-4}	1.3×10^{-10}
400	6.5	0.820	0.21	4.6×10^{-4}	7.2×10^{-11}
800	11.0	0.747	0.24	6.2×10^{-4}	5.6×10^{-11}
1600	20.1	0.667	0.26	5.4×10^{-4}	2.7×10^{-11}
3200	41.5	0.590	0.26	4.8×10^{-4}	1.2×10^{-11}

Table 6.10. Compressibility parameters from sample S2-C1 (loading stage only).

Effective vertical stress, σ'v	Constrained modulus, M	Void ratio, e	Re- and Compression index, c_r and c_c	Coefficient of vertical consolidation, c_v	Vertical hydraulic conductivity, k_v
(kPa)	(MPa)	(-)	(-)	(cm^2/s)	(m/s)
12.5	1.1	0.749	0.02	4.3×10^{-4}	4.0×10^{-10}
25	2.0	0.738	0.04	3.4×10^{-4}	1.7×10^{-10}
50	1.7	0.712	0.09	3.3×10^{-4}	1.9×10^{-10}
100	2.6	0.678	0.11	8.7×10^{-4}	3.4×10^{-10}
200	4.9	0.642	0.12	8.0×10^{-4}	1.6×10^{-10}
400	8.7	0.602	0.13	8.5×10^{-4}	9.8×10^{-11}
800	15.3	0.555	0.15	1.0×10^{-3}	6.7×10^{-11}
1600	30.0	0.508	0.16	1.4×10^{-3}	4.6×10^{-11}
3200	47.6	0.449	0.20	3.6×10^{-4}	3.3×10^{-12}

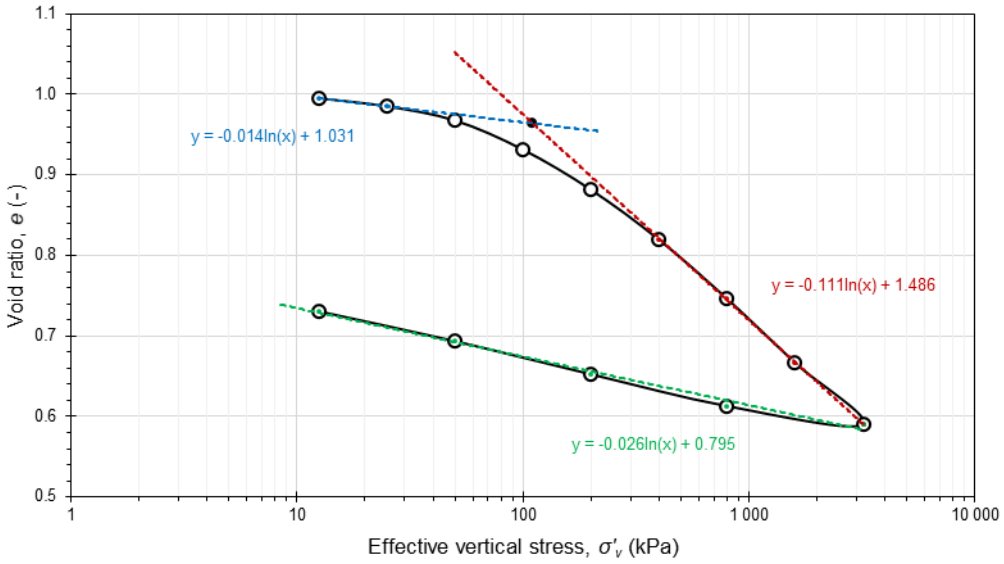

Figure 6.37. Compressibility curve for sample S1-C2.

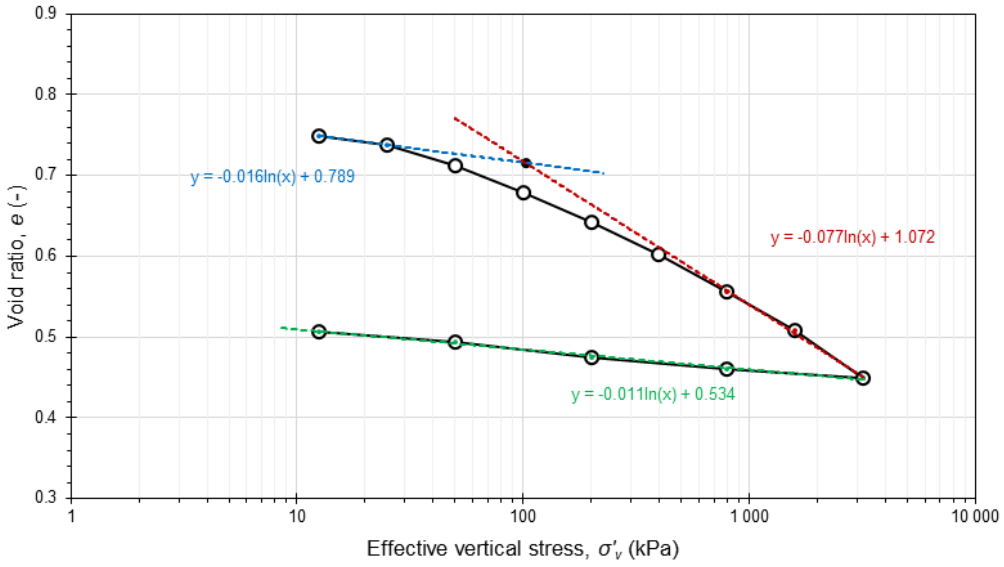

Figure 6.38. Compressibility curve for sample S2-C1.

6.2.2.4 Shear strength

From the sample S1-C2 taken at 2.5 m depth, it was possible to obtain five specimens for isotropically consolidated undrained triaxial compression (CIUC) tests: two of the specimens were obtained from undisturbed clayey sediment, while the other three were reconstituted.

CIUC testing on reconstituted specimens was intended to derive drained shear strength parameters, φ' and c', and the undrained shear strength, s_u, for the normally consolidated (NC)

state of the clayey sediment. The poor consistency of reconstituted clay dictated the minimum value of cell pressures set to be applied, i.e. σ'_3 = 50 kPa; the other two values were 80 kPa and 150 kPa. In order to obtain a further point on the failure envelop, the third specimen was used in the "multi-stage" mode (Head & Epps, 2011): namely, once the stress-strain curve of the specimen compressed under σ'_3 = 150 kPa (stage A) indicated that failure was imminent, drainage lines were reopened and the axial load released; the cell pressure was then raised to the second value (stage B), σ'_3 = 200 kPa, and compression resumed.

Figure 6.39a and Figure 6.39b plot the deviator stress, q, and the pore pressure change, Δu, versus the axial strain, ε_z. From the curves it is apparent that the sediment exhibits a contractive behaviour during shearing, as typical for NC soils: the deviator stress grows monotonically until reaching a maximum value at axial strains larger than 10%, while positive excess pore pressure is generated. In the stress space q-p' (Figure 6.39c), effective stress paths are curved and deviate to the left from the total stress paths (not represented) of a quantity $\Delta u+u_0$, where u_0 is the applied backpressure. The critical state line was obtained by linear regression of the points corresponding to the ultimate strength, q_f; its slope is M = 1.155, which means that the angle of shear resistance is φ' = 29°, while intercept is zero, as also shown by the tangent line common to the four effective stress circles in the Mohr space τ-σ' (Figure 6.39d). For each stress circle at failure, the undrained shear strength, s_u, was derived (values listed in Table 6.11).

The two specimens from the undisturbed sample were used to derive the drained and undrained shear strength parameters of the sediment layer. Consolidation pressures of 50 kPa and 80 kPa were applied, for comparison with the NC sediments.

The two q-ε_z curves (Figure 6.40a) exhibited a non-linear ductile behaviour: as the axial strain grows, the deviator stress gradually increases until it stabilises on a maximum value at large strain. In particular, at axial strains greater than 10%, the specimen consolidated at σ'_3 = 50 kPa attained a maximum deviator stress at failure, q_f, of about 60 kPa, while that consolidated at σ'_3 = 80 kPa reached a maximum value of about 66 kPa. In parallel, the Δu-ε_z curves (Figure 6.40b) show that the specimens developed positive pore pressures during shearing.

In Figure 6.40c the effective stress-paths are reported. The slope of the critical state line is M = 1.178, implying an angle of shear resistance φ' = 29.5° and c' = 0. The undrained shear strength of the specimen consolidated at σ'_3 = 50 kPa resulted equal to 30 kPa, while for that consolidated at σ'_3 = 80 kPa, a slightly higher value was obtained, s_u = 33.6 kPa. All the results are summarised in Table 6.12.

These findings show that the consolidation treatment actually increased the undrained shear resistance of sediments with respect to the NC pre-consolidation condition, but attained values are still quite modest because of the extremely low initial values.

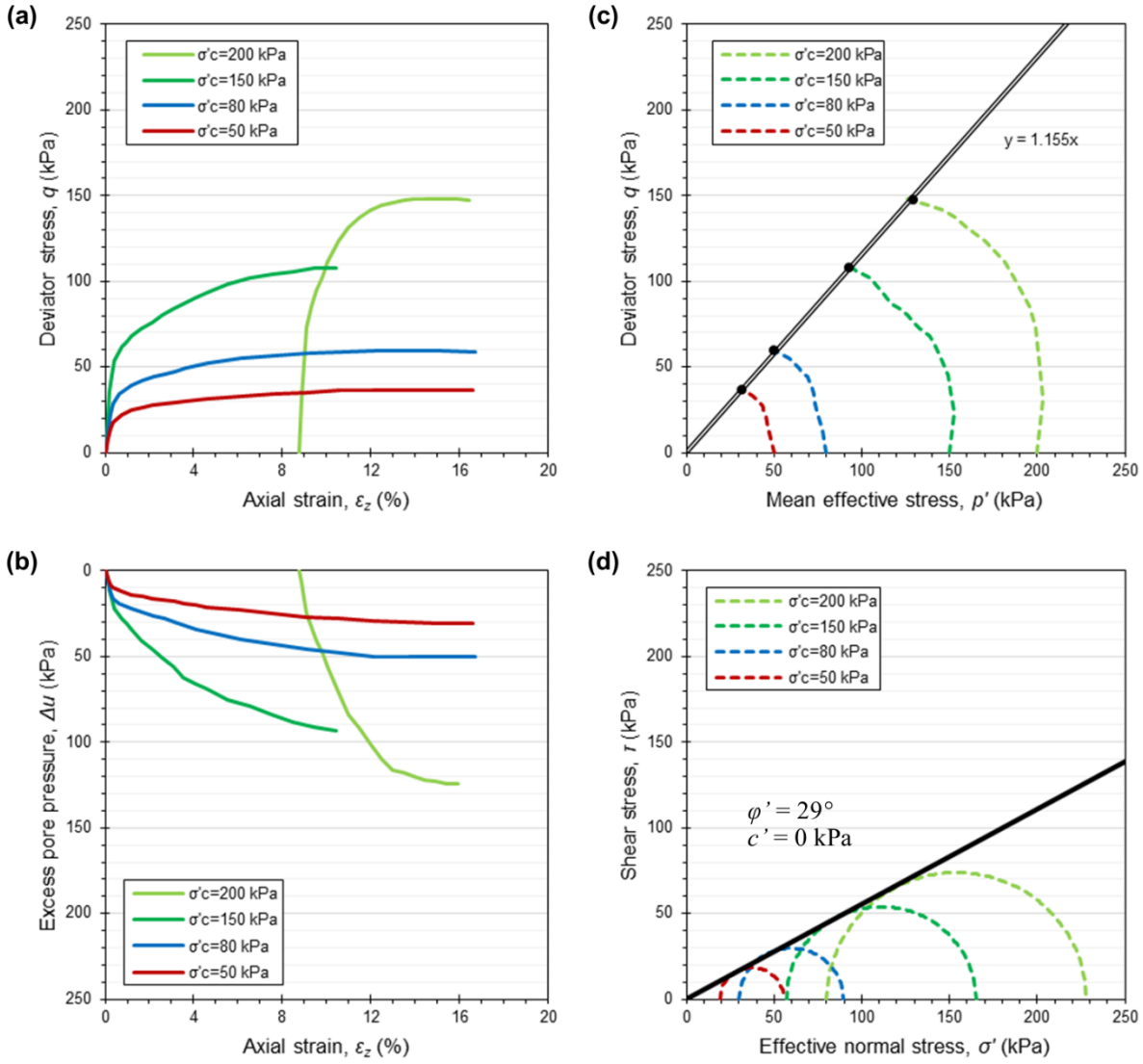

Figure 6.39. Results of triaxial CIUC test on reconstituted clay of sample S1-C2: (a) q-ε_z curves; (b) Δu-ε_z curves; (c) effective stress paths and critical state line in the q-p' space; (d) effective stress circles and failure envelop in the Mohr space.

Table 6.11. Results of triaxial CIUC test on reconstituted clay of sample S1-C2.

Consolidation stress, σ'_c	Deviator stress at failure, q_f	Undrained shear strength, s_u
(kPa)	(kPa)	(kPa)
50	36.8	18.4
80	59.6	29.8
150	108.0	54.0
200	147.9	74.0

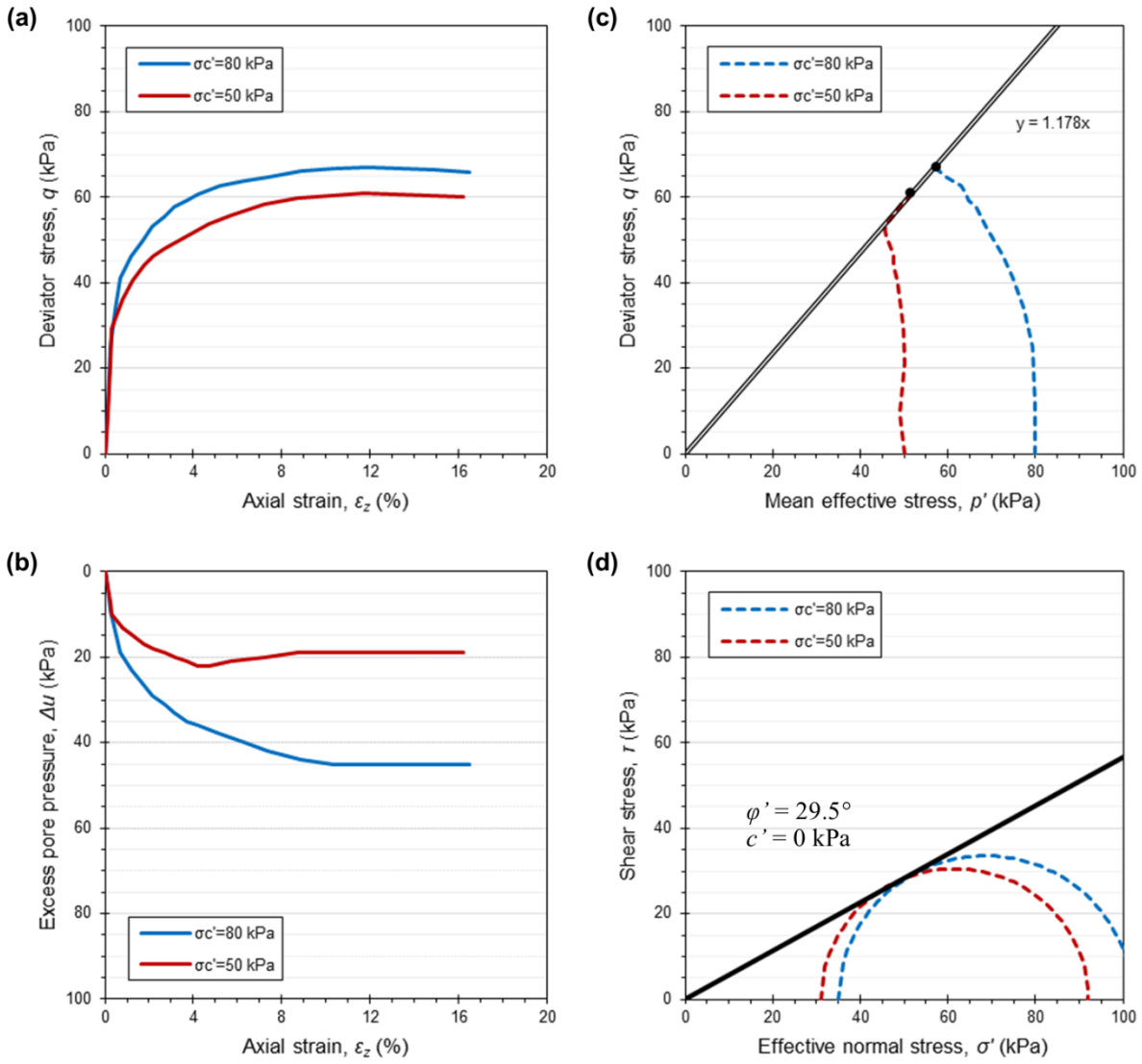

Figure 6.40. Results of triaxial CIUC test on undisturbed clay of sample S1-C2: (a) q-ε_z curves; (b) Δu-ε_z curves; (c) effective stress paths and critical state line in the q-p' space; (d) effective stress circles and failure envelop in the Mohr space.

Table 6.12. Results of triaxial CIUC test on undisturbed clay of sample S1-C2.

Consolidation stress, σ'_c	Deviator stress at failure, q_f	Undrained shear strength, s_u
(kPa)	(kPa)	(kPa)
50	61.1	30.6
80	67.1	33.6

From the sample S1-C3 taken at 5.0 m depth, it was possible to obtain four undisturbed specimens. Three of them were used in a consolidated undrained test, while the remainder was tested in unconsolidated-undrained conditions.

For the CIUC test, the three specimens were tested at the isotropic confining pressures of 50 kPa, 80 kPa (like the sample S1-C2) and 35 kPa, this latter to represent the mean effective stress at the sampling depth. Figure 6.41a and Figure 6.41b show the variation of the deviator stress and excess pore pressure versus the axial strain until failure. The specimens confirmed the contractive behaviour. In comparison with the CIUC test on the sample S1-C2, in this case the maximum shear strength resulted lower. Namely, for the maximum confining pressure, $\sigma'_3 = 80$ kPa, the maximum deviator stress resulted equal to 55 kPa, which is lower than the minimum value recorded for the sample S1-C2 (either NC or OC); for $\sigma'_3 = 50$ kPa and $\sigma'_3 = 35$ kPa, the values of q_f were equal to 43 kPa and 40 kPa, respectively. The effective stress paths are reported in Figure 6.41c, while the Mohr circles in terms of effective stresses are depicted in Figure 6.41d; an angle of shear resistance of 27.7° and a negligible apparent cohesion can be inferred. The values of the undrained shear resistance for the three different confining pressures are reported in Table 6.13.

The remainder undisturbed specimen was used for a UU test to assess the s_u value to be assigned to the sampling depth (4.5-5.0 m). The results, reported in Figure 6.42 as q-ε_z curve and Mohr circle, are consistent with those of the CIUC test at the consolidation stress of 35 kPa representing the mean stress state at the depth of sampling. In particular, a deviator stress at failure $q_f = 38.5$ kPa was obtained corresponding to $s_u = 19$ kPa, practically the same as the specimen isotropically consolidated at the mean effective stress of the sampling depth.

It is worth noting that, despite the greater sampling depth, sample S1-C3 resulted to be less resistant compared to sample S1-C2, both in drained and undrained conditions, the confining pressure being equal. This gap could be ascribed to the fact this sediment layer was less affected by the effect of preloading, and/or to a reduced draining capacity of the PVDs at the greater depths due to distortions.

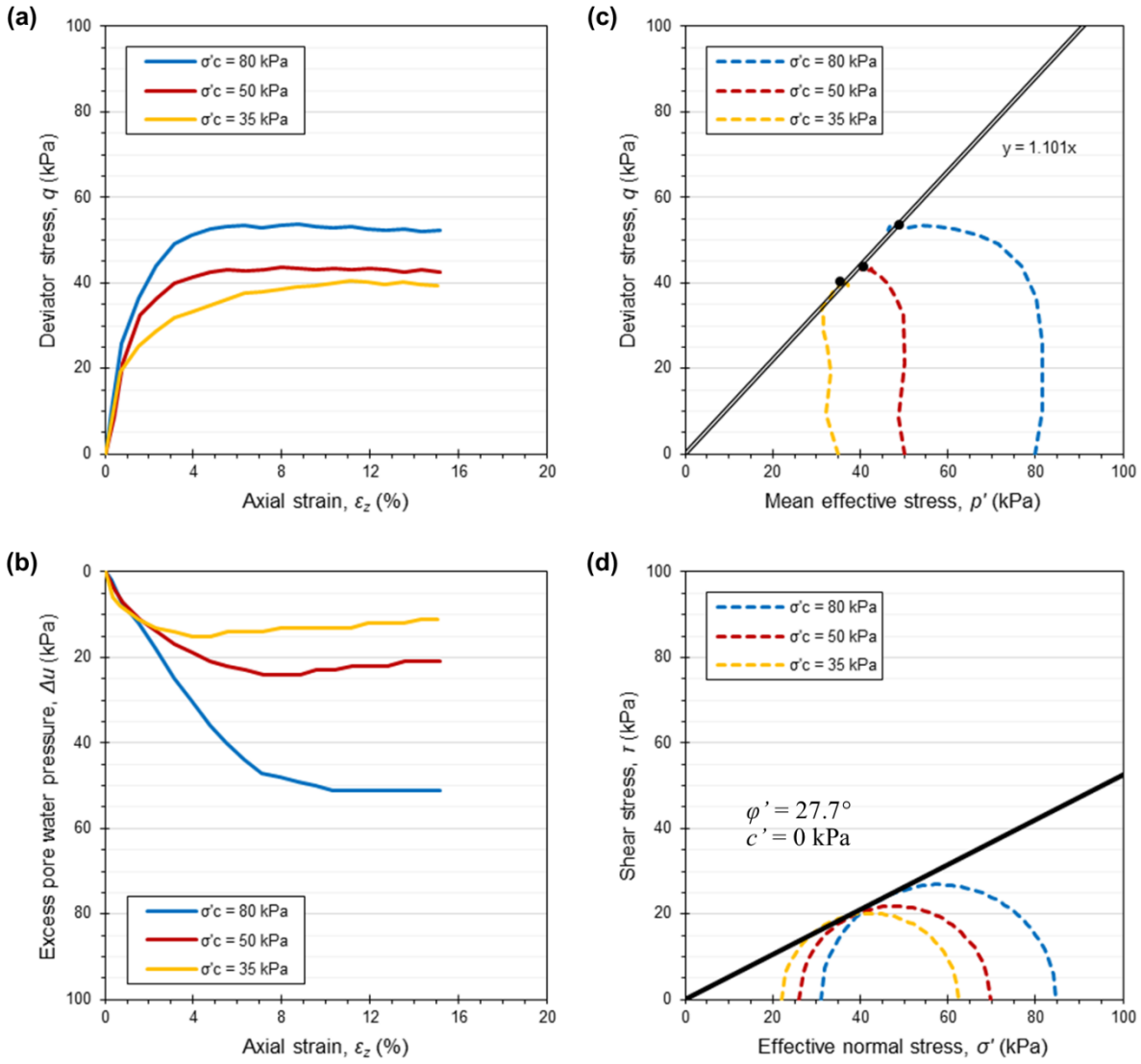

Figure 6.41. Results of triaxial CIUC test on undisturbed clay of sample S1-C3: (a) q-ε_z curves; (b) Δu-ε_z curves; (c) effective stress paths and critical state line in the q-p' space; (d) effective stress circles and failure envelop in the Mohr space.

Table 6.13. Results of triaxial CIUC test on sample S1-C3 (undisturbed clay).

Consolidation stress, σ'_c	Deviator stress at failure, q_f	Undrained shear strength, s_u
(kPa)	(kPa)	(kPa)
35	40.4	20.2
50	43.7	21.9
80	53.7	26.9

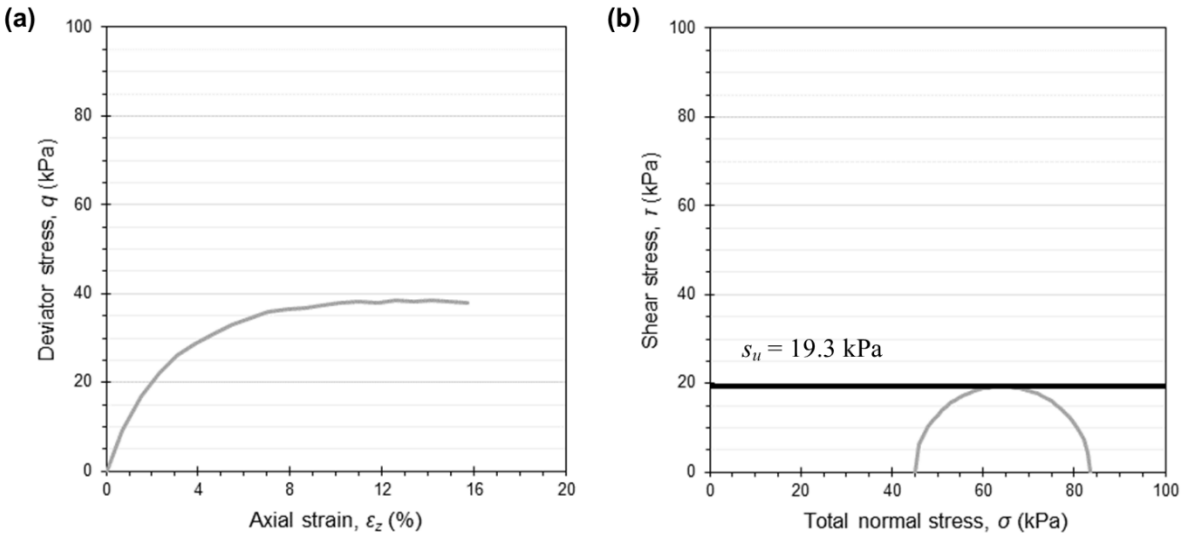

Figure 6.42. Results of triaxial UU test on undisturbed clay of sample S1-C3: (a) q-ε_z curves; (b) total stress circle and failure envelop in the Mohr space.

The same triaxial tests performed on the samples taken along the vertical S1 were repeated on the sample taken from the borehole S2 at a depth of 1.75 m from the ground level. It was possible to obtain only three specimens to be tested in triaxial compression tests, therefore one was used in UU test and the other two in CIUC test. In this case, the confining stress set for the two CIUC tests was chosen to represent the in situ mean effective stress at the sampling depth and at those of the other sample (σ'_3 = 20 kPa and 40 kPa).

The results of the CIUC test are illustrated in Figure 6.43. The stress-strain curves (a) indicated that, also in this case, the sediment shows a ductile behaviour, even if the specimen consolidated at the lower cell pressure, a dilatant tendency can be observed both in the Δu-ε_z curve (b) and in the effective stress path (c). The slope of the critical state line in the space of stress invariants, M = 1.187, and the envelop of the Mohr circles at failure (d) returned an effective shear angle of φ' = 29.7° and c' = 0 kPa, while the undrained shear strength resulted equal to 18.9 kPa and 22.4 kPa for confining stresses of 20 kPa and 40 kPa, respectively.

The results of the UU test on the only specimen tested are shown in Figure 6.44. A very modest peak of deviator stress can be discerned at a strain level of about 10% (q_f = 35.4 kPa). As expected, the value of the undrained shear strength from the UU test, s_u = 17.7 kPa, was slightly lower than that obtained from the CIUC specimen consolidated at a stress equal to the in situ effective mean stress.

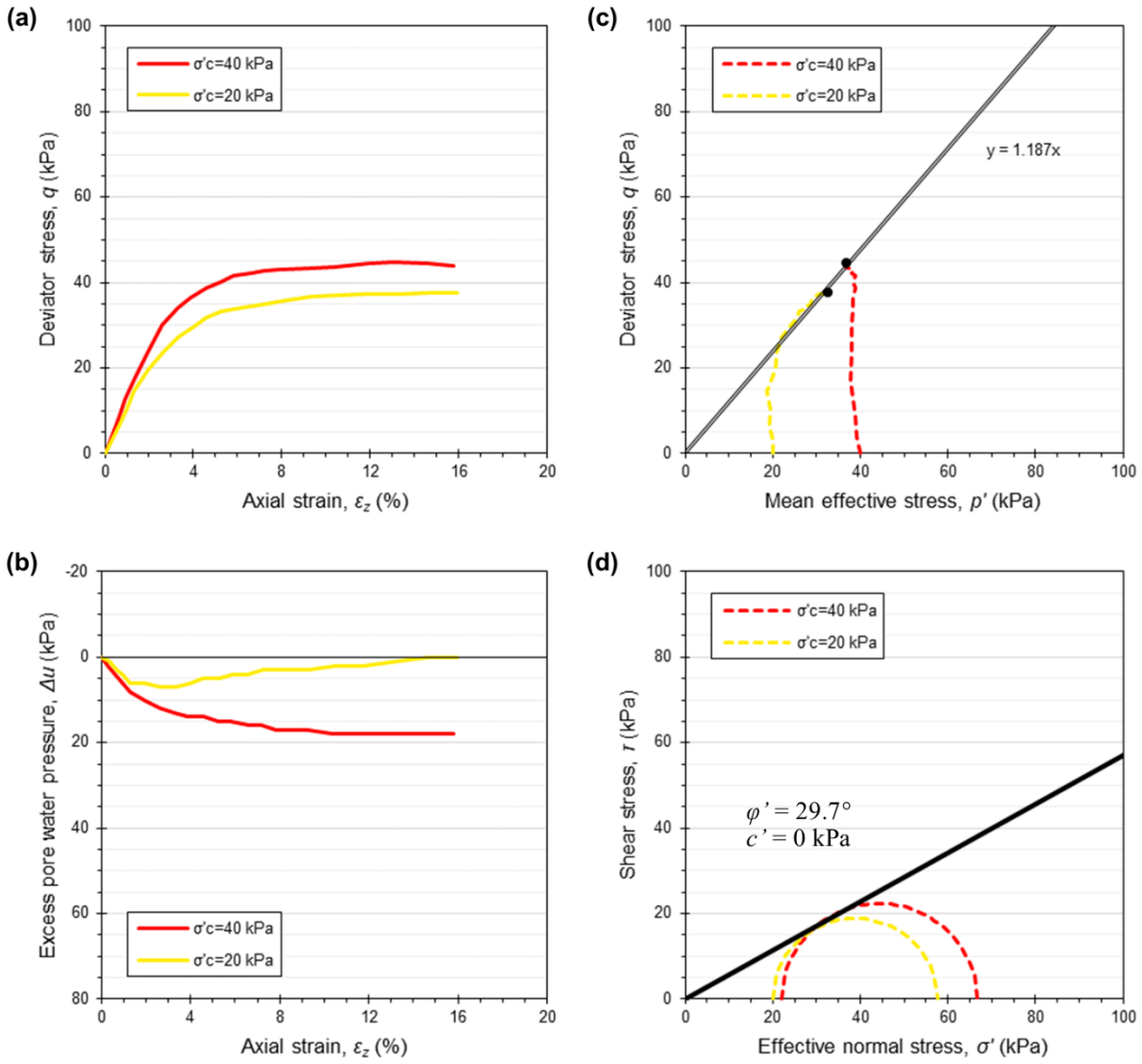

Figure 6.43. Results of triaxial CIUC test on undisturbed clay of sample S2-C1: (a) q-ε_z curves; (b) Δu-ε_z curves; (c) effective stress paths and critical state line in the q-p' space; (d) effective stress circles and failure envelop in the Mohr space.

Table 6.14. Results of triaxial CIUC test on sample S2-C1 (undisturbed clay).

Consolidation stress, σ'_c	Deviator stress at failure, q_f	Undrained shear strength, s_u
(kPa)	(kPa)	(kPa)
20	37.7	18.9
40	44.7	22.4

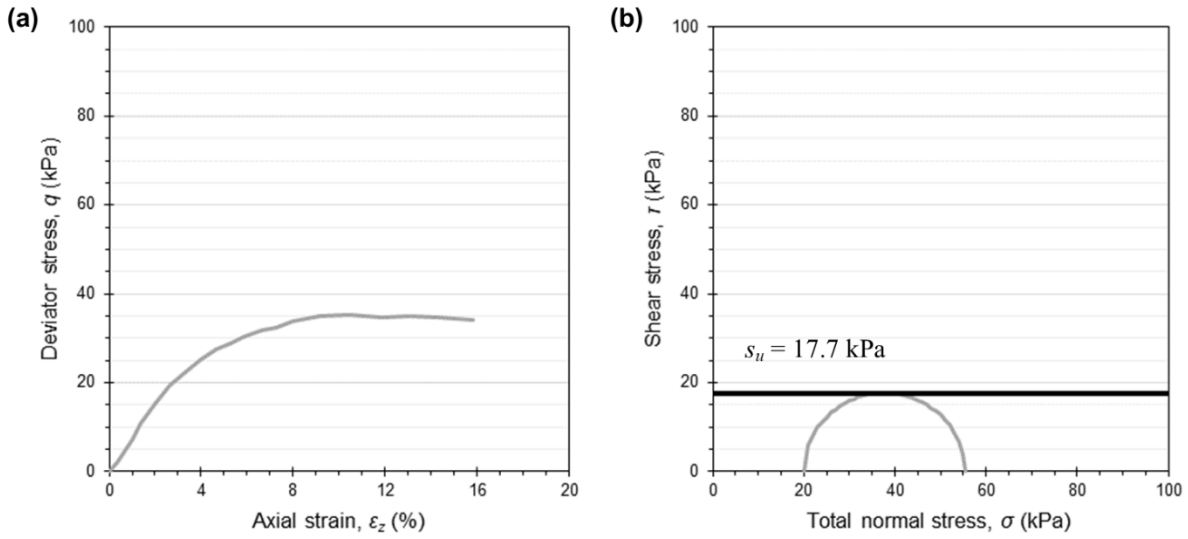

Figure 6.44. Results of triaxial UU test on undisturbed clay of sample S2-C1: (a) q-ε_z curves; (b) total stress circle and failure envelop in the Mohr space.

As far as the deeper sample S2-C2, taken at 4.25 m from the ground level, the value of s_u obtained from the UU test, assigned to the effective stress corresponding to the in situ sampling depth, was s_u = 24.9 kPa, as shown in Figure 6.45.

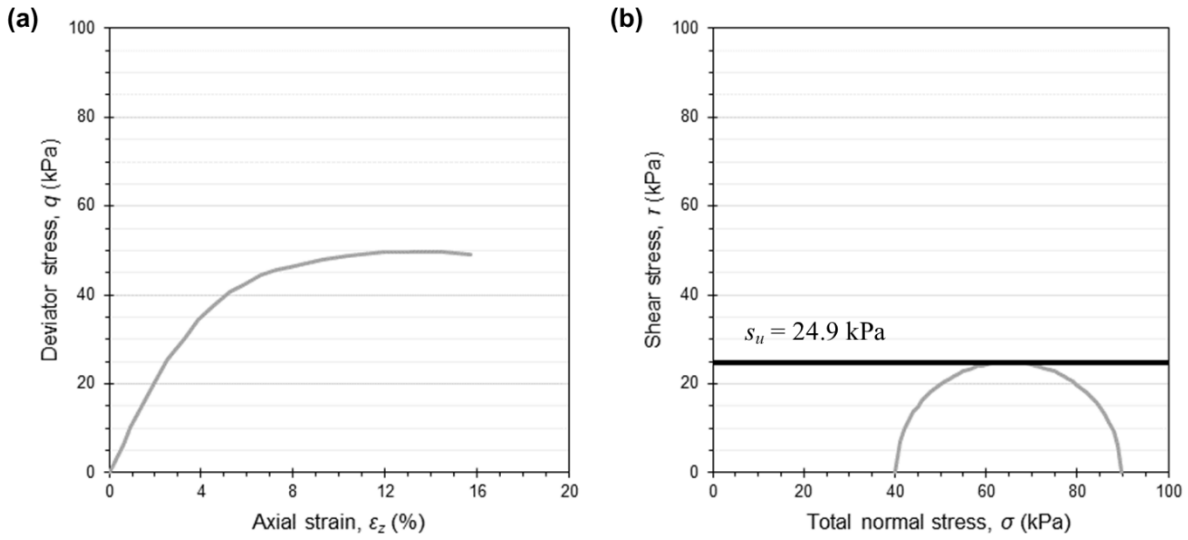

Figure 6.45. Results of triaxial UU test on undisturbed clay of sample S2-C2: (a) q-ε_z curves; (b) total stress circle and failure envelop in the Mohr space.

6.3 Calibration of s_u-q_t correlation for marine dredged sediments

In the state of the art chapter, interpretation of undrained shear strength from CPT results has been examined (§ 2.3), showing that the issue generally comes down to determine a cone factor linking s_u to the net cone resistance. Special focus has been devoted in the literature to empirical correlations, usually preferred over theoretical approaches because of the various uncertainties related to the choice of the appropriate theoretical model (Kulhawy & Mayne, 1990). It has been shown that a lot of work has been done on the topic (e.g. Rémai, 2013), but an interpretative framework for marine dredged sediments is still missing in the literature.

In the present research, an empirical s_u-q_t relationship for the fine-grained dredged sediments disposed (and to be disposed) in the Ancona CDF has been sought by calibrating CPTU results with known values of s_u, to provide a general guidance for post-consolidation stability analyses in the future sectors of the CDF.

Since the measured value of s_u is affected by many factors (e.g. stress history, strain rate, soil anisotropy, confining stress level, mode of failure), when searching for a relationship between cone penetration resistance and undrained shear strength it is crucial to clearly state which testing method the s_u data refer to.

In the initial intention of this research, the field vane test would have been adopted as reference test for the undrained shear strength, given that this test can be performed in close proximity of CPTU sounding, providing values of s_u for discrete depth intervals directly in situ. This is a great advantage because it allows to bypass all the drawbacks connected to sample small volume and disturbance and the measure refers to the actual in situ effective stress conditions. Moreover, most of correlations available in the literature for clayey soils refer to this type of test. However, despite a thorough market-research, it was not possible to retrieve a reliable field vane equipment in Italy since it is no more used in practice.

Therefore, in the present research the CIUC test has been used as reference test, since it is considered to be the standard and the minimum quality laboratory test for evaluating the undrained shear strength of cohesive soils (Kulhawy & Mayne, 1990). Compared to the field vane test, the number of s_u measurements available to develop the s_u-q_t correlation is dramatically reduced, but a relationship with the in situ effective vertical stress has been established to get the values of the undrained shear strength with depth.

CPTU1 and CPTU3 *post operam* soundings have been selected as reference verticals, given their proximity with boreholes S1 and S2 from which the tested undisturbed samples were collected. Of course, the correlation has been sought only in those stratigraphic units regarded as fine-grained sediments.

Preventively, a check on the normalised penetration rate has been performed, in order to exclude a partially drained penetration, which would lead to an overestimation of cone factors

(Salgado, 2022). By using the definition proposed by Finnie & Randolph, 1994, the non-dimensional velocity number, V, is:

$$V = v\, d_c / c_v \tag{6.3}$$

where v is the rate of penetration (= 20 mm/s), d_c is the diameter of the penetrometer (= 36 mm), c_v is the coefficient of vertical consolidation of the soil (in this case, of the order of 10^{-8} m^2/s). In the case of concern, V resulted much greater than 20, which is the limit value indicated in the literature for fully undrained penetration (Salgado, 2022; Watson et al., 2000). Hence, fully undrained conditions existed for CPTU tests in the Ancona CDF.

The procedure for data processing was articulated in the following four steps:

- identification of homogeneous sediment units;
- smoothing of cone penetration data;
- processing of triaxial tests results;
- calculation of the resulting cone factors.

Each phase is briefly described below.

6.3.1 Identification of homogeneous soil units

The first step of the procedure consisted in the identification of sediment depths where it would be meaningful to assess the undrained shear strength, i.e. in the fine-grained portion of the sediment deposit. The presence of coarser lenses in the stratigraphy indeed disrupted sediment homogeneity.

Silty and clayey sediment units were identified based on the soil classification system by Robertson (2009), according to which the normalised soil behaviour type index, I_c, can be used to discriminate between soils having a clay-like ($I_c > 2.6$) or a sandy-like ($I_c < 2.6$) response to penetration. The resulting layering is depicted in Figure 6.46 for the two reference verticals, where the clay-like layers are light-blue coloured. In CPTU1, two clay-like units have been identified at depths of 2.3÷3.6 m and 4.7÷5.8 m; in CPTU3, two clay-like units have been detected at depths of 0.8÷1.9 m and 3.3÷4.7 m.

A good agreement between the CPT-based soil behaviour description and USCS-based classification criteria is generally accepted (Molle, 2005). As a further confirmation, classification tests and XRD analyses performed on the clayey samples taken in the adjacent borehole at the depths of interest proved that such layers are effectively very similar in terms of grain-size distribution, plasticity, and mineralogy (§ 6.2.2.1 and § 6.2.2.2).

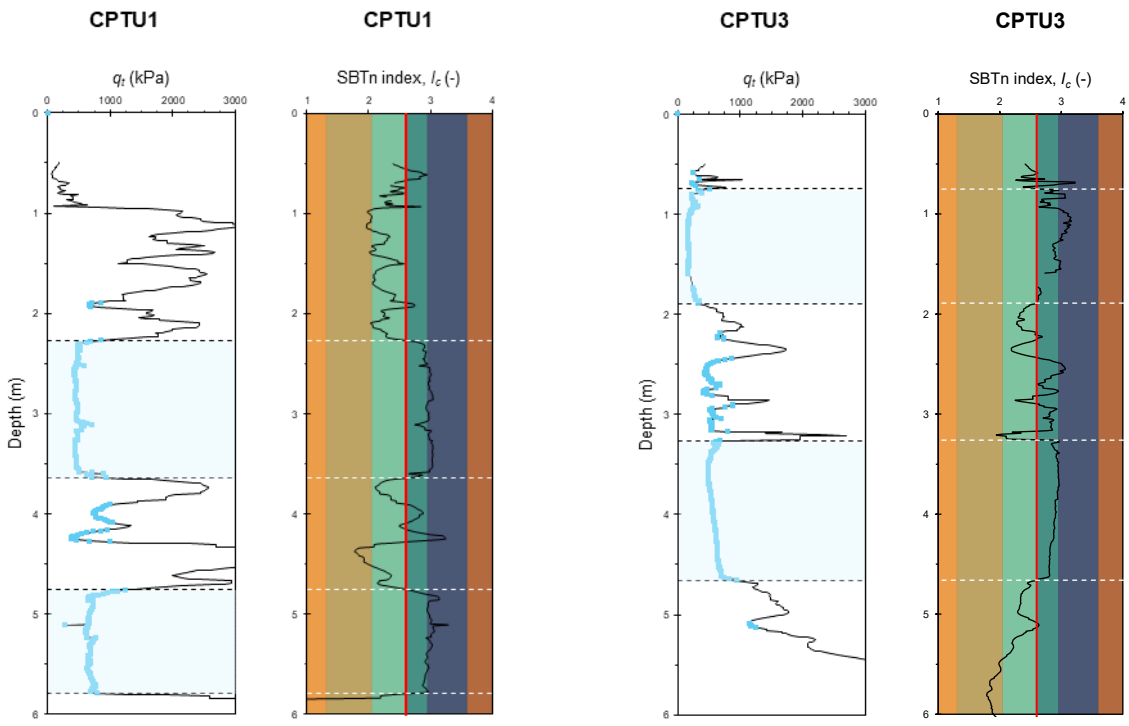

Figure 6.46. Identification of clay-like units in CPTU1 and CPTU3 soundings.

6.3.2 Smoothing of the cone penetration data

Once the clay-like layers were identified, a further filtering of the q_t values was required, in order to remove peaks and troughs from the raw data and to homogenise them. As suggested by Fellenius (2014), the smoothing was performed by applying a geometric average running over a moving window of 50 cm length. This procedure implied that the first and latest 25 cm of the layers were inevitably disregarded from the computation, however without loss of significance. In Figure 6.47 the red dots indicate the values of q_t after averaging.

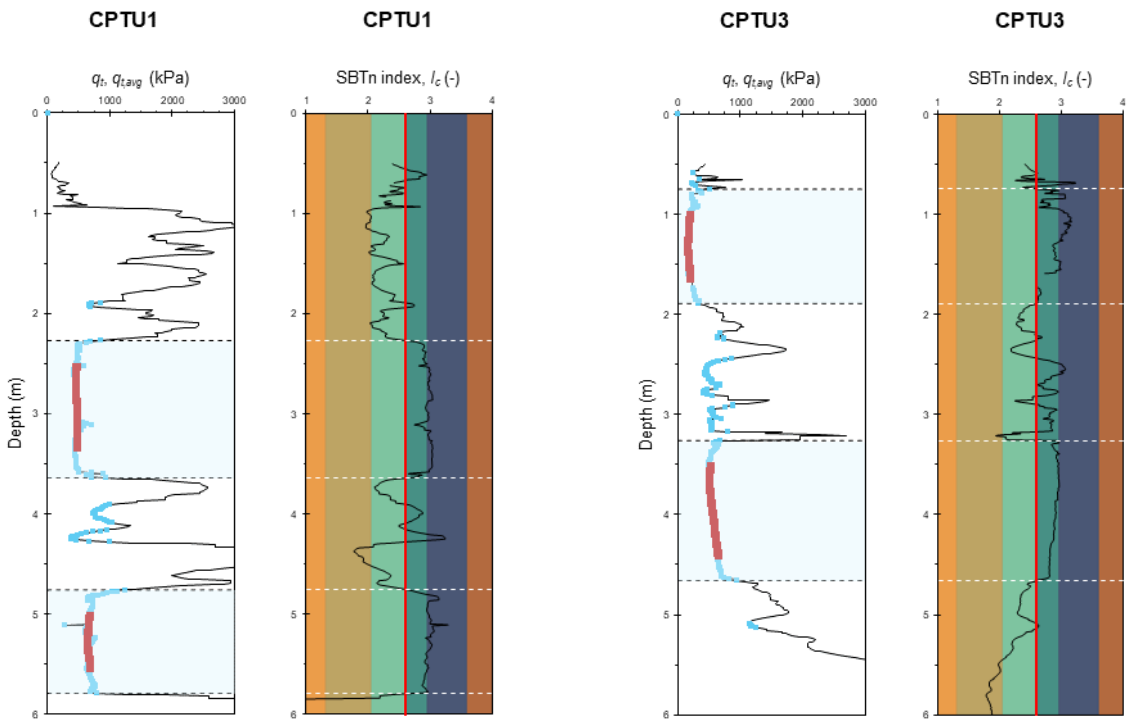

Figure 6.47. Smoothing of q_t values in the clay-like layers.

6.3.3 Processing of triaxial tests

In order to develop a s_u-q_t correlation, the undrained shear strength values determined by the CIUC tests have be assigned to a given depth (or effective stress) with reference to the mean effective stress. The *in-situ* stress state has been determined based on the stress history, stratigraphy and depth of water table, and the determined shear resistance angle. Such data are known with a certain accuracy, especially the stress history, since the maximum vertical stress experienced by the deposit was actually imposed. From these data the overconsolidation ratio, OCR, and the coefficient of earth pressure at rest for the OC sediments, $K_{0,OC}$, have been calculated at each depth along the vertical:

$$OCR = (\sigma'_{v0} + \Delta\sigma v')/\sigma'_{v0} \tag{6.4}$$

$$K_{0,OC} = (1 - \sin\varphi') \times OCR^{\alpha} \tag{6.5}$$

assuming $\alpha = 0.5$ (Meyerhof, 1976). This allowed to determine the mean effective stress along the depth (Figure 6.48):

$$\sigma'_m = \sigma'_{v0}\left(1 + 2K_{0,OC}\right)/3 \tag{6.6}$$

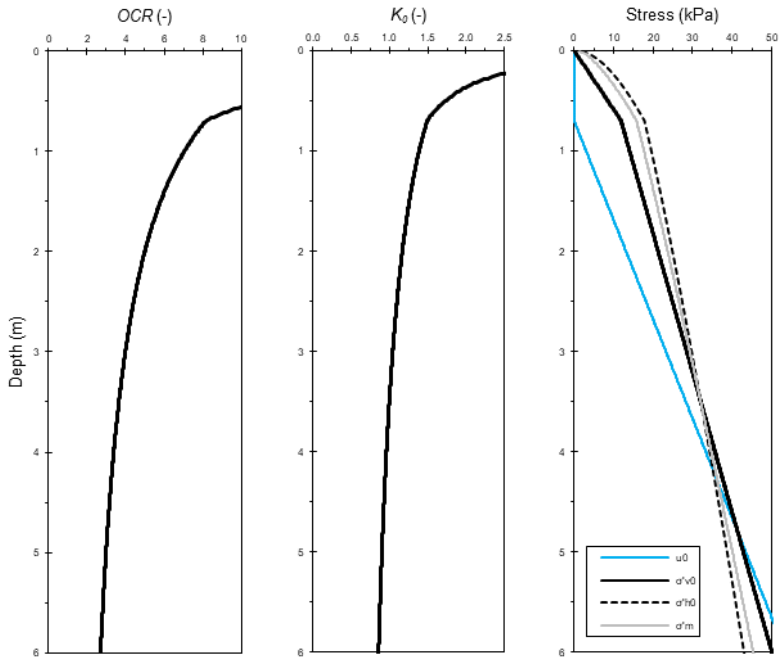

Figure 6.48. In-situ stress state. From the left: overconsolidation ratio (OCR); coefficient of earth pressure at rest (K_0); hydrostatic pressure (u_0) and effective vertical (σ'_{v0}), horizontal (σ'_{h0}), and mean stresses (σ'_m).

For each CIUC undisturbed sample, the s_u values measured at the different isotropic consolidation pressures (§ 6.2.2.4) have been associated to the *in-situ* mean effective stress, based on the equivalence $\sigma'_c = \sigma'_m$, and in turn to the corresponding in-situ effective vertical stress, σ'_{v0}, as reported in Table 6.15. These results have been interpolated by linear regression to estimate the undrained shear strength of the overconsolidated sediment as a function of the *in-situ* effective vertical stress, $s_u = s_u(\sigma'_{v0})$, as shown in Figure 6.49. The linear regression for OC sediment resulted in the following law:

$$s_u = 0.143\sigma'_{v0} + 16.647 \qquad (6.7)$$

which is indicated by the bold dash-dot line in Figure 6.49. In the same graph, the triangles indicate the UU results, which provided slightly lower s_u values compared to CIUC to parity of σ'_{v0}, as documented by Ladd & Lambe, 1964. Finally, the cross symbols indicate the results of CIUC tests on reconstituted samples, which are referred to the normally consolidation condition.

Table 6.15. Results of CIUC tests.

Sample	Measured undrained shear strength, s_u	Consolidation pressure, σ'_c ($= \sigma'_m$)	Effective vertical stress, σ'_{v0}
	(kPa)	(kPa)	(kPa)
CIU S1-C2	30.6	50	56.5
	33.6	80	98.9
CIU S1-C3	20.2	35	36.0
	21.9	50	56.5
	26.9	80	98.9
CIU S2-C1	18.9	20	16.8
	22.4	40	42.8

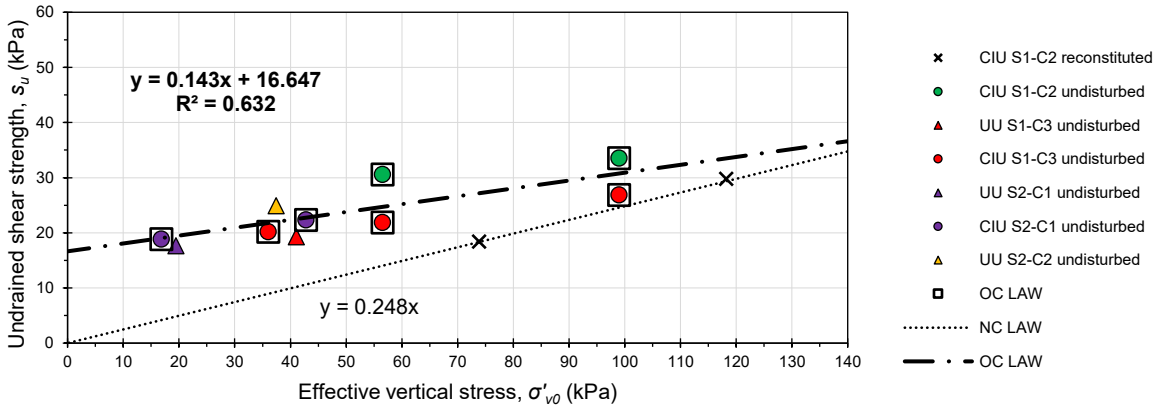

Figure 6.49. Linear regression of CIUC undisturbed samples (bold dash-dot line) and reconstituted samples (dotted line).

Equation (6.7) served as a mathematical expedient to extrapolate the values of s_u at the depths of interest, because in CIUC tests some samples were reconsolidated at a confining pressure higher than the *in-situ* mean effective stress.

The undrained shear strength has also been estimated following the well-established empirical Stress History And Normalised Soil Engineering Parameters (SHANSEP) approach (Ladd et al., 1977; Ladd & Foott, 1974). The SHANSEP concept considers that the undrained strength ratio increases with the overconsolidation ratio, according to the following equation:

$$\left(\frac{s_u}{\sigma'_{v0}}\right)_{OC} = S \times OCR^m \tag{6.8}$$

where S and m are the SHANSEP parameters to be obtained from test data. In particular, S is the undrained strength ratio for normally consolidated soils.

For the specific case, S has been obtained from the single CIUC test performed on reconstituted specimens, considering the angle of shear resistance $\varphi' = 29°$ (cfr. Figure 6.39), the coefficient of earth pressure at rest for NC clayey sediment $K_{0,NC} = 0.515$, and of course $OCR = 1$. The corresponding effective vertical stress has been inferred by:

$$\sigma'_{v0} = 3\sigma'_m/(1 + 2K_0) \tag{6.9}$$

Results are listed in Table 6.16. Notice that the values of the undrained strength ratio for all the NC specimens resulted to be practically constant and around 0.25, in agreement with the values reported in the literature (Ladd, 1991). For use in the SHANSEP model, the average value, $S = 0.248$, has been assumed (dotted line in Figure 6.49).

The parameter m has been calibrated based on the results of unconsolidated-undrained triaxial tests. In particular, for each UU test (§ 6.2.2.4) the exponent m has been input in Equation (6.8) to fit the calculated undrained shear strength, $s_{u,calc}$, to the measured value, $s_{u,meas}$, as summarised in Table 6.17. The average value, $m = 0.722$, complies with the range reported in the literature ($m = 0.7 \div 0.98$ for triaxial compression mode, Yang et al., 2019).

Table 6.16. Determination of the S parameter.

Reconstituted specimen	Measured undrained shear strength, $s_{u,meas}$	Consolidation pressure, σ'_c (= σ'_m)	In situ effective vertical stress, σ'_{v0}	Undrained shear strength ratio for NC soil, $(s_u/\sigma'_{v0})_{NC}$
	(kPa)	(kPa)	(kPa)	(-)
(1)	18.4	50	73.88	0.249
(2)	29.8	80	118.20	0.252
(3)	54.0	150	221.63	0.244
(3)bis	74.0	200	295.51	0.250

Table 6.17. Determination of exponent m.

Test	Sampling depth, z	Effective vertical stress, σ'_{v0}	Measured undrained shear strength, $s_{u,meas}$	SHANSEP exponent, m
	(m)	(kPa)	(kPa)	(-)
UU S1-C3	4.75	41.1	19.3	0.565
UU S2-C1	1.75	19.5	17.7	0.77
UU S2-C2	4.25	37.5	24.9	0.83

Based on the average values of the S and m parameters, and on the in-situ OCR and effective vertical stress level, the trend of the undrained shear strength along the depth expected by the SHANSEP model has been plotted in Figure 6.50, together with that extrapolated by

Equation (6.7). A quite good agreement between the two models is reached below 2 m of depth, i.e. for OCR < 5.

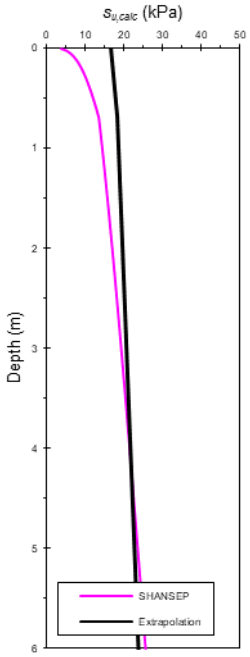

Figure 6.50. Comparison between the undrained shear strength computed from the SHANSEP model and the site-specific extrapolated law.

6.3.4 Determination of cone factors and correlation

The values of the undrained shear strength computed by Equation (6.7) have been associated to the averaged value of the cone resistance, $q_{t,avg}$, for each centimetre of depth included in the light-blue zones of Figure 6.47, thus enabling the back-calculation of the N_{kt} according to the following equation:

$$N_{kt} = \frac{q_{t,avg} - \sigma_{v0}}{s_u} \tag{6.10}$$

Figure 6.51 summarises all the findings obtained in the reference verticals CPTU1 and CPTU3. It may be noted that values of the cone factor are included in the range N_{kt} = 19÷26 for the layers below 2.5 m of depth, while N_{kt} < 10 for the shallower layer in the vertical CPTU3. These results seem to suggest that cone factors decrease upwards, with a more evident variation the more pronounced is the increase of the overconsolidation ratio. Therefore, a trend between the Nkt and the *OCR* has been sought.

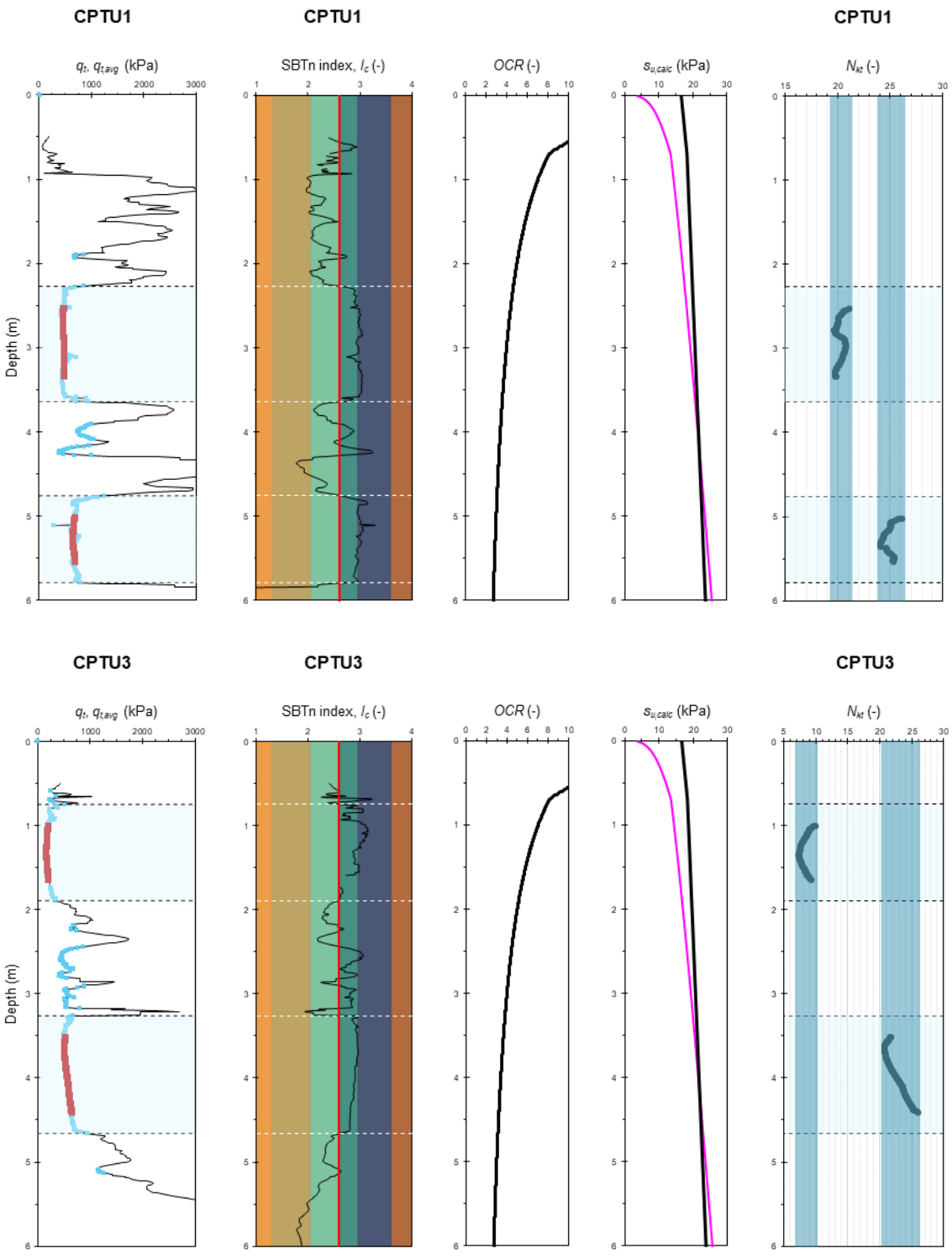

Figure 6.51. Back-calculation of cone factors for the reference verticals CPTU1 and CPTU3.

The same procedure described so far has been extended to the other four CPTUs *post*, assuming that Equation (6.7) is valid for the sediment layers identified as clay-like ($I_c > 2.6$) and having a thickness > 0.5 m. The resulting N_{kt} factors for all the six CPTU *post* are plotted against *OCR* in Figure 6.52. A linear regression analysis has been performed, leading to the following equation:

$$N_{kt} = -3.00\,OCR + 34.18 \tag{6.11}$$

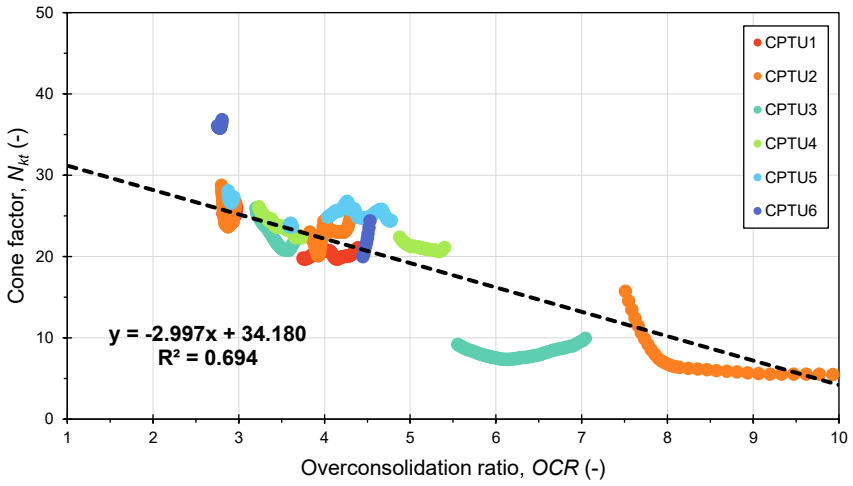

Figure 6.52. Plot of back-calculated cone factors against the corresponding OCR.

From Figure 6.52, the following conclusions can be drawn:

- a clear negative correlation exists between cone factors and overconsolidation ratio for the consolidated sediments in the Ancona CDF, as attested by the sample correlation coefficient close to -1 (R = -0.833);
- about 70% of the variance in N_{kt} data is explained by the predictor variable *OCR*, as testified by the coefficient of determination (R^2 = 0.694);
- for the NC sediment (*OCR* = 1) a value of $N_{kt} \approx 31$ would seem to be expected.

The evidence that N_{kt} decreases as *OCR* grows is consistent with common experience, for which higher s_u values (i.e., lower N_{kt} factors) are expected in clayey soils subjected to mechanical overconsolidation. From a qualitative standpoint, this trend can be reasonably explained as follows. It is known that the cone tip resistance is mainly affected by the *in situ* horizontal effective stress, which is in turn a function of the square root of the overconsolidation ratio through the coefficient of earth pressure at rest: $q_t = f(OCR^{0.5})$. Likewise, the SHANSEP concept demonstrated that the undrained shear strength basically depends on *OCR* to the power of m, where typically $m > 0.5$. This suggests that $N_{kt} = N_{kt}(1/OCR^{m-0.5})$, hence that cone factors and

overconsolidation ratio seemed to be inversely proportional. This finding is consistent with the results by (Karlsrud et al., 1996).

Equation (6.11) shows a satisfactory goodness of fitting (R^2 = 0.7, Figure 6.52), although data for $OCR > 5.5$ are less numerous and more dispersed. The lower cone factors at higher *OCR*, relative to the shallower stratum, are likely to be affected by the penetration of the coarse material of the top layer, as well as by the proximity to the top draining boundary which leads to a faster consolidation, hence and improved undrained shear strength. It must also be said that some major uncertainties are inherent in the procedure followed; one above all is due to the derivation of law (6.8) – which is *de facto* based on very little available s_u data – and its extrapolation along all the depth of the investigated verticals. An outlook for future directions of research will definitely supplement the testing program with a large number of calibration tests, to improve the reliability of the correlation.

Finally, it is worth recalling that Equation (6.11) has been calibrated on OC sediments, therefore its extrapolation back to $OCR = 1$ to get the N_{kt} factors for NC sediments must be viewed with great caution. Indeed, from the q_t values of the CPTUs *ante* and assuming the values of s_u resulting from the triaxial tests on the remoulded samples (cfr. Figure 6.39), N_{kt} values in the range of 8÷40 were obtained. This wide range did not allow to have evidence of the reliability of Equation (6.11) for NC sediments.

By combining Equations (6.10) and (6.11), the following empirical correlation can be used to derive the undrained shear strength of the overconsolidated dredged sediments:

$$s_u = \frac{q_t - \sigma_{vo}}{-3.0OCR + 34.2} \tag{6.12}$$

Figure 6.53 confirms a quite good agreement between the undrained shear strength determined from the proposed Equation (6.12) and the reference empirical SHANSEP method, especially where *OCR* varies between 2 and 5, with N_{kt} = 20÷30.

Further research is necessary to confirm the proposed equation which can be currently considered as site-specific and related to the physical characteristics of the clay-like sediments of the Ancona CDF, where it can be used for geotechnical design purposes.

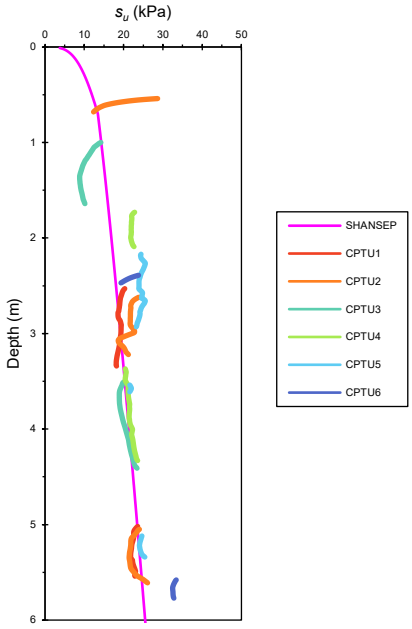

Figure 6.53. Comparison between the undrained shear strength determined by the SHANSEP model and the proposed empirical correlation.

7 CONCLUSIONS

This research was mainly aimed at assessing the feasibility and effectiveness of an innovative and sustainable design strategy for disposal of marine dredged sediments in confined facilities when they have to be integrated in land reclamation projects. To the purpose, the research proposed and experimented the subdivision of a CDF into sectors to be progressively filled and consolidated by means of PVDs-assisted preloading by a moving embankment. This solution was designed to significantly reduce the times required to make the reclaimed area available for its intended use and to optimise resources and costs. The application of the new strategy has been investigated in the CDF of the Ancona Harbour that was built to host marine contaminated dredged sediments.

An advantageous solution for sectorisation of a CDF has been set up by means of a special geotube filled with the sediments themselves. It minimises CDF volume losses and it is versatile due to possible overlapping. The placement and filling procedures of the geotube have been developed in the Ancona CDF resulting in a quick and easy installation. This solution, that is going to be used to divide the whole Ancona CDF into sectors, can be usefully employed for sectorisation of CDFs independently of the sediment nature.

On the first sector built in the Ancona CDF, a full scale instrumented test field has been created, which, first of all, allowed to set up the procedures and operational sequences of the consolidation technique (PVDs installation, construction of the moving embankment, etc.), particularly difficult on a very compressible soil as fine-grained dredged sediments just disposed in a CDF. The experiences documented in the present thesis can help future working in similar conditions.

The instrumented test field, combined with a wide set of laboratory and field investigation, allowed to study the full-scale consolidation process by the PVDs-assisted preloading with the moving embankment and to quantify the efficiency and the timing of the treatment for the future management and geotechnical design of the sectors in the Ancona CDF. With reference to these last aims, the following conclusions have been drawn.

- The coarse material of the moving embankment, to be reused in all the sectors, placed in thin lifts without compaction, has a unit weight of 17.5 kN/m^3; by this value the embankment height can be selected to obtain the desired loading level.

- Two months are sufficient to reach an average degree of consolidation of 80%, with drains installed according to a square pattern of 1 m per side. This period is significantly lower in the case of lenses of sandy sediments.
- The used type of PVD did not exhibit significant biological or physical clogging up to 4-5 months after installation. Therefore, this consolidation time can be acceptable depending on the time necessary or scheduled for the filling of adjacent sectors. This means that, in such cases, a spacing of the PVDs higher than 1 m can be usefully considered.
- Preloading of 85 kPa results in an increase in the cone tip resistance of the clay-like sediments from about 100 kPa to at least 500 kPa after about 2 months from its removal.
- Values of the recompression index in the range of 0.02-0.09, increasing with the vertical effective stress, were obtained on the consolidated clayey sediments, which can be used for settlement calculation under the service loads.

Monitoring of loads, settlements and excess pore pressures in the full-scale test field allowed also to validate the design assumptions and to verify existing theories in the literature for a reliable modelling of PVDs-assisted consolidation for fine-grained sediments in CDFs. The theory by Tang & Onitsuka (2000), which accounts for time-dependent loading, drain resistance and smear effect, both radial and vertical drainage (not negligible for small layer thickness, as in the case of concern), was found to well reproduce the consolidation process of the fine-grained dredged sediments, since the final vertical deformations resulted lower than 5% under the maximum applied effective vertical stress (85 kPa). However, accuracy in modelling the consolidation process can be further improved if consolidation constitutive laws are introduced in the model and large strains are taken into account. To this purpose, the hydraulic conductivity constitutive laws, originally presented by Felici (2017) for the sediments of the Ancona CDF, have been confirmed by further testing and will be used in the future development of the research to account for large strains.

As an alternative to complex modelling, basic pre-design charts have been derived and validated on the basis of the theory by Hansbo (1981), which can be useful to address design choices. The charts can be easily obtained from preliminary geotechnical characterisation of the disposed sediments to assess the relative influence of the three main variables involved in design of PVD-assisted consolidation in sectors of a CDF, i.e. drains spacing, preloading stress and waiting time.

Finally, an empirical s_u-q_t correlation has been proposed to estimate the undrained shear strength of clay-like dredged sediments after mechanical overconsolidation from CPTU results. Isotropically consolidated, undrained compression tests have been used as the calibration test. The resulting cone factors suggest the existence of a decreasing trend with the overconsolidation ratio, which has been considered in the s_u-q_t correlation. The results thus obtained agree

quite well with the SHANSEP empirical approach, whose reliability is well-established in the literature. Further research is necessary and will be developed in the near future in this field to corroborate the reliability of the proposed correlation that can be useful in geotechnical design for reusing CDFs hosting clay-like sediments after their consolidation by preloading.

REFERENCES

Aas, G., Lacasse, S., Lunne, T., & Høeg, K. (1986). Use of in situ tests for foundation design on clay. *Proceedings of the ASCE Specialty Conference In Situ '86: Use of In Situ Tests in Geotechnical Engineering, Blacksburg*, 1–30.

Anagnostopoulos, A., Koukis, G., Sabatakakis, N., & Tsiambaos, G. (2003). Empirical correlations of soil parameters based on Cone Penetration Tests (CPT) for Greek soils. *Geotechnical and Geological Engineering*, *21*(4), 377–387. https://doi.org/10.1023/B:GEGE.0000006064.47819.1a

Andresen, A., Berre, T., Kleven, A., & Lunne, T. (1979). Procedures used to obtain soil parameters for foundation engineering in the North Sea. *Marine Georesources & Geotechnology*, *3*(3), 201–266. https://doi.org/10.1080/10641197909379804

ASTM D2216-19. (2019). *Standard Test Method for Laboratory Determination of Water (Moisture) Content of Soil and Rock by Mass*. ASTM International. https://doi.org/10.1520/D2216-19.

ASTM D2435/D2435M-11. (2020). *Standard Test Methods for One-Dimensional Consolidation Properties of Soils Using Incremental Loading (Reapproved 2020)*. ASTM International. https://doi.org/10.1520/D2435

ASTM D2487-17. (2017). *Standard Practice for Classification of Soils for Engineering Purposes (Unified Soil Classification System)*. ASTM International. https://doi.org/10.1520/D2487-17E01.2

ASTM D2850-15. (2015). *Standard Test Method for Unconsolidated-Undrained Triaxial Compression Test on Cohesive Soils*. ASTM International. https://doi.org/10.1520/D2850-15.2

ASTM D3441-16. (2016). *Standard Test Method for Mechanical Cone Penetration Testing of Soils*. ASTM International. https://doi.org/10.1520/D3441-16

ASTM D4318-17. (2017). *Standard Test Methods for Liquid Limit, Plastic Limit, and Plasticity Index of Soils*. ASTM International. https://doi.org/10.1520/D4318-17E01.

ASTM D4542-15. (2015). *Standard Test Methods for Pore Water Extraction and Determination of the Soluble Salt Content of Soils by Refractometer*. ASTM International. https://doi.org/10.1520/D4542-15.2

ASTM D4767-11. (2020). *Standard Test Method for Consolidated Undrained Triaxial Compression Test for Cohesive Soils (Reapproved 2020)*. ASTM International. https://doi.org/10.1520/D4767-11R20.2

ASTM D5778-20. (2020). *Standard Test Method for Electronic Friction Cone and Piezocone Penetration Testing of Soils*. ASTM International. https://doi.org/10.1520/D5778-20.2

ASTM D6913/D6913M-17. (2017). *Standard Test Methods for Particle-Size Distribution (Gradation) of Soils Using Sieve Analysis*. ASTM International. https://doi.org/10.1520/D6913

ASTM D7928-21. (2021). *Standard Test Method for Particle-Size Distribution (Gradation) of Fine-Grained Soils Using the Sedimentation (Hydrometer) Analysis*. ASTM International. https://doi.org/10.1520/D7928-21E01

Atkinson, M. S., & Eldred, P. J. L. (1981). Consolidation of soil using vertical drains. *Géotechnique*, *31*(1), 33–43. https://doi.org/10.1680/geot.1981.31.1.33

Bailey, S. E., Estes, T. J., Schroeder, P. R., Myers, T. E., Rosati, J. D., Welp, T. L., Lee, L. T., Gwin, W. V., & Averett, D. E. (2010). *Sustainable Confined Disposal Facilities for Long-term Management of Dredged Material* (pp. 1–23). http://hdl.handle.net/11681/8726

Baligh, M. M. (1975). *Theory of deep site static cone penetration resistance (Publication No. R75-56)*.

Baligh, M. M., & Levadoux, J. N. (1986). Consolidation after undrained piezocone penetration. II: Interpretation. *Journal of Geotechnical Engineering*, *112*(7), 727–745. https://doi.org/10.1061/(ASCE)0733-9410(1986)112:7(727)

Barden, L., & Berry, P. L. (1965). Consolidation of Normally Consolidated Clay. *Journal of the Soil Mechanics and Foundations Division*, *91*(5), 15–35. https://doi.org/10.1061/JSFEAQ.0000790

Barron, R. A. (1944). *The influence of drain wells on the consolidation of fine-grained soils*.

Barron, R. A. (1948). Consolidation of fine-grained soils by drain wells by drain wells. *Transactions of the American Society of Civil Engineers*, *113*(1), 718-742 (Paper no. 2346). https://doi.org/10.1061/TACEAT.0006098

Bartholomeeusen, G., Sills, G. C., Znidarčić, D., Van Kesteren, W., Merckelbach, L. M., Pyke, R., Carrier, W. D., Lin, H., Penumadu, D., Winterwerp, H., Masala, S., & Chan, D. (2002). Sidere: numerical prediction of large-strain consolidation. *Géotechnique*, *52*(9), 639–648. https://doi.org/10.1680/geot.2002.52.9.639

Battaglio, M., Jamiolkowski, M., Lancellotta, R., & Maniscalco, R. (1981). Piezometer probe test in cohesive deposits. *Proceedings of the Session ASCE National Convention*.

Been, K., & Sills, G. C. (1981). Self-weight consolidation of soft soils: an experimental and theoretical study. *Géotechnique*, *31*(4), 519–535. https://doi.org/10.1680/geot.1981.31.4.519

Begemann, H. K. S. (1953). Improved method of determining resistance to adhesion by sounding through a loose sleeve placed behind the cone. *Proceedings of the 3rd International Conference on Soil Mechanics and Foundation Engineering*, Vol. 1, pp. 213–217.

Begemann, H. K. S. (1965). The friction jacket cone as an aid in determining the soil profile. *Proceedings of the 6th International Conference on Soil Mechanics and Foundation Engineering (ICSMFE)*, 1, 17–20.

Bellezza, I., & Fentini, R. (2008). Prefabricated vertical drains: A simplified design procedure. *Proceedings of the Institution of Civil Engineers: Ground Improvement*, *161*(4), 173–178. https://doi.org/10.1680/grim.2008.161.4.173

Berezantev, K., & Golubkov. (1961). Load bearing capacity and deformation of piles

foundations. *Proceedings of the 5th International Conference on Soil Mechanics and Foundation Engineering*, Vol. 2, 11-15.

Bergado, D. T., Asakami, H., Alfaro, M. C., & Balasubramaniam, A. S. (1991). Smear effects of vertical drains on soft Bangkok clay. *Journal of Geotechnical Engineering*, *117*(10), 1509–1530. https://doi.org/10.1061/(ASCE)0733-9410(1991)117:10(1509)

Biarez, J., Burel, M., & Wack, B. (1961). Contribution a l'étude de la force portante des fondations. *Proceedings of the 5th International Conference on Soil Mechanics and Foundation Engineering*, Vol. 1, 603-609.

Bjerrum, L. (1973). Problems of soil mechanics and construction on soft clays and structurally unstable soils (collapsible, expansive and others). *State-of-the-Art Rep. 8th International Conference on Soil Mechanics and Foundation Engineering, Moscow*, 3, 111–159. https://doi.org/10.1016/0148-9062(75)92238-x

Bo, M. W., Bawajee, R., Chu, J., & Choa, V. (2000). Investigation of smear zone around vertical drain. *Proceedings of the 3rd International Conference on Ground Improvement Techniques*, 109–114.

Burghignoli, A., & Calabresi, G. (1975). Determinazione del coefficiente di consolidazione di argille tenere su campioni di grandi dimensioni. *XII Italian National Conference*, Vol. 3 (in Italian).

Burland, J. B. (1990). On the compressibility and shear strength of natural clays. *Géotechnique*, *40*(3), 329–378. https://doi.org/10.1680/geot.1990.40.3.329

Burns, S. E., & Mayne, P. W. (1998). Monotonic and dilatory pore-pressure decay during piezocone tests in clay. *Canadian Geotechnical Journal*, *35*(6), 1063–1073. https://doi.org/10.1139/cgj-35-6-1063

Campanella, R. G., Gillespie, D., & Robertson, P. K. (1982). Pore pressures during cone penetration testing. *Proceedings of the 2nd European Symposium on Penetration Testing (ESOPT-2)*, 507–512.

Caquot, A., & Kérisel, J. (1956). *Traité de mécanique des sols*. Gauthier-Villars, Paris.

Cargill, K. W. (1982). *Consolidation of soft layers by finite strain analysis* (Issue Miscellaneous Paper GL-82-3). https://hdl.handle.net/11681/10139

Carrier, W. D., Bromwell, L. G., & Somogyi, F. (1983). Design capacity of slurried mineral waste ponds. *Journal of Geotechnical Engineering*, *109*(5), 699–716. https://doi.org/10.1061/(ASCE)0733-9410(1983)109:5(699)

Carrillo, N. (1942). Simple two and three dimensional case in the theory of consolidation of soils. *Journal of Mathematics and Physics*, *21*(1–4), 1–5. https://doi.org/10.1002/sapm19422111

Carter, J. P., Booker, J. R., & Yeung, S. K. (1986). Cavity expansion in cohesive frictional soils. *Géotechnique*, *36*(3), 349–358. https://doi.org/10.1680/geot.1986.36.3.349

Casagrande, A. (1936). The determination of the pre-consolidation load and its practical significance. *Proceedings of the 1st International Conference on Soil Mechanics and Foundation Engineering*, Vol. III, pp. 60–64.

Cetin, K. O., & Isik, N. S. (2007). Probabilistic assessment of stress normalization for CPT data. *Journal of Geotechnical and Geoenvironmental Engineering*, *133*(7), 887–897. https://doi.org/10.1061/(ASCE)1090-0241(2007)133:7(887)

Chai, J. C., Miura, N., & Sakajo, S. (1997). A theoretical study on smear effect around vertical drain. *Proceedings of the 14th International Conference on Soil Mechanics and Foundation Engineering*, 1581–1584.

Chai, J. C., Shen, S. L., Miura, N., & Bergado, D. T. (2001). Simple method of modeling PVD-improved subsoil. *Journal of Geotechnical and Geoenvironmental Engineering*, *127*(11), 965–972. https://doi.org/10.1061/(ASCE)1090-0241(2001)127:11(965)

Chen, C. (2001). Evaluating undrained shear strength of Klang clay from Cone penetration test. *Proceedings of the International Conference of In-Situ Measurement of Soil Properties and Case Histories*, 141–148.

Cheshomi, A. (2018). Empirical relationships of CPTu results and undrained shear strength. *Journal of GeoEngineering*, *13*(2), 49–57. https://doi.org/10.6310/jog.201806_13(2).1

Cianca, C. (2015). *Le vasche di colmata. Aspetti geotecnici*. PhD Dissertation, Università Politecnica delle Marche (in Italian).

Danziger, F. A. B., Almeida, M. S. S., & Sills, G. C. (1997). The significance of the strain path analysis in the interpretation of piezocone dissipation data. *Géotechniqueotechnique*, *47*(5), 901–914. https://doi.org/10.1680/geot.1997.47.5.901

Davis, E. H., & Raymond, G. P. (1965). A non-linear theory of consolidation. *Géotechnique*, *15*(2), 161–173. https://doi.org/10.1680/geot.1965.15.2.161

de Almeida, M. S. S., Marques, M. E. S., & Baroni, M. (2010). Geotechnical parameters of very soft clays from CPTu. *Proceedings of the 2nd International Symposium on Cone Penetration Testing (CPT'10)*, 01–08.

de Beer, E. E. (1948). Données concernant la résistance au cisaillement déduites des essais de pénétration en profondeur. *Géotechnique*, *1*(1), 22–40. https://doi.org/10.1680/geot.1948.1.1.22

de Beer, E. E. (1977). Static cone penetration testing in clay and loam. *Sondeer Symposium*.

de Lillis, A., & Miliziano, S. (2016). Geotechnical aspects of the design of the containment area of the port of Gaeta. *Italian Geotechnical Journal - Rivista Italiana Di Geotecnica*, *50*(4), 3-22 (in Italian).

de Lillis, A., Rotisciani, G. M., & Miliziano, S. (2020). Numerical investigation of the behaviour of hydraulically dredged fine-grained soils during and after filling of the containment facility of the port of Gaeta. *Geotextiles and Geomembranes*, *48*(4), 591–601. https://doi.org/10.1016/j.geotexmem.2020.03.005

Diplas, P., & Papanicolaou, A. N. (1997). Batch analysis of slurries in zone settling regime. *Journal of Environmental Engineering*, *123*(7), 659–667. https://doi.org/10.1061/(ASCE)0733-9372(1997)123:7(659)

Douglas, B. J., & Olsen, R. S. (1981). Soil classification using electric cone penetrometer. *Proceedings of Conference on Cone Penetration Testing and Experience*, 209–227.

Duan, W., Cai, G., Liu, S., Puppala, A. J., & Chen, R. (2019). In-situ evaluation of undrained shear strength from seismic piezocone penetration tests for soft marine clay in Jiangsu, China. *Transportation Geotechnics*, *20*. https://doi.org/10.1016/j.trgeo.2019.100253

Dubin, B., & Moulin, G. (1986). Influence of a critical gradient on the consolidation of clays. In *Consolidation of soils: testing and evaluation, ASTM STP 892* (pp. 354–377).

Durgunoglu, H. T., & Mitchell, J. K. (1975). Static penetration resistance of soils. I: Analysis. *Proceedings of the ASCE Specialty Conference on In Situ Measurement of Soil Properties*, Vol. 1, 151-171.

Eid, H. T., & Stark, T. D. (1998). Undrained shear strength from cone penetration tests. *Proceedings of the 1st International Conference on Site Characterization*, *98*, 1021–1025. https://doi.org/10.1016/0148-9062(91)92413-s

Eslami, A., & Fellenius, B. H. (1997). Pile capacity by direct CPT and CPTu methods applied to 102 case histories. *Canadian Geotechnical Journal*, *34*(6), 886–904. https://doi.org/10.1139/t97-056

Eslami, A., & Fellenius, B. H. (2004). CPT and CPTu data for soil profile interpretation: review of methods and a proposed new approach. *Iranian Journal of Science & Technology*, *28*(No. B1), 69–86.

Felici, M. (2017). *Aspetti geotecnici connessi con la gestione dei sedimenti marini dragati*. PhD Dissertation, Università Politecnica delle Marche (in Italian).

Felici, M., Domizi, J., & Fratalocchi, E. (2019). Consolidation of dredged sediments in a confined disposal facility: Hydraulic conductivity constitutive relations. In *Environmental Science and Engineering*. Springer Singapore. https://doi.org/10.1007/978-981-13-2221-1_27

Felici, M., Fratalocchi, E., Di Sante, M., Pasqualini, F., & Pasqualini, E. (2021). PVD-assisted consolidation of dredged sediments in a CDF: design of the test field. *Japanese Geotechnical Society Special Publication*, *9*(4), 124–129. https://doi.org/10.3208/jgssp.v09.cpeg092

Felici, M., Pasqualini, F., Bellezza, I., Pasqualini, E., & Fratalocchi, E. (2022). Optimization of consolidation procedures for dredged fine sediments in confined disposal facilities. *Proceedings of the 20th International Conference on Soil Mechanics and Geotechnical Engineering*.

Fellenius, B. H. (2014). *Basics of Foundation Design* (Electronic).

Fellenius, B. H., & Castonguay, N. G. (1985). *The efficiency of band shaped drains: a full scale laboratory study. Report to National Research Council and the Industrial Research Assistance Programme*.

Finnie, I. M. S., & Randolph, M. (1994). Punch-through and liquefaction induced failure of shallow foundations on calcareous sediments. *Proceedings of the 7th International Conference on the Behaviour of Offshore Structure*, 217–230.

Fox, P. J., & Berles, J. D. (1997). CS2: a piecewise-linear model for large strain consolidation. *International Journal for Numerical and Analytical Methods in Geomechanics*, *21*(7), 453–475. https://doi.org/10.1002/(SICI)1096-9853(199707)21:7<453::AID-NAG887>3.0.CO;2-B

Gebreselassie, B. (2003). *Experimental, analytical and numerical investigations of excavations in normally consolidated soft soils*. PhD Dissertation, University of Kassel.

Gibson, R. E. (1950). Discussion to "The bearing capacity of screw piles and screwcrete cylinders" by G. Wilson. *Journal of the Institute of Civil Engineers*, *34*, 382–383.

Gibson, R. E., England, G. L., & Hussey, M. J. L. (1967). The theory of one-dimensional consolidation of saturated clays. I. Finite non-linear consolidation of thin homogeneous

layers. *Géotechnique*, *17*(3), 261–273. https://doi.org/10.1680/geot.1967.17.3.261

Gibson, R. E., Schiffman, R. L., & Cargill, K. W. (1981). The theory of one-dimensional consolidation of saturated clays. II. Finite nonlinear consolidation of thick homogeneous layers. *Canadian Geotechnical Journal*, *18*(2), 280–293. https://doi.org/10.1139/t81-030

Govindaraju, R. S., Ramireddygari, S. R., Shrestha, P. L., & Roig, L. C. (1999). Continuum bed model for estuarine sediments based on nonlinear consolidation theory. *Journal of Hydraulic Engineering*, *125*(3), 300–304. https://doi.org/10.1061/(ASCE)0733-9429(1999)125:3(300)

Hansbo, S. (1960). *Consolidation of clay, with special reference to influence of vertical sand drains*. PhD Dissertation, Chalmers University of Technology.

Hansbo, S. (1979). Consolidation of clay by band-shaped prefabricated drains. *Ground Engineering*, *12*(5), 16–25.

Hansbo, S. (1981). Consolidation of fine-grained soils by prefabricated drains. *Proceedings of the 10th International Conference on Soil Mechanics and Foundation Engineering*, *3*, 677–682. https://doi.org/10.1016/0148-9062(84)91874-6

Hansbo, S. (1997). Aspects of vertical drain design: Darcian or non-Darcian flow. *Géotechnique*, *47*(5), 983–992. https://doi.org/10.1680/geot.1997.47.5.983

Hansbo, S., Jamiolkowski, M., & Kok, L. (1981). Consolidation by vertical drains. *Géotechnique*, *31*(1), 45–66. https://doi.org/10.1680/geot.1981.31.1.45

Harris, W., & Norman White, G. (2015). X-ray Diffraction Techniques for Soil Mineral Identification. In *Methods of soil analysis part 5 - Mineralogical methods* (pp. 81–115). https://doi.org/10.2136/sssabookser5.5.c4

Hawlader, B. C., Muhunthan, B., & Imai, G. (2008). State-dependent constitutive model and numerical solution of self-weight consolidation. *Géotechnique*, *58*(2), 133–141. https://doi.org/10.1680/geot.2008.58.2.133

Head, K. H., & Epps, R. J. (2011). *Manual of Soil Laboratory Testing. Volume 2: Permeability, Shear Strength and Compressibility tests* (Third Edit, Vol. 2, Issue 3). Whittles Publishing. https://doi.org/10.2113/gseegeosci.21.3.247

Holtz, R. D., & Holm, G. (1973). Excavation and sampling around some sand drains in Skå-Edeby, Sweden. *Proceedings of the Nordic Geotechnical Meeting*.

Holtz, R. D., & Kovacs, W. D. (1981). *An Introduction to Geotechnical Engineering*. Prentice-Hall.

Hong, S. J., Lee, M. J., Kim, J. J., & Lee, W. J. (2010). Evaluation of undrained shear strength of Busan clay using CPT. *Proceedings of the 2nd International Symposium on Cone Penetration Testing (CPT'10)*, *2*, 313–320.

Houlsby, G. (1988). Discussion session contribution. In *Penetration Testing in the U.K.* (pp. 141–146). Thomas Telford, London.

Houlsby, G., & Teh, C. I. (1988). Analysis of the piezocone in clay. *Proceedings of International Symposium on Penetration Testing 1988*, *2*, 778–783.

Hu, G. C. Y. (1965). Bearing capacity of foundations with overburden shear. *Sols Soils*, *13*, 11–18.

Idriss, I. M., & Boulanger, R. W. (2004). Semi-empirical procedures for evaluating liquefaction

potential during earthquakes. *Proceedings of the 11th International Conference on Soil Dynamics and Earthquake Engineering, ASCE*, 32–56.

Indraratna, B., & Redana, I. W. (1998). Laboratory determination of smear zone due to vertical drain installation. *Journal of Geotechnical and Geoenvironmental Engineering*, *124*(2), 180–184. https://doi.org/10.1061/(ASCE)1090-0241(1998)124:2(180)

Jamiolkowski, M. (1995). Opening address. *Proceedings of the International Symposium on Cone Penetration Testing (CPT'95)*, Vol. 3, pp. 7–15.

Jamiolkowski, M., & Robertson, P. K. (1988). Closing address: future trends for penetration testing. *Geotechnology Conference: Penetration Testing in the UK*, 321–342.

Janbu, N. (1965). Consolidation of clay layers based on non-linear stress-strain. *Proceedings 6th International Conference on Soil Mechanics and Foundation Engineering*, Vol. 2, pp. 83–87.

Janbu, N., Bjerrum, L., & Kjaernsli, B. (1956). *Soil mechanics applied to some engineering problems*. Norwegian Geotechnical Institute.

Janbu, N., & Senneset, K. (1974). Effective stress interpretation of in situ static penetration tests. *Proceedings of the 1st European Symposium on Penetration Testing*, Vol. 2, pp. 181–193.

Jefferies, M. G., & Davies, M. P. (1993). Use of CPTu to estimate equivalent SPT N60. *Geotechnical Testing Journal*, *16*(4), 458. https://doi.org/10.1520/GTJ10286J

Jones, G. A., & Rust, E. (1982). Piezometer penetration testing, CUPT. *Proceedings of the 2nd European Symposium on Penetration Testing (ESOPT-2)*, 2, 607–614.

Karlsrud, K., Lunne, T., & Brattlien, K. (1996). Improved CPTU interpretations based on block samples. *Proceedings of the 12th Nordic Geotechnical Conference*, 195–201.

Karlsrud, K., Lunne, T., Kort, D. A., & Strandvik, S. (2005). CPTU correlations for clays. *Proceedings of the 16th International Conference on Soil Mechanics and Geotechnical Engineering: Geotechnology in Harmony with the Global Environment*, *2*, 693–702. https://doi.org/10.3233/978-1-61499-656-9-693

Keaveny, J. M., & Mitchell, J. K. (1986). Strength of fine-grained soils using the piezocone. *Use of In-Situ Tests in Geotechnical Engineering*, 668–699.

Kjekstad, O., Lunne, T., & Clausen, C. J. F. (1978). Comparison between in situ cone resistance and laboratory strength for overconsolidated North Sea clays. *Marine Geotechnology*, *3*(1), 23–36. https://doi.org/10.1080/10641197809379792

Kjellman, W. (1948a). Accelerating consolidation of fine-grained soils by means of cardboard wicks. *Proceedings of the 2nd International Conference on Soil Mechanics and Foundation Engineering*, 302–305.

Kjellman, W. (1948b). Consolidation of fine-grained soils by drain wells. *Transactions of the American Society of Civil Engineers*, *113*(1), 748-751 (Contribution to the discussion on Paper.

Konrad, J. M., & Law, K. T. (1987). Undrained shear strength from piezocone tests. *Canadian Geotechnical Journal*, *24*(3), 392–405. https://doi.org/10.1139/t87-050

Koppula, S. D., & Morgenstern, N. R. (1982). On the consolidation of sedimenting clays. *Canadian Geotechnical Journal*, *19*(3), 260–268. https://doi.org/10.1139/t82-033

Koumoto, T., & Kaku, K. (1982). Three-dimensional analysis of static cone penetration into

clay. *Proceedings of the 2nd European Symposium on Penetration Testing (ESOPT-2)*, 2, 635–640.

Krizek, R. J., & Somogyi, F. (1984). Perspectives on modelling consolidation of dredged materials. *Sedimentation Consolidation Models-Predictions and Validation*, 296–332, ASCE.

Kulhawy, F. H., & Mayne, P. W. (1990). *Manual on estimating soil properties for foundation design (No. EPRI-EL-6800)*.

La Rochelle, P., Zebdi, P. M., Leroueil, S., Tavenas, F., & Virely, D. (1988). Piezocone tests in sensitive clays of eastern Canada. *Proceedings of the 1st International Symposium on Penetration Testing (ISOPT-1)*, 2, 831–841.

Ladanyi, B., & Johnston, G. H. (1974). Behavior of circular footings and plate anchors embedded in permafrost. *Canadian Geotechnical Journal*, *11*(4), 531–553. https://doi.org/10.1139/t74-057

Ladd, C. C. (1991). Stability evaluation during staged construction. *Journal of Geotechnical Engineering*, *117*(4), 540–615. https://doi.org/10.1061/(ASCE)0733-9410(1991)117:4(540)

Ladd, C. C., & Foott, R. (1974). New design procedure for stability of soft clays. *Journal of the Geotechnical Engineering Division*, *ASCE 100*(7), 763–786. https://doi.org/10.1061/AJGEB6.0000066

Ladd, C. C., Foott, R., Ishihara, K., Schlosser, F., & Poulos, H. G. (1977). Stress-Deformation and Strength Characteristics. *Proceedings of the 9th International Conference on Soil Mechanics and Foundation Engineering*.

Ladd, C. C., & Lambe, T. W. (1964). The strength of 'undisturbed' clay determined from undrained tests. In *Laboratory Shear Testing of Soils, STP 361, ASTM* (pp. 342–371).

Lancellotta, R. (2008). *Geotechnical Engineering* (Taylor & Francis (ed.); Second Edi). https://doi.org/10.4324/9780203927830

Leo, C. J. (2004). Equal strain consolidation by vertical drains. *Journal of Geotechnical and Geoenvironmental Engineering*, *130*(3), 316–327. https://doi.org/10.1061/(asce)1090-0241(2004)130:3(316)

Levadoux, J. N., & Baligh, M. M. (1986). Consolidation after undrained piezocone penetration. I: Prediction. *Journal of Geotechnical Engineering*, *112*(7), 707–726. https://doi.org/10.1061/(ASCE)0733-9410(1986)112:7(707)

Liu, J., & Znidarčić, D. (1991). Modeling one-dimensional compression characteristics of soils. *Journal of Geotechnical Engineering*, *117*(1), 162–169. https://doi.org/10.1061/(ASCE)0733-9410(1991)117:1(162)

Lo, K. Y. (1960). Discussion on Rowe, Measurement of the coefficient of consolidation of lacutrine clay. *Géotechnique*, *10*(1), 36–39.

Long, R. P., & Covo, A. (1994). Equivalent diameter of vertical drains with an oblong cross section. *Journal of Geotechnical Engineering*, *120*(9), 1625–1630. https://doi.org/10.1061/(ASCE)0733-9410(1994)120:9(1625)

Low, H. E., Lunne, T., Andersen, K. H., Sjursen, M. A., Li, X., & Randolph, M. F. (2010). Estimation of intact and remoulded undrained shear strengths from penetration tests in soft clays. *Géotechnique*, *60*(11), 843–859. https://doi.org/https://doi.org/10.1680/geot.9.P.017

Lunne, T., Christoffersen, H. P., & Tjelta, T. I. (1985). Engineering use of Piezocone data in North Sea clays. *Proceedings of the 11th International Conference on Soil Mechanics and Foundation Engineering, San Francisco*, 2, 907–912. https://doi.org/10.1007/978-3-319-73568-9_174

Lunne, T., Eide, O., & de Ruiter, J. (1976). Correlation between cone resistance and vane shear strength in some Scandinavian soft to medium stiff clays. *Canadian Geotechnical Journal*, *13*(4), 430–441. https://doi.org/10.1139/t78-044

Lunne, T., & Kleven, A. (1981). Role of CPT in North Sea foundation engineering. *Session at the ASCE National Convention: Cone Penetration Testing and Materials, St. Louis*, 76–107.

Lunne, T., Robertson, P. K., & Powell, J. J. M. (1997). Cone Penetration Testing in Geotechnical Practice. In *Blackie Academic & Professional*.

Mayne, P. W. (2007). *Cone penetration testing state-of-practice. NCHRP Project 20-05*.

Mayne, P. W. (2014). Interpretation of geotechnical parameters from seismic piezocone tests. In P. K. Robertson & K. I. Cabal (Eds.), *Proceedings of the 3rd International Symposium on Cone Penetration Testing (CPT'14)* (pp. 47–73).

Mayne, P. W., Kulhawy, F. H., & Kay, J. N. (1990). Observations on the development of pore-water stresses during piezocone penetration in clays. *Canadian Geotechnical Journal*, *27*(4), 418–428. https://doi.org/10.1139/t90-058

McNabb, A. (1960). A mathematical treatment of one-dimensional soil consolidation. *Quarterly of Applied Mathematics*, *17*(4), 337–347. https://doi.org/10.1090/qam/113405

McVay, M., Townsend, F., & Bloomquist, D. (1986). Quiescent consolidation of phosphatic waste clays. *Journal of Geotechnical Engineering*, *112*(11), 1033–1049. https://doi.org/10.1061/(ASCE)0733-9410(1986)112:11(1033)

Merckelbach, L. M., & Kranenburg, C. (2004). Equations for effective stress and permeability of soft mud–sand mixtures. *Géotechnique*, *54*(4), 235–243. https://doi.org/10.1680/geot.2004.54.4.235

Meyerhof, G. G. (1951). The ultimate bearing capacity of foundations. *Géotechnique*, *2*(4), 301–332. https://doi.org/10.1680/geot.1951.2.4.301

Meyerhof, G. G. (1961). The ultimate bearing capacity of wedge-shaped foundations. *Proceedings of the 5th International Conference on Soil Mechanics and Foundation Engineering*, 2, 105–109.

Meyerhof, G. G. (1976). Bearing capacity and settlement of pile foundations. *Journal of the Geotechnical Engineering Division*, *102*(3), 197–228. https://doi.org/10.1061/AJGEB6.0000243

Mikasa, M. (1965). *The consolidation of soft clay-a new consolidation theory and its application*.

Miller, R. J., & Low, P. F. (1963). Threshold gradient for water flow in clay systems. *Soil Science Society of America Journal*, *27*(6), 605–609. https://doi.org/10.2136/sssaj1963.03615995002700060013x

Mitchell, J. K., & Soga, K. (2005). *Fundamentals of Soil Behavior* (Third Edit). John Wiley & Sons.

Molle, J. (2005). *The accuracy of the interpretation of CPT-based soil classification methods in soft soils*. M.Sc. Thesis, Delft University of Technology.

Monte, J. L., & Krizek, R. J. (1976). One-dimensional mathematical model for large-strain consolidation. *Géotechnique*, *26*(3), 495–510. https://doi.org/10.1680/geot.1976.26.3.495

Moss, R. E. S., Seed, R. B., & Olsen, R. S. (2006). Normalizing the CPT for overburden stress. *Journal of Geotechnical and Geoenvironmental Engineering*, *132*(3), 378–387. https://doi.org/10.1061/(ASCE)1090-0241(2006)132:3(378)

Olsen, R. S., & Malone, P. G. (1988). Soil classification and site characterization using the cone penetrometer test. *Proceedings of the 1st International Symposium on Penetration Testing (ISOPT-1)*, 887–893.

Olson, R. E. (1977). Consolidation under time dependent loading. *Journal of the Geotechnical Engineering Division*, *103*(1), 55–60. https://doi.org/10.1061/AJGEB6.0000369

Onoue, A. (1988). Consolidation by vertical drains taking well resistance and smear into consideration. *Soils and Foundations*, *28*(4), 165–174. https://doi.org/10.3208/sandf1972.28.4_165

Parez, L., & Fauriel, R. (1988). Le piezocone améliorations apportées à la reconnaissance des sols. *Revue Française de Géotechnique*, *44*, 13–27. https://doi.org/10.1051/geotech/1988044013

Pasqualini, F., Felici, M., Bellezza, I., & Fratalocchi, E. (2021). Ottimizzazione delle procedure di consolidazione di sedimenti. *Atti Dell'Incontro Annuale Dei Ricercatori Di Geotecnica 2021 – IARG2021_online*, *November*, (in Italian).

Powell, J. J. M., & Quarterman, R. S. T. (1988). The interpretation of cone penetration tests in clays, with particular reference to rate effects. *Proceedings of the 1st International Symposium on Penetration Testing (ISOPT-1)*, 903–910.

Prandtl, L. (1920). Über die härte plastischer körper. *Nachrichten von Der Gesellschaft Der Wissenschaften Zu Göttingen, Mathematisch-Physikalische Klasse*, 74–85.

Rad, N. S., & Lunne, T. (1988). Direct correlations between piezocone test results and undrained shear strength of clay. *Proceedings of the 1st International Symposium on Penetration Testing (ISOPT-1)*, 2, 911–917.

Randolph, M. F., & Wroth, C. P. (1979). An analytical solution for the consolidation around a driven pile. *International Journal for Numerical and Analytical Methods in Geomechanics*, *3*(3), 217–229. https://doi.org/10.1002/nag.1610030302

Rémai, Z. (2013). Correlation of undrained shear strength and CPT resistance. *Periodica Polytechnica Civil Engineering*, *57*(1), 39–44. https://doi.org/10.3311/PPci.2140

Richart, F. E. (1957). A review of the theories for sand drains. *Journal of the Soil Mechanics and Foundations Division*, *83*(3), 1301–1. https://doi.org/10.1061/JSFEAQ.0000064

Rixner, J. J., Kraemer, S. R., & Smith, A. D. (1986). *Prefabricated vertical drains, vol. 1: Engineering Guidelines (No. FHWA/RD-86/168)*.

Robertson, P. K. (1990). Soil classification using the cone penetration test. *Canadian Geotechnical Journal*, *27*(1), 151–158. https://doi.org/10.1139/t90-014

Robertson, P. K. (2009). Interpretation of cone penetration tests - A unified approach. *Canadian Geotechnical Journal*, *46*(11), 1337–1355. https://doi.org/10.1139/T09-065

Robertson, P. K. (2012). Interpretation of In-situ Tests — Some Insights. *Proceedings of the 4th International Conference on Site Characterization*, 1–22.

Robertson, P. K. (2016). Cone penetration test (CPT)-based soil behaviour type (SBT) classification system — An update. *Canadian Geotechnical Journal*, *53*(12), 1910–1927. https://doi.org/10.1139/cgj-2016-0044

Robertson, P. K., & Campanella, R. G. (1983). Interpretation of cone penetration tests. Part I: Sand. *Canadian Geotechnical Journal*, *20*(4), 718–733. https://doi.org/10.1139/t83-078

Robertson, P. K., Campanella, R. G., Gillespie, D., & Greig, J. (1986). Use of Piezometer Cone Data. In S. Clemence (Ed.), *Proceedings of American Society of Civil Engineers, ASCE, In-Situ 86 Specialty Conference* (pp. 1263–1280). Geotechnical Special Publication GSP No. 6.

Robertson, P. K., Sully, J. P., Woeller, D. J., Lunne, T., Powell, J. J. M., & Gillespie, D. G. (1992). Estimating coefficient of consolidation from piezocone tests. *Canadian Geotechnical Journal*, *29*(4), 539–550. https://doi.org/10.1139/t92-061

Robertson, P. K., & Wride, C. E. (1998). Evaluating cyclic liquefaction potential using the cone penetration test. *Canadian Geotechnical Journal*, *35*(3), 442–459. https://doi.org/10.1139/t98-017

Rollin, A. L., & Lombard, G. (1988). Mechanisms affecting long-term filtration behavior of geotextiles. *Geotextiles and Geomembranes*, *7*(1–2), 119–145. https://doi.org/10.1016/0266-1144(88)90021-0

Runesson, K., Tägnforss, H., & Wiberg, N. E. (1977). *Finite Element analysis of some geotechnical and geohydrological problems*.

Salgado, R. (1993). *Analysis of penetration resistance in sands*. PhD Dissertation, University of California, Berkeley, Berkeley, California.

Salgado, R. (2022). *The Engineering of Foundations, Slopes and Retaining Structures* (2nd Edit.). CRC Press.

Sanglerat, G., Nhim, T. V., Sejourne, M., & Andina, R. (1974). Direct soil classification by static penetrometer with special friction sleeve. *Proceedings of the 1st European Symposium on Penetration Testing (ESOPT-1)*, 2.2, 337–344.

Schiffman, R. L. (1980). Finite and infinitesimal strain consolidation. *Journal of the Geotechnical Engineering Division*, *106*(2), 203–207. https://doi.org/10.1061/AJGEB6.0000924

Schiffman, R. L., & Gibson, R. E. (1964). Consolidation of nonhomogeneous clay layers. *Journal of the Soil Mechanics and Foundations Division*, *90*(5), 1–30. https://doi.org/10.1061/JSFEAQ.0000648

Schmertmann, J. H. (1975). Measurement of in situ shear strength, State-of-the-Art Report. *Proceedings, ASCE Specialty Conference on In Situ Measurement of Soil Properties*, Vol. 2, pp. 57–138.

Schmertmann, J. H. (1978). *Guidelines for cone penetration test: performance and design (Publication No. FHWA TS-78-209)*.

Schnaid, F. (2008). *In Situ Testing in Geomechanics*. https://doi.org/10.1201/9781482266054

Searle, I. W. (1979). The interpretation of Begemann friction jacket cone results to give soil

types and design parameters. *Proceedings of the 7th European Conference on Soil Mechanics and Foundation Engineering (ECSMFE)*, 2265–2270.

Senneset, K., Janbu, N., & Svanø, G. (1982). Strength and deformation parameters from cone penetration tests. *Proceedings of the 2nd European Symposium on Penetration Testing (ESOPT-2)*, 863–870.

Shen, S. L., Chai, J. C., Hong, Z. S., & Cai, F. X. (2005). Analysis of field performance of embankments on soft clay deposit with and without PVD-improvement. *Geotextiles and Geomembranes*, *23*(6), 463–485. https://doi.org/10.1016/j.geotexmem.2005.05.002

Shin, Y. J., & Kim, D. (2011). Assessment of undrained shear strength based on Cone Penetration Test (CPT) for clayey soils. *KSCE Journal of Civil Engineering*, *15*(7), 1161–1166. https://doi.org/10.1007/s12205-011-0808-6

Sivaram, B., & Swamee, P. K. (1977). A computational method for consolidation-coefficient. *Soils and Foundations*, *17*(2), 48–52. https://doi.org/10.3208/sandf1972.17.2_48

Skempton, A. W. (1951). The Bearing Capacity of Clays. *Proceedings of the Building Research Congress, London*, 1, 180–189. https://doi.org/10.1680/sposm.02050.0008

Somogyi, F. (1979). *Analysis and prediction of phosphatic clay consolidation: implementation package*.

Stark, T. D., & Delashaw, J. E. (1990). Correlations of unconsolidated-undrained triaxial tests and cone penetration test. *Transportation Research Record*, *1278*, 96–102. http://onlinepubs.trb.org/Onlinepubs/trr/1990/1278/1278-012.pdf

Sully, J. P., Robertson, P. K., Campanella, R. G., & Woeller, D. J. (1999). An approach to evaluation of field CPTU dissipation data in overconsolidated fine-grained soils. *Canadian Geotechnical Journal*, *36*(2), 369–381. https://doi.org/10.1139/cgj-36-2-369

Tang, X. W., & Onitsuka, K. (2000). Consolidation by vertical drains under time-dependent loading. *International Journal for Numerical and Analytical Methods in Geomechanics*, *24*(9), 739–751. https://doi.org/10.1002/1096-9853(20000810)24:9<739::AID-NAG94>3.0.CO;2-B

Tavenas, F., Leroueil, S., Roy, M., & Verruijt, A. (1982). The piezocone test in clays: use and limitations. *Proc. of 2nd European Symposium on Penetration Testing, Amsterdam*, 889–894.

Taylor, D. W. (1948). *Fundamentals of Soil Mechanics*. John Wiley & Sons, New York.

Teh, C. I. (1987). *An Analytical Study of Cone Penetration Test*. PhD Dissertation, University of Oxford.

Teh, C. I., & Houlsby, G. (1988). Analysis of the cone penetration test by the strain path method. *Proceedings of the 6th International Conference on Numerical Methods in Geomechanics Volume 1*.

Teh, C. I., & Houlsby, G. T. (1991). An analytical study of the cone penetration test in clay. *Géotechnique*, *41*(1), 17–34. https://doi.org/10.1680/geot.1991.41.1.17

Terzaghi, K. (1925). *Erdbaumechanik auf bodenphysikalisher Grundlage*. F. Deuticke.

Terzaghi, K. (1943). *Theoretical soil mechanics*. John Wiley & Sons, New York.

Terzaghi, K., Peck, R. B., & Mesri, G. (1996). *Soil mechanics in engineering practice* (Third Edit). John Wiley & Sons. https://doi.org/10.1097/00010694-194911000-00029

Torstensson, B. A. (1975). Pore pressure sounding instrument. *Proceedings of the ASCE Specialty Conference on In Situ Measurement of Soil Properties*, 48–54.

Torstensson, B. A. (1977). The pore pressure probe. *Nordiske Geotekniske*, 1–15.

van Kessel, T., & van Kesteren, W. G. M. (2002). Gas production and transport in artificial sludge depots. *Waste Management*, *22*(1), 19–28. https://doi.org/10.1016/S0956-053X(01)00021-6

Vesic, A. S. (1963). Bearing capacity of deep foundations in sand. In *Highway research board record No. 39*.

Vesic, A. S. (1972). Expansion of cavities in infinite soil mass. *ASCE Journal of the Soil Mechanics and Foundations Division*, *98*(SM3), 265–290.

Vesic, A. S. (1975). *Principles of Pile Foundation Design*. Duke University.

Vesic, A. S. (1977). *Design of pile foundations*.

Vos, J. D. (1982). The practical use of CPT in soil profiling. *Proceedings of the 2nd European Symposium on Penetration Testing (ESOPT-2)*, 2, 933–939.

Walker, R., & Indraratna, B. (2006). Vertical drain consolidation with parabolic distribution of permeability in smear zone. *Journal of Geotechnical and Geoenvironmental Engineering*, *132*(7), 937–941. https://doi.org/10.1061/(ASCE)1090-0241(2006)132:7(937)

Watson, P. G., Suemasa, N., & Randolph, M. F. (2000). Evaluating Undrained Shear Strength Using the Vane Shear Apparatus. *Proceedings of the 10th International Offshore and Polar Engineering Conference*.

Winterwerp, J. C. (1999). *On the dynamics of high-concentrated mud suspensions*. PhD Dissertation, Delft University of Technology.

Wroth, C. P. (1984). The interpretation of in situ soil tests. *Géotechnique*, *34*(4), 449–489. https://doi.org/10.1680/geot.1984.34.4.449

Wroth, C. P. (1988). Penetration testing — A more rigorous approach to interpretation. *Proceedings of the 1st International Symposium on Penetration Testing (ISOPT-1)*, 303–311.

Xiao, D. (2001). *Consolidation of soft clay using vertical drains*. PhD Dissertation.

Xie, K. H. (1987). *Sand drained ground: analytical and numerical solutions and optimal design*. PhD Dissertation, Zhejiang University.

Yamauchi, H., Imai, G., Watanabe, K., & Ogata, K. (1991). Sedimentation-consolidation analysis of pump-dredged cohesive soils. *Proceedings of the International Conference on Geotechnical Engineering for Coastal Development (Geo-Coast '91)*, 129–134.

Yang, S. L., Lunne, T., Andersen, K. H., D'Ignazio, M., & Yetginer, G. (2019). Undrained shear strength of marine clays based on CPTU data and SHANSEP parameters. *Proceedings of the XVII European Conference on Soil Mechanics and Geotechnical Engineering (ECSMGE-2019) 'Geotechnical Engineering Foundation of the Future'*. https://doi.org/10.32075/17ECSMGE-2019-0048

Yasufuku, N., & Hyde, A. F. L. (1995). Pile end-bearing capacity in crushable sands. *Géotechnique*, *45*(4), 663–676.

Yoshikuni, H., & Nakanodo, H. (1974). Consolidation of soils by vertical drain wells with finite

permeability. *Soils and Foundations*, *14*(2), 35–46. https://doi.org/10.3208/sandf1972.14.2

Yu, H. S. (1993). Discussion: “Singular Plastic Fields in Steady Penetration of a Rigid Cone”. *Journal of Applied Mechanics*, *60*(4), 1061–1062.

Yu, H. S. (2000). *Cavity Expansion Methods in Geomechanics*. Springer Science & Business Media. https://doi.org/10.1007/978-94-015-9596-4

Yu, H. S., & Mitchell, J. K. (1998). Analysis of Cone Resistance: Review of Methods. *Journal of Geotechnical and Geoenvironmental Engineering*, *124*(2), 140–149. https://doi.org/10.1061/(asce)1090-0241(1999)125:9(812)

Zhang, G., Robertson, P. K., & Brachman, R. W. I. (2002). Estimating liquefaction-induced ground settlements from CPT for level ground. *Canadian Geotechnical Journal*, *39*(5), 1168–1180. https://doi.org/10.1139/t02-047

Zhu, G., & Yin, J. H. (2004). Consolidation analysis of soil with vertical and horizontal drainage under ramp loading considering smear effects. *Geotextiles and Geomembranes*, *22*(1–2), 63–74. https://doi.org/10.1016/S0266-1144(03)00052-9

Zou, Y. (1996). A non-linear permeability relation depending on the activation energy of pore liquid. *Géotechnique*, *46*(4), 769–774. https://doi.org/10.1680/geot.1996.46.4.769